UNIVERSITY OF SOUTHAMPTON

FINITE ELEMENT ANALYSIS OF THE PROXIMAL IMPLANTED TIBIA IN RELATION TO IMPLANT LOOSENING

Antonio Perillo-Marcone

Doctor of Philosophy

Faculty of Engineering and Applied Science

Bioengineering Sciences and Research Group

December 2001

UNIVERSITY OF SOUTHAMPTON

ABSTRACT

FACULTY OF ENGINEERING AND APPLIED SCIENCE
BIOENGINEERING SCIENCE RESEARCH GROUP

Doctor of Philosophy

FINITE ELEMENT ANALYSIS OF THE PROXIMAL IMPLANTED TIBIA IN RELATION TO IMPLANT LOOSENING

by Antonio Perillo-Marcone

Aseptic loosening of the tibial component is the main cause of failure of TKR. RSA can be used during the first two years after surgery to predict the risk of component loosening at five or more years. Furthermore, it has been suggested that migration of the tibial component can be determined at the time of surgery. Fatigue failure of cancellous bone has been proposed as a mechanism of implant migration. In particular, it has been suggested that the initial cancellous bone stresses at the bone-implant interface may be able to predict the likelihood of migration (and hence subsequent loosening).

Tibial component alignment is one of the parameters that have most influence on implant loosening. The effect of varus-valgus and antero-posterior angles on the cancellous bone stress at the bone-implant interface was examined by means of finite element analysis. The lowest stress was obtained when the tibial tray was orientated in valgus. Moreover, the larger the valgus tilt was, the lower were the stresses within the cancellous bone. It was observed that higher stresses were produced with a posterior angle, as compared to a perfectly horizontal tibial cut. These findings were in line with clinical observations related to prosthesis orientations.

In general, previously reported finite element models did not include patient specific data. Therefore, a comprehensive convergence study was performed in order to determine the finite element mesh characteristics (element size) and material property distribution (number of material groups) necessary to accurately describe the stress and risk ratio distributions at the bone-implant interface in patient-specific FE models. It was observed that with a logarithmic discretisation of the material properties within the bone convergence was reached with fewer material groups, as compared to the linear discretisation. Convergence was assessed at two levels, locally by examining variations at the nodal points and globally, by examining the mean and peak values within a pre-defined volume. This study has shown that accurate assignment of the material properties is critical in achieving convergence of other parameters such as stress and risk ratio. If convergence of the assigned material properties is not achieved, errors are then propagated through to other parameters of interest. There has been found no evidence of previous studies that show that the assigned material properties in models of bony structures are influenced by the mesh density, as was demonstrated here.

In the final part of the thesis, based on the convergence study, a combined, prospective FE and RSA migration study was performed. Accurate patient-specific FE models were created in order to perform a comparative analysis of the FE predictions with clinical migration (RSA) data from four different patients. The objective was to determine whether patient-specific FE models can predict the short term behaviour of tibial components in terms of aseptic loosening. For the first time, good correlation was observed between the results from the finite element models of four patients and the migration data corresponding to the same patients. It was concluded that patient-specific FE models could predict future performance of tibial components, as long as there is some knowledge of the kinematics and kinetics of the examined knee.

TABLE OF CONTENTS

LIST OF FIGURES

LIST OF TABLES

ACKNOWLEDGMENTS

I would like to thank Dr. Mark Taylor for his outstanding supervision, friendly treatment and enthusiastic guidance. Special thanks to Prof. Leif Ryd for kindly providing indispensable data, Ana Alonso Vazquez and Dr. John Cotton for their help and contributions and Dr. Marco Viceconti for his valuable and interesting remarks. Thanks to the staff of both Mechanical Engineering and Engineering Materials departments for being so kind and helpful.

Thanks to all my friends, my brother and sister for their support.

Thanks to CONICIT and Universidad Simón Bolívar (Venezuela) for providing the financial support to carry out this Ph.D.

Many thanks to my parents for their unconditional support at all times, helping me through the most difficult times in my life, making it possible for me to be where I am now.

Finally, I would like to thank Catia for her love and support when I needed it most, lightening up my last and hardest year in Southampton.

LIST OF ABBREVIATIONS

TKR…total knee replacement

PMMA…polymethylmethacylate cement

RSA…roentgen stereophotogrammetric analysis

MTPM…maximum total point motion

HA…hydroxyapatite

CT…computed tomography

QCT…quantitative computed tomography

HU…Hounsfield units

DICOM…digital imaging and communications in medicine (image format)

HKA...hip-knee-ankle angle

CH...condylar-hip angle

CP…condylar-plateau angle

PA…plateau-ankle angle

AP…antero-posterior angle

LBA…load-bearing axis

HS…heel strike

FF…foot flat

HO…heel off

TO…toe off

BW…body weight

FE…finite element

E…Young's modulus

ΔE…Young's modulus increment

ρ…bone apparent density

S, σ, σ_u…ultimate compressive strength

R…risk ratio

PVFB…percentage of volume of failing bone (bone with $R > 100\%$)

MRE…mean residual error

SD…standard deviation

PTH…parathyroid hormone

CHAPTER 1

BONE

Bone is one of the hardest of all connective tissues found in the human body. It provides the mechanical support for static posture, locomotion and protection of the internal organs (e.g. the brain). In addition, bone contributes in the formation of blood cells (*haematopoiesis*) and the storage of calcium (*mineral homeostasis*) [111].

In adults, bone has two basic components: *cortical* (or *compact*) and *cancellous* (or *spongy*) bone. The cortical bone is the dense, solid material that composes the external surfaces of bones. Its thickness is variable and dependent on the mechanical requirements of its location. Cancellous bone is formed by struts called *trabeculae*. This type of bone is found mainly in the *epiphyses* (see section 1.1) of long bones, in short bones and sandwiched between two layers of compact bone (*diploe*). There are irregular spaces or cavities among the trabeculae that reduce the density of cancellous bone [111]. The bone undergoes self-regulated modelling that not only maintains the shaft and other portions of the bone, but also keeps a joint shape that is capable of optimally distributing the load. It has been suggested that the loading conditions (magnitude, direction and position) has an important effect on the distribution of bone density within the cancellous bone (see section 1.4.2).

1.1. STRUCTURE OF LONG BONES

Despite the huge variety of shapes and dimensions of the different bones in the human skeleton, the morphology of the bone at the organ, tissue and cellular levels is relatively consistent. With few exceptions, all long bones have the same general structure (Figure 1.1):

- **Diaphysis**. The tubular diaphysis constitutes the long section of the bone. It is made up by a relatively thick layer of cortical bone that surrounds the central *medullary* (or *marrow*) *cavity*. In adults, this cavity contains fat (*yellow marrow*) [97].

- **Epiphysis**. The epiphyses constitute the bone ends. In most cases, they are larger than the diaphysis. They are composed by compact bone on the exterior and

cancellous bone on the interior. The articular surface of the epiphysis is covered with a layer of *articular cartilage*, which has the function of reducing contact stresses in the joint by cushioning the opposing bone ends [97].

- **Membranes**. The outer surface of the diaphysis is covered with a white, double-layered membrane called the *periosteum*. The outer *fibrous* layer of the periosteum is dense and irregular, whereas the inner *osteogenic* layer consists mainly of *osteoblasts* (bone-forming cells), and *osteoclasts* (bone-destroying cells). The periosteum is rich in nerve fibres, lymphatic vessels and blood vessels. It is fixed to the underlying bone by *Sharpey's fibres* (clusters of collagen fibres). The internal bone surface is coated with a delicate membrane called the *endosteum,* which covers the trabeculae of the spongy bone in the medullary cavities. Like periosteum, endosteum contains both osteoblasts and osteoclasts [97].

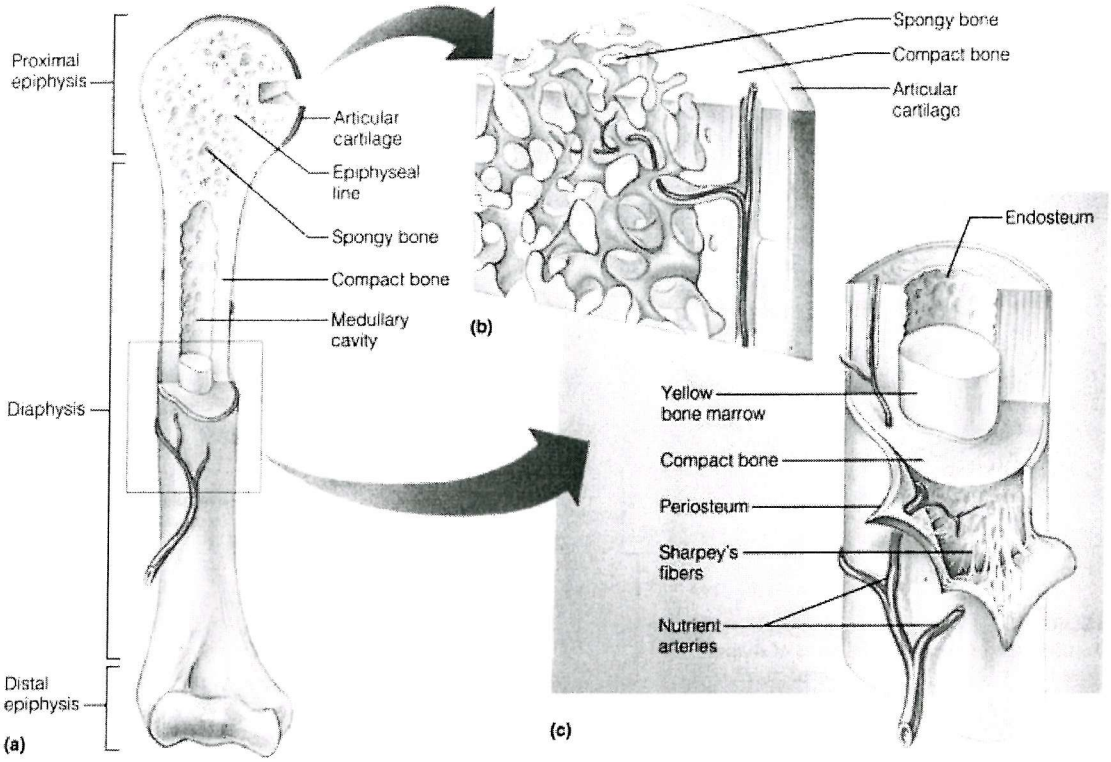

Figure 1.1. Structure of long bones (humerus of arm) [97].

Bone provides also an active site of haematopoiesis, as it contains *red marrow*, which is a tissue that produces red and white blood cells as well as platelets. As red marrow is

usually found within cavities of cancellous bone, the latter are also called *red marrow cavities* [97,111].

1.2. MICROSCOPIC STRUCTURE OF BONE

Bone consists of an organic (cells and matrix) and an inorganic (or mineral) component. The organic (or extracellular) matrix contains primarily type I collagen (about 90%) [60]. It also contains reticular fibres, and elastin fibres. The organic component consists of various cells including fibroblasts, fibrocytes, osteoblasts, osteocytes, osteoclasts and osteoprogenitor cells. The fibroblasts and fibrocytes are responsible for the production of collagen. The osteoblasts preserve bone whereas the osteoclasts are responsible for bone resorption. The base substance in bone contains minerals in addition to glycosaminoglycans, which are mainly in the form of proteoglycans, hyalunoric acid and water. The elastic properties of bone are derived from the organic component [97].

The collagenous extracellular matrix in bones is highly calcified and takes different forms. The inorganic substance (65% of the bone mass [97]), which forms a supporting framework for the fibrous component, is basically made up by hydroxyapatites, mostly calcium phosphate crystals ($C_{10}(PO_4)_6(OH)_2$) that are embedded among the collagen fibrils [24]. The inorganic part contributes in giving the bone its strength and hardness.

1.2.1. Cortical Bone

The structural unit of cortical bone is called the *osteon* or *Haversian system*, and is an elongated cylinder oriented in the direction of the long axis of the bone (Figure 1.2). It is composed by concentric cylindrical layers called *lamellae*. All of the collagen fibres in a particular lamella are in a specific direction, but in the adjacent lamella, these fibres are in the opposite direction. This is in order to resist torsion stresses [97]. Blood, lymph and nerve fibres run through the Haversian canals. The small spaces between the lamellae, called *lacunae*, contain mature bone cells called *osteocytes*, which are nourished through fluid-filled channels called *canaliculi*. In addition, smaller perforating (or Volkmann's) canals run obliquely and perpendicularly in order to connect the central canals with those in the periosteum [97,111].

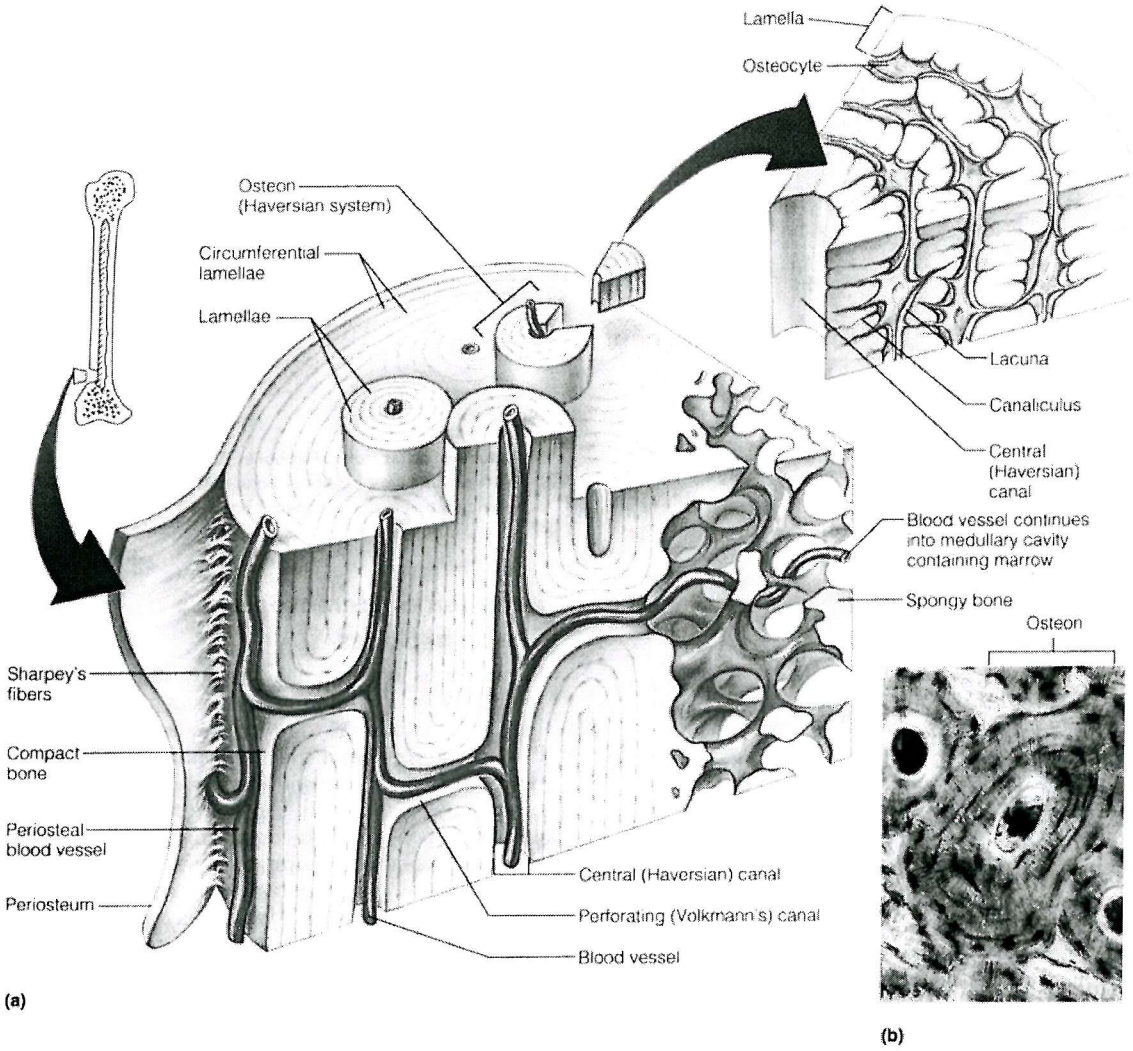

Figure 1.2. Cortical bone. (a) Microscopic structure of compact bone [97] (b) Microphotograph of a cross-sectional view of one osteon (144x) [97].

1.2.2. Cancellous Bone

Despite its disordered-looking arrangement, trabeculae are aligned with the stresses they are subjected to. Trabeculae contain irregularly arranged lamellae and osteocytes interconnected by canaliculi. No osteons are present. Nutrients reach the osteocytes of cancellous bone by diffusing through the canaliculi from the marrow spaces between the trabeculae [97].

Mature bone cells are responsible for forming, resorbing and maintaining bone. By releasing calcium into the serum, osteoclasts cause the bone to resorb. On the other hand, osteoblasts are responsible for the bone generation, by synthesising the collagen matrix (osteoid) and depositing bone mineral (hydroxyapatite) within the matrix,

producing mineralised bone. Once surrounded with mineralised bone, the osteoblasts are referred to as osteocytes, the bone cell believed to be responsible for maintaining the bone mass. The aforementioned process (which normally happens through life) is known as remodelling [111].

1.3. BONE REMODELLING

Considerable amounts of bone are constantly being removed or replaced. It is estimated that, every week, the human body recycles around 5-7% of its bone mass. In healthy young adults, the bone mass remains constant, indicating that the rates of bone resorption (removal) and deposition are equal. Bone deposition generally occurs when bone is injured or when additional bone strength is required. Bone resorption is carried out by osteoclasts, which produce lysosomal enzymes (that digest the organic matrix) and metabolic acids that convert the calcium salts into soluble forms that pass easily into solution. As the organic matrix is demineralised, the released calcium and phosphate ions enter the interstitial fluid and then the blood [97].

Two different mechanisms control the continuous process of bone remodelling. One is a hormonal system that controls that the Ca^{2+} homeostasis in the blood, and the other consists of readjusting the bone mass as a response to mechanical loads acting on the skeleton.

1.3.1. Hormonal mechanism

This process is governed by the interaction of *parathyroid hormone* (PTH) and *calcitonin* (Figure 1.3). When calcium levels in blood are low, PTH is released to stimulate osteoclasts to resorb bone and hence, release calcium to the blood. When a rise in the blood concentration of calcium is detected, the PTH stops being released. Calcitonin acts in opposition to PTH, as it is secreted when calcium concentrations in blood are sensed. The latter stimulates calcium deposit on bone, reducing calcium levels in blood [97].

This mechanism has as primary function to maintain a specific level of calcium in the blood, rather than the well being of the skeleton. If calcium levels in blood are too low

for an extended period of time, this mechanism will produce a weakening of bones, by attempting to reach the required calcium concentration in blood.

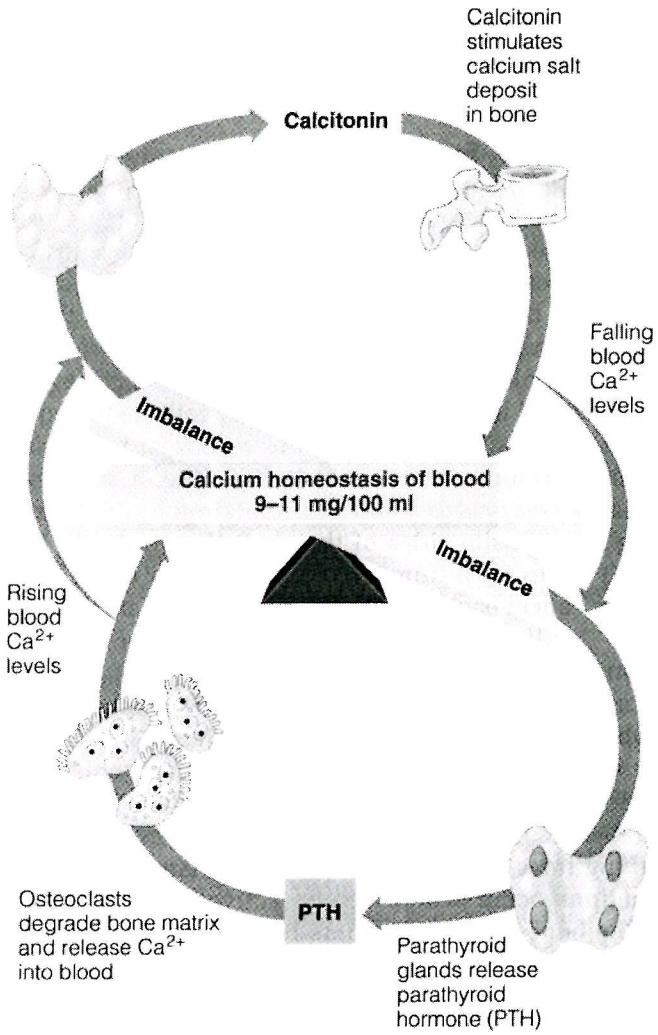

Figure 1.3. Diagram of hormonal mechanism for remodelling [97].

1.3.2. Mechanical stresses

Loads due to gravitational forces and muscle action also generate bone remodelling. Essentially, this mechanism aims at keeping the strength of the bones where it is needed. This process, often referred to as Wolff's law [160], suggests that bone grows and remodels in response to the magnitude and location of the stresses it is submitted to. For example, long bones are thickest in the middle of their diaphysis as that is where the stresses they have to bear are greatest [97].

Bone mass certainly has an equilibrium point that when reached, no mass is either deposited or removed. Both remodelling mechanisms act in conjunction, and it is believed that the hormonal influence is the main determinant of whether and when remodelling will occur (as a response to calcium levels), whereas mechanical stresses determine where remodelling occurs [97].

This remodelling process may involve several phases of bone resorption and enlargement. All bone formed by bone resorption and subsequent deposition is called *secondary bone*, whereas the original bone (*primary bone*) is formed in a region through endochondral ossification or direct subperiosteal deposition [60,111].

1.4. MECHANICAL PROPERTIES OF BONE

As mentioned before, there are two types of bone, cortical and cancellous bone. The main difference between them is their porosity (proportion of volume occupied by the non-mineralised tissue). Cortical bone porosity ranges between 5 and 30% (approximately), whereas cancellous bone has a much higher porosity ranging from 30 to 90% [24].

1.4.1. Cortical Bone

Several factors influence the material properties of cortical bone. The stress-strain behaviour of cortical bone is also very much dependent upon the orientation of the bone microstructure with respect to the direction of loading. It has been demonstrated that cortical bone is stiffer in the longitudinal direction than in the transverse one [24,122,123]. This characteristic makes of bone an *anisotropic* material.

Young's moduli of femoral and tibial cortical bone for different loading cases are outlined in Table 1.1. The elastic modulus is dependent on the direction in which the load is exerted on the specimen. From Table 1.1, it can be observed that both femur and tibia are stiffest on the longitudinal direction, whereas a lower value of elastic modulus is detected when the bones are loaded in the transversal plane. It can also be noticed that in the transversal plane, the mechanical properties are very similar in the transverse and circumferential directions, and therefore cortical bone may be considered as transversally isotropic.

Table 1.1. Elastic moduli of femoral and tibial cortical bone (values measured with ultrasonic techniques).

Author	Anatomic Site	Young's Modulus (GPa)
Hobatho *et al.* [65]	Tibia	8.8 (circumferential) 9.6 (transversal) 17.6 (axial)
Ashman *et al.* [7].	Femur	12.0 (circumferential) 13.4 (transversal) 20.0 (axial)

As well as the Young's modulus, ultimate strength values of adult femoral cortical bone for different loading conditions are shown in Table 1.2. These confirm the fact that the material properties of cortical bone depend upon the type and direction of the loads it is supporting.

Table 1.2. Ultimate strength of the femoral cortical bone [124].

Loading case		Ultimate strength (MPa)
Longitudinal	Tension	133
	Compression	193
	Shear	68
Transverse	Tension	51
	Compression	133

Cortical bone exhibits strength asymmetry with the compressive strength being greater than the tensile strength in both longitudinal and transverse directions. In general, the transverse strength is much lower than the longitudinal strength. It is to be emphasised that the mechanical properties of bone are also dependent on the anatomic site (Table 1.1). Material properties of bone are also dependent on the rate at which the load is applied (strain rate). A cortical bone sample that is rapidly loaded displays a higher Young's modulus than one that is loaded more slowly (Figure 1.4). A material that shows this behaviour is called *viscoelastic* (or time dependent). Nonetheless, in bone tissue, this dependency is poor.

Previous studies [22,23] have suggested that the longitudinal strength and stiffness of the bone are approximately proportional to the strain rate raised to the 0.06^{th} power (Figure 1.4).

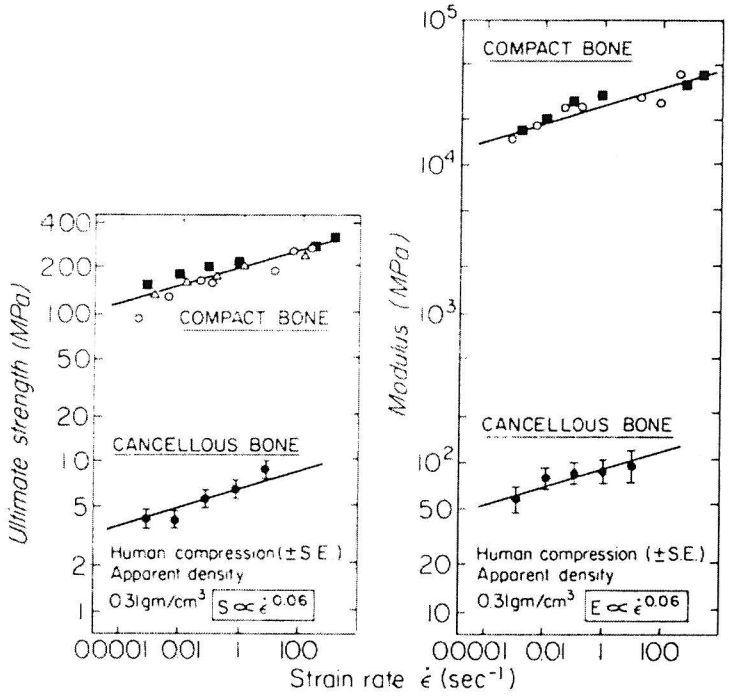

Figure 1.4. Influence of applied strain rate on the strength and Young's modulus of both compact (cortical) and cancellous bone [22,23].

1.4.2. Trabecular Bone

Trabecular bone differs from cortical bone mainly in the degree of porosity, with the former being considerably more porous than the latter. Typical values of cortical bone porosity vary from 3% to 5%, whereas in cancellous bone these values can be as high as 90% [24,108].

1.4.2.1. Mechanical properties

A number of studies have demonstrated that trabecular bone presents the characteristics of a porous engineering material due to its cellular structure and energy absorption capabilities.

Tensile and compressive strengths of cancellous bone are significantly different, nonetheless there does not seem to be an agreement on which one is higher. There is

considerable debate on whether the compressive strength is greater than [78,82,138], equal to [25] or less [129] than the tensile strength.

While there is so much disagreement on the cancellous bone strength, most authors suggest that the tensile and compressive Young's moduli are similar [8,25,129].

A typical stress-strain curve of cancellous bone under tensile loading is shown in Figure 1.5-a. This curve exhibits an approximately linear behaviour in the elastic region, followed by a post-yield region showing a negative slope after fracture is reached. Since tensile fracture is associated with disruption of two fractured surfaces, no further energy is absorbed by continuing to load after fracture [80]. On the other hand, although the material shows a similar behaviour in the elastic region under both tension and compression loading [60], the post-yield regions are significantly different. In compression, the stress-strain curve presents a large plastic region where the stress remains constant due to the collapse of the trabeculae within the cancellous bone. As the cellular pores continue to collapse, the stiffness starts increasing again, when compacting of the trabeculae occurs (Figure 1.5-b). Consequently, trabecular bone is capable of absorbing considerably more energy in compression than in tension.

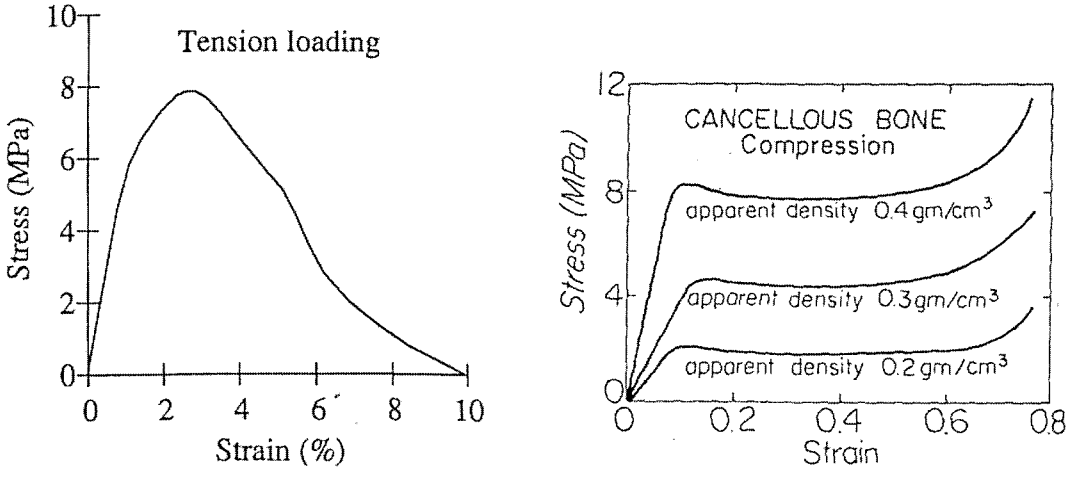

(a) (b)

Figure 1.5. Stress-strain behaviour of trabecular bone in (a) tension [80] and (b) compression [25].

As described in Section 1.4.2.2, Figure 1.5-b also shows the dependence of the compressive strength of cancellous bone upon its apparent density.

It has been widely accepted that cancellous bone presents anisotropic material behaviour [8,53,80,158]. A survey of the published mechanical properties of cancellous bone is presented in Table 1.3.

Table 1.3. Mechanical properties of human cancellous bone.

Author	Anatomic Site	E_{33} (MPa) Mean (range) ±SD	S_{33} (MPa) Mean (range) ±SD	Other measured parameters Mean (range) ±SD
Behrens *et al.* [12]	Proximal tibia	—	(1.8 - 63.6)	—
Lindahl [91]	Proximal tibia	(1.4 - 79)	(0.2 - 6.7)	—
Carter and Hayes [23]	Proximal tibia	(10 - 500)	(1.5 - 45)	—
Williams and Lewis [158]	Proximal tibia	227 (44.7 - 457.8)	(1.5 - 6.7)	E_{11}: 50 (8 - 130) E_{22}: 37 (9 - 84)
Goldstein *et al.* [52]	Proximal tibia	(4 – 500))	(1 - 13)	—
Hvid and Hansen [69]	Proximal tibia	—	(13.8 – 116.4)	—
Ciarelli *et al.* [30]	Proximal tibia	(5 – 552)	0.52 - 11	—
Linde *et al.* [93]	Proximal tibia	267 (67 – 734)	—	E_{11}: 83 (18-481) E_{22}: 84 (17-493)
Røhl *et al.* [129]	Proximal tibia	489 ± 331	2.2 (0.5 – 5.6)	E_{ten}: 487 ± 329 S_{UTS}: 2.54 (0.9 - 5.38)
Hvid [70]	Proximal tibia and distal femur	—	7.2 (2.4 – 14.5)	—
Pugh *et al.* [118]	Distal femur	(413 – 1516)	—	—
Behrens *et al.* [12]	Distal femur	—	(2.25 – 66.2)	—
Ducheyne *et al.* [38]	Distal femur	—	(0.98 – 22.5)	—
Ciarelli *et al.* [30]	Distal femur	(7.6 – 800)	(0.56 –18.6)	—
Rohlman *et al.* [130]	Proximal and distal femur	389 (43 – 1531)	7.4 (0.5 –22.9)	—

E_{33}: Compressive Young's modulus measured parallel to the principal orientation of the trabeculae
S_{33}: Ultimate compressive strength measured parallel to the principal orientation of the trabeculae
E_{11}, E_{22}: Compressive Young's moduli measured perpendicular to the principal orientation of the trabeculae
E_{ten}: Tensile Young's modulus measured parallel to the principal orientation of the trabeculae
S_{UTS}: Ultimate tensile strength measured parallel to the principal orientation of the trabeculae

1.4.2.2. Apparent density vs. mechanical properties

Bone mechanical properties are closely correlated with apparent density (e.g. compressive strength, Young's modulus, etc) of the trabecular bone. As mentioned above, the cancellous bone is much less dense than the cortical bone, therefore the elasticity of the former is also considerably greater.

One of the most important properties of trabecular bone is the fact that both Young's modulus and strength present a correlation with the apparent density. Apparent density

ρ_a can be determined by multiplying the density of the material that makes up the individual trabeculae (tissue density ρ_t) and the fraction of volume V_f of bone present in the bulk specimen:

$$\rho_a = \rho_t \cdot V_f \tag{1.1}$$

where the volume fraction typically ranges between 0.05 (porous trabecular bone) and 0.60 (dense trabecular bone) [80]. The tissue density is usually in the range of 1.6 to 2.0 g/cm^3 [80]. On the other hand, the apparent density is a more variable than the tissue density, the former having typical values of 0.05-1.00 g/cm^3 [80].

Table 1.4. Linear and power law regressions that correlate apparent density (g/cm^3) and ultimate compressive strength (MPa) [80].

Study	Specimens	$\sigma=a\,\rho+b$			$\sigma=a\,\rho^b$		
		a	b	r^2	a	b	r^2
Tibia							
Carter and Hayes [23]	80	—	—	—	68.0	2.00	—
Hvid *et al.* [71]	94	19.0	-1.14	0.74	25.3	1.49	0.80
Linde *et al.* [92]	121	—	—	—	34.2	1.56	0.79
Linde *et al.* [94] (@ $\dot{\varepsilon} = 0.01s^{-1}$)	60	26.51	-4.14	0.87	28.72 37.74	1.65 2.00	0.87 0.67
Femur							
Esses *et al.* [41]	49	—	—	—	7.30	1.40	0.87
Lotz *et al.* [96]	49	—	—	—	25.00	1.80	0.93
Lumbar spine							
Galante *et al.* [48]	17	12.6	-0.68	>0.80	—	—	—
Hanson *et al.* [58]	231	—	—	—	85.30	2.24	0.76

Table 1.5. Young's modulus (MPa) in the longitudinal direction as function of apparent density (g/cm^3) for the human tibia.

Study	Specimens	$E=a\,\rho+b$			$E=a\,\rho^b+c$			
		a	b	r	a	b	c	r
Ashman *et al.* [8]	25	4360	-41.24	0.93	4606	1.07	0	0.93
Carter and Hayes [23] (@ $\dot{\varepsilon} = 0.01s^{-1}$)	80	—	—	—	2875	3.0	0	
Linde *et al.* [93]	118				1012 1593	1.13 2	0 119	0.71
Linde *et al.* [94] (@ $\dot{\varepsilon} = 0.01s^{-1}$)	60	1742.8	-258.5	0.84	2003 2555.6 5209.9	1.56 2 3	0 0 0	0.84 0.82 0.66

The precise equation that correlates the apparent density with the mechanical properties of trabecular bone remains an open question. Several authors have proposed different correlations. Some of these equations are presented in Table 1.4 and Table 1.5.

1.5. EFFECT OF AGING ON THE MATERIAL PROPERTIES OF BONE

It is believed that the bone mass reaches its maximum before the age of 30 [165]. After that, the bone mass remains stable for another decade, and then begins to drop significantly. The rate of bone mass loss is relatively stable in men, whereas women experience an enormous increase in the rate of bone loss during menopause. In the post-menopausal stage the rate of bone mass loss returns to the pre-menopausal levels. By age 90, women have lost 20% of their maximum cortical bone mass and 40-50% of the trabecular bone mass. On the other hand, men at that age have lost only 5% of their cortical bone mass and 10-25% of their trabecular bone mass [126].

Between ages of 20 and 80, the mechanical properties of bone undergo a reduction of 5-40% [126], providing there are no unusual factors that could improve or worsen the situation (e.g. exercise or menopause, respectively).

Values of mechanical properties of femoral cortical bone against age (specimens ranging from 20 to 90 years of age) have been reported (Figure 1.6) in previous research works [18,162]. A large reduction of most mechanical properties can be observed.

A study that considered the tensile strength of 235 femoral cortical bone specimens of ages between 20 and 102 years has reported a curve that shows a similar behaviour (Figure 1.7) [101].

The age-related reductions in material strength may be partially compensated by geometric changes in the bone. Yet, this phenomenon is more efficient in males than in females as radial expansion has been noted in men but not in women [99]. In Figure 1.8, the difference in compressive breaking force between male and female femoral specimens can be observed. It is clear that female specimens are much weaker.

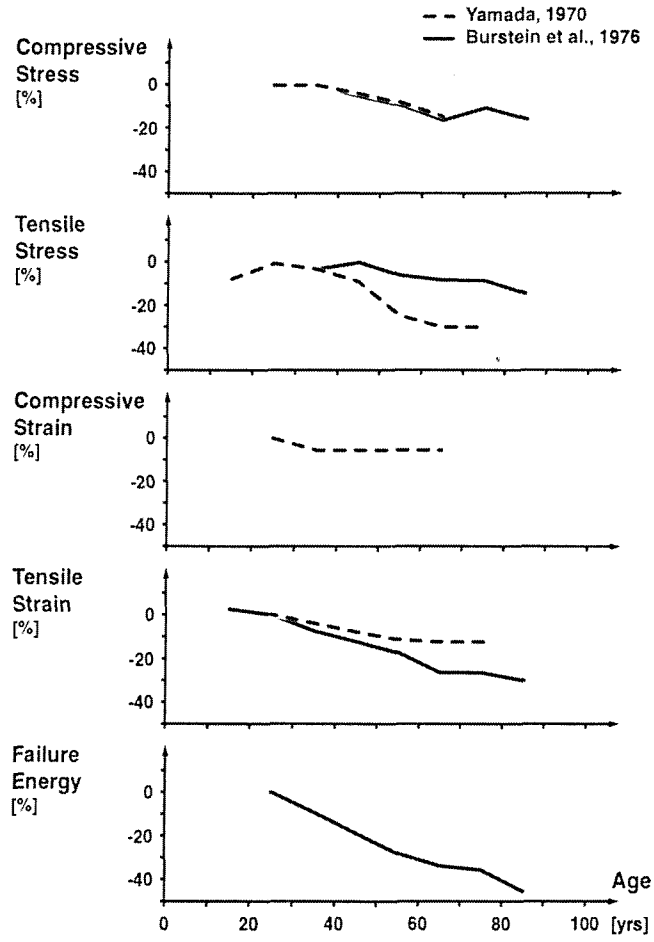

Figure 1.6. Effect of age on mechanical properties of femoral cortical bone (expressed as percent differences) [18,162].

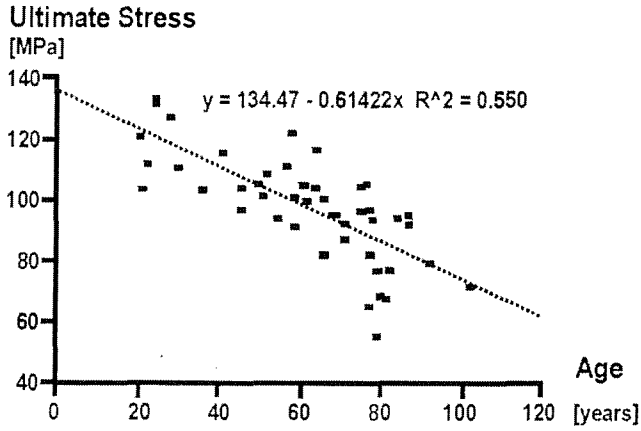

Figure 1.7. Relation between ultimate stress of femoral cortical bone and age [101].

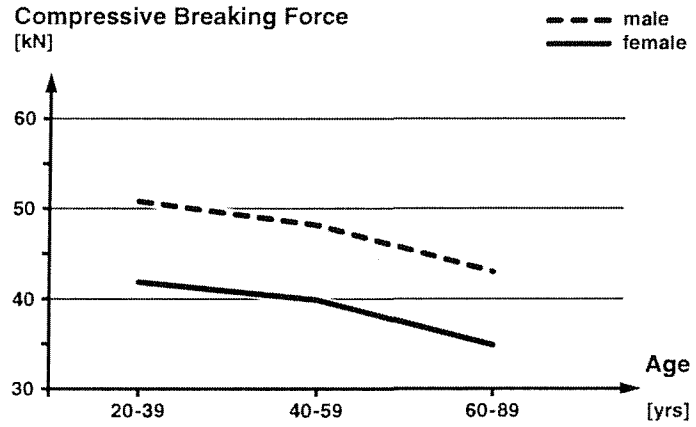

Figure 1.8. Compressive breaking forces in the middle portion of wet femoral shafts in the longitudinal direction [162].

1.6. MECHANICAL PROPERTY ESTIMATION BY MEANS OF COMPUTED TOMOGRAPHY

Due to the necessity of determining the material properties of bone in order to increase the accuracy of biomechanical studies, non-invasive techniques have been developed. In this regard, Quantitative Computed Tomography (QCT) is significantly more advantageous than the other methods, such as single or dual absorptiometry, dual energy X-ray absorptiometry or conventional radiography. With CT scans, the cross-sectional geometric information is directly available. Additionally, with special calibration phantoms, densitometric information from both cortical and trabecular bone can be obtained in a scale that can be directly converted to bone density units (e.g. g/cm^3) and thus mechanical properties (see Section 1.4.2.2).

A CT dataset consists of a series of cross-sectional slices of a certain thickness, which can be as small as one third of a millimetre with modern scanners. This slice is divided into several small, identical elements of volume (voxels). An X-ray attenuation value is assigned to each element, based on the density and atomic number of the tissue corresponding to it [50]. The attenuation values are expressed in Hounsfield Units (HU), typically on a scale of –1000 for air, zero for water and +1000 for dense bone, but in

some scanners, this window varies form –1000 to +3000 or +4000, in order to allow a better analysis of bony structures [37].

For display purposes, the reconstructed slice is regarded as a two-dimensional matrix of picture elements (pixels). This matrix is usually stored in an image format called DICOM (Digital Imaging and COmmunications in Medicine). The DICOM format provides a great flexibility regarding the organisation and the structure of the pixel data. Every pixel is made of one or more samples, each one of them is described by a given number of bits ("Bits Stored"), and is packed in a cell that can use an even greater number of bits ("Bits Allocated") (Figure 1.9).

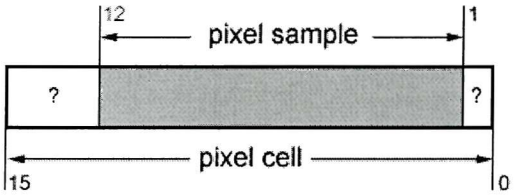

Figure 1.9. Diagram of a pixel cell utilised by the DICOM format.

There are several works on the experimental determination of the correlation between QCT data and the material properties of trabecular bone. A summary of the equations obtained by some of the authors is presented in Table 1.6.

Table 1.6. Relationship between mechanical properties of human cancellous bone and QCT values.

Authors	Anatomic Location	Young's modulus (MPa)	Strength* (MPa)
Bentzen *et al.* [14]	Proximal tibia	$10^{(1.55\pm0.06)}\cdot r_o^{(11.7\pm0.7)}$	$10^{(-0.18\pm0.04)}\cdot r_o^{(11.2\pm0.6)}$
McBroon *et al.* [100]	Vertebra	—	$1.93\cdot H^{1.21}$
Hvid *et al.* [71]	Proximal tibia (linear correlation)	$1.54\cdot H+25.0$ @100kVp $1.76\cdot H+30.4$ @120kVp $1.91\cdot H+33.2$ @140kVp	$0.0242\cdot H+0.122$ @100kVp $0.0276\cdot H+0.203$ @120kVp $0.0299\cdot H+0.250$ @140kVp
Hvid *et al.* [71]	Proximal tibia (power-law correlation)	$78.3\cdot r_o^{6.96}$ @100kVp $80.6\cdot r_o^{7.74}$ @120kVp $82.3\cdot r_o^{8.29}$ @140kVp	$1.034\cdot r_o^{7.68}$ @100kVp $1.073\cdot r_o^{8.55}$ @120kVp $1.095\cdot r_o^{9.15}$ @140kVp
Rho *et al.* [125]	Proximal tibia	$296 + 5.20\cdot H$	—
Rho *et al.* [125]	Proximal femur	$269 + 4.86\cdot H$	—
Rho *et al.* [125]	Distal femur	$367 + 6.28\cdot H$	—
Rho *et al.* [125]	Lumbar spine	$-94 + 6.68\cdot H$	—
Rho *et al.* [125]	Proximal humerus	$454 + 2.81\cdot H$	—

H: QCT number in Hounsfield Units
r_o: Relative attenuation coefficient $(1+0.001\cdot H)$
* Ultimate compressive strength

CHAPTER 2

ANATOMY AND FUNCTION OF THE KNEE

2.1. REFERENCE PLANES

The description of the movement of most joints in the human body is expressed in terms of rotation or displacement about one of the three perpendicular planes: frontal, transverse and sagittal (Figure 2.1).

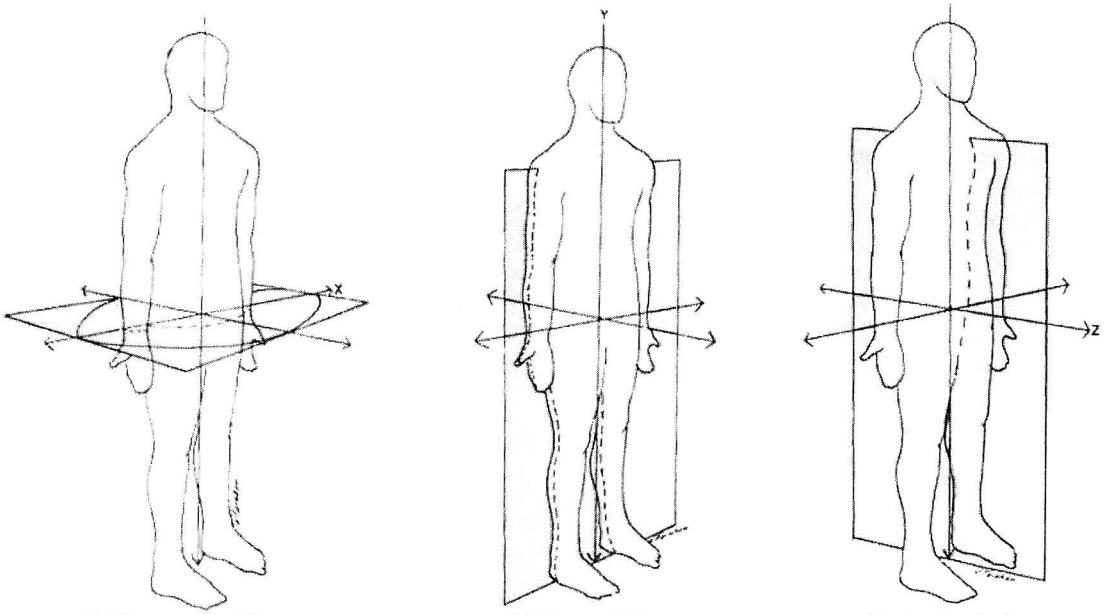

(a) Transverse Plane (b) Frontal Plane (c) Sagittal Plane

Figure 2.1. Reference Planes of Motion [114].

2.2. SYNOVIAL JOINTS (DIARTHROSES)

Synovial joints are those in which the ends of the bones can move relative to one another, as the adjacent bony surfaces are not directly connected by any cartilaginous tissue. The bony components are indirectly connected to one another by means of a joint capsule that encloses the joint. Synovial joints allow for virtually free movement within a defined but limited range and are able to transfer forces.

All Synovial joints are similarly constructed and have the following features: (a) a joint capsule that, made of fibrous tissue, encircles the ends of the bony components; (b) a

joint cavity that is enclosed by the joint capsule; (c) a synovial membrane that serves as a coating for the inner surface of the capsule; (d) synovial fluid that forms a film between the contact surfaces; and (e) hyaline cartilage that covers the joint surfaces.

The most representative examples of synovial joints are the knee and the hip, as they transfer forces (during normal walking) of several times the body weight. From this point forward, this work is going to deal only with the knee.

2.3. THE KNEE (ANATOMY AND FUNCTION)

The knee is one of the largest and most complex joints in the human body. It plays a crucial role in providing static and dynamic support to the body, as well as mobility. The knee works in conjunction with the hip and ankle to support the body weight in the static upright position. When in motion, the knee structure is responsible for allowing the leg to flex and to support and transfer the body weight.

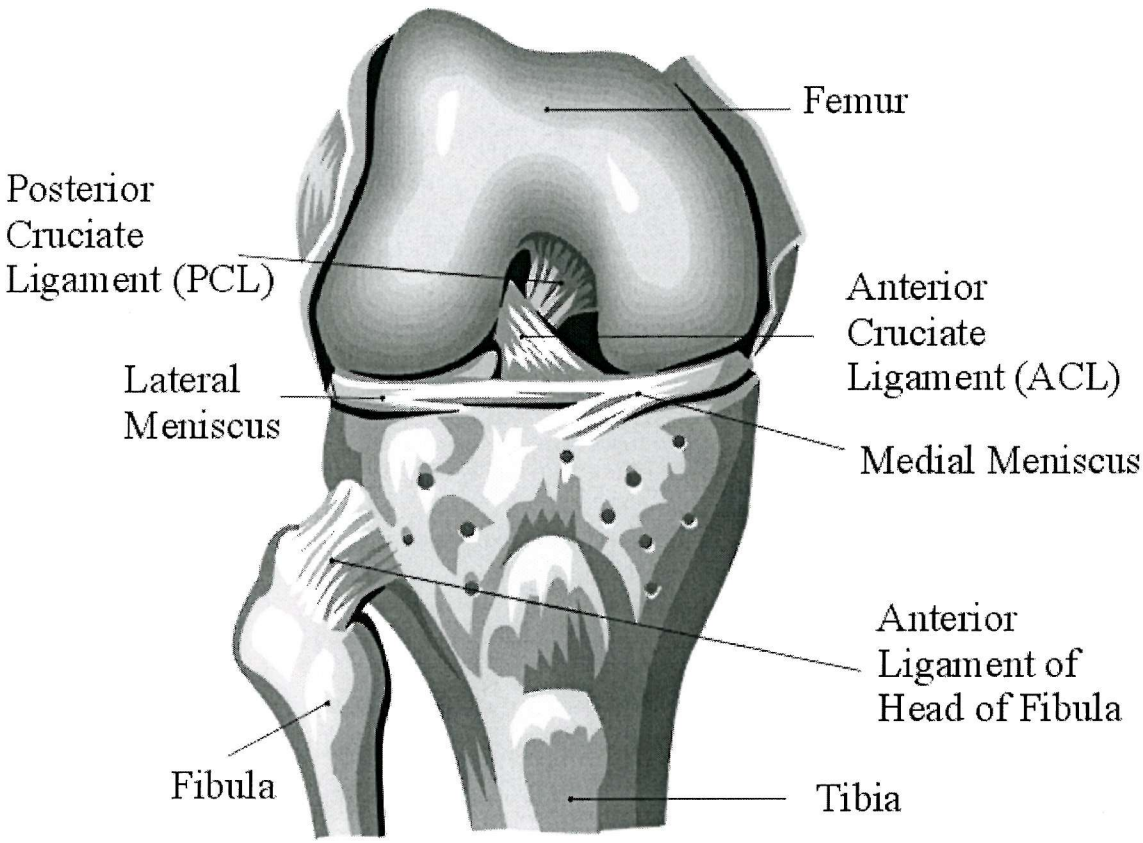

Figure 2.2. The knee complex.

The knee complex consists of two joints: the tibiofemoral joint (articulation between the distal femur and the proximal tibia) and the patellofemoral joint (articulation between the patella and the femur) as shown in Figure 2.2. Both joints are synovial and share the same joint capsule. The movement of the tibiofemoral joint basically determines the patellofemoral joint movement. From a skeletal point of view the tibiofemoral joint is very unstable, however this is compensated by the menisci, ligaments and muscles. The shape and orientation of these components enable the joint to operate as a modified hinge with flexion and extension as the principal degree of freedom.

2.3.1. Femoral articular surface

The large medial and lateral condyles on the distal femur form the proximal articular surfaces of the knee joint. The two condyles are separated by the intercondylar notch or fossa through most of their length, but are joined anteriorly by an asymmetric groove called the patellar groove or surface (Figure 2.3-a). The shaft of the femur is not vertical but is angled in such a way that the femoral condyles do not lie immediately below the femoral head, but slightly angulated to the medial side (Figure 2.3-b), by approximately 5 to 10° [114].

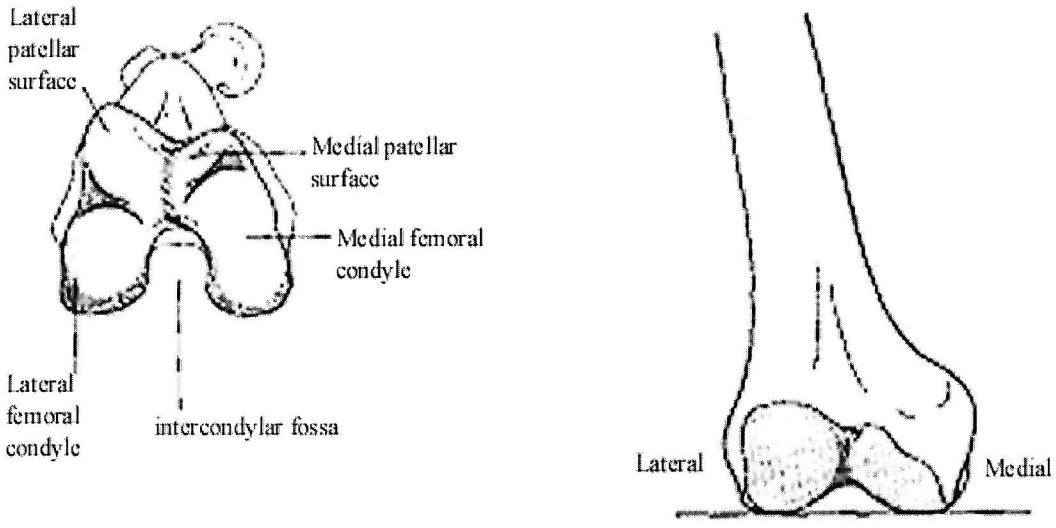

Figure 2.3. Inferior (a) and posterior (b) views of the distal femur [114].

2.3.2. Tibial articular surface

There are two articulating surfaces on the tibia: the medial and lateral condyles or plateaus (Figure 2.4-a). The articular surface of the medial condyle is 50% larger than that of the lateral condyle, and the cartilage on the medial tibial condyle is three times thicker [114]. A roughened area and two bony spines called the intercondylar tubercles separate the two tibial condyles. These tubercles are accommodated in the intercondylar notch of the femur during knee extension (Figure 2.4-b) [114].

2.4. FUNCTION

The knee has two main functions: (a) to have stability in full extension when its components undergo large forces generated by the muscles acting on short lever arms; and (b) to have great mobility at certain flexion angles. This mobility is essential for running and the optimal orientation of the foot relative to the irregularities of the ground. The knee solves this problem by means of fairly complex mechanisms, but on doing so, the poor degree of congruence between surfaces (vital for appropriate mobility) makes it likely to experience injuries and dislocations. During flexion, the knee is unstable and the menisci and ligaments are most susceptible to injury. During extension, harm to the joint is most likely to result in fractures of the articular surfaces and rupture of the ligaments.

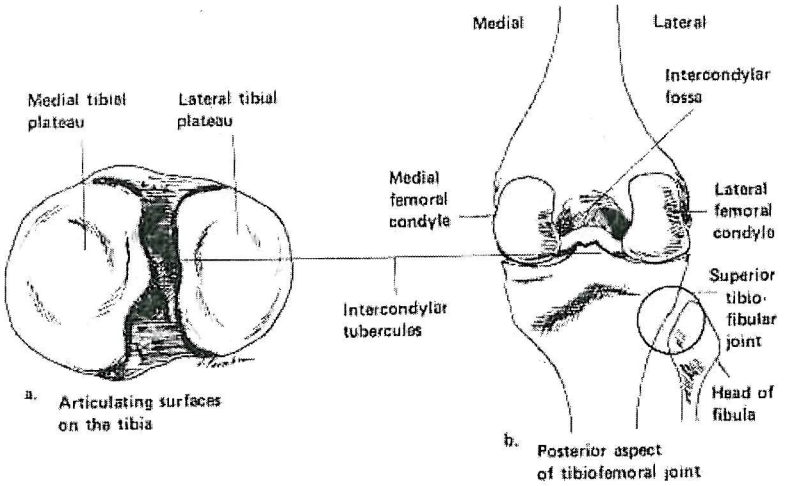

Figure 2.4. (a). Superior view of the proximal tibia. (b). Posterior view of the tibiofemoral joint [114].

The primary motions of the knee joint are flexion and extension and, to a lesser extent, internal-external rotation and antero-posterior displacements. Other movements of lower magnitudes can be observed in the knee, such as lateral-medial and compression-distraction displacements (see section 2.6.2 - Figure 2.14). The knee is extended by the quadriceps femoris, assisted by the tensor fasciae latae. The hamstrings are responsible for flexion, assisted by the gracilis and sartorious. Gastrocnemius and plantaris are also flexors of the knee. Movements of the joint in other directions are restricted mainly by the combined action of ligaments and geometry of the articular surfaces. The joint can also undergo tibial and femoral displacements anteriorly and posteriorly, as well as abduction and adduction (caused by varus-valgus forces). Nevertheless, these movements are generally not regarded as part of the function of the joint, but as part of the cost of the tremendous compromise between mobility and stability. The small amounts of anterior-posterior displacement and varus-valgus forces that can occur in a normal flexed knee are a consequence of joint incongruence and variation of elasticity of ligaments. The magnitude of such motions varies from person to person, and from side to side in the same individual [77]. Excessive amounts of such motions are abnormal, and generally indicate ligamentous malfunction. Anterior-posterior displacements of the tibia are restricted by the posterior and anterior cruciate ligaments, respectively. Abduction and adduction are limited and constrained by the medial and lateral collateral ligaments, respectively. Together, collateral and cruciate ligaments limit the internal rotation of the femur relative to the tibia.

The range of knee flexion varies according to the position of the hip and whether there is active or passive motion. Active flexion of the knee can reach angles of up to 140^{o} (Figure 2.5-a) if the hip is already flexed, and only 120^{o} when the hip is extended (Figure 2.5-b). Passive flexion of the knee achieves a maximum angle of 160^{o} (Figure 2.5-c).

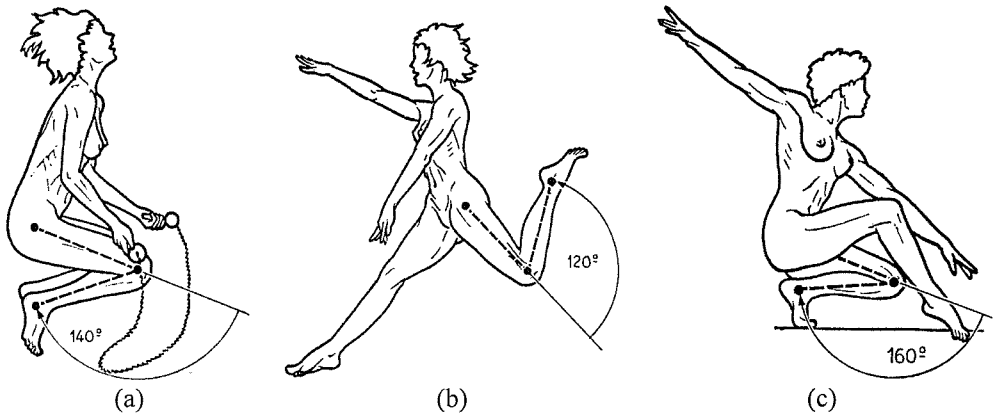

Figure 2.5. Maximum possible angles of knee flexion. a) Active flexion (hip flexed). b) Active flexion (hip extended). c) Passive flexion [77].

Rotation of the leg around its long axis can only be performed with the knee flexed. Medial and lateral rotations bring the toes to point toward the medial or lateral side, respectively (Figure 2.6). Lateral rotation has a range of 40° and medial rotation a range of 30°. This range varies with the range of knee flexion [77].

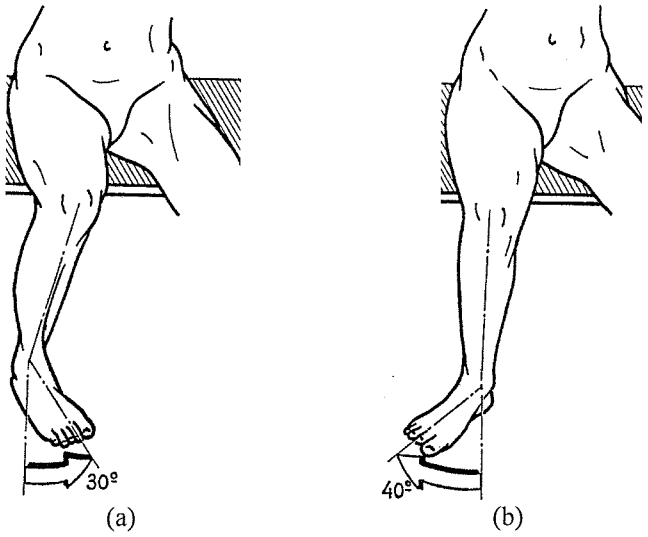

Figure 2.6. Medial (a) and lateral (b) rotation of the knee [77].

2.5. TIBIOFEMORAL ALIGNMENT

In healthy, non-arthritic adults, the Load-Bearing Axis (LBA, mechanical axis), of the lower limb is closely aligned to the mechanical axes of the bones so that the hip, knee and ankle are nearly co-linear when the knee is extended (Figure 2.7-b). The LBA stretches from the centre of the head of the femur to the centre of the top surface of the talus (Figure 2.7-b). This line normally passes through the centre of the knee joint between the intercondylar tubercles, and is generally at about 3^{o} from the vertical [114]. The longitudinal axis of the femur is oblique, laterally tilted. The anatomic axis of the tibia is almost vertical. Therefore, the femoral and tibial anatomic axes normally form an angle of 185^{o} to 187^{o} measured on the medial side (Figure 2.7-a) [114,156].

From a mechanical point of view, the Hip-Knee-Ankle (HKA) angle is often used. This is defined as the angle between the mechanical long axes of the femur and the tibia (Figure 2.7-c). By convention, a zero HKA indicates co-linearity. Negative values of HKA denote the amount of *genu varus* (bow knees) and positive the amount of *genu valgus* (knock knees) (Figure 2.8) [31]. The angle between the articulating surface of the distal femur and the mechnical axis of the bone is defined as the condylar-hip (CH) angle. The angle between the articulating surface of the proximal tibia and the mechanical axis of the tibia is defined as the plateau-ankle (PA) angles. CH and PA angles are expressed as deviations from 90^{o}. Similar to the HKA, negative values of CH or PA indicate varus ($<90^{o}$) and positive ones indicate valgus ($>90^{o}$) [31]. The angle between the articulating surfaces in the tibiofemoral joint is measured by the condylar-plateau (CP) angle. CP may have either negative or positive values depending on whether the joint surfaces converge medially or laterally, respectively. These four angles are related by equation 2.1.

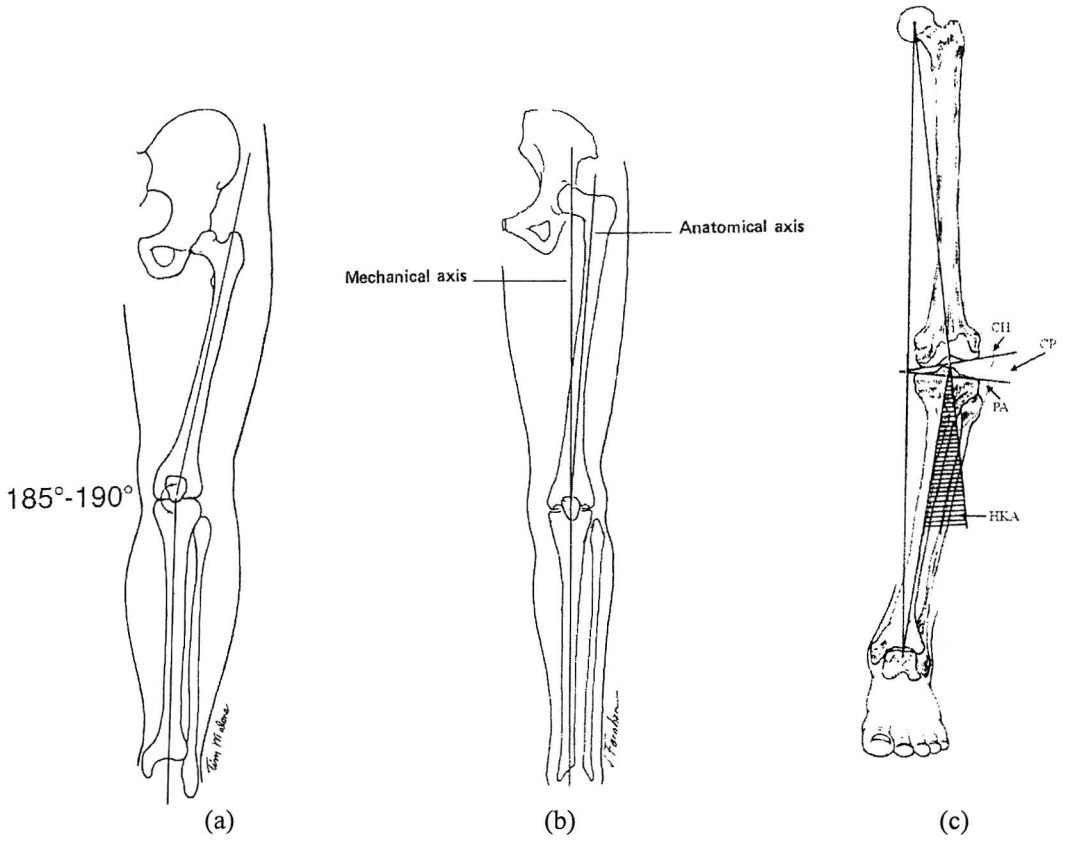

Figure 2.7. Angles between the longitudinal axes of the femur and tibia [114].

$$HKA = CH + PA + CP \tag{2.1}$$

In healthy knees, the average CH angle is 3-4 degrees in valgus ($CH>0^{o}$) whereas the mean PA angle is 3-4 degrees in varus ($PA<0^{o}$) [31]. The tangent of tibial plateaus is generally parallel to the femoral condyles ($CP= -1.7^{o}$). These angles describe the nearly co-linear alignment of non–arthritic knees with normal alignment ($HKA=0^{o}$) [31]. Although variation of these angles occur in non-arthritic knees, even more variation can be found in arthritic ones [31].

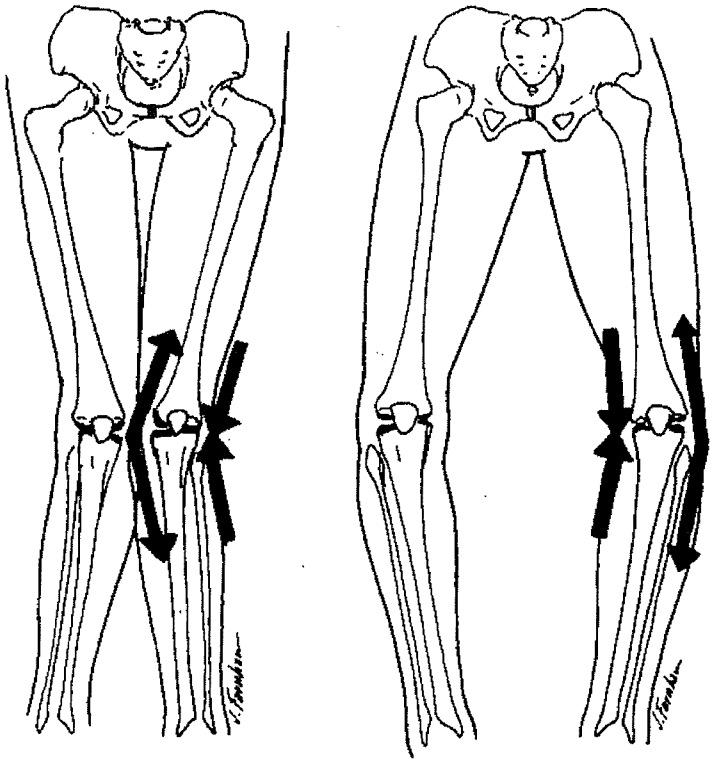

(a) (b)

Figure 2.8. (a) Genu valgus. (b) Genu varus [114].

2.6. LOADING OF THE KNEE

Knowledge of the various parameters that define the load transmitted by the knee joint (magnitude, pressure distribution, variation of the load) is of vital importance for knee prosthesis design. In the following sections, these parameters are described.

2.6.1. Static forces

There is very little data in the literature about static forces transferred through the tibiofemoral joint, as under these circumstances the loads in the knee are significantly lower than those occurring during dynamic activities (e.g. walking, cycling, etc); hence, most of the work in this area has been concentrated on the assessment of the dynamics loads, in order to use them as design parameters, as they represent a worse case scenario. When the body weight is borne equally on both feet at rest, the force transmitted by the knee is lower than when the load is supported by only one leg. In fact, when looking at an X-ray image in double leg stance with the feet shoulder-width apart (Figure 2.9-a), which represents the normal stance position, the orientation of the

lower extremity is different from that observed in single leg stance (Figure 2.9-b), and the degree of deformity caused by such eccentric loading of the knee cannot be appreciated.

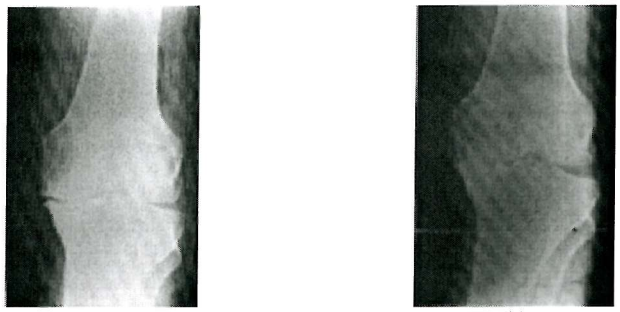

(a) (b)

Figure 2.9. (a) X-ray of patient with significant arthritis in two-legged stance, (b) Same patient in single leg stance showing dramatic increase in the deformity [68].

In the single leg stance condition, it is important to observe the orientation of the mechanical axis of the limb. As the body weight passes onto the single leg, the centre of gravity moves away and upwards from the supporting leg (Figure 2.10). This shift occurs because, unlike the suspended leg, the weight of the lower section of supporting leg (shank) is not included in the body mass to be borne by the knee. This new functional centre of gravity must be vertically aligned with the point of contact of the foot with the ground, in order to satisfy the equilibrium condition. In this case, the force transmitted by the joint is mainly borne by the medial condyle [86].

Values of normal and shear force, peak pressure, medial plateau force and medial plateau contact area, under single legged stance conditions, have been reported in a previous study [86] (Table 2.1). It can be seen that the majority of the normal contact force is applied on the medial condyle (75.0±12.0 %). The resultant force transferred through the tibiofemoral joint was found to be mainly perpendicular to the knee joint line (normal force = 94.3 % BW), with only a small shear component (0.9% BW) pointing medially. The static forces presented in Table 2.1 are significantly lower than those observed in dynamic analyses (section 2.6.2).

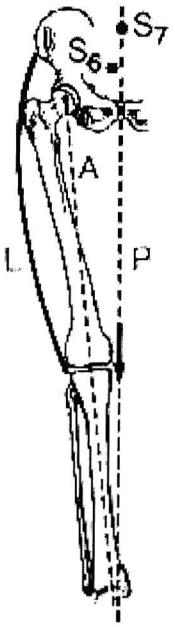

Figure 2.10. Displacement of the centre of gravity, S_6, proximally and away from the supporting leg, S_7. P = partial weight of the body supported by the knee, A = mechanical axis, L = lateral stabilizing forces [68].

Table 2.1. Knee joint static forces and contact pressure distribution, under single-legged stance conditions, for a population of 120 individuals [86].

Joint alignment parameters	Men		Women		Overall (n = 120)
	25-40 years (n = 30)	41-60 years (n = 30)	25-40 years (n = 30)	41-60 years (n = 30)	
Normal force at knee joint (% BW)	95.3 ± 5.9	93.6 ± 3.6	94.1 ± 5.1	94.3 ± 6.8	94.3 ± 5.4
Shear force at knee joint (% BW)	-1.9 ± 2.5	-1.6 ± 2.6	0.3 ± 3.5	0.5 ± 2.1	-0.9 ± 2.9
Joint peak pressure (% BW/mm)	3.5 ± 1.0	3.3 ± 0.9	4.3 ± 1.1	3.8 ± 1.4	3.8 ± 1.2
Medial plateau force (% knee force)	77.7 ± 10.6	72.8 ± 12.7	76.5 ± 11.4	72.8 ± 12.6	75.0 ± 12.0
Medial plateau contact area (% joint area)	60.0 ± 8.8	58.6 ± 5.8	61.2 ± 10.4	59.2 ± 4.9	60.0 ± 7.8

Studies preformed on the hip joint have reported significantly higher static loads [15,33,87] (2.1–2.8 x BW) than those presented in Table 2.1. It should be mentioned that the values in Table 2.1 were obtained by means of a parametric 2D model; hence it is possible that the approximations made in this study have resulted in an underestimation of the static loads in the knee.

2.6.2. Dynamic Forces

Normal gait is divided into two phases: stance phase and swing phase. One of the differences between walking and running is that during walking, at some point of the

gait cycle, both feet are on the ground, and thus providing double support. Each stance phase begins and ends with double support. In a stance phase, four instants are of particular interest: *heel strike* (HS), *foot flat* (FF), *heel off* (HO) and *toe off* (TO) (Figure 2.11). The length of the period of double support depends upon the gait velocity. Stance phase will equal 50% of the cycle plus the length of the double support time. At a normal velocity (3-4 mph), there will be two double support phases in a full gait cycle, each lasting 10-12% of the entire cycle.

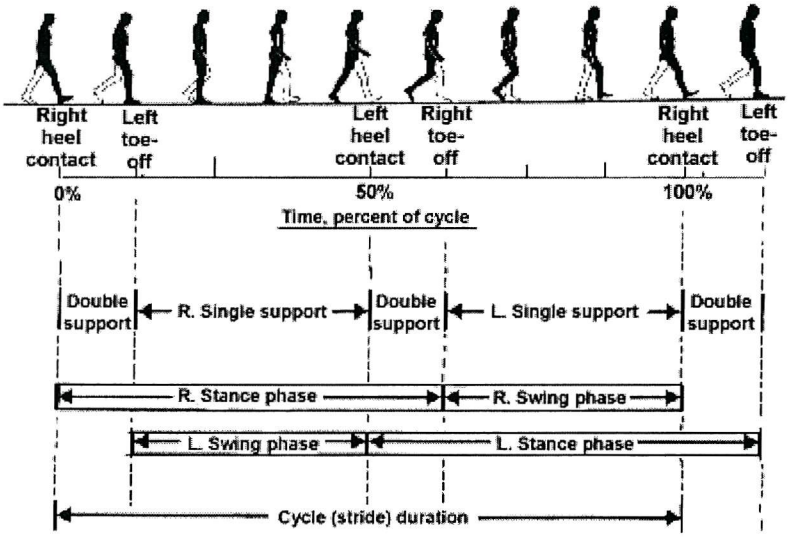

Figure 2.11. Time dimensions of the gait cycle [68].

Little data on the forces occurring in the natural knee have been reported due to the difficulty of accurately measuring the internal movement of the joint caused by the surrounding tissue. Therefore, most authors have developed mathematical models to calculate these forces from the general dynamics of the joint. Morrison [105] was the first investigator to publish in detail forces acting across the knee joint throughout an entire gait cycle. He measured the direct compressive force acting in the direction of the longer axis of the tibia, as well as a side or shear force acting in the medio-lateral direction, for 12 different subjects. The variation of these forces is shown in Figure 2.12. For the compressive force (R_y), the maximum, minimum and average curves obtained from the 12 subjects tested are plotted. The dashed line represents the average force obtained in the study. The shear component in the medio-lateral direction (R_z), was also reported. Since the difference in the shear forces between all 12 subjects was

negligible as compared to the magnitudes of the other component (R_y), only the curve corresponding to one subject was reported. The peak values of compressive force (R_y) for the minimum, average and maximum curves were 2.06, 3.03 and 4.00 times the body weight respectively, whereas the maximum value reported for the shear component (R_z) was 0.26 times the body weight.

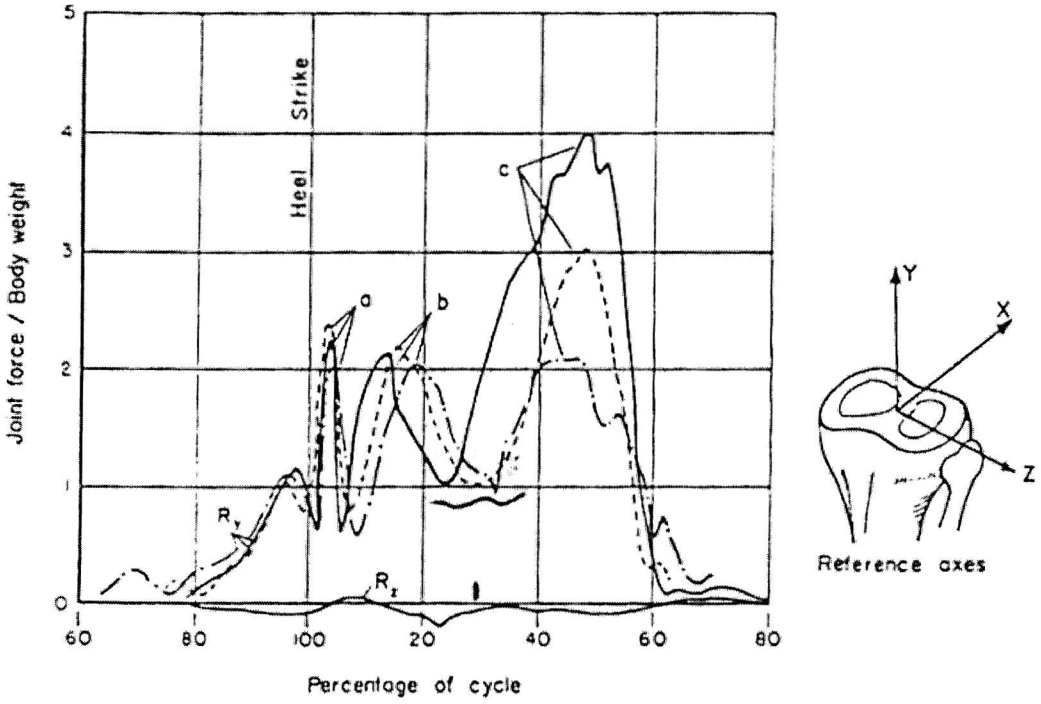

Figure 2.12. Variation of the knee joint force in the gait cycle [105].

Currently, the curves shown in Figure 2.13 [75] are being used as the standards for testing of total knee replacements. Notice that the axial force curve (Figure 2.13-a) is similar to that proposed by Morrison [105], as both curves present three peaks. However, the maximum load (2600 N) is observed at 13% of the gait cycle (second peak on the left) whereas the third peak (45% of gait) shows a slightly lower force value (2433.5 N). It should be noticed that the axial force is in compression for the whole cycle.

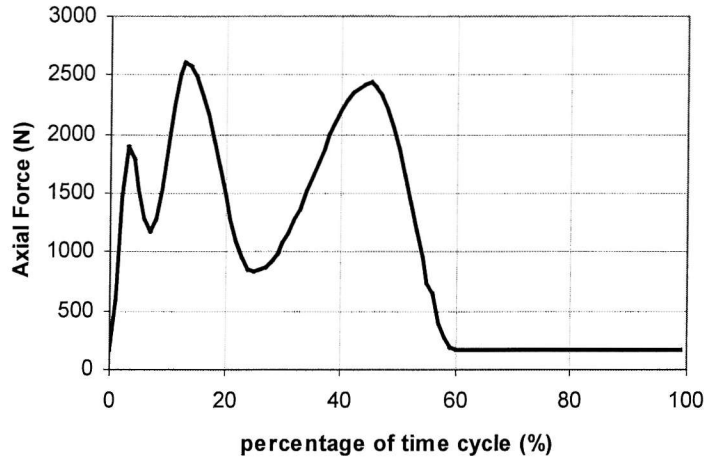

(a)

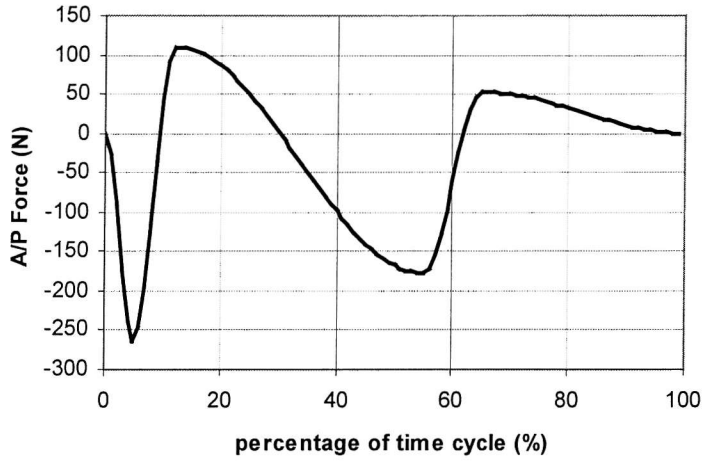

(b)

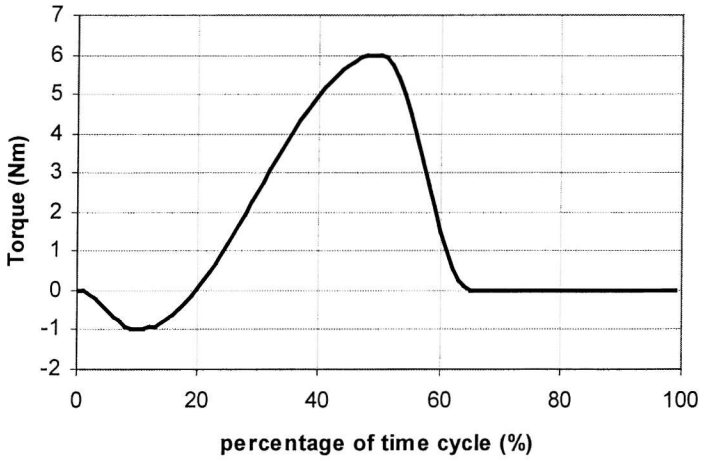

(c)

Figure 2.13. Loads recommended by the ISO standards for TKR testing. (a) Axial force, (b) antero-posterior force and (c) rotation torque.

The antero-posterior force (Figure 2.13-b) presents four peak values, two pointing anteriorly (positive values) and two pointing posteriorly (negative values). These values are -265.0, 110.0, -177.0 and 52.0 N, occurring at 5, 12, 55 and 65 % of the gait cycle respectively. The rotational torque (Figure 2.13-c) shows only two peak values, one external (negative sign) and one internal (positive sign). The maximum external and internal torques are 1.0 and 6.0 Nm respectively, and occur at 10 and 50 % of the gait cycle, respectively.

The maximum tibiofemoral compressive forces for different activities and joint angles have been reported by various investigators (Table 2.2). These activities generate compressive forces ranging between 3.0 and 9.0 times the body weight.

Table 2.2. Tibiofemoral joint forces (compression) [79].

Author	Activity	Knee Angle (degrees)	Force (x BW)
Morrison (1969)	Downstairs	60	3.8
	Upstairs	45	4.3
Morrison (1970)	Walking	15	3.0
Smidt (1973)	Isometric extension	60	3.1
	Isometric flexion	5	3.3
Harrington (1976)	Walking		3.5
Dahlkvist *et al.* (1982)	Squat-rise	140	5.0
	Squat-descent	140	5.6
Ellis *et al.* (1984)	Rising form chair		
Ericson and Nisell (1986)	Cycling	60-100	1.2
Nisell *et al.* (1989)	Isokinetic extension at 30°/sec	65	9.0
Kaufman (1991)	60°/sec	55	4.0
	180°/sec	55	3.8

BW = Body Weight

The maximum tibiofemoral posterior shear forces for various activities are presented in Table 2.3. In everyday activities, the posterior shear forces vary from 0.05 to 3.6 times the body weight.

In Table 2.4, the maximum tibiofemoral anterior shear forces can be found. These forces range from 0.04 to 0.4 times the body weight.

Table 2.3. Tibiofemoral joint forces (posterior shear) [79].

Author	Activity	Knee Angle (degrees)	Force (x BW)
Morrison (1969)	Downstairs	5	0.6
	Upstairs	45	1.7
Morrison (1970)	Walking	5	0.4
Schmidt (1973)	Isometric flexion	45	1.1
Dahlkvist *et al.* (1982)	Squat-rise	140	3.0
	Squat-descent	140	3.6
Ericson and Nisell (1986)	Cycling	105	0.05
Nisell *et al.* (1989)	Isokinetic extension at 30°/sec	50	1.0
Kaufman (1991)	60°/sec	75	1.7
	180°/sec	75	1.4

BW = Body Weight

Table 2.4. Tibiofemoral joint forces (anterior shear) [79].

Author	Activity	Knee Angle (degrees)	Force (x BW)
Morrison (1969)	Downstairs	30	0.04
	Upstairs	15	0.1
Morrison (1970)	Walking	15	0.2
Smidt (1973)	Isometric extension	30	0.4
Ericson and Nisell (1986)	Cycling	65	0.05
Kaufman (1991)	60°/sec	25	0.3
	180°/sec	25	0.2

BW = Body Weight

Figure 2.14 displays the variation of knee angles and displacements observed during normal gait. In Figure 2.14-a, it can be observed that when the maximum force in the knee occurs (~50% of gait cycle – Figure 2.12), the flexion angle is very small (stance phase), whereas higher values of these angles are observed during the swing phase of the gait cycle (lower loads – Figure 2.12).

Figure 2.14-b shows the motion of the tibia relative to the femur during gait. These graphs were obtained by fixing intra-cortical traction pins to both tibiae and femurs of five healthy male subjects [88]. It can be seen that the lateral-medial, anterior-posterior and compression-distraction relative displacements between both bones at the knee joint are not negligible, with the average curves showing peak values of 5.6, 14.3 and 7.0 mm, respectively. It should be noted that due to the way the measurements were performed in that study, the terms compression and distraction refer to the entire joint structure (joint capsule, ligaments and cartilage), indicating that the whole structure is being shortened or stretched respectively, in the direction of the long axis of the tibia.

Compression and distraction do not simply refer to contact or separation of the articular surfaces.

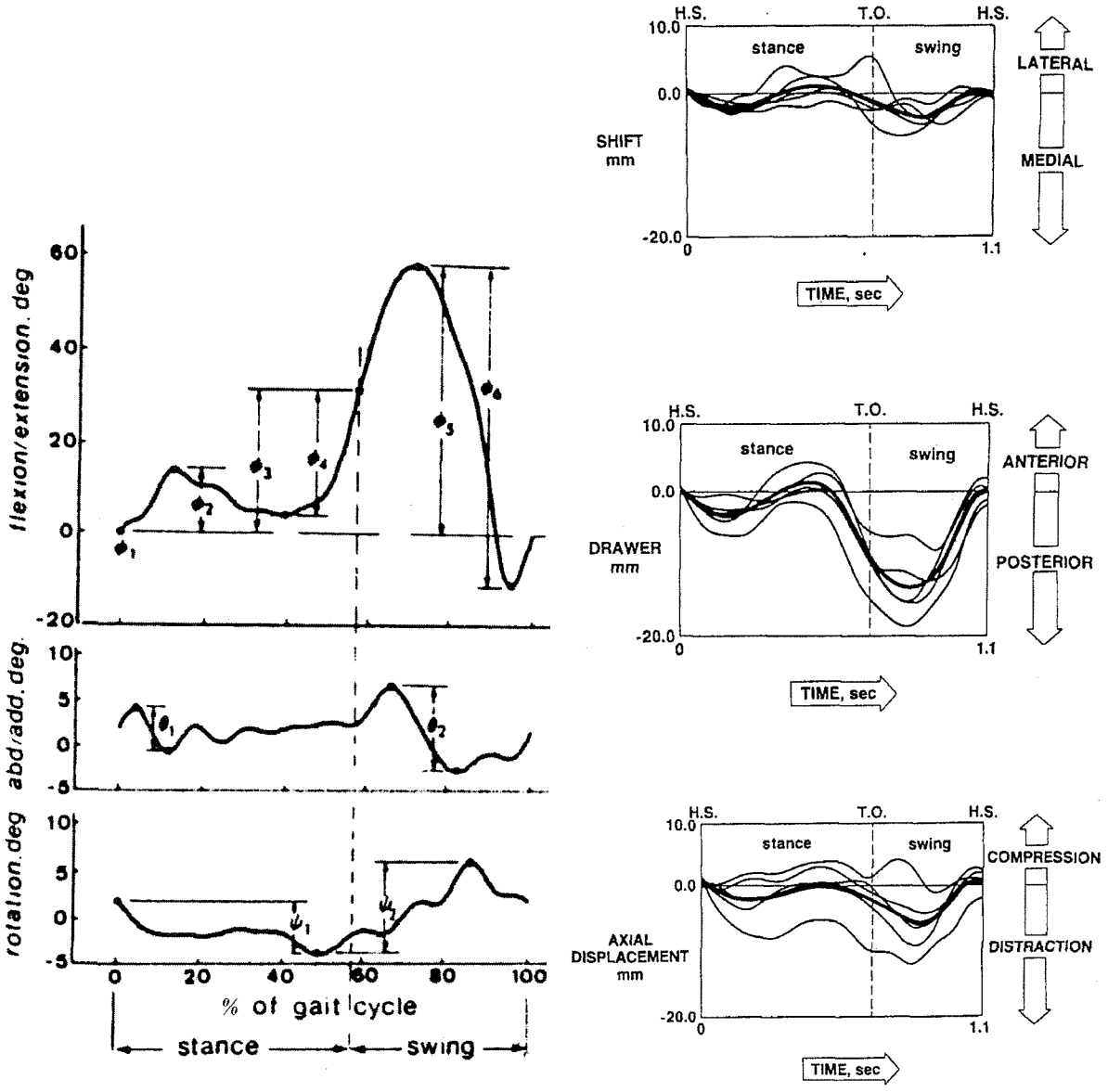

Figure 2.14. (a) Flexion/extension, abduction/adduction and rotation angles of the knee vs. percentage of gait cycle [86]. (b) Lateral/medial, anterior/posterior and compression/distraction displacements observed in the knee [88]. Each curve represents the values observed in a specific subject examined (5 in total). The thicker line represents the average curve of all subjects included in the study.

CHAPTER 3

KNEE REPLACEMENTS

A painful knee can severely affect the ability to carry out a full active life. Many conditions can result in degeneration of the knee joints, and in general, this is caused by arthritis. There are many types of arthritis: rheumatoid, degenerative (osteoarthritis), post-traumatic, autoimmune induced, etc. Osteoarthritis and rheumatoid arthritis are, by far, the conditions that most frequently require patients to undergo knee replacement surgery [4,16,38,89]. Over the last twenty-five years, major advancements in artificial knee replacements have greatly improved the outcome of the surgery, and are becoming increasingly common as the population of the world begins to age.

3.1. KNEE OSTEOARTHRITIS

Osteoarthritis is often referred to as degenerative joint disease. The most common feature observed in osteoarthritic knees is the damage of articular cartilage [36]. Articular cartilage is a firm rubbery protein-based material covering the end of a bone. It acts as a cushion or shock absorber between the bones. When articular cartilage breaks down, this cushion is lost, and the bones will grind together. This causes the development of symptoms such as pain, swelling, bone spur formation and reduction in the range of motion. However, it is clear that osteoarthritis is a condition of the whole joint, not only the cartilage [36].

Although its causes are not well understood yet, several investigators have stated that tissue destruction is produced by alterations of the cellular function. Nonetheless, mechanical factors are also important in the joint degeneration process, as it has been observed that some occupational factors predispose a subject to osteoarthritis [36].

Osteoarthritis is a condition, which progresses slowly over a period of many years and cannot be cured. Treatment is directed at decreasing the symptoms, and slowing the progress of the condition. The treatment of osteoarthritis depends on how far advanced the condition is. In the early stages, treatment for this is usually directed at decreasing the inflammation in the joint. Anti-inflammatory medications, such as aspirin and

ibuprofen, are useful in decreasing the pain and swelling from the inflammation. If the symptoms continue, a cortisone injection may be used to bring the inflammation under better control and ease the pain. There are also braces that can reduce the pressure on the side of the knee that is most involved. Physiotherapy and exercise give the patient some degree of pain relief but does not necessarily change the course of the condition. Arthroscopy allows the surgeon to debride the knee joint (surgical removal of lacerated, devitalised, or contaminated tissue).

Proximal tibial osteotomy, which consists of realigning the angles of the lower extremity by removing a wedge of bone from the proximal tibia, will generally reduce pain but will not entirely eliminate it. The advantage to this approach is that very active people still have their own knee joint, and once the bone heals, there are no restrictions to activity level. It is thought that this operation buys some time before ultimately needing to perform a total knee replacement.

3.2. RHEUMATOID ARTHRITIS

Rheumatoid arthritis is a disease that can be found in many organs, however, in most cases affects the locomotor system [161]. Rheumatoid arthritis is observed worldwide, with an incidence in western countries that varies from 1% to 3% of the population [3]. Incidence in women is three times higher than in men, and this difference is even larger at younger ages [3]. Although rheumatoid knees do not show a noticeable inflammation at the early stages of the disease, gonarthrosis later appears in more than 80% of the patients [161]. Gonarthrosis can result in quadriceps atrophy, flexion contracture and valgus instability. The intra-articular pressure usually is increased during this condition, leading to possible bone erosion. The quality of bones is affected as well, as generalised (and in some cases extreme) osteoporosis is present in the entire skeletal system [161].

There is an increasing number of drugs used to treat rheumatoid arthritis (described in detail by Wolheim [161]), which provide a symptomatic relief but do not modify the course of the disease. Ever since it was first introduced, total knee replacements have become a popular alternative for treatment of the rheumatoid knee.

3.3. TOTAL KNEE REPLACEMENT

The ultimate solution for osteoarthritis and rheumatoid arthritis of the knee is to replace the joint surfaces with an artificial knee joint (Figure 3.1). The decision to proceed with a total knee replacement is usually considered in people aged over 55 years [143], although younger patients sometimes require surgery simply because no other acceptable solution is available to treat their condition. The main reason why orthopaedic surgeons are reluctant to perform this type of surgery on younger individuals is that the younger the patient, the more likely the artificial joint will fail [35]. Replacing the knee for a second or third time (revision) is considerably more complicated and the relative advantages seem to diminish with each operation [73].

Figure 3.1. Total Knee Replacement.

Previous studies suggest that 95% of the artificial knee joints last for 10 years and 85-90% for 15 years [103]. Since younger patients are more active, they often place more stress on the artificial joint, which can lead to an earlier loosening and failure. For obvious reasons, younger patients are also more likely to outlive their artificial joint, and will most probably require a revision at some point [35].

There are two major types of fixation for artificial knee replacements: cemented and uncemented, being both still widely used. In many cases a combination of the two types are used. The patellar portion of the prosthesis is commonly cemented into place. The choice to use a cemented or uncemented artificial knee is usually made by the surgeon,

based on the patient's age, their lifestyle, and the surgeon's experience (see section 3.5.3).

Each prosthesis is made up of three parts:

- The *tibial component* replaces the top of this bone with a polyethylene-topped metallic device (Figure 3.2).
- The *femoral component* (made of cobalt-chrome alloy) replaces the two femoral condyles and the groove where the patella runs.
- The *patellar component* replaces the joint surface on the side of the patella that slides in the femoral groove. This component is optional and is not always replaced.

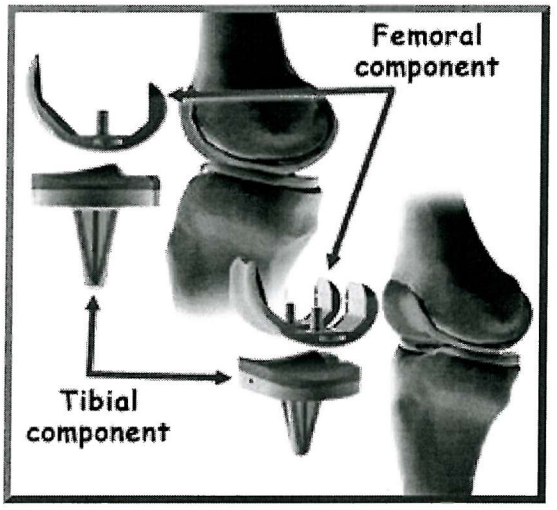

Figure 3.2. Femoral and tibial components.

A cemented prosthesis is held in place by polymethylmethacylate cement (PMMA) that attaches the metal to the bone (Figure 3.3-a). Uncemented prostheses have a fine mesh of holes on the surface that allows bone to grow into the mesh and attach the prosthesis to the bone (Figure 3.3-b), and are typically referred to as porous coated implants. A recent technique, which consists of spraying a layer of calcium phosphate (hydroxyapatite) onto a component, can be employed in order to induce bone growth and hence, to improve fixation (see section 3.5.3 for details).

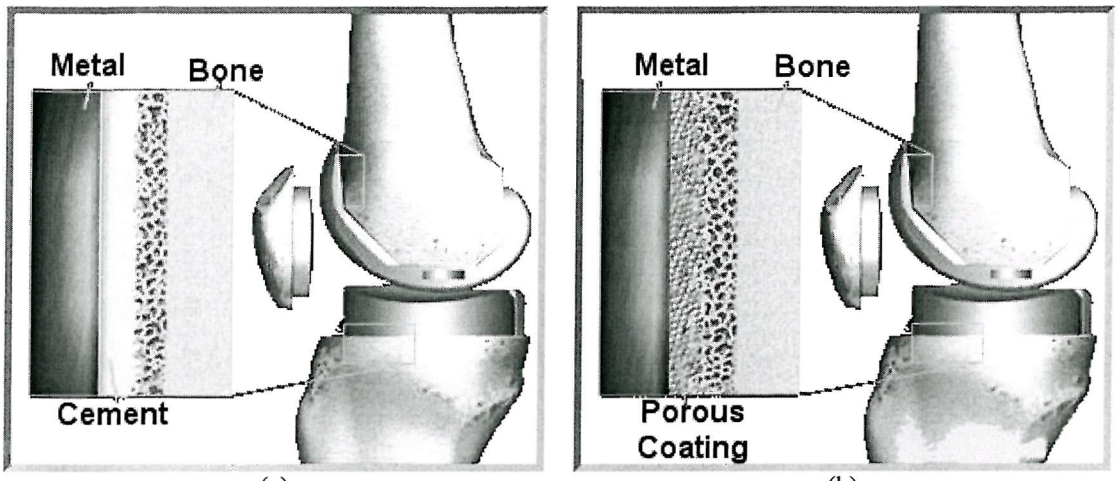

(a) (b)

Figure 3.3. (a) Cemented prosthesis. (b) Uncemented prosthesis (porous coated).

3.3.1. Surgical Procedure

Before conventional knee replacement surgery, a standard X-ray of the whole leg (front-view) is examined to determine the proper alignment of femoral and tibial components, as well as the overall limb alignment (section 3.5.2).

During surgery, a hole is drilled at the end of the femur and a rod is placed down the centre of the bone. A jig is placed on the rod, adjusted to the preoperatively determined angle, and holes are drilled into the bone where indicated by the jig. Guide pins are inserted in these holes, a cutting block is placed on the pins, and a cut is made with a powered oscillating bone saw that defines the horizontal plane of the femoral surface. A second jig is inserted on the rod and the femoral component's remaining cut locations are determined largely by inspection (Figure 3.4-a). The tibial component is placed in a similar manner, except that an alignment jig external to the leg is used to direct its positioning (Figure 3.4-a) [156].

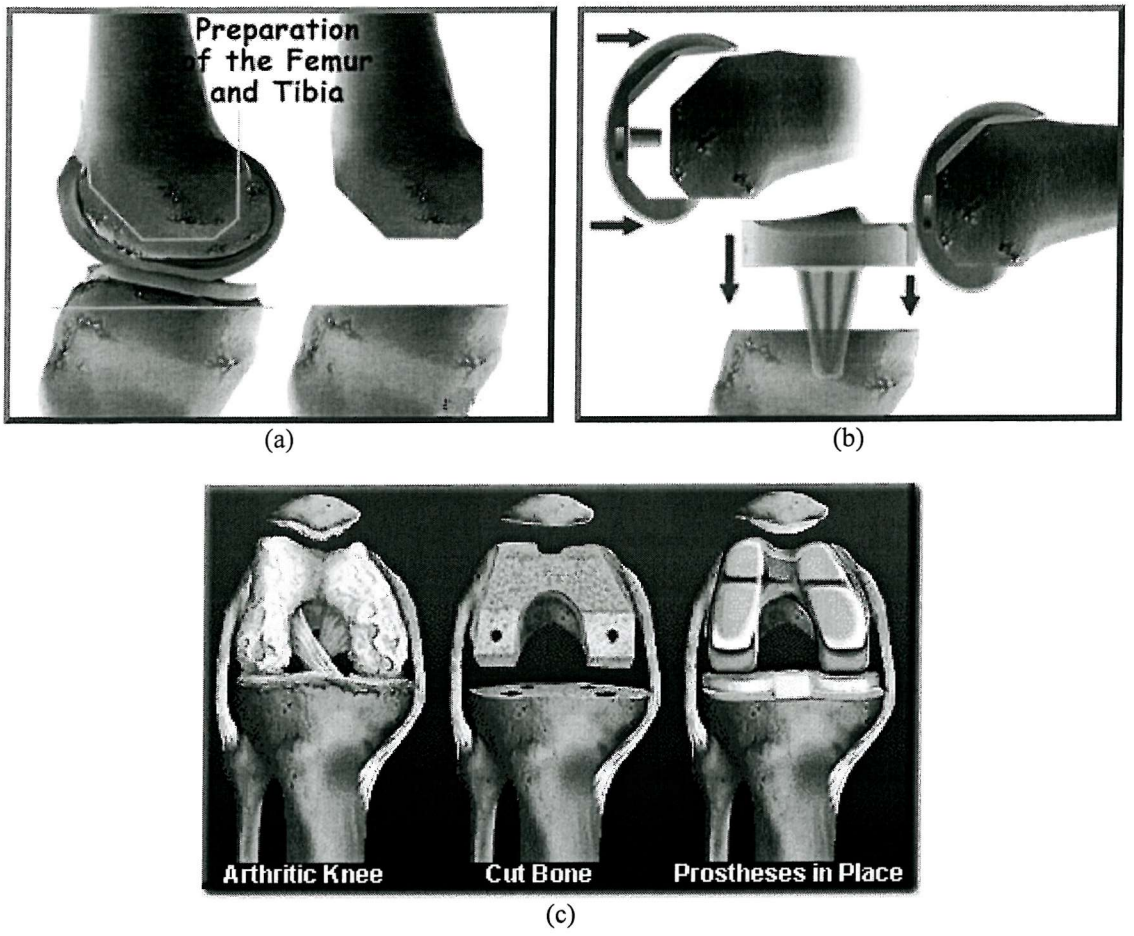

Figure 3.4. (a) Preparation of the femoral and tibial components. (b) Placement of the femoral and tibial component. (c) Overview of a total knee replacement.

3.3.2. Complications

As with all major surgical procedures, complications can occur. Some of the most common complications following knee replacement are: thrombophlebitis, infection, stiffness, wear and loosening. Loosening is the primary cause of artificial knee failure and is described in more depth in section 3.5.1.

3.3.2.1. Thrombophlebitis

Thrombophlebitis, sometimes called Deep Venous Thrombosis (DVT), can occur after any operation, but is more likely to occur following surgery on the hip, pelvis, or knee. DVT occurs when the blood in the large veins of the leg forms clots. This may cause the leg to swell and become warm and painful to the touch. If the blood clots in the veins

break apart, they can travel to the lungs, where they are lodged in the capillaries and cut off the blood supply to a portion of the lung. This is called a pulmonary embolism. There are many ways to reduce the risk of DVT, but probably the most effective one is to enable the patient to undertake physical activity as soon as possible [20,57]. In a study carried out by Insall *et al.* [72], 4% of the knees (9 out of 220 subjects) presented thrombophlebitis.

3.3.2.2. Infection

Infection can be a very serious complication following artificial joint replacement. The incidence of deep infection ranges from less than 1% for resurfacing arthroplasty to 16% for hinged implants [120]. Some infections may show up very early, even before the patient leaves the hospital. Others may not become apparent for months, or even years, after the operation. Out of 220 cases studied, Insall *et al.* [72] observed three patients with deep infection. One infection was secondary to necrosis of the skin, and in the other two cases the prostheses were removed and arthrodesis was obtained in both cases.

3.3.2.3. Stiffness

In some cases, the ability to bend the knee does not return to normal after an artificial knee replacement. Many orthopaedic surgeons are now using a device known as a CPM machine (Constant Passive Motion) immediately after surgery to try and increase the range of motion following a knee replacement. Other surgeons rely on physical therapy beginning immediately after surgery to regain the motion. It is not clear which is the best approach. Both have benefits and risks, and the choice is usually made by the surgeon based on his experience and preferences. To be able to use the leg effectively to rise from a chair, the knee must bend at least to 90^{o}. A desirable range of motion should be greater than 110^{o}. Balancing of the ligaments and soft tissues (during surgery) is the most important determining factor in regaining an adequate range of motion following knee replacement, but sometimes scarring after surgery can lead to a stiff knee. If this occurs, the surgeon may consider taking the patient back to the operating room, placing them under anaesthesia, and forcefully manipulating the knee to regain motion. This allows the surgeon to break-up and stretch the scar tissue. The goal is to increase the motion in the knee without injuring the joint.

3.3.2.4. Polyethylene Wear

Wear of polyethylene tibial inserts is one of the main causes of failure of total knee prostheses. Moreover, in a previous study [40], it was observed that 51% of the cases that had failed for any reason showed severe delamination of the tibial polyethylene insert. That study included 86 prostheses, and their time in site prior to failure ranged between 8 and 91 months (39.5 average). It has been noticed that high conformity designs have significantly less wear problems than the incongruent designs, although the latter, allows for translational and rotational movements [54].

In general, wear of polyethylene components depends on several parameters: molecular weight, homogeneity, thickness (the thicker the polyethylene insert, the less is the wear), geometry, articular surface irregularities, manufacturing process, eccentric loading, surface finish of femoral component (cobalt-chromium alloys produce less wear than titanium alloys) and the sterilisation technique used [55].

3.3.2.5. Aseptic loosening

Component aseptic loosening, specifically the tibial component, has been found to be the cause of the majority of knee replacement failures. Several studies on this particular problem have been performed in order to better understand this phenomenon, as well as the factors related to it. Tibial component loosening is discussed in more depth in section 3.5.1.

3.4. TYPES OF KNEE REPLACEMENTS

Four major categories of knee replacements can be identified:

- Partial, uni-compartmental knee replacements
- Condylar total knee replacements (fixed bearing)
- Constrained condylar total knee replacement (hinges)
- Meniscal total knee replacement (mobile-bearing)

Knee replacement surgery originated in 1951 with the use of a *hinged implant*, first introduced by Borje Walldius [151]. The Stanmore knee joints were introduced in the 1950's and widely used until the 1980's. In general, these implants were composed of two components connected by a hinge, assuming that the knee motion consisted of simple flexion-extension. Unfortunately, the knee is more complex than that and these early implants failed. A later design of a hinged replacement is shown in Figure 3.5.

With a better appreciation of knee kinematics, the *condylar total knee replacements* (Figure 3.1) appeared in the late 1960's, with the introduction of the Polycentric knee (by Frank Gunston) and the Freeman-Swanson knee designs [46,153], followed by the Geometric knee which has been widely used since 1971. Early total condylar designs showed in general, high loosening rates (specifically tibial components), mainly owing to inappropriate fixation and alignment, as well as high metal-plastic constraint [153]. The amount of bone removed compensates for the thickness of the eventual metal and polyethylene added with the prosthesis. Long stems into the tibia or femur are not necessary in standard cases. Many sizes are available so that each patient will have an implant that best fits them depending on their size. Good performance of these implants is very dependent upon the integrity of the collateral ligaments. The role of the cruciate ligaments remains debatable among the specialists in the area (section 3.4.1.2). The fixation of the implant can be carried out with or without cement, but which method gives the best results still remains disputable (section 3.5.3). At present, the fixed-bearing condylar knee is the most commonly used type of knee replacement [154].

One of the improvements in knee replacement design, introduced in the mid 1970's [154], is the use of a movable polyethylene component, known as *mobile-bearing or meniscal knees*. This can be achieved by means of one solid piece of plastic (polyethylene) or two separate components, which are designed to replace the menisci, with the aim of attempting to imitate more closely the natural knee. The rotation of the plastic improves the wear characteristics of the whole prosthesis. The freedom of the plastic to rotate leads to a greater uncoupling of the femoral and tibial motion. These qualities decrease the stresses at the bone-implant interface and minimise the risk of implant loosening. Although they seem to be advantageous compared to condylar designs, relative displacements between femoral and tibial components in condylar knees can occur by rolling, whereas this is less likely to take place in mobile-bearing knees, due to their highly congruent tibiofemoral designs. Furthermore, there is fear that additional wear

due to friction between the polyethylene component and the tibial plateau will contribute to loosening [154].

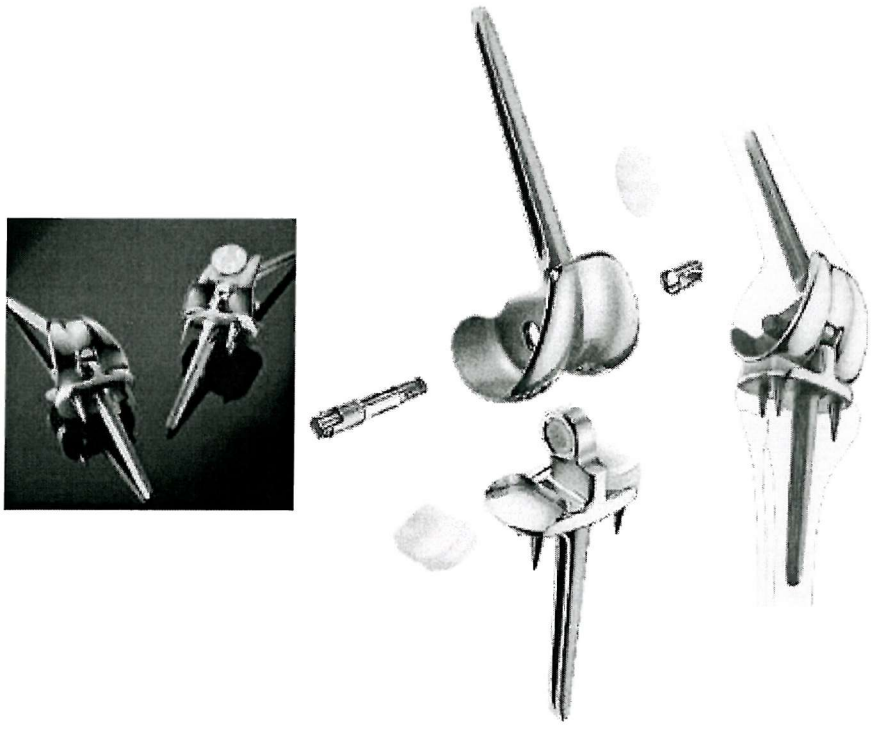

Figure 3.5. The Blauth Knee-Joint Endoprosthesis

Uni-compartmental knee prostheses also appeared in the mid 1970's [110]. This type of prosthesis consists of covering a single condyle of the tibia with a small piece of polyethylene and the femur with a relatively small piece of metal (Figure 3.6).

When the ligaments are intact and two out of three compartments of the knee are healthy, it is reasonable to consider a uni-compartmental replacement for the unhealthy compartment. Unicompartmental knee replacements are mostly used for single compartment osteoarthritis (usually the medial condyle) [153]. If more than one compartment is involved, standard condylar total knee replacement is preferred.

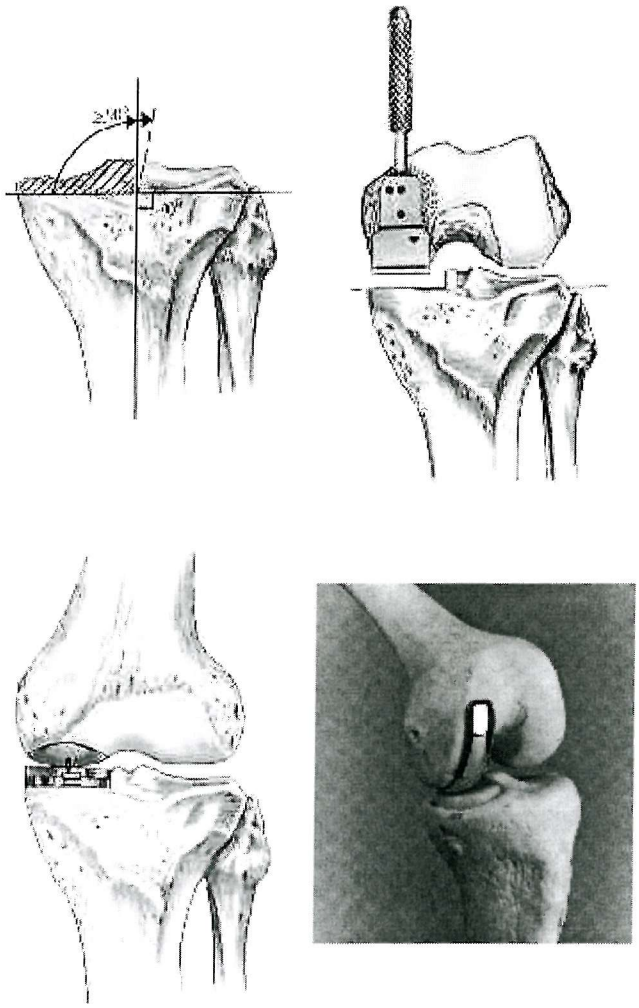

Figure 3.6. Uni-compartmental knee replacement

The original tibio-femoral uni-compartmental replacements have been used as a model for the patello-femoral uni-compartmental replacements, whereby the patella is resurfaced with polyethylene and the opposing trochlea is resurfaced with metal. Such an implant is of course only used when the tibio-femoral contact surfaces are healthy.

Knee replacement surgery is difficult and precise. The bony cuts must be carried out with great care, in order to control the varus-valgus alignment of the limb (section 3.5.2). This aspect is particularly important for uni-compartmental replacements, as an excessively thick implant may put extreme pressure on the opposite condylar surface and lead to arthritis in that compartment.

Occasionally, there has been significant bone loss associated with patients' deformity. This bone loss precludes adequate seating of the implant. In such situations, bone is commonly used to fill these defects. The bone is obtained from the bony cuts of the other compartments or more rarely is an "allograft" required from a bone bank. There must be the appropriate amount of resected bone as well as the ligament tension to ensure smooth flexion and extension of the knee. Errors in the technique can lead to limitations of motion and/or instability. Proper instrumentation and adequate experience of the surgeon are critical.

The last group of prostheses that will be discussed in this section are the hinged implants with rotating platforms. These are related to the hinged implants of the 60's with the major difference that they feature a rotating plastic component. This allows the implant to rotate as the knee flexes. This type of implant requires greater fixation and usually feature a stem inserted in both femur and tibia. These implants are typically used for major ligamentous insufficiencies as they provide varus-valgus stability.

3.4.1. Design considerations and complications in TKR's

When selecting a total knee replacement (or designing a new one), previous experience from clinical, experimental or theoretical studies has to be taken into account.

The first condylar polythene-metal total replacement ever used was the Freeman-Swanson prosthesis, and was inserted at the London Hospital in 1968 [46]. This device had a large contact surface and required cruciate ligament sacrifice, but did not account for the large antero-posterior rocking moments or the patellar tracking [153].

The Geometric knee, used from 1971, featured excessive metal-plastic constraint, thus showing high loosening rates and limited motion [153].

In the early 1970s, three designs displayed a long-term successful performance: the Townley, the Eftekhar and the total condylar. The first provided low tibio-femoral constraint, allowed for cruciate preservation and included a patellar flange. The other two designs achieved a balance between stability and laxity by showing partial conformity between the femoral and tibial components. This avoided high loosening rates. Short pegs where introduced in order to improve fixation in both femoral and tibial components [153].

By the end of that decade, based on biomechanical studies, various concepts where accepted by the scientific society in the field [153]:

- Enclosure of the polyethylene tibial component in a metal tray, to provide better fixation
- Partial femoral-tibial conformity, offering both laxity and stability with acceptable contact stresses on the plastic surface
- A patellar flange, in order to avoid patellar pain and grant the option of plastic resurfacing

Additionally, instrumentation has evolved to achieve better accuracy in alignment and ligamentous tension, and hence providing accurate component fit.

3.4.1.1. Geometry of the femoral and tibial components

Between the low and high conformity designs of the femoral-tibial articulating surfaces, there is no agreement on which one shows a better performance. As mentioned in the previous section, it has been demonstrated that the use of a high conformity surface design will reduce the contact stresses but increase the risk of loosening of the tibial component [152]. Ewald and Walker [42], by means of a clinical study, compared different total knee designs. They observed that three basic designs could be found: a round ball contacting against a flat plastic surface, which gives point contact; a cylindrical femoral component in contact with a flat surface, donating a line contact; and a rounded femoral component in both sagittal and lateral plane in contact with a dished tibial component, obtaining a rounded contact area (rather than a point or a line). The latter design was found to give the lowest contact stresses. The Kinematic II Total Condylar knee was one of the designs that was shown to be satisfactory in terms of contact stresses. On the other hand, some of the other designs studied showed significantly higher contact stresses (Insall-Burstein Posterior Stabilizer, Kinematic II Stabilizer, Microlock, Townley, Tricom-M).

3.4.1.2. Ligament preservation vs. resection

There are knee replacement designs that require the sacrifice of both cruciate ligaments, only the anterior cruciate or neither of them. The latter (preservation of both cruciates) is only used in unicompartmental designs. The practice of cruciate preservation was based on preserving the anatomical structures as much as possible, and hence obtaining near-to-normal kinematic patterns. Preserving both cruciate ligaments is indicated for younger, active patients. The practice of this technique was mainly limited by the complexity of the surgical procedure, and the fact that significantly high loosening rates were observed, as the surface area and the fixation method of many unicompartmental designs were inadequate [154].

With cruciate sacrifice (both cruciates resected), the lever arm of the quadriceps is affected through the entire range of motion. Besides, if this procedure is carried out in a knee with a previous patelloctomy, the knee becomes anteriorly unstable, especially climbing stairs [153]. The advantage of this practice is that, due to the low level of constrain used, loosening rates are reduced. Also, the surgical procedure is simpler than that of the posterior cruciate preservation. The advantage of preserving the posterior cruciate ligament is that stability and motion of the knee are good compared to the cruciate sacrifice method [153]. Walker and Sathasivam [154] concluded that:

- The posterior cruciate ligament should be preserved when total condylar knees with a low conformity design are used.
- Both methods would give good results with designs of moderate conformity (tibial sagittal radius 60-80 mm).
- With highly conforming tibio-femoral designs, both ligaments should be resected.

3.5. TIBIAL COMPONENT OF TKR

As will be explained in detail in the following sections, the tibial component is the one that most commonly fails in total knee replacements. Furthermore, this thesis deals exclusively with the cancellous bone stress analysis of the implanted proximal tibia and the micromotions of the implant relative to the host bone. For these reasons, the

remainder of the literature survey will concentrate only on matters related to the tibial component, rather than the whole of the knee prosthesis.

3.5.1. Loosening

Mechanical loosening is currently the major cause of failure in knee prostheses [17,19,38,73,128,145]. There have been great advances in extending the effective life of an artificial joint, but in many cases, implants will eventually loosen and require revision [16,17,73].

There is a general agreement among previous studies in that, of the three components that make up a total knee replacement (tibial, femoral and patellar components), the tibial component is the one that presents, by far, the highest rates of loosening [19,38]. In a study that included 65 noninfected total knee arthroplasties that were revised, Thornhill *et al.* [145] found that in 57% of the failed knees the mechanism of failure was loosening of the tibial component. Cameron *et al.* [19] analysed 700 knee replacements implanted between 1969 and 1979, of which 94 failed. The majority of these failures appeared in the form of loosening of the tibial component. They detected various mechanical factors related to loosening, such as tilt, subsidence, torsion, and a combination of all of them. The most common manner in which loosening is manifested in knee replacements is by pain and persistent sterile effusion in the knee [38].

Ducheyne *et al.* [38], who followed up 100 UCI knee replacements for a period of two years, observed tibial component loosening in seven knees. In all of the failed knees, common observations were found: radiolucency along the bone-cement interface, prosthetic obliquity, fragmentation of trabecular bone and cement, changes in the alignment of the extremity, and permanent deformation of the tibial component. Although radiolucent lines were found also in prostheses that did not fail, it is important to emphasise that all but one of the seven failed knees presented initial radiolucency. In later studies, radiolucent lines were found mainly near the bone-cement interface in tibial components [39,74,127]. Nevertheless, the same authors concluded that there is no clear correlation between radiolucency and component loosening.

In the vast amount of data found in the Swedish Knee Register up to year 1997 (41,223 knees), loosening was by far the major cause of failure of all knee arthroplasties. Out of

3198 implants that underwent primary revision in the period studied (1975-1997), 1411 (44.1% of all revised knees) failed due to loosening [128]. The rest of the knees were revised for other reasons.

The main factors that influence prosthetic loosening have been found to be tibial component alignment and overall limb alignment, as well as the fixation method (sections 3.5.2 and 3.5.3, respectively).

3.5.2. Alignment

It is universally agreed that the single most important cause of aseptic total knee arthroplasty failure is limb mal-alignment or improper prosthetic positioning [9,66,95,127]. Proper alignment is difficult to obtain as existing total knee replacement jig systems introduce several sources of inaccuracy in alignment of the prosthetic components [61].

By means of laboratory and clinical (5 to 9 year follow-up) studies, Bargren *et al.* [9] demonstrated that malalignment of the knee can lead to mechanical loosening of the tibial component. Of 32 patients examined, 11 showed varus alignment, three were in neutral position and 18 were in valgus. The knees presenting valgus alignment showed a lower failure rate (11% of knees failed) than those in varus (91% of knees failed) or neutral (100% of knees failed). This finding was later supported by Jeffery *et al.* [76]. They evaluated 115 Denham total knee replacements (102 patients) for up to 12 years after implantation, of which 11 (10%) either loosened or had to be revised. The risk of subsequent loosening was found to be considerably lower if the limb presented a correct alignment, as only two of the 11 knees that failed were properly aligned. Tew and Waugh [144] examined 428 knee replacements and noticed that those knees with HKA angles around 7^{o} (valgus) were most likely to remain stable. In the 71 knee prostheses that failed (out of 209 analysed) in the 10-year follow-up carried out by Lewallen *et al.* [89], in general the lowest failure rate was observed when alignment of 0^{o} to 8^{o} of valgus was present after surgery.

All of the above studies examined the overall alignment of the replaced knee using the HKA angle. In order to assess the factors that influence loosening, specific measurements of the alignment of the femoral and tibial components relative to the femur and tibia respectively are needed. If the incidence of tibial component loosening

is higher than that of the femoral component, it could be stated that the orientation of the tibial component (PA and AP angles) is of paramount importance. Only a few studies have examined this. Lotke and Ecker [95] observed a significant correlation between the positioning of the prosthesis, clinical performance and the *roentgenographic index*. The roentgenographic index evaluates the knee in terms of over-all alignment as well as the tibial and femoral component positioning separately. This index includes PA angles of up to $\pm 10^{o}$. They suggest that the ideal position for the tibial component is perfectly horizontal in both planes (perpendicular to the longer axis of the tibia), though this assumption was not supported by any results. After studying 70 knees, before and after surgery (1 to 3 years of follow-up), they concluded that in general terms there is a strong correlation between good positioning of the prosthesis and good clinical results. Nevertheless, although they evaluated each component individually, all these values were summed to produce a unique roentgenographic score per knee, and the latter was compared with the evaluation one.

Hilding *et al.* [61] compared two different inter-operative alignment systems and although one of them was proved to be much more accurate than the one traditionally used, it still produced some surgical error. Forty-five knees of patients with gonarthrosis were included in their work. The measured angles in the frontal and sagittal plane of the tibia showed deviations from the ideal, which they defined as 3^{o} varus in the frontal plane and perfectly horizontal in the sagittal plane. The error in the frontal plane (PA angle) was $\pm 4^{o}$ from the ideal position, whereas the maximum error detected in the sagittal plane was a posterior slope of 8^{o}.

Coull *et al.* [32] evaluated 79 total knee arthroplasties in order to assess the alignment of the tibial component. They reported a mean PA angle of 86.88^{o} (in varus), with 38 knees (48%) having a PA angle smaller than that. These knees are therefore expected to show a poor performance. The PA angles observed in that study ranged between 81^{o} and 96^{o}, representing a significant deviation from the mean value.

Hsu *et al.* [66] have analysed, by means of experimental tests, the influence of overall and individual component alignment upon the load distribution on the tibial plateau, for two different total knee designs (Kinematic and Total Condylar). Their results suggest that, for the Kinematic design, a tibial cut of 2^{o} in varus would produce the best (even) force distribution between the medial and lateral condyle. For the Total Condylar knee,

the best force distribution was observed when the tibial plateau was perpendicular to the mechanical axis of the tibia. Nonetheless, it should be noticed that the validity of these results may be limited by the fact that, in all experiments, the magnitude of the load applied was constant and always in the same direction (vertical), and in real knees, this may not be the case.

3.5.3. Fixation Method

Another controversial area in total knee arthroplasty is component fixation. Concerns about the early loosening of cemented total knee arthroplasty led to the experimentation with uncemented femoral, tibial and even patellar components. In spite of its considerable higher cost, this fixation method does not show a significant improvement for pain or mobility. Various studies comparing cementless and cemented total knee replacements [5,102,148,159] have suggested that, in general, the performance of the prosthesis is similar with either type of fixation, although some authors support the use of cemented prostheses due to their greater reliability [5,6,102].

Of the 41,223 knees (operated between 1988 and 1997) considered in the Swedish Knee Register [128], cementless tibial components (3.5% of all tibial components included in the study) showed 1.4 times higher risk of revision as compared to cemented devices. When analysed separately, the difference in risk of revision was only significant for osteoarthritic knees and not for knees rheumatoid arthritis.

Toksvig-Larsen *et al.* [148] analysed 26 knees (25 patients), of which 11 were inserted a tibial component with cement and 15 without cement. They noticed that, after a two-year follow-up, both fixation methods showed similar values of migration (which was the variable considered in the study). These findings correlate with the results reported by Albrektsson *et al.* [5], who measured the tibial component migration during one year in 13 uncemented and 16 cemented knees and found it to be very similar in both groups. Nevertheless, they consider that cemented prostheses are safer than the uncemented ones, as they observed very low progression of migration after six months with the former type of fixation. Consequently, they recommend that cement be used under stemmed tibial trays, specifically in elderly patients and in those with poor bone quality. Nafei *et al.* [107], compared two groups of patients implanted with cemented and press-fit Kinemax prostheses (26 and 49 knees respectively). After an average follow-up period

of 14 months (ranging from 3 to 28 months), they observed that press-fit, smooth-surfaced Kinemax prosthesis should not be used without cement as the latter fixation method produced lower rates of loosening and higher scores (The Hospital Special Surgery score – HSS).

Winemaker *et al.* [159] considered in their study 32 consecutive revision total knee arthroplasties performed in 30 patients. There were 17 stemmed tibial trays inserted with cement and 15 were inserted without cement. All patients had a minimum follow-up of two years and were evaluated using the Knee Society Total Knee Arthroplasty Scoring System. They observed that although fewer radiolucent lines were found around cemented revision stems, both cementless and cemented tibial stems showed excellent short-term clinical results. Therefore, whether the stem should be cemented or uncemented in revision tibial trays should be determined at the time of surgery, as it depends on the characteristics of each patient.

McCaskie *et al.* [102] compared 58 uncemented with 81 cemented prostheses and in spite of observing a significantly greater number of radiolucent lines in the cemented devices, they do not support the use of the more expensive cementless implants, as the clinical results at five years were similar for both fixation methods.

Conversely, there are authors like Whiteside [156] that believe that cementless tibial components can be advantageous in young and old individuals as well as in degenerative and inflammatory diseased patients. It is to be noticed that this type of fixation requires extra accessories, such as pegs and screws attached to the tibial plateau, to guarantee an acceptable clinical performance [156]. In any case, if a cementless tibial component were to be used, Ewald and Walker [42] recommend a design including a central stem with wings rather than a long cruciate stem.

A new technique, using hydroxyapatite (HA) has been introduced with the purpose of improving the fixation of tibial components. This procedure consists in spraying calcium phosphate (hydroxyapatite) onto a planar porous surface of the tibial component and implanting it without cement, in order to induce growth of bone onto the prosthetic surface [109]. By doing this, the initial stability of the implant is expected to improve [109]. Nelissen *et al.* [109] compared the performance of three groups of prostheses fixed with different methods: with cement (11 prostheses), without cement

(10 prostheses) and with hydroxyapatite (10 prostheses). After a 2-year follow-up by means of RSA (section 3.5.4), the authors observed that, as they had expected, the non-coated, uncemented tibial components presented considerably larger micromotion that the other two types of fixation, which showed similar values of initial migration. They believe that this improvement was achieved because hydroxyapatite not only induces bone growth into gaps of up to 2 mm wide, but also decreases the size of these gaps. Other studies that compared different fixation methods for tibial trays by measuring component migrations with RSA [13,113,115,121] will be described in the following section.

3.5.4. Migration measurements in TKR (RSA studies)

Since aseptic loosening of the tibial component is the major cause of failure in total knee replacements (section 3.5.1), it has now become a major concern in practice [17,19,45,73,104,145]. Mechanical loosening arises as a result of migration of the component into the bone [16]. It has been discovered that in most knee prostheses, migration of the tibial component occurs, even in clinical successful cases [4,21,112,134,132,133,131]; therefore, this variable is not a direct symptom of mechanical loosening. It has been noted that most tibial components migrate during the first year [112], but then equilibrium is reached. In this case, the risk of subsequent loosening is considered to be minimal [134].

Roentgen stereophotogrammetric analysis (RSA) has been used for about 20 years [112] to accurately measure the three-dimensional micromotion of the implant [135] with respect to the host bone. It can be used for measuring implant motion over time (migration) as well as instantaneous component motion (usually referred to as micromotion) caused by loading (inducible displacement). Apart from the translation along and rotations about three perpendicular directions (predefined coordinate system), the most commonly reported parameter is the maximum total point motion (MTPM). The latter represents the length of the total vector translation of the marker that moves the most [131]. This research tool requires the previous insertion of tantalum markers, which are later used in combination with repeated radiography with simultaneous exposure of two X-ray tubes. Despite the exposure to X-rays involved, the radiation used by this method has been found to be less than that of conventional radiography [112]. Basically, RSA consists of the following steps [163]:

1. Implantation of radiopaque markers into the prosthesis and the host bone. Markers are normally spherical balls with diameter of 0.5, 0.8 or 1 mm, typically made of tantalum.

2. Radiographic examination of the implanted bone together with the calibration cage, from two different directions simultaneously.

3. Bi-dimensional measurement of radiographic images to locate the relative marker positions in the measurement coordinate system.

4. Reconstruction of spatial marker coordinates (three dimensions).

5. Calculation of rigid body motion based on relative marker positions between different examinations.

Migration (permanent motion over time) measurements are usually performed at one week, six weeks, six months and yearly. These measurements are compared with a reference examination, which is performed immediately after surgery.

Inducible displacements (movement induced by external forces) are measured at different times (e.g. six weeks, one year and two years post-operatively) in the following positions:

1) Supine.

2) Standing with weight borne on the operated leg.

3) Standing with the operated leg on a rotating plate with an outward torque of 10 Nm applied, which the patient should resist.

4) Same as 3) but with an inward torque.

5) Standing on the operated leg flexed 45-60 degrees.

Ryd *et al.* [132] performed a two-year follow-up of eight Freeman-Samuelson arthroplasties without cement for gonarthrosis. Using RSA they found that migration of the tibial component, in all cases, ranged between 0.7 and 4.8 mm at two years after surgery. The majority of this migration was observed (in all but one case) during the first six weeks, followed by a reduction in the motion. Despite these values of

migration, all the analysed knees were scored as clinically successful. These findings were further supported by including a greater number of knees (32) in the study, and obtaining similar results [4]. It is believed that this initial migration of tibial components is related to a remodelling maturation process [131]. In other words, after initial necrosis of the bone underlying the prosthesis, a mature implant foundation made up by fibrocartilage and fibrous and connective tissue, is produced [157]. The latter statement is also supported by a work performed by Ryd *et al.* [133], who followed three patients by means of RSA, for a period varying between 5 and 7 years, after which the prostheses had to be revised for reasons unrelated to mechanical loosening. In all cases, the bone was well attached to the tibial component, for which a resection was performed 5 mm below the prosthesis. A histological study was performed on the extracted components, which showed fibrous tissue and fibrocartilage in the bone-cement interface. The implants showed migration during the first three years after surgery and stabilised later. The results from that study strongly suggest that fibrocartilage may function exceptionally well over time, as it is mechanically favourable in terms of fixation.

In most RSA studies, initial migration of the tibial component was found to be a common factor but in the majority of cases, this movement ceases after one year. If the implant continues to migrate it has been suggested that this migration may predict future loosening [134]. It should be pointed out that though loosening is usually detected several years after operation by using conventional clinical assessment methods, RSA has shown that it is a continuous process that begins shortly after the arthroplasty.

Hilding *et al.* [62,64,63] have analysed 45 osteoarthritic patients treated with total knee arthroplasty. In the first study [63], they compared three uncemented tibial components (Tricon-M, Tricon stem and PCA), in order to assess the effects of the employment of a stem and the correlation between the immediate-interlocking peg concept with long term fixation. The patients were followed up for two years after implantation by means of RSA, observing that the three implants showed similar migration during the period of study (MTPM in the region of 1.4 mm). A relevant finding of this work was the strong correlation observed between inducible micromotions as MTPM and migration values as MTPM. In a separate study, Hilding *et al.* [62] performed RSA measurements on the same 45 patients during normal gait, at six months and two years after surgery. Gait patterns of all patients were also analysed pre-operatively. Two groups of patients were defined in terms of migration of the tibial component. The unstable group (MTPM >

200 μm) consisted of 15 patients, whereas the stable group (MTPM < 200 μm) included 28 patients (2 patients died during the follow-up period). They found for the first time a correlation between pre and post-operative knee joint loading and tibial component loosening. Larger peak flexion moments were observed in the unstable group of patients as well as significantly different mean sagittal plane flexion moments. These differences were noticed before surgery, which led the authors to suggest that certain gait patterns are detrimental to tibial component long-term stability. Another important conclusion drawn from that work was that the fixation strength achieved at surgery may be insufficient, which suggests that the implant may already be loose immediately after an unsuccessful operation.

Another parameter that helps to predict aseptic loosening of the tibial component is the initial micromotion or inducible displacement. In a study performed by Toksvig-Larsen *et al.* [148], in which 27 osteoarthritic patients (28 knees) were followed-up for a period of two years by means of RSA. A reference RSA measurement was performed immediately after implantation and migration values were examined at six weeks, six months, one year and two years after surgery. Inducible displacement measurements at six weeks and one year post-operatively were performed with the knee in five different positions: (i) supine, (ii) standing on the operated limb, (iii-iv) standing on the operated limb with internal and external torques of 10 Nm and (v) squatting to approximately 60 degrees of flexion). It was concluded that when there is little micromotion of the implant six weeks after surgery there will be little micromotion and migration after two years.

Adalberth *et al.* [1] followed up 34 patients by means of RSA, whose diagnosis was primary gonarthrosis. The patients were divided in two groups of 17 patients each in order to compare migrations of a metal-backed tibial component with an all-polyethylene version of the same design. Both tibial component designs were cemented to the bone. They observed that the all-polyethylene components showed similar or lower migration than their metal-backed counterpart. Specifically, the lift-off displayed by the metal-backed tibial component was significantly larger than that observed in the all-polyethylene implant. Since no all-polyethylene implants presented continuous migration between the first and second year after surgery, the authors suggested that

these implants have positive prognosis regarding future aseptic loosening, based on a previous study performed by Ryd *et al.* [134].

3.5.4.1. Fixation methods of tibial components assessed by RSA

As explained in section 3.5.3, there are basically three types of fixation that have been used for tibial components: cemented, uncemented (porous coated) and hydroxyapatite sprayed underneath the tibial component. In a randomised RSA study including 116 osteoarthritic patients (146 knee replacements), Önsten *et al.* [115] reported the migration observed in three groups of patients with different fixation methods for the tibial component, in order to compare the effect of HA coating with normal porous coating and cement fixation. They observed that even though the migration values measured at 3 months after implantation were higher for the HA coated implants, these values did not show significant variations between 12 and 24 months, as opposed to the plain porous coated implants, which showed less stability over a longer time (between 12 and 24 months after surgery). They concluded that HA coated tibial trays develop a better fixation than their plain porous coated counterparts, however, observing no difference in stability between the HA coated and the cemented groups, they concluded that hydroxyapatite has no advantage over cement. These findings were supported by Regnér *et al.* [121], who examined 45 patients (51 knees) with osteoarthrosis, which were subdivided in two groups: HA coated and plain porous tibial components. After a 5-year follow-up of these patients, in which RSA was used to measure the implant migrations, they concluded that hydroxyapatite produces a significantly more stable fixation than the plain porous surfaces. In another 5-year follow-up study performed by Nilsson *et al.* [113], 53 patients (57 knees) with osteoarthrosis and rheumatoid arthritis were examined by means of RSA, in order to compare two tibial tray fixation methods: hydroxyapatite and cement. In the same way as Önsten *et al.* [115], they observed most of the migration of the HA coated implants during the first 3 months, but later stabilised. On the other hand, the cemented tibial components displayed an initial lower migration that progressively increased over time. These results lead to the conclusion that there are no differences between these two types of fixation.

Bellemans *et al.* [13] examined three different types of uncemented porous coatings underneath the tibial components of total knee replacements implanted on 40 adult sheep, creating three groups. Group 1 was implanted a cast mesh coated tibial

component (1.5 x 1.5 mm constant pore size), group 2 received identical tibial trays as group 1 but with an additional hydroxyapatite plasma sprayed coating, and group 3 was implanted with a multiple layer beads coating tibial component (irregular pore size approximately 150 μm). They used RSA to measure the tibial component migrations at 3, 6, 12 and 24 months after surgery. Additionally, they performed *post mortem* analyses in order to inspect the level of bone (or fibrous) ingrowth into the implant. Comparing groups 1 and 3, they noticed that larger pore sizes are more appropriate as they lead to a better growth of the bone into the pores. However, as a natural body reaction to foreign materials, a fibrous layer (which is poorly vascularised) is formed on the bone-implant interface, leading to continuous migration that may be followed by complete mechanical loosening. They observed that this fixation was significantly improved by hydroxyapatite, as it induces bone ingrowth, instead of fibrous ingrowth, producing a far superior osseointegration, which leads to a more rigid fixation and hence less migration. They also concluded that RSA is an adequate tool to indirectly assess the quality of osseointegration of knee replacement components by measuring the stability of the implant.

A summary of the RSA studies performed to date can be found in Table 3.1. Only the maximum total point migration (MTPM) was included in order to provide an idea of the levels of migration that can be observed in tibial components.

Table 3.1. Summary of migration of tibial components reported in the literature.

Authors	Nr of knees	Fixation type	MTPM (mm)		
			1 year	2 years	5 years
Ryd *et al.* [131]	27	cemented	——	0.8 (0.2–2.1)	——
Ryd *et al.* [132]	8	uncemented	——	(0.7–4.8)	——
Ryd *et al.* [133]	3	cemented	1.5 (0.7–2.7)	1.8 (1.0–3.3)	1.9 (1.0–3.3)
Albrektsson *et al.* [4]	9	stem **	1.3 (0.7–1.6)	1.3 (0.7–2.0)	——
	24	no stem **	2.0 (0.9–4.6)	2.4 (1.0–4.9)	
Albrektsson *et al.* [5]	13	uncemented	1.5 ± 1.1	——	——
	16	cemented	0.5 ± 0.3		
Hilding *et al.* [62]	45	uncemented	1.3	1.4	
Ryd *et al.* [134]	97	cemented	0.7	0.8	1.1 †
	46	uncemented	1.7	1.7	2.2 †
Toksvig-Larsen *et al.* [147]	40 Osteotomy	cemented and uncemented	1.1 ± 0.2	1.1 ± 0.3	2.3 ± 0.9
	40 Primary		0.8 ± 0.1	1.0 ± 0.1	1.3 ± 0.2
Toksvig-Larsen *et al.* [148]	11	cemented	1.0 ± 0.2	1.0 ± 0.1	——
	15	uncemented	1.4 ± 0.2	1.5 ± 0.2	
Önsten *et al.* [115]	50	HA coated	1.0 ± 1.5	1.0 ± 1.4	——
	47	porous coated **	1.0 ± 0.6	1.0 ± 0.6	
	49	cemented	0.5 ± 0.5	0.6 ± 0.5	
Bellemans [13]	16*	cast mesh **	1.4	4.6	——
	16*	HA cast mesh	0.3	3.2	
	8*	multilayer beads**	1.6	5.6	
Nilsson *et al.* [113]	19	HA coated	0.6	0.7	0.7
	21	uncemented	0.4	0.6	0.8
Regnér *et al.* [121]	25	HA coated	0.5	0.5	0.6
	26	porous coated **	0.6	0.7	0.8
Fukuoka *et al.* [47]	31	HA coated	1.25	1.29	——
Adalberth *et al.* [1]	17	Metal backed***	(0.3-0.8)	(0.4-0.9)	——
	17	all-polyethylene***	(0.3-1.0)	(0.2-0.8)	

* These prostheses were implanted on sheep.
** Uncemented
*** Cemented
† Data corresponding to 6 years (instead of 5)

3.5.5. Micromotion and migration as predictors of implant loosening

Several investigators have concentrated their efforts on predicting future implant loosening and concluded that RSA is the most appropriate tool to perform this task. Grewal *et al.* [56], performed a combined migration and survivorship study over a period of five years for three different designs implanted on a large number of knees with the aim of correlating this data with previously published RSA migration studies on these designs. They defined three groups of patients according to the tibial component with which they were implanted. Group 1 had an all-polyethylene component whereas group 2 and 3 were implanted with a metal-backed tibial component with a central stem, fixed without and with cement respectively. They noticed that early migration was directly

correlated with the long-term survival of the prosthesis, as the designs that produced the lowest migration at one year after surgery (group 3) also showed 100% cumulative survival rate at 5 years. Likewise, all-polyethylene prostheses (group 1) produced the highest migration at one year post-operatively and the cumulative survival reported for this group at five years was the worst of the three designs examined (76%). The results from this study support the hypothesis that RSA of a small number of knees can predict in one year what survival analysis of a large number of knees can achieve in five years. They finally concluded that measurements of early migration are of essential clinical value, as they can predict late aseptic loosening of prosthetic components. This view was supported by the study performed by Ryd *et al.* [134], in which additional variables such as long-term migration, fixation method and alignment, were evaluated. They examined 158 total knee replacements (paying most attention to the tibial component) with a minimum follow-up of 11 years (143 cases were followed for up to 13 years). They found that in most cases, although a mean migration of 1 mm was observed after one year, after ten years it was not substantially larger (mean migration of 1.5 mm). Cemented implants ended up showing a much better long-term performance, as their subsidence was either zero or significantly lower than that found in uncemented devices (presenting a mean final subsidence of 1.0 mm). A varus tilt of 0.7^{o} was observed for uncemented components, whereas the cemented ones showed no tilting at all. They also compared patients with rheumatoid arthritis with those with osteoarthritis and the former had a greater tendency for continuous migration. The other demographic parameters (gender, type of arthroplasty, weight and the presence of stem or metal backing) had no influence on migration. Finally, the overall knee angle was also noted to have influence on continuous migration, as knees in varus showed migration more often than those in valgus (see section 3.5.2). In conclusion, they stated that RSA can be used during the first two years after surgery to predict, with a reliability of around 85%, the risk of component loosening at five or more years after implantation.

In a recent study, Fukuoka *et al.* [47], proposed a method to predict long-term migration and, therefore, loosening. They measured the *Initial Stability* via micromotion measurements of 31 uncemented total knee replacements. These measurements consist in applying a 20-kgf perpendicular force on the tibial plateau at the moment of operation, and by means of non-contact sensors, recording the tilting (lift-off) of this component. They also followed the studied knees for two years using RSA, and

observed a strong correlation between migration and initial stability ($p<0.05$). In this way, they affirm that future migration of the tibial component can be estimated at the moment of operation, as a prosthesis which may become loose is likely to do so from the time of surgery.

3.6. FE STUDIES OF THE PROXIMAL IMPLANTED TIBIA

Relatively few finite element analyses of the implanted proximal tibia have been performed in comparison with implanted proximal femurs [29,67,81] (see Appendix E for a brief overview of the finite element method). Several two-dimensional models have been developed to study the effect of specific parameters such as interface characteristics and loading conditions. One of the earliest of this type of study found in the literature is the 2D model analysed by Hayes *et al.* [59], who performed a parametric study varying the bone's stiffness. They considered a cemented tibial component and homogeneous material properties for cortical and cancellous bone and studied the stress distribution in the model for three different load cases, with the aim of evaluating prosthesis design improvements. They also analysed a second model with a graded cancellous bone material property distribution. They observed that the latter model produced lower peak cancellous bone stresses. The latter were further reduced when the Young's modulus of the cortical shell was increased. In all cases, the peak stresses were found around the tip of the tibial component stem. In general, they concluded that the cancellous bone stress distribution is highly sensitive to material property variations as well as the load case used. Beaupre *et al.* [11] attempted to model more realistically the loads acting on the tibia by including the patellar ligament force applied on the frontal aspect of the bone. Their 2D model was based on two sagittal slices taken from an adult male cadaver. Six different regions with uniform material properties were defined in the bone model. A cementless, metal-backed, polyethylene tibial component was included in the model, assuming perfect bonding between bone and implant. They concluded that the patellar ligament force should be considered, as this results in a stress field that corresponds better with the epiphyseal, trabecular and cortical morphology.

Garg *et al.* [49] addressed the problem of imperfectly bonded interfaces by analysing a 2D model representing sagittal slices of the tibia. They chose the sagittal plane based on the observation that the trabeculae in the frontal plane are mainly vertical, hence the

lines of equal stress would likely be similar. The geometry and material properties of the bone were obtained using computer tomography. They established a correlation between the pixel intensity value and the Young's modulus by means of experimental tests performed on several bone samples taken from different tibiae. After performing a convergence analysis, they concluded that 17 material properties produced sufficiently accurate results. Stresses in the bone supporting the implant were calculated as a function of (i) amount of bone resected, (ii) fixation type and (iii) localisation or completeness of bone-implant contact. They observed that bone resection may not be unfavourable, as the supporting area increases allowing the utilisation of a larger tibial component. They also observed that both cemented and cementless implants produced very similar stresses on the underlying bone. Finally, they concluded that the nature and location of the contact regions are important for the stress distribution on the supporting bone.

Rakotomanana *et al.* [119] performed a 2D finite element analysis (frontal plane) with the purpose of investigating the interface load transfer and relative micromotions, taking into account anisotropic, elastic-plastic properties of the bone as well as interface discontinuities. Only three regions with uniform material properties within the bone model were defined. Three different tibial component designs were analysed: (i) cemented, metal backed with a central peg and (ii) cemented and (iii) uncemented porous coated with two short pegs. They concluded that the effects of bone transverse isotropy and interface discontinuity are significant for the behaviour of the bone-implant interface.

A series of axisymmetric models have been analysed by several authors. Murase *et al.* [106] studied various models of the proximal tibia implanted with a cemented prosthesis. The tibial component design was parametrically varied and submitted to different loading conditions in order to study the effect of the metal reinforcements and central fixation posts on the stress distribution in the bone. They concluded that metal backing of the tibial component is advantageous with respect to the all-polyethylene components. They also noticed that longer central stems considerably unload the proximal tibia in combination with adequate distal cement. Conversely, long polyethylene central posts were observed to provide poor rigidity, affecting the load transfer.

Forcione *et al.* [44] included non-linear friction in an axisymmetric model of the tibia implanted with a porous coated component. Various parameters were varied in order to study their effects on the interface stresses and relative micromotions. As a result, friction reduced the relative micromotions by about 10%. Ahmed *et al.* [2] studied the effects of dynamic loading on the underlying bone of a cemented tibial component, concluding that a static analysis is sufficient to characterise the stress field on the proximal implanted tibia, as the dynamic effects are relatively small. Dawson *et al.* [34] analysed an axisymmetric model of a portion of tibia around a peg with the purpose of studying the effect of an interference fit on the cancellous bone stresses. They concluded that the residual stresses produced around the pegs are beneficial for bone ingrowth in that region, but it also relaxes the stresses beneath the tibial tray, resulting in higher micromotions that may induce the formation of a layer of fibrous tissue.

Three-dimensional finite element studies have been performed mostly on cemented tibial components [10,28,90]. Bartel *et al.* [10] studied a simplified 3D finite element model of a total condylar cemented tibial component. They analysed three cases: all-polyethylene tibial components with and without a central peg, and a metal backed tibial component with a metal peg. After examining the cancellous bone stress with different loading conditions, they concluded that the addition of a peg reduces the cancellous bone stresses at the bone-cement interface, and these stresses are further reduced when a metal peg and tibial tray are used. These results are supported by the three-dimensional finite element study carried out by Lewis *et al.* [90], who analysed several tibial component designs and observed that, of all designs, a single-post, metal-backed tibial tray produced the lowest cancellous bone stresses at the bone-cement interface. As mentioned above, similar results were also found with the axisymmetric model analysed by Murase *et al.* [106]. Bartel *et al.* [10] have also suggested that, if the tibial component were in contact with the cortical bone, the load borne by the underlying trabecular bone would be reduced. A consistent result was found by Murase *et al.* [106], as they noted that when a longer central stem was used the cement-bone interface stresses were lower than those of a shorter stem. This can be related to the fact that with this longer stem, the cement in their model was in contact with both tibial component and cortical bone.

Cheal *et al.* [28] found that the prosthesis supported purely by cancellous bone produced slightly higher stresses than those generated by one resting on cortical bone. They

observed that an undersized component might cause resorption of the unloaded peripheral bone. They also observed that the addition of cement in the region around the posts produces an increase in the cancellous bone stresses. Nevertheless, this is compensated for by the increase in the bone-cement interface bonding strength.

Keja *et al.* [83] compared the relative motion between a proximal tibia model implanted with two different prostheses. A heterogeneous material property distribution (588 different moduli) was used, where the values were obtained from experimental tests. An axial load was equally distributed between medial and lateral condyles. They observed little lift-off in all models undergoing axial compressive loads and in all cases, the posterior aspect of the tibial plateau sunk more that the anterior one, and the lateral side subsided more than the medial side. They concluded that the effect of the anterior screw used in one of the designs reduced micromotions by only 7%. In general, the results from that study suggest that a perimeter fixation allows smaller micromotions. They observed that deeper bone cuts resulted in a stiffness decrease that generated 15% higher micromotions. This contradicts Garg *et al.* [49] who observed negligible variations in bone stiffness with the depth of the cut-out and actually suggested that deeper cuts may be beneficial due to the increase in the supporting area, allowing the utilisation of a bigger implant size.

Tissakht *et al.* [146] performed a 3D analysis of the proximal implanted tibia to assess the micromotions of three different fixation types: (i) close-fit (no interference between bone and prosthesis), (ii) press-fit (with interference between bone and implant) and (iii) screw fixation. The effect of friction was included in the analysis by using different coefficients (0, 0.1, 0.25 and 0.45). The trabecular bone was divided in 13 regions with uniform elastic moduli ranging between 25 and 300 MPa. The cortical bone was subdivided into eight material property regions with moduli ranging from 1140 to 8650 MPa. They noticed that the relative displacements for the press-fit fixation were larger than those produced by the close-fit prosthesis. These displacements were further reduced with the use of screws instead of pegs. Increasing the friction coefficient from 0 to 0.15 resulted in substantial reductions in the micromotions, but when the friction coefficient was further increased, the change in relative displacements was much smaller.

Taylor *et al.* [142] studied the cancellous bone stresses induced by cemented and uncemented tibial components by means of three-dimensional finite element models of the proximal tibia using different load cases. They observed that the largest cancellous bone stresses were generated with the all-polyethylene prostheses. These stresses were attenuated by adding a stemmed metal backing, but the lowest risk of cancellous bone failure was produced by the cemented metal-backed prosthesis. They found a good correlation between the predicted cancellous bone stresses and the clinical data, as the implants generating the lowest cancellous bone stresses were those found to present the lowest migration and revision rates. Some studies have tried to predict the risk of global or local cancellous bone failure. This parameter has usually been defined as the percentage of the ultimate strength that the cancellous bone stress represents [142]. The majority of the analyses performed employed bi-condylar load cases [11,28,150], hence they reported relatively low risks of failure by compressive cancellous bone stress, usually in the order of 30%. Taylor *et al.* [142] predicted a maximum of 30% risk of global cancellous bone failure in the medial condyle for an all-polyethylene tibial component under a bi-condylar load case, whereas this value increased to 50% with a uni-condylar load case. Lewis *et al.* [90] found a risk of global failure between 13% and 21% for three different cemented prostheses with bi-condylar loading conditions. The prosthesis model used was also different from the one used by Taylor *et al.* [142]. Utilising similar loading conditions, Bartel *et al.* [10] reported risks of global failure between 9% and 33% for a number of cemented, metal-backed and all-polyethylene prostheses. In these works, ultimate compressive strength values of 11 and 18.3 MPa were assumed, respectively for cancellous bone.

3.7. EXCESSIVE CANCELLOUS BONE STRESSES AS A MECHANISM OF MIGRATION

In all of the migration studies, it has been shown that the majority of the prostheses migrate. This migration is higher in the first post-operative months, followed by an attenuation of this movement in the successful cases, or continuous migration in the cases were aseptic loosening is present [112,134]. There is a clear difference between prostheses that migrate and those that become aseptically loose. Successful prostheses migrate to a lesser extent than aseptically loose implants, which show excessive amounts of migration. The migration rate is dependent on several factors, namely

fixation method, implant design, activity level, bone quality and cancellous bone remodelling capacity. In general, significantly lower migration levels have been observed when cemented prostheses are used (Table 3.1). These observations suggest that migration is more related to a mechanical phenomenon, or at least mechanically triggered, than a biological process. As Ryd *et al.* [134] and Fukuoka *et al.* [47] have suggested, aseptic loosening is basically the manifestation at a late stage of high early migration, resulting usually from an initial poor fixation.

Various theories have been proposed with the aim to explain the process of aseptic loosening of proximal femoral prostheses (which has been proved to show similar migration patterns to proximal tibial implants), such as bone resorption, stress shielding and osteolysis (resorption due to wear debris) [141], but each one of them is only applicable to specific situations. On the other hand, in their finite element studies, Taylor *et al.* [142,139] have observed a correlation between cancellous bone stresses and reported migration data, suggesting that implant migration may well be a consequence of fatigue failure of the cancellous bone. Furthermore, they suggested that initial cancellous bone stresses in the bone-tibial plateau interface may be able to predict the likelihood of migration (and hence, subsequent loosening), as they observed that the models showing the highest cancellous bone stresses are those that include the type of implant that usually migrates the most (all-polyethylene uncemented tibial tray). These observations suggest the possibility of using finite element analysis even before implantation to predict both initial stability and future migration of the prosthetic components, based on different sets of initial parameters, such as component alignment, loading conditions and bone-implant interface characteristics (fixation method).

3.8. AIMS AND OBJECTIVES

As described in section 3.6, despite the magnitude of the problem, finite element modelling of the proximal implanted tibia has been relatively ignored (few, very simplified studies) as compared to studies on other joint replacements (e.g. hip [29,67,81]). All of the above studies have assumed perfectly horizontal tibial components (PA=AP=0^{o}). No previous finite element analysis has evaluated the effect of tibial alignment on cancellous bone stresses, and hence the potential risk of migration and

loosening. For this reason, a finite element analysis of the proximal implanted tibia has been performed [116], as described in chapter 4.

In general, in the studies previously reported, the finite element models have not included patient specific data, such as bone material properties, body weight and component alignment. In orthopaedics biomechanics, finite element analysis is still only a comparative tool; the predictive capabilities of finite element analysis can only be evaluated by performing prospective clinical trials in conjunction with patient specific finite element modelling. Advances in image analysis tools and mesh generation software now make it possible to combine clinical and FE studies. In chapter 5, a study was performed in order to determine the finite element mesh characteristics (e.g. element size) and material property distribution (number of material groups) necessary to accurately describe the stress and risk ratio distributions at the bone-implant interface. This was carried out by means of a comprehensive convergence analysis to assess the effect of these variables (mesh characteristics and material property distribution) on the stress and risk ratio distributions at the bone-implant interface. Special attention was paid to the portion of cancellous bone in contact with the implant, as was previously suggested by Taylor *et al.* [142] that the stresses in this region are correlated with the implant migration.

Based on the results obtained in chapter 5, accurate FE models were created in order to perform a comparative study that includes pre and post-operative data from four different patients (CT scans, X-rays, measured tibial component micromotions), as described in chapter 6. From the studies performed by Fukuoka *et al.* [47], who demonstrated that future migration of tibial components can be predicted from the moment of surgery and Taylor *et al.* [142], who suggested that cancellous bone stresses are correlated with tibial component migration, the objective of the work described in chapter 6 was to determine whether patient-specific FE models can predict the short term behaviour of tibial trays.

CHAPTER 4

EFFECT OF PA AND AP ANGLES ON THE CANCELLOUS BONE STRESSES OF THE PROXIMAL IMPLANTED TIBIA

As explained in section 3.5.1, aseptic loosening of the tibial component is a major cause of failure. Tibial component alignment is one of the parameters that have more influence on this problem. Clinical studies have shown that varus oriented implants have a higher risk of failure than those in the neutral or valgus position (section 3.5.2). For this reason, a finite element study, in which various PA and AP angles were examined, was performed in order to find out which is the position of the tibial component that produces the lowest cancellous bone stresses. This work was published in the Journal of Arthroplasty [116] and is included in Appendix A.

4.1. MATERIALS AND METHODS

A three-dimensional finite element model of a proximal right tibia was generated based on a set of serial transverse CT scans of a cadaveric specimen [142]. The tibia was implanted with a flanged type tibial plateau (Dual Bearing Knee, MMT Ltd, UK) as shown in Figure 4.1.

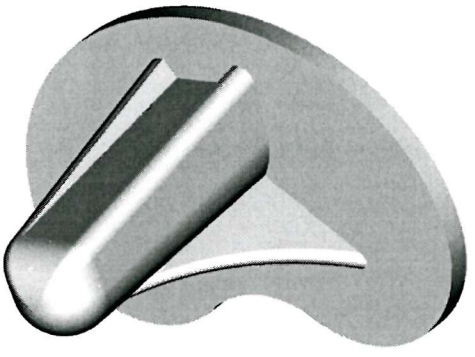

Figure 4.1. Tibial component of the Dual Bearing Knee system.

The material properties used in the model are shown in Table 4.1 [142]. The tibia was divided into 5 different regions, those of diaphyseal and metaphyseal cortical bone and the medial, intercondylar and lateral cancellous bone. Cemented fixation was modelled by adding a 1-mm layer of cement mantle on top of the resected surface of the proximal tibia. No cement was considered around the stem or the flanges of the tibial component, however the metal-cancellous bone interface was modelled as bonded (Figure 4.2). All materials were assumed isotropic, homogeneous and linear elastic. The ultimate compressive strength of the medial cancellous bone was assumed to be 6.0 MPa [142].

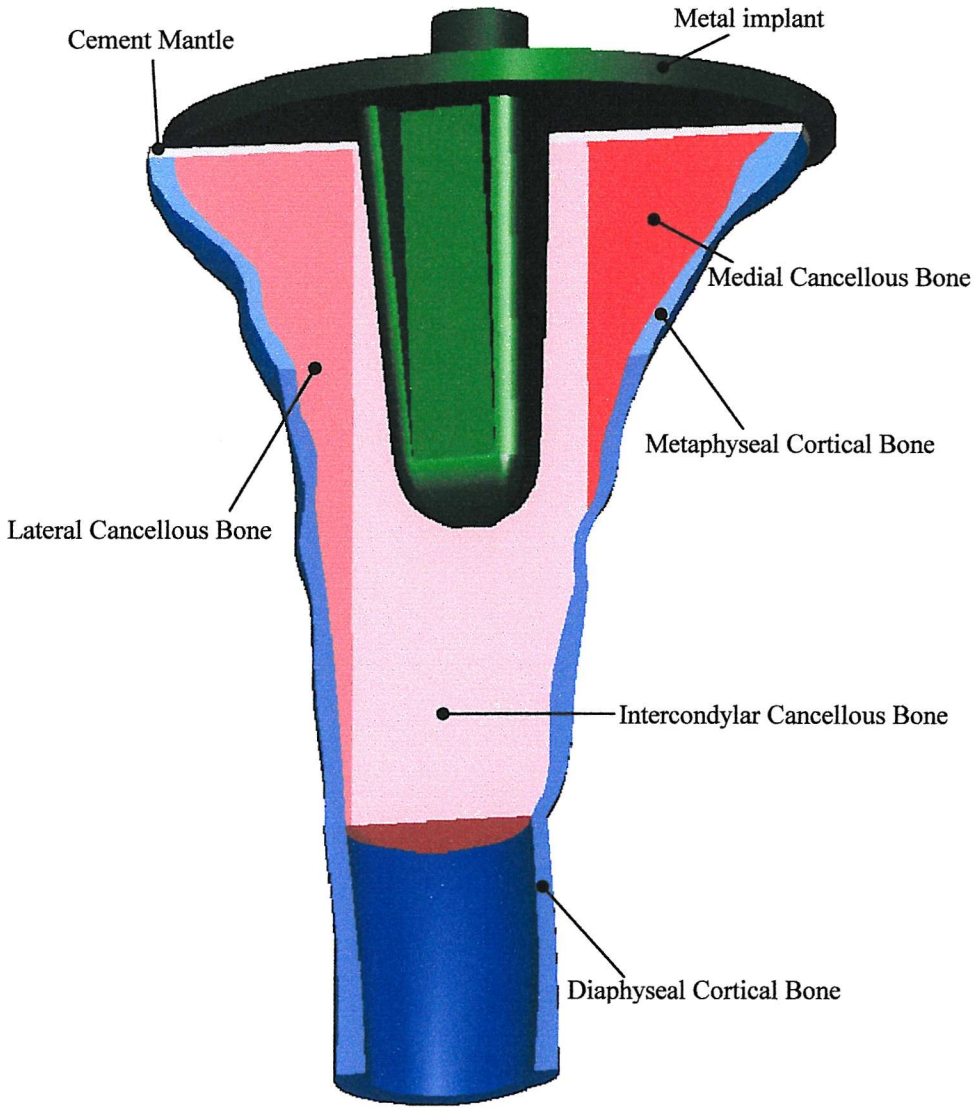

Figure 4.2. Longitudinal cut of the proximal implanted tibia.

Table 4.1. Material Properties of the Implanted Tibia [142].

Material	Modulus (MPa)	Poisson Ratio	Ultimate Compressive Strength (MPa)
Diaphyseal cortical bone	17.0	0.29	——
Metaphyseal cortical bone	5.0	0.29	——
Medial cancellous bone	0.4	0.29	6.0
Intercondylar cancellous bone	0.1	0.29	1.5
Lateral cancellous bone	0.3	0.29	4.0
Metal (titanium)	110,000.0	0.33	——
Cement	2.0	0.30	——

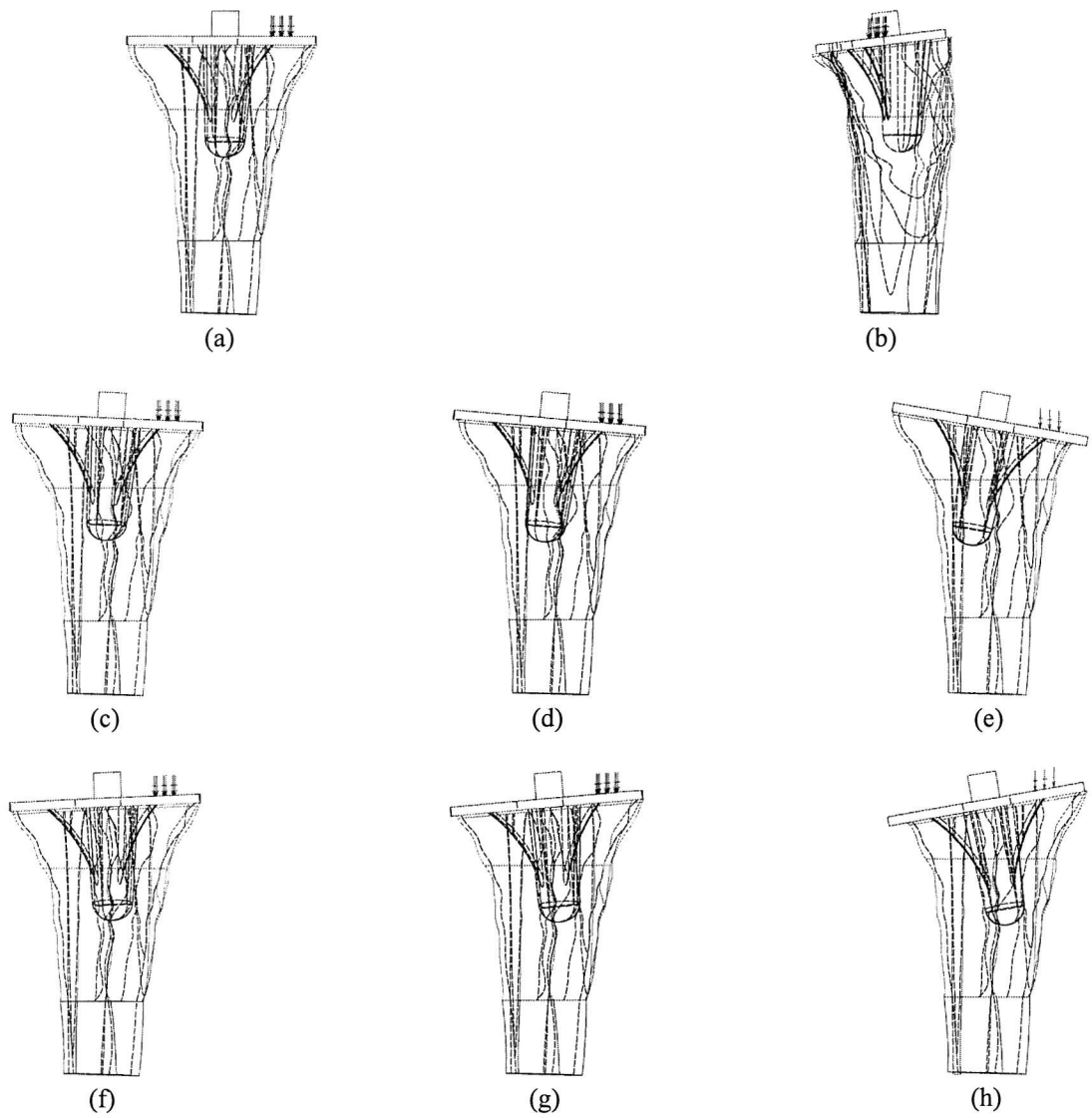

Figure 4.3. Frontal view of the tibial plateau positions analysed (except for (b), which is viewed laterally). (a) 0°; (b) 7° posterior, (c) 2.5° varus, (d) 5° varus, (e) 10° varus, (f) 2.5° valgus, (g) 5° valgus, (h) 10° valgus.

The proximal tibia was resected at seven different PA angles, as shown in Figure 4.3 (0^o, $\pm 2.5^o$, $\pm 5^o$ and $\pm 10^o$). From previous investigations [61], it was observed that, since alignment is very dependant on the surgeon's expertise as well as on the accuracy of the instruments used for this purpose, errors of up to $\pm 5^o$ in the PA angle could be present. An extreme case of $\pm 10^o$ was also chosen as the worst possible, as these values were present in the Lotke scoring system [95]. In addition, two AP angles were included in the analysis, neutral (0^o) and 7^o posterior slope.

A uniformly distributed uni-condylar load of 2.2 kN was applied on a circular patch, 10 mm in diameter, in the centre of the medial side of the tibial plateau, in the same direction as the long axis of the tibia in all cases (Figure 4.3). A uni-condylar load was used to represent the worst-case scenario. Stiehl *et al.* [137] have shown that 18 of the 20 patients analysed using fluoroscopy exhibited significant lift-off at one point of the gait cycle (heel-strike), subjecting the tibia to uni-condylar loading. This load represents the maximum force transmitted by the joint during the gait cycle for a 75-kg person (~3 times body weight) [105]. In order to simplify the analysis, the polyethylene insert was not considered in the models; therefore, the force was exerted directly on the tibial plateau. The distal end of the tibia was rigidly constrained. All analyses were performed using I-DEAS^{TM} Master Series 6. Tetrahedral second order (10-noded) elements were used in all models. A convergence analysis of the mesh refinement (section 4.1.1) was performed with the implant in the neutral position (PA=AP=0^o). The element size found to be most suitable for this study (1-mm edge length) was used in the rest of the models. The total number of elements and nodes used for each model are presented in Table 4.2.

Table 4.2. Number of elements and nodes used in each model.

PA angle	No of Elements	No of Nodes
10^o varus	31 865	45 943
5^o varus	28 437	41 265
2.5 varus	35 145	50 861
0^o	32 349	46 432
2.5 valgus	41 294	59 108
5^o valgus	34 054	48 422
10^o valgus	29 792	42 637
7^o posterior	43 711	61 959

Migration and subsequent aseptic loosening of tibial trays is thought to be due to fatigue failure of the supporting cancellous bone [141] (section 3.7). This is a result of excessive compressive stresses occurring at the bone-implant interface. For the purpose of this study, the minimum principal stresses (i.e. the largest compressive stress component) have been reported. For migration to occur, global failure of the underlying cancellous bone is required. Therefore, in a similar fashion to Bartel *et al.* [10] and Taylor *et al.* [142], the average cancellous bone stresses in the medial compartment have been reported as a percentage of the ultimate compressive strength. This represents the risk factor for global failure of the supporting cancellous bone.

4.1.1. Convergence analysis for mesh refinement

As mentioned before, mesh refinements were performed only on the surface of interest (medial compartment-cement interface) until the average stresses on that surface were observed to converge. This convergence analysis was executed only for the model with a horizontal tibial cut (PA=AP=0^{o}).

Table 4.3 shows the characteristics of the mesh on the surface of interest, which is the medial side of the bone-cement interface. In Figure 4.4, the surface of interest can be clearly identified, as it is that with the highest mesh density.

For this analysis, the elements sizes were reduced progressively in each finite element model and the average minimum principal stress within the cancellous bone-cement interface was compared with that of the previous model until the difference between two consecutive models was acceptable.

Table 4.3. Mesh refinement. Convergence analysis

Element edge length (mm)	Nr. of elements on the surface of interest	Average stress on the surface of interest (MPa)	Average stress change (%)
4	130	1.472	——
2	352	1.695	15.1%
1	1426	1.652	2.6%

After solving three finite element models, convergence was observed, as the difference between the two models with the shortest element edge length, did not show an appreciable difference in the stresses in the region of interest. Although the number of

models included in this analysis seems small, it was considered that further mesh refinement would not have given significantly different results. In fact, it can be seen that if there were limitations in terms of computational resources, an edge length of 2 mm could have been used with an acceptable accuracy.

4.2. RESULTS

The stress distribution on the cancellous bone in the different models (varus-valgus angles) is shown in Figure 4.4. Regardless the orientation of the implant, the maximum cancellous bone stresses always appeared in the medial compartment. Between 10° of valgus to neutral, the load bearing area of the medial condyle remains relatively constant. However, from neutral to 10° of varus, the load bearing area tends to decrease. In general, the peak cancellous bone stresses occurred at the medial-anterior rim of the resected surface in all of the models and varied between 9.27 MPa at neutral position and 3.78 MPa at 10° of valgus. There was a general trend for the peak cancellous bone stresses to increase as the position of the prosthesis was rotated from valgus into varus. There was some variability in the peak cancellous bone stresses and this was thought to be due to local variations in the degree of cortical bone contact present in each model.

The average cancellous bone stresses occurring in each model are shown in Table 4.4. A general trend in the stresses was observed, suggesting that the more tilted to valgus the tibial plateau, the lower are the stresses on the resected surface.

Table 4.4. Average cancellous bone stress on the medial compartment

PA angle	Stress (MPa)
10° varus	2.527
5° varus	2.398
2.5° varus	1.700
0°	1.652
2.5° valgus	1.569
5° valgus	1.555
10° valgus	1.306
7° posterior	1.806

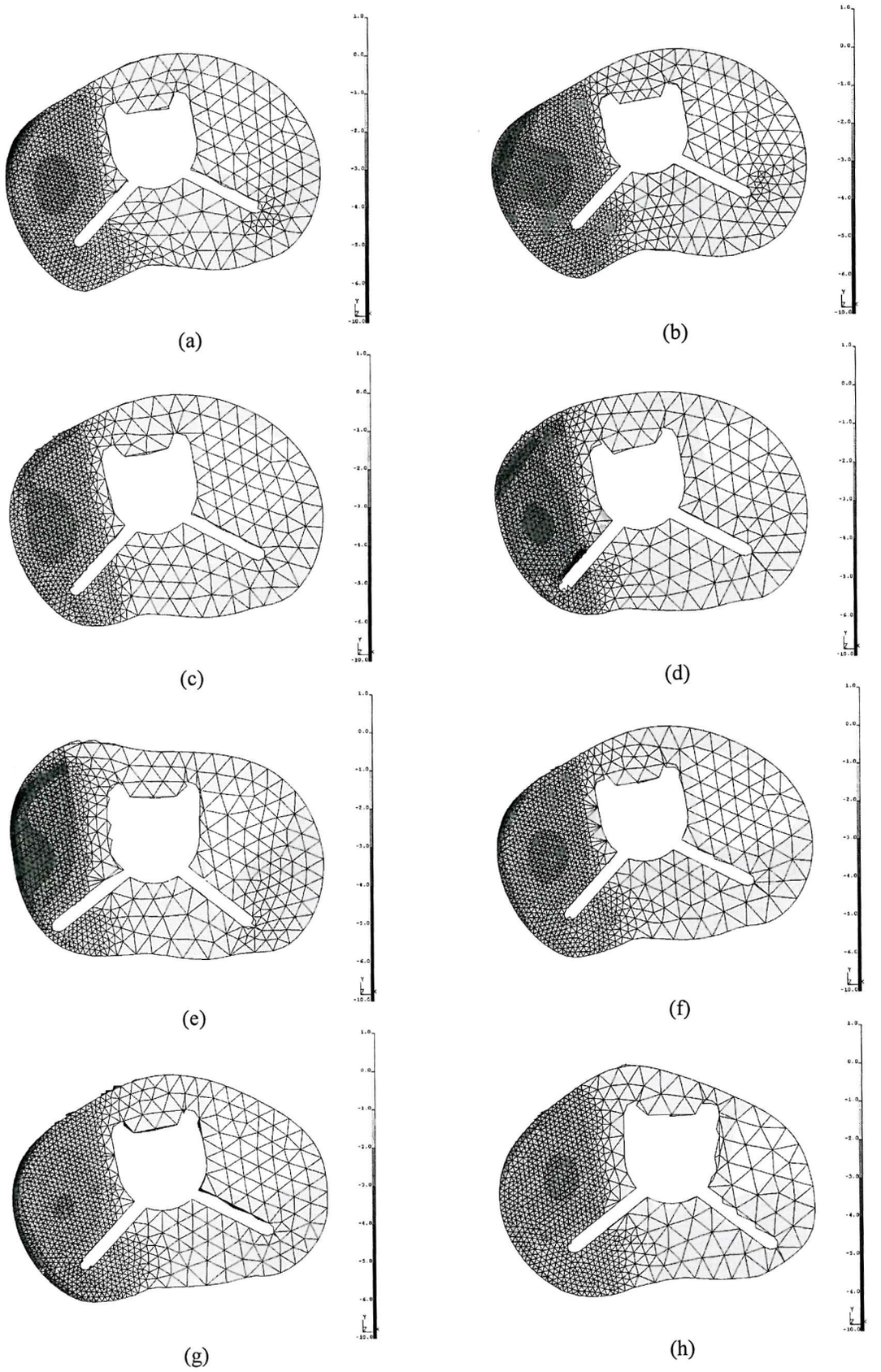

Figure 4.4. Minimum principal cancellous bone stresses at the bone-implant interface for (a) 0°; (b) 7° posterior, (c) 2.5° varus, (d) 5° varus, (e) 10° varus, (f) 2.5° valgus, (g) 5° valgus, (h) 10° valgus.

First, let us concentrate the analysis on the range of PA angles in which prostheses are most commonly implanted (5° varus to 5° valgus). In the range from 5° valgus to 2.5° varus there is a 9% increase in the average cancellous bone stresses. Increasing the varus angle from 2.5° to 5° resulted in a substantial increase of 41% in the average stress on the medial resected surface. Comparing both extreme cases (±10°), the average cancellous bone stresses on the surface of the model in varus are nearly double that of the model in valgus. The posterior slope implanted prosthesis (Figure 4.4-b) generated stresses 9% greater than those observed in the implant in a neutral position (Figure 4.4-a). The predicted risk of global failure in all models ranged from 22% in 10° valgus to 42% in 10° varus.

4.3. DISCUSSION AND CONCLUSIONS

The aim of this work was to examine the influence of the orientation of the tibial tray on the cancellous bone stresses, since they are believed to closely correlate to migration and aseptic loosening [142,140,139,141]. The lowest stress, and therefore the lowest risk of cancellous bone failure, was obtained when the tibial tray was orientated in valgus. Moreover, according to the tendency observed, the larger this valgus tilt is, the lower are the stresses within the cancellous bone. It should be noted that in this work, the varus-valgus angle is referred to as PA angle (Figure 4.3).

Between 5° of valgus and 2.5° of varus, there was only a 9% increase in the global risk of cancellous bone failure. However, increasing the varus angle by a further 2.5° produced a significant increase (of 41%) in the potential risk for cancellous bone failure. This was due to the reduction of the available load bearing area on the higher strength medial cancellous bone. That is, the same load was being spread over a smaller area, leading to a significant elevation in the predicted cancellous bone stresses.

A number of implant designs are now available which include a posterior slope. This study has shown that the introduction of a posterior slope produces a marginal increase (of 9%) in the global risk for cancellous bone failure. This agrees with the score system used by Lotke *et al.* [95], which assumes that the optimal position of the tibial plateau is horizontal in both planes.

Comparison of these results with previous finite element studies is not easy since most of them used different bone and prosthesis geometries, material properties and loading conditions. The majority of the studies previously performed employed bi-condylar load cases [11,28,150], hence they reported relatively low compressive cancellous bone stresses, of the order of 2 MPa. However, Taylor *et al.* [142] analysed a similar uni-condylar load case, using the same tibia geometry and material properties, and reported stresses of magnitudes comparable to those reported here. In the present study, the maximum risk of global cancellous bone failure of 42% was observed at 10^{o} of varus, whereas the minimum of 22% was observed with the tibial tray orientated in 10^{o} valgus. These values are marginally lower than those of Taylor *et al.* [142], who also predicted a maximum of 42% risk of global failure for a cemented, stemmed, metal-backed prosthesis, as well as for a metal backed tibial tray, assuming the same ultimate compressive strength for the medial cancellous bone. However, slightly higher risks of global failure were observed for an all-polyethylene prosthesis (50%). Lewis *et al.* [90] found a risk of global failure between 13% and 21% for three different cemented prostheses with bi-condylar loads. Utilising similar loading conditions, Bartel *et al.* [10] reported risks of global failure between 9% and 33% for cemented, metal-backed and all-polyethylene prostheses. These works assumed ultimate compressive strength values of 11 and 18.3 MPa respectively. In this investigation, a lower ultimate compressive strength was assumed, as it was believed to be closer to the experimental values reported for human tibial cancellous bone [70,129].

It should be pointed out that this study has a number of limitations, which include the cancellous bone being divided into three distinct isotropic regions, as opposed to being transversely isotropic and heterogeneous. The influence of these limitations is discussed in depth by Taylor *et al.* [142]. Also, extreme varus-valgus angles of 10^{o} were examined. It is accepted that these angles are unlikely to be achieved in surgery, as they would affect many other parameters including the kinematics of the replaced joint and cause potential patellar instability. Moreover, in order to be positioned in such large varus-valgus angles, the tibial tray had to be displaced medially or laterally to avoid contact or penetration of the stem with the cortex of the medullar cavity and provide adequate coverage of the resected surface.

Another important limitation of this study is that the load was applied only on the medial side. Different loading situations would result in different stresses, and therefore

different conclusions. Additionally, this loading condition may not be an appropriate assumption when large valgus angles are analysed (10^{o}), as under these circumstances, the load may not be transmitted through the medial condyle, as was assumed here. Consequently, even though the finite element models studied have shown lower cancellous bone stresses with large valgus tibial cuts, excessive valgus orientation of the tibial tray may still lead to significant clinical complications.

Despite its limitations, this study supports the clinical findings reported in the literature. Various clinical studies have shown that the orientation of the components of total knee arthroplasty has a critical effect on the performance of the replaced joint [9,32,39,76,89,127,144]. In general, these investigations suggest that HKA angles of a few degrees in valgus minimise the likelihood of failure and that varus orientations lead to a higher risk of failure. This study has shown that varus orientation of the tibial plateau tends to increase the risk of cancellous bone failure, whereas valgus orientation of the prosthesis reduces the risk of failure. This work further supports the hypothesis proposed by Taylor *et al.* [141] that implant migration and aseptic loosening are a result of progressive failure of the supporting cancellous bone.

CHAPTER 5
QUALITY ASSESSMENT OF QCT-BASED FE MODELS

The quality of patient-specific finite element models is dependent on three parameters: the quality of the computed tomography (CT) images; the assignment of material properties to the mesh and the mesh density. One of the major problems found in finite element modelling of bony structures is the accurate determination of the mechanical properties from the CT data set and then their assignment to the finite element model. In previous studies, quantitative computed tomography (QCT) has been used for the generation of FE models with a heterogeneous material distribution throughout the bone [26,27,85,149,155,164]. There are essentially two methods to generate QCT-based FE models, which consist of: (a) generating finite elements from the voxels of the CT scan dataset [27,85,149,155] and (b) defining first the bone geometry (e.g. IGES format) from the CT scans, creating an FE mesh from this geometry and then assigning the moduli to the elements [26,164]. The moduli can either be assigned as unique values to each element [155] or by grouping elements with similar moduli together [26,164]. In this study, the geometry based modelling technique was employed, as this uses smooth surfaces that more accurately simulate the real geometry of the bone. In addition, it has been demonstrated that voxel-based FE models are likely to introduce errors in the results as all surfaces present sharp edges (discontinuities), hence regions of stress concentration [98].

Various authors have performed convergence analyses of voxel-based QCT FE models in which only the mesh density was varied. Keyak and Skinner [85] have examined variation of the stress and strain distribution as well as the strain energy of models of a human proximal femur. They generated their models from CT scans with a pixel size of 1.38 mm and a separation between slices of 3 mm. Three different models were created with cubic elements of constant sizes of 4.8, 3.8 and 3.1 mm, respectively. They concluded that, for that case, a minimum element size of 3 mm (which is the same size of the voxels in the vertical direction, and 2.2 times the in-plane pixel size) should be used in order to describe sharp variations in the material properties within the bone, and consequently, the stress/strain field within the model. They also suggest that due to the

sensitivity of the results to the element size, the comparison of the stresses and strains predicted by different finite element models may not be valid if the element sizes used are not the same. In a later study, Marks and Gardner [98] demonstrated that the use of the strain energy value as a parameter to assess convergence is not appropriate for this type of study. They tested a simple model and observed that even though the total strain energy appeared to have converged, the stress value at some points in fact diverged. In a recent work, Weinans *et al.* [155] examined the influence of two different density-modulus correlations and four different load cases upon the stress-shielding behaviour of a prosthesis implanted in proximal femurs of dogs. They performed the study on voxel-based FE models of intact and implanted femurs of two dogs, with different stem stiffness values. They found that the difference in stress shielding between subjects was not dependent on the load case or the density-modulus correlation used, although there were slight differences in the stress shielding produced by the two density-modulus equations. Therefore, they suggested that, as long as the same load case and density-modulus correlation is used for all of the subjects, the difference in stress shielding between them can be examined.

Zannoni *et al.* [164] analysed a model of a distal femur grouping the elements based on their material properties. They verified the convergence of the total strain energy by changing the number of groups of material properties, however, they used the same mesh density for the entire study. Cattaneo *et al.* [26] compared two methods of assigning material properties to the glenoid part of a left embalmed scapula. The CT images that they used to create the models had a pixel size of 0.26 mm and a slice thickness of 2 mm. They checked convergence by analysing only the displacement of three sample nodes of five models with different mean element sizes, which ranged from 2.7 mm to 2.1 mm. Therefore, the elements used were significantly larger than the pixel resolution in the plane of each CT slice, but of a similar size to the slice thickness.

In the majority of the finite element models, the stress distribution is highly dependent upon the characteristics of the mesh used, i.e. element type and element edge length. If the material properties (i.e. Young's Modulus) are assigned to each element based on the QCT values, the results obtained from a finite element analysis could be even more dependent on the mesh quality, as the mechanical property distribution within the bone model may not be adequately described. Therefore, variations in the predicted stress distribution between patients may be masked by errors induced in the mesh itself. The

purpose of this study was to evaluate the effect of the mesh density and the material property assignment on the resulting material property, stress and risk ratio distributions of three-dimensional FE models of an implanted tibia. This study was divided in two sections, the first (section 5.3) analysing the influence of the assignment of modulus and the second (section 5.4) examining the influence of mesh density.

5.1. GENERATION OF MODELS

The general procedure followed to generate all the models analysed in this chapter and the remainder of the thesis is summarised in the diagram of Figure 5.1.

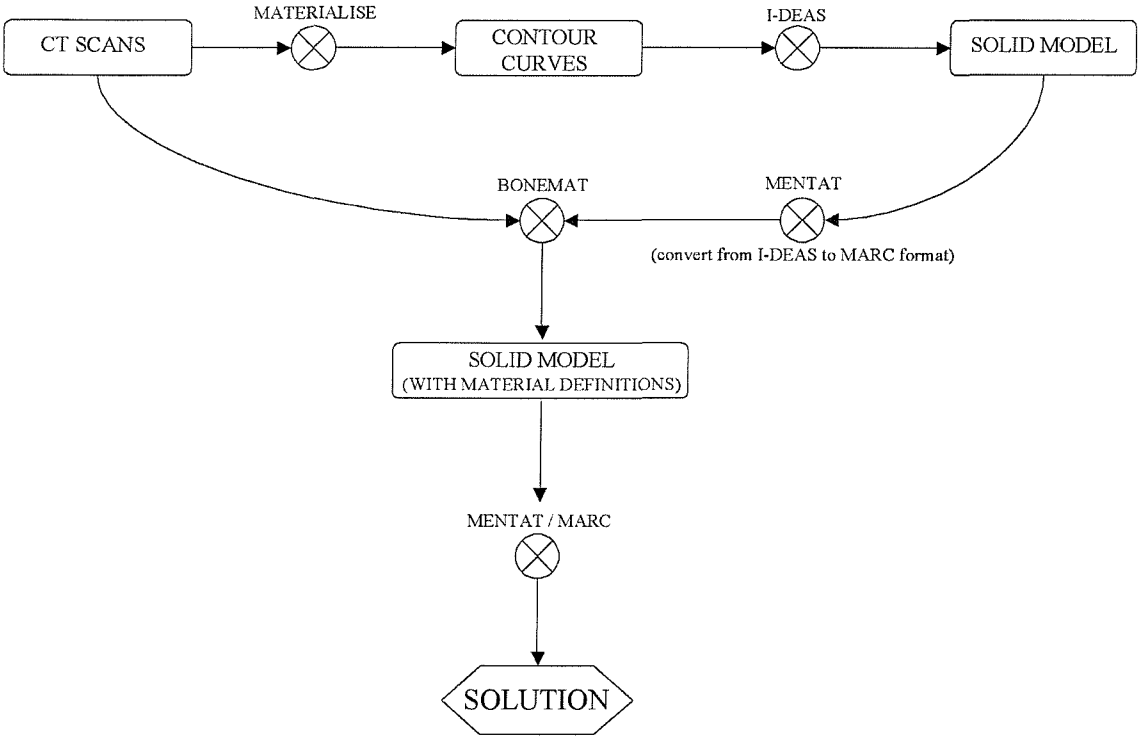

Figure 5.1. General procedure followed to create the finite element models.

The first step is carried out in a piece of segmentation software called Materialise, where the CT image set is used to define the outer and inner contour curves that characterise the boundaries between bone and soft tissue. Since the finite element mesh was created from the geometries obtained from the CT scans, it is required that the surfaces of the bone be as smooth as possible in order to facilitate the mesh generation.

For this reason, the contour curves are smoothed out by spline approximation (Figure 5.2). Notice that this process ends up with a curve drawn in a way that small portions of bone are left out and regions corresponding to soft tissue are included in the bone model, leading to an error in the material properties assigned to the finite elements located on outer surface of the cortical bone. Nonetheless, this problem does not significantly affect the analyses carried out in this thesis as they were entirely focused on the cancellous bone.

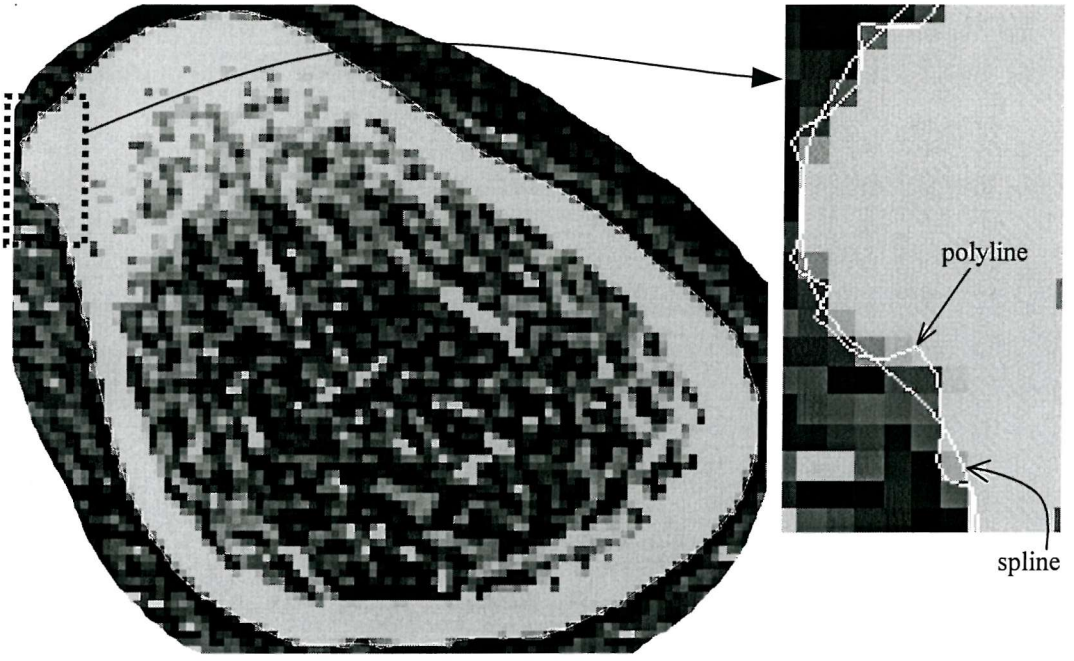

Figure 5.2. Generation of contour curves from the CT slice.

Once the contour curves for each slice have been created in Materialise, they are exported into I-DEAS as an IGES file. In I-DEAS, the curves are lofted together to create the bone geometry (Figure 5.3).

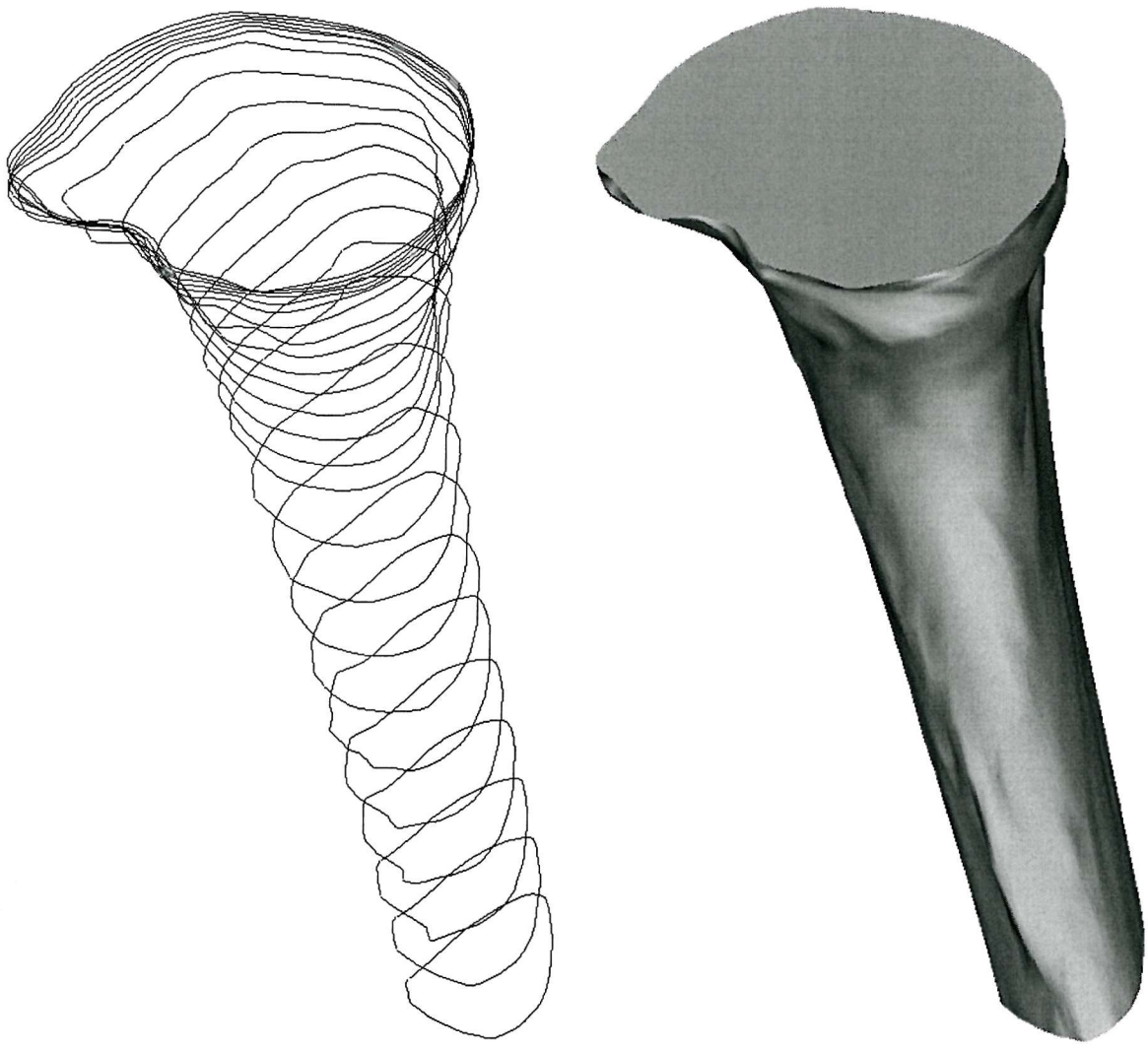

Figure 5.3. Bone model created in I-DEAS. (a) Contour curves. (b) Solid model

Here, based on post-operative X-rays of the prosthesis, the tibial resection angle and vertical position is reproduced by cutting out the proximal end of the bone model appropriately (Figure 5.4-a and b). It should be noted that due to the low quality of the X-rays and the lack of clear landmarks, the tibial component position and alignment in the model may have an error of 1 or 2 degrees for the tilt and 1-2 millimetres for the vertical position. Following this, a solid model of the tibial component is used to cut out the necessary bone to allow the perfect coupling between prosthesis and tibia (Figure 5.4-c).

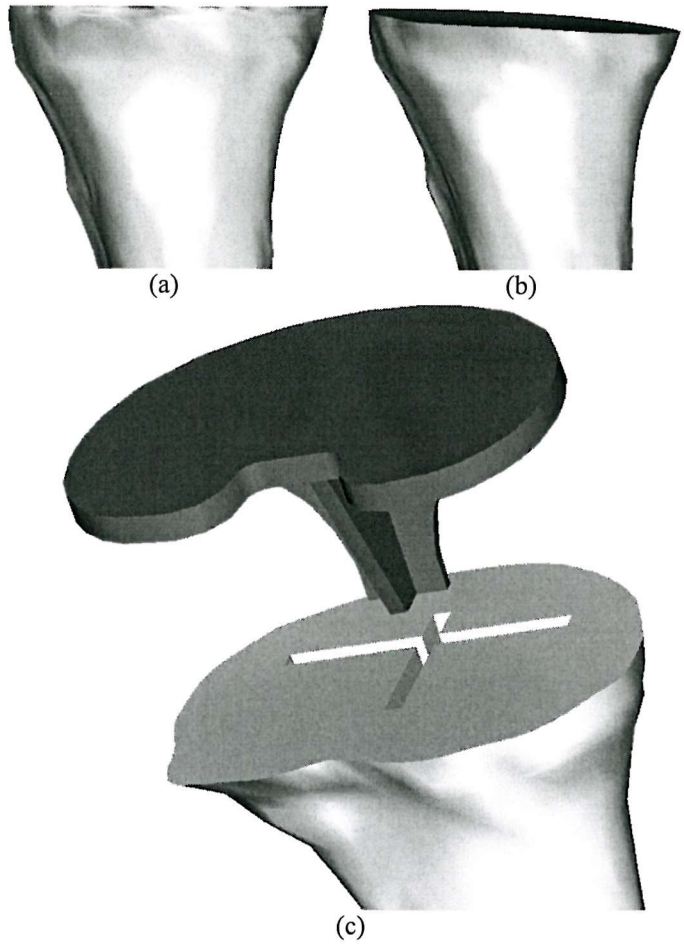

Figure 5.4. Proximal tibia resection. (a) Intact tibia. (b) Tibial cut performed based on the post-operative X-rays. (c) Cavity created by using the prosthesis to cut-out the bone.

The next step is the generation of the finite element meshes of both implant and tibia, which consist of linear tetrahedral elements (four nodes). The mesh is then exported as an I-DEAS universal file (plain text), which is converted to a MARC format (plain text, as well) by taking it through Mentat.

The material properties of the bone were assigned on an element-by-element basis by means of a freeware program called Bonemat, created at the Laboratorio di Tecnologia Medica – Istituti Ortopedici Rizzoli [164]. This program functions by correlating the pixel intensity of the different slices of the CT dataset and the apparent bone density [100,136] and between apparent density and Young's modulus [8,23,94,93].

The CT scan image set used here included calibration phantoms that gave the necessary information to define the linear equation to convert image intensity in Hounsfield Units

(HU) to apparent density (ρ) in g/cm^3 (Equation 5.1, Figure 5.5). Since this equation did not work properly for small or negative values of HU, another linear equation was defined for this range (-1000 ≤ HU ≤ 138), in order to avoid negative values of apparent bone density. The two points displayed in Figure 5.5 correspond to the two calibration phantoms found in the CT images.

$$\begin{aligned} \rho &= 1.037 \cdot 10^{-4} \cdot (HU+1000) && \text{for} \quad -1000 \le HU \le 138 \\ \rho &= 1.011 \cdot 10^{-3} \cdot (HU-2000) + 2 && \text{for} \quad HU > 138 \end{aligned} \tag{5.1}$$

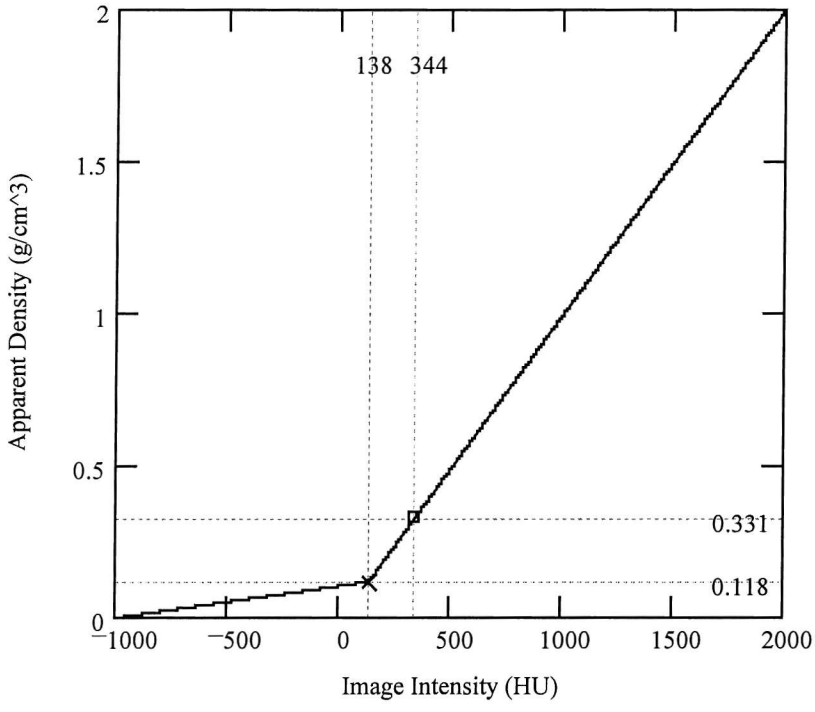

Figure 5.5. Correlation between pixel intensity (HU) and bone apparent density (ρ).

Several investigators have proposed equations to correlate apparent material density with Young's modulus (E) [8,23,94,93]. In this study, the equation reported by Carter and Hayes [23] was found to be the most suitable for cortical bone, whereas for trabecular bone, the correlation published by Linde *et al.* [94] was considered more accurate, as it was generated from experimental tests performed on specimens obtained from proximal tibiae. Therefore, two different equations were used depending on the apparent bone density values (Equation 5.2 and Figure 5.6).

$$\begin{aligned} E &= 2003 \cdot \rho^{1.56} \quad \text{for} \quad 0 \le \rho \le 0.778 \quad \text{Linde } et\ al.\ [94] \\ E &= 2875 \cdot \rho^{3.0} \quad \text{for} \quad \rho > 0.778 \quad \text{Carter and Hayes } [23] \end{aligned} \tag{5.2}$$

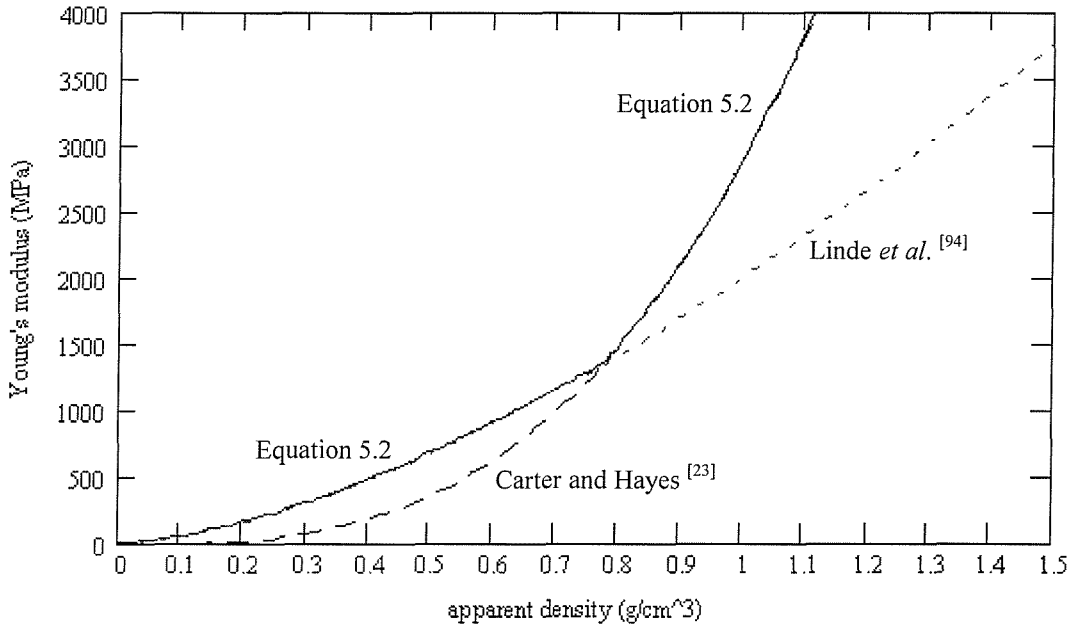

Figure 5.6. Correlation between Young's modulus and apparent density.

Likewise, the equation reported by Linde *et al.* [94] (equation 5.3) was used to determine the ultimate strength based on local apparent density. This parameter was used to calculate the risk ratio as explained in section 5.2.

$$\sigma_u = 28.723 \cdot \rho^{1.65} \tag{5.3}$$

Smoothing of CT images

A process of "smoothing" of the CT data set was performed in order to attenuate excessive differences between neighbouring pixels. The purpose of smoothing the pixel intensity distribution throughout the image was to reduce the sensitivity of the results to the mesh density. The smoothing process was performed by converting each image from a 512 x 512 pixel format to 256 x 256 pixels of double the size (0.936 x 0.936 mm) and then converting it back to a format of 512 x 512 pixels of the original size (0.468 x 0.468 mm). The smoothing takes place in the first step as large peaks of intensity values present in a pixel are averaged with lower values of the neighbouring

pixels. In the second conversion step, the pixels are halved in both dimensions and the values of the new pixels are determined by means of a bilinear interpolation with the neighbouring ones. Even though this process losses some of the information contained in the images, it was deemed appropriate as in this way, the material property distribution was more stable and continuous. It should be noted that partially, the large variation in the pixel intensities is caused by the instability of the scanner; hence, it was believed that the smoothing would attenuate this problem. In the original images, mean and peak deviations of 26 HU and 133 HU, respectively, were found in the regions corresponding to air, acetal and plexiglas, which are supposed to have constant values (-1044.5, 2392.1 and 2181.8 HU, respectively).

In order to assess the magnitude of the changes produced in the CT data set by performing a smoothing process, random images where analysed. Regions of the CT slice corresponding to materials with known uniform densities (i.e. air, acetal and plexiglas) were selected in order to examine the standard deviation of the pixel intensity values. From each of these regions, more than 100 pixels were considered for the analysis. Table 5.1 and Figure 5.7 show how the deviation from the mean value for each region is dramatically reduced when the smoothing is performed.

Table 5.1. Mean and Standard Deviation (S.D.) values of pixel intensity before and after smoothing.

	Original CT image		Smoothed CT image	
	Mean	S.D.	Mean	S.D.
Air	-1044.5	30.3	-1044.2	14.2
Acetal	2392.1	37.0	2389.2	16.4
Plexiglas	2181.8	34.8	2178.7	17.8

It should be noticed that this technique does not affect the mean intensity value of the original images. This means that in general, it can be assumed that the overall material property distribution assigned to the FE model does not undergo significant changes when a smoothing process is performed.

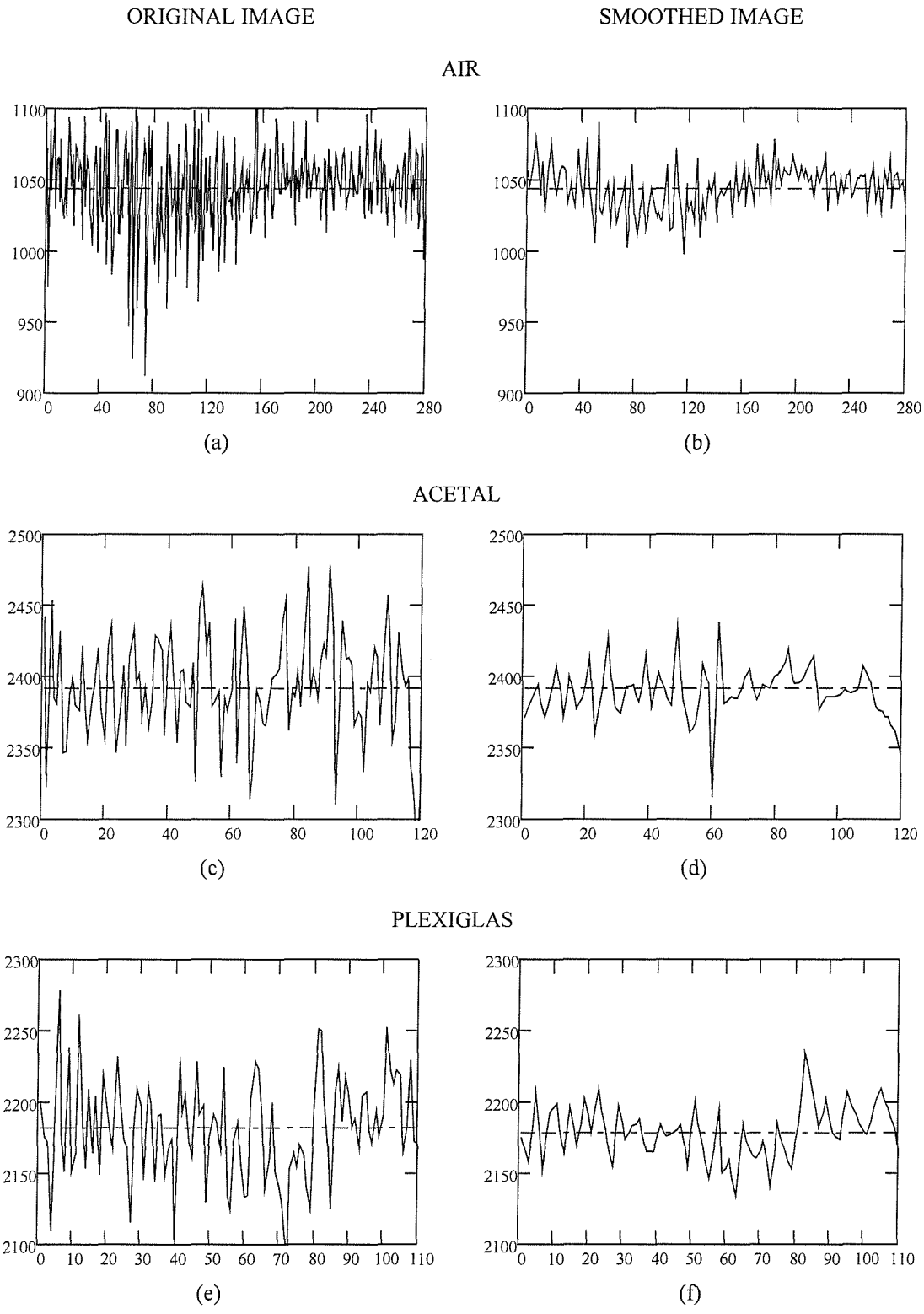

Figure 5.7. Pixel intensity value vs. pixel number corresponding to: air in original (a) and smoothed (b) images, acetal in original (c) and smoothed (d) images and plexiglas in original (e) and smoothed (f) images.

Once Bonemat has calculated the material property of each element, it creates groups of elements with Young's moduli that fall within a certain range and assigns the maximum stiffness found in each group [164]. In this way, the user controls the number of material properties utilised in the model by defining an increment in the Young's modulus (ΔE). Bonemat outputs a text file (in MARC format) including all the mesh characteristics with the material property definitions. Finally, this file is imported into Mentat, where it is merged with the mesh corresponding to the implant. The boundary conditions are applied at this stage.

Up to this point, the process described in this section may take between one and two days to complete, depending mainly on the characteristics of the CT data set, as in some cases, after the segmentation, some images needs to be edited manually one by one, in order to identify the contour lines properly.

5.2. RISK RATIO AS A PARAMETER TO ANALYSE THE RESULTS

Even though the von Mises stress is reported throughout this study, it is considered that due to the heterogeneous nature of the supporting bone, the stresses themselves are not enough to describe the likelihood of failure of the underlying bone, as it does not account for the strength of the material undergoing a particular stress. In other words, if a region of bone experiences high stresses but its strength is greater than the stress, this region may be less likely to fail than another region undergoing lower stresses but with poorer mechanical properties. Therefore, it was deemed as more appropriate to use a parameter that accounts for both stress and strength of the material. The parameter chosen here was the risk ratio (equation 5.4), which was defined as the quotient between the von Mises stress and the ultimate compressive strength of the material (section 5.1, equation 5.3). The risk ratio is reported as a percentage value, meaning that portions of bone undergoing risk ratios exceeding 100% are likely to fail.

$$\text{risk ratio} = \frac{\text{von Mises stress}}{\sigma_u} \times 100 \qquad (5.4)$$

5.3. EFFECT OF THE MATERIAL PROPERTY DISTRIBUTION

In this section, the number of material groups assigned to the bone model is varied as well as the manner in which they are defined, in order to study the effect that this parameter has on the calculated material property distribution, stresses and risk ratios.

5.3.1. Materials and Methods

A finite element model of a proximal tibia was generated from CT scan data (voxel size 0.468 x 0.468 x 1 mm) of a patient implanted with a Howmedica-Crucifix knee replacement. The model of the prosthesis was an approximation of the real design (Figure 5.8) with all small fillet radii removed. A mesh of linear tetrahedral elements was created in I-DEAS Master Series 7.0 for both bodies (tibia and implant). The element edge length was set to 2 mm for the region around the stem, and 3-mm for the elements on the resected surface of the tibia (Figure 5.9). For the rest of the model the element edge length was set to 5 mm. By defining these parameters, meshes of 15907 and 5636 elements were obtained for the bone and the tibial tray, respectively.

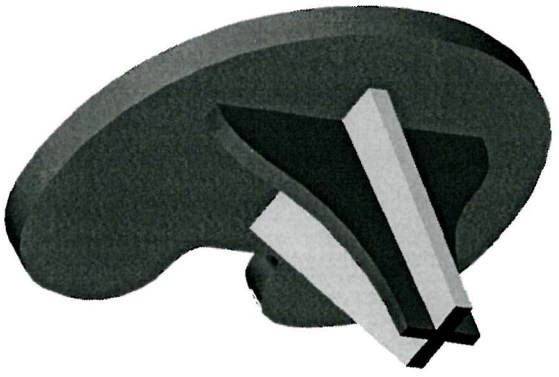

Figure 5.8. Tibial component analysed.

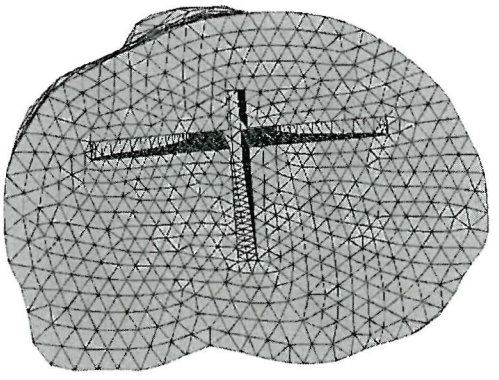

Figure 5.9. Finite element mesh of the resected surface of the tibia.

A bi-condylar load case was analysed, consisting of a medial force of 1200 N and a lateral force of 800 N applied directly on the tibial plateau. The total force of 2000 N corresponds to the maximum force observed in the knee of a 68-kg person during a normal gait cycle [105]. The tibial polyethylene insert was not included in the model in order to simplify the analysis. Both forces were distributed between nodes situated on

circular patches of 10 mm in diameter. The distal end of the tibia was rigidly fixed on all the nodes of the bottom surface of the model (Figure 5.10).

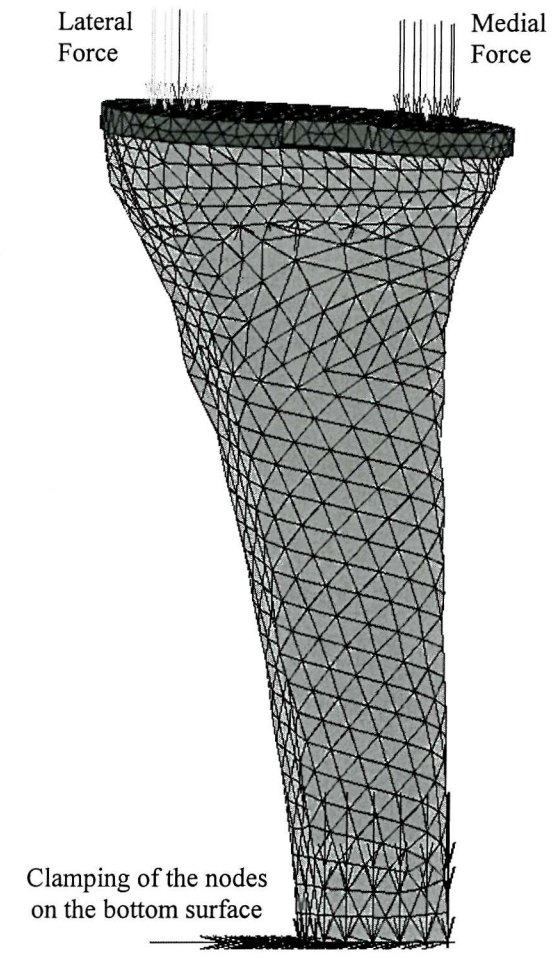

Figure 5.10. Boundary Conditions used in the models (posterior view).

The material properties were defined as described in section 5.1. In the original version of Bonemat, the user controls the number of material properties utilised in the model by defining an increment in the Young's modulus (ΔE). In other words, the greater ΔE is, the lower is the number of material properties used in the model. With this method, ΔE remains constant throughout the whole range of stiffness values in the model; therefore, it is necessary to use a large number of different Young's moduli (small ΔE) to get a suitable distribution of material properties between the elements of the proximal tibia, which is mostly cancellous bone (see section 5.3.2).

In order to optimise the material property distribution throughout the model, a logarithmic increment was introduced with the aim of obtaining a finer discrimination of mechanical properties at lower stiffness values, i.e. within the range of material properties corresponding to cancellous bone. With this method, the values of ΔE in the proximal tibia ranged between 0.5 and 10 MPa, approximately.

Maximum and average values of Young's moduli, von Mises stresses and risk ratios on the resected surface of the tibia were examined for various numbers of material properties (using both linear and logarithmic ΔE values), in order to evaluate the convergence of these parameters.

5.3.2. Results

The peak and mean values of Young's modulus, von Mises stress and risk ratio on the resected surface of the tibia, for different number of material properties are shown in Figure 5.11. Each graph displays the values obtained using both linear and logarithmic ΔE to generate the groups of material properties within the model. The percentage error was calculated by comparing the value obtained using a certain number of material properties with the one obtained from the model with the highest number of material properties. It can be seen that insufficient discretisation of the material properties results in an over estimation of the stiffness of the resected surface. In general, the parameters studied converged to a constant value when a logarithmic ΔE was used, as opposed to the behaviour observed by the models with linear ΔE. In Figure 5.11-b, it can be observed that with a linear increment the difference in mean Young's modulus between the two models with the highest number of material groups is still over 4% whereas with logarithmic ΔE that difference is just 0.1%. It can be observed that the curve corresponding to the linear ΔE is converging to the value obtained with a logarithmic ΔE (~208 MPa). The tendency shown by the linear ΔE curve suggests that a mean Young's modulus of 208 MPa would eventually be reached, but a considerably larger number of material groups would be needed. The overestimation of modulus by the linear ΔE method results in a corresponding under estimation of both the peak and mean values for the predicted stresses and risk ratios. In general, with logarithmic increments the difference in the results between the models with 304 and 522 material groups, for

all the parameters studied ranged between 0.0 and 1.1 %, therefore, it can be assumed that all the parameters reached convergence with 304 different material properties.

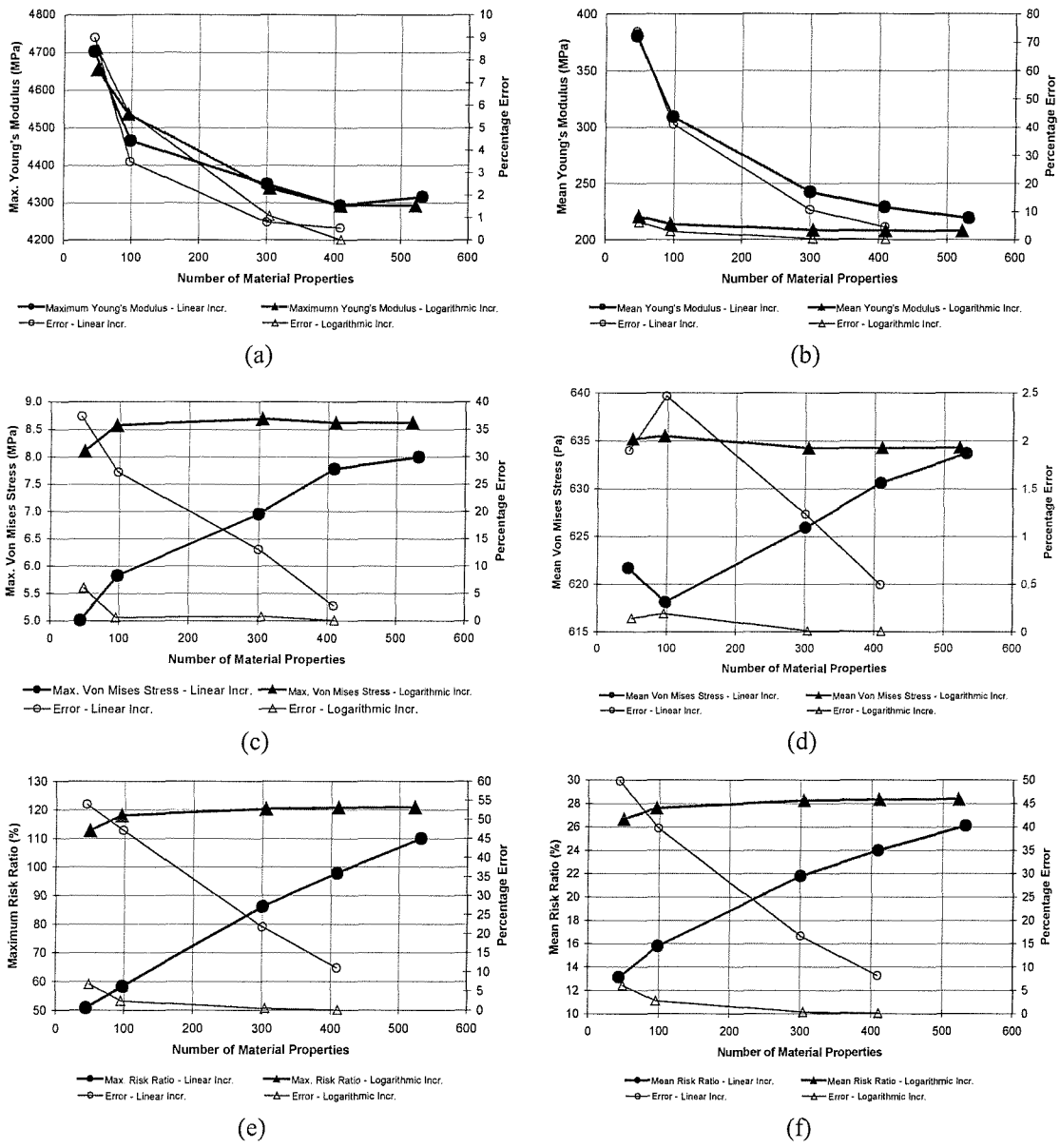

Figure 5.11. Convergence analysis on the resected surface using linear and logarithmic ΔE. (a) Max. Young's modulus, (b) Mean Young's Modulus, (c) Max. von Mises Stress, (d) Mean von Mises, (e) Max. Risk Ratio, (f) Mean Risk Ratio.

On the other hand, when linear stiffness increments were used, in most cases no clear convergence was observed. In particular, the mean and maximum risk ratios were the parameters that showed least convergence, with minimum errors of 11.0 and 8.1 %, respectively.

5.3.2.1. Effect of using material groups instead of a unique modulus for each element

Even though it could be argued that the best way to produce an accurate material property distribution would be the assignment of one unique Young's modulus to each element instead of grouping these material properties in ranges of values (as implemented in chapters 5 and 6). The problem with the former method is that an extremely large number of material properties would be obtained and the FE code used here (MARC) is limited to 600 different material properties per model. If more than 600 material properties are need, external subroutines can be created to overcome this limitation. Nevertheless, as explained below, the method used here produces accuracy levels virtually equivalent to assigning a unique Young's modulus to each finite element.

As mentioned in section 5.3.1, by using a logarithmic increment to assign the material properties, ΔE is smaller for lower stiffness values. Specifically, in the models studied here the majority of the elements in the proximal end of the tibia have Young's moduli of less than 1000 MPa. Figure 5.12 shows the maximum error in the material property that an element may present with respect to its "real" value (actual value that it would have if each element were assigned a unique material property). Each circle in the graph corresponds to a material group (Young's modulus values assigned to each group indicated on the horizontal axis), for which the maximum error of the elements contained in it (i.e. ΔE) was calculated as a percentage of its assigned material property (vertical axis). In this graph, only the material groups with Young's moduli corresponding to the proximal tibia ($50 \lesssim E \lesssim 1000$) are represented.

It can be observed that in this case, the majority of elements have an error below 2% (i.e. less than 2% difference between their real and assigned modulus), with only one material group having an error of 2.5%. It should be mentioned that the latter group is composed of only two elements, meaning that at worst one of them has the exact material property corresponding to the pixels contained in it ("real" value), and the other one may have a maximum error of 2.5% with respect to its correspondent "real" value. Therefore, it can be stated that in the region of interest the maximum difference in the material property assignment is approximately 2% as compared to the unique

assignment method. It can be argued that an error of this magnitude would have negligible effects on the overall results.

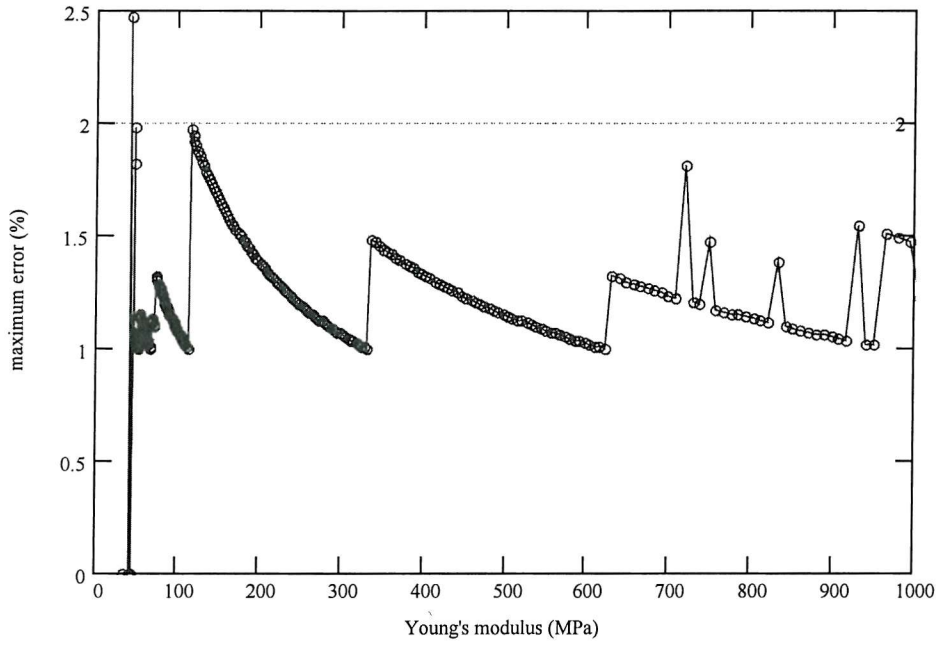

Figure 5.12. Maximum error in the material properties of the elements within each material group in the proximal tibia.

5.4. INFLUENCE OF MESH DENSITY

In this section, the effect of the finite element mesh density on the modulus distribution, von Mises stresses and resultant risk ratios is analysed by varying the element edge length at the bone-implant interface.

5.4.1. Materials and Methods

The aim of this section was to refine the mesh density (element edge length) of the bone in order to examine the convergence of the Young's modulus, von Mises stress and risk ratio distributions on the resected surface of the tibia. For this reason, only the meshes on the contact surfaces were refined, while the rest of the settings for the mesh of the entire model remained constant. The meshes of both bodies perfectly matched each other on the contact surfaces. Five different element edge lengths on the contact

surfaces were examined: 3, 2, 1.4, 1 and 0.8 mm. The number of nodes and elements used in each model are reported in Table 5.2.

Table 5.2. Number of nodes and elements in each model.

Element size	BONE		IMPLANT		TOTAL	
(mm)	Nodes	Elements	Nodes	Elements	Nodes	Elements
3	1956	7345	1054	2983	3010	10328
2	3180	11790	2095	6466	5275	18256
1.4	5988	22710	4420	14813	10408	37523
1	12216	49119	8801	30562	21017	79681
0.8	19701	80995	14393	51865	34094	132860

The geometrical models of the tibia and the prosthesis described in section 5.1 were also used for this part of the analysis, with the only difference that a volume partition was artificially created in order to enable the selection of a 2-mm layer of elements on the proximal end of the tibia, independently of the mesh morphology (Figure 5.13).

The material properties were assigned in the same way as described in section 5.1. Since all the analyses were carried out using MARC 2000, the number of materials used was limited to 600. If more than 600 material groups were needed, it would be necessary to write an external subroutine in order to overcome this limitation. In section 0, it was demonstrated that for this type of analysis, this number of material properties was sufficient to accurately describe the distribution of Young's modulus. In each of the five models analysed here the number of material groups used was greater than 500.

A bi-condylar load case was analysed, consisting of a medial force of 2029 N (60% of total) and a lateral force of 1352 N (40% of total) applied directly on the tibial plateau. The total force of 3381 N corresponds to three times the weight of the patient (115 kg) from whom the CT data was obtained. According to Morrison *et al.* [105], this is the maximum force observed during a normal gait cycle (3 x BW). In the same way as in section 0, the tibial polyethylene insert was not included in the model in order to simplify the analysis; hence, the forces were applied directly on the tibial plateau. Both forces were distributed between nodes situated on circular patches of 10 mm in diameter. The distal end of the tibia was rigidly fixed at all the nodes on the bottom surface of the model (Figure 5.13-b).

The Young's modulus, von Mises stress and risk ratio distributions were reported along an arbitrarily chosen line (Figure 5.14). In addition, mean and peak values of these parameters were assessed for the 2-mm layer described above.

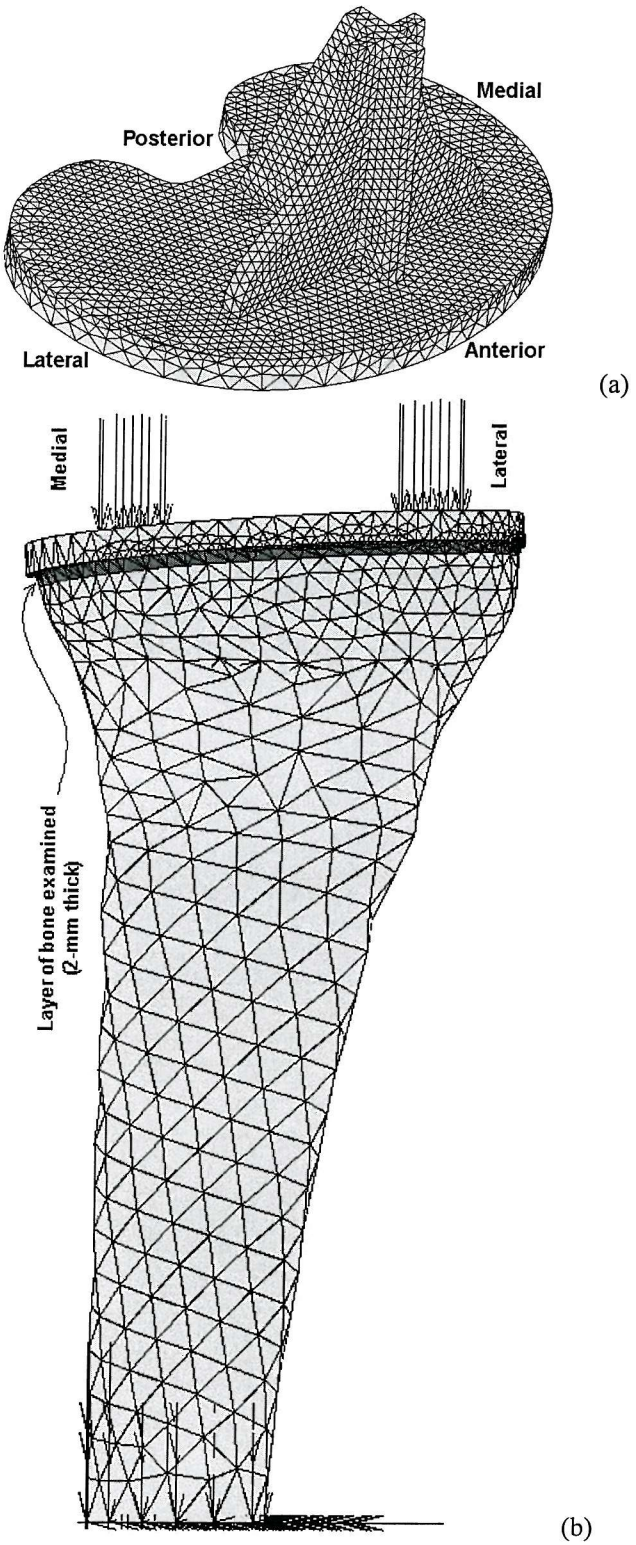

Figure 5.13. Model analysed (the figure displays the model corresponding to an element size on the contact surfaces of 2 mm). (a) FEM of the implant. (b) Complete model including boundary conditions.

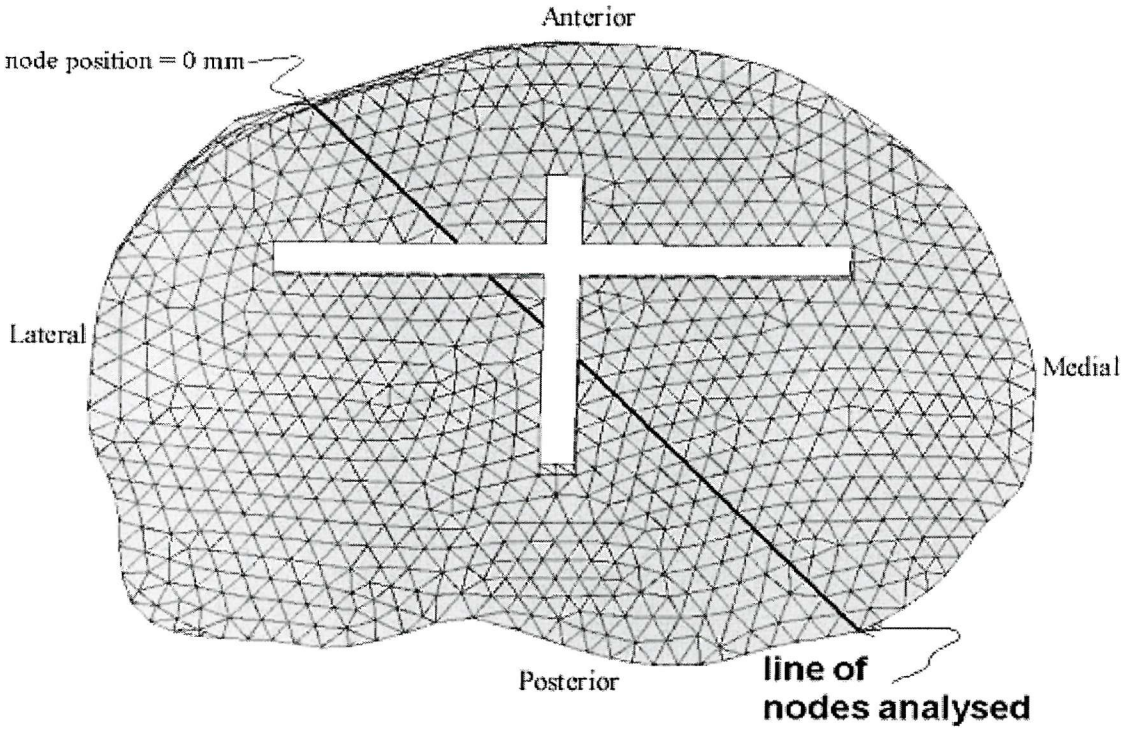

Figure 5.14. Line of interest (model with an element edge length of 2 mm).

5.4.2. Results

The influence of mesh density was analysed in two ways, at a local level by comparing the nodal values along an arbitrarily chosen line and at the global level, by comparing the mean, peak and distribution of a given parameter within a pre-defined volume. First, let us examine the distribution of modulus, stress and risk ratio at the local level. The variation of these parameters along the line of interest (shown in Figure 5.14) for the coarsest and finest meshes are depicted in Figure 5.15-a to c. Due to the large element size, the coarsest mesh is unable to capture the localised variations in the Young's modulus, particularly in the anterior-lateral aspect of the resected surface. In some places, there are differences of over 400% between the moduli assigned to the finest and coarsest meshes.

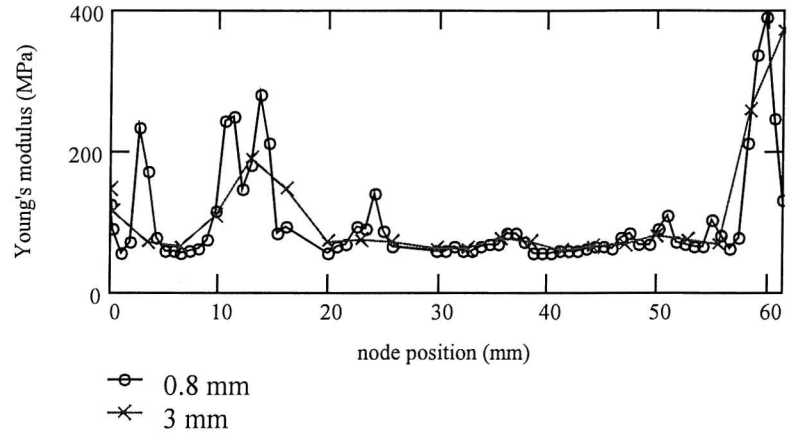

(a)

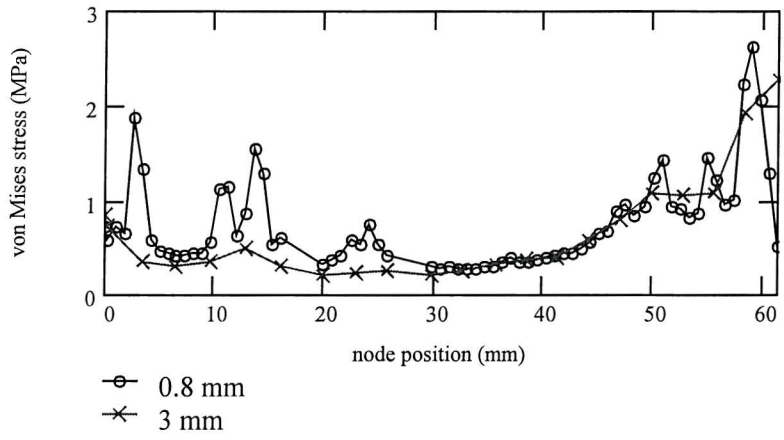

(b)

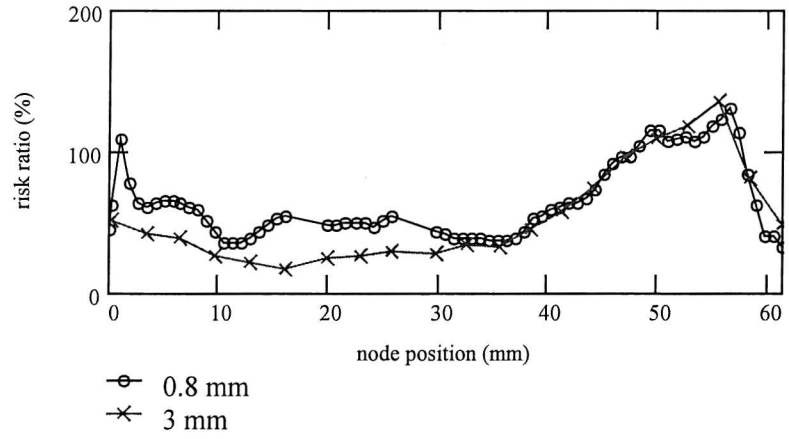

(c)

Figure 5.15. (a) Stiffness, (b) stress and (c) risk ratio values on the nodes along the line of interest for the coarsest and finest meshes.

Although the coarse mesh tends to follow the same general trend, it "averages out" the localised variations captured by the finer meshes. As a direct consequence of this poor discretisation of the material properties, large errors are propagated into the predicted von Mises stresses and the risk ratio, as shown in Figure 5.15-b and Figure 5.15-c. Both von Mises stresses and risk ratios are underestimated by the coarsest mesh in the regions where the material property distribution is poorly discretised.

The convergence of the Young's modulus, von Mises stress and risk ratio distributions along the line of selected nodes were quantified by comparing the values of each node lying on the line of interest of a given mesh, with the values corresponding to the same position in the finest mesh (0.8 mm). Since in general, the node positions of any mesh are not the same as those of another mesh, a spline for each parameter (Young's modulus, stress and risk ratio) was generated with the data corresponding to the 0.8 mm mesh, in order to compare between different meshes. The degree of convergence obtained with the mesh refinement was assessed by examining the correlation coefficients and the mean residual errors (mean distance from regression line to data points) of each set of data, as shown in Table 5.3 and Figure 5.16.

Table 5.3. Correlation coefficient (r) and mean residual error (MRE) for each mesh compared with the 0.8 mm mesh.

Element size	MODULUS		VON MISES		RISK RATIO	
(mm)	r	MRE (MPa)	r	MRE (MPa)	r	MRE (%)
3.0	0.660	11.140	0.588	0.106	0.921	8.957
2.0	0.819	12.088	0.732	0.096	0.911	9.866
1.4	0.915	7.383	0.858	0.026	0.907	3.223
1.0	0.983	4.595	0.952	0.047	0.952	1.016

Close examination reveals that the coarser mesh densities tend to produce substantial errors in the modulus distribution by failing to capture the true modulus variations. This is reflected by low correlation coefficients (0.66) and large residual errors (approximately 11 MPa) for the coarser meshes. However, these values were drastically improved as the element size was reduced, with the correlation coefficients and residual errors improving to 0.98 and 4.60 MPa, respectively. Comparison of the results from the two finest meshes would suggest that the modulus distribution along the line of nodes has converged. Similar behaviour was observed in the von Mises stress (Figure 5.16-b). There is clear evidence of improvement in the regression parameters as the element size was reduced. For the risk ratio, the regression lines and correlation coefficients did not

show such large differences between models (Figure 5.16-c and Table 5.3); nevertheless, the mean residual error notably decreased as the element sizes were reduced, from approximately 9% with the coarsest mesh to 1% with the finest mesh.

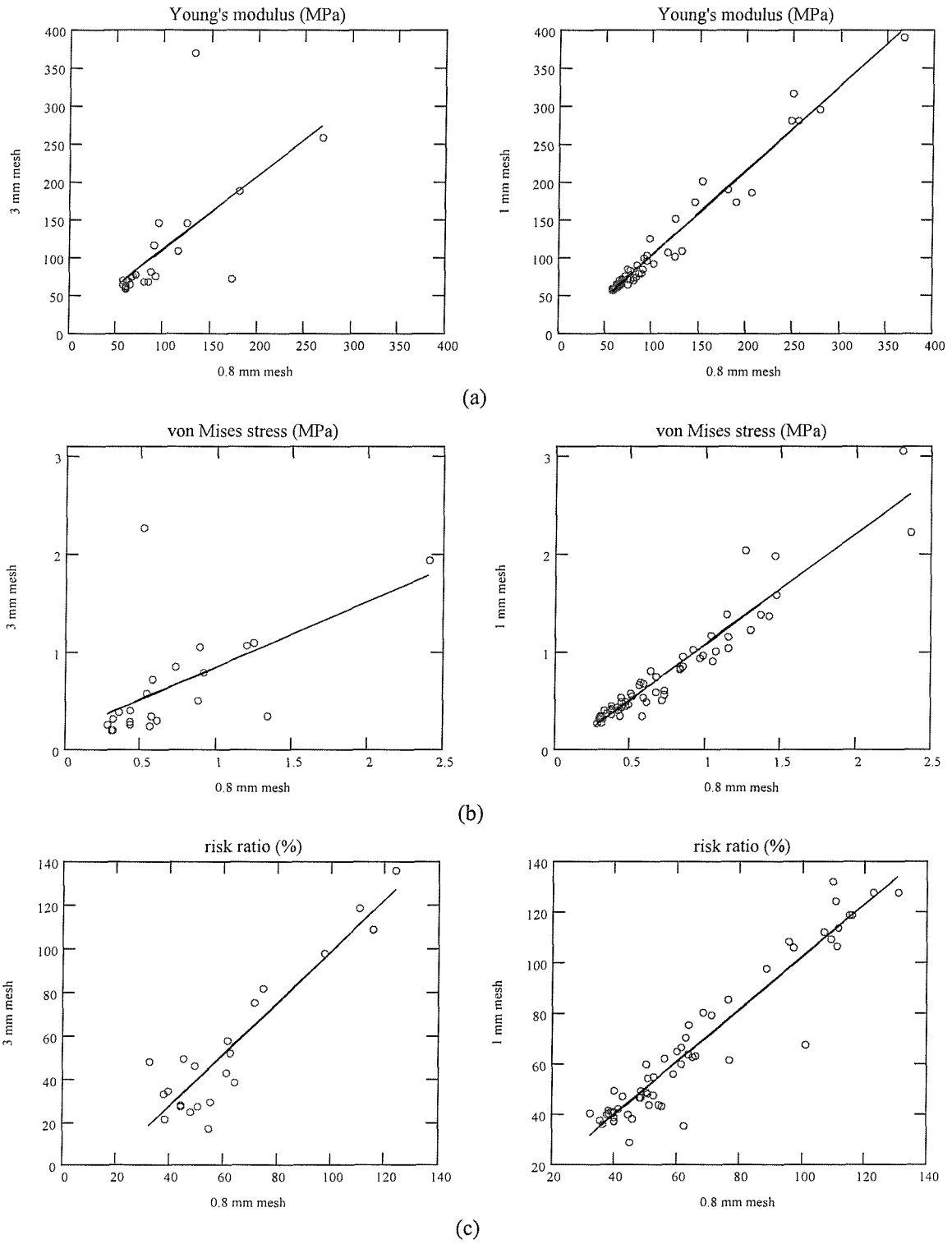

Figure 5.16. Regression lines for the values at the nodes along the line of interest of the 3 mm and 1 mm meshes. (a)Young's modulus, (b) von Mises stress, (c) risk ratio.

The influence of mesh density was also assessed by examining the mean and peak values and the general distribution of each parameter within a 2-mm slice of bone immediately adjacent to the implant (Table 5.4). The mean Young's modulus value appears to have converged for all the mesh densities examined, at a value of approximately 213 MPa. However, the magnitude of the peak modulus value continued to increase as the mesh density was refined, rising from 3011 to 9310 MPa. For both the stress and the risk ratio, convergence of the mean values was slower. For the mean stress and risk ratio values, there was a difference of approximately 20 and 22% respectively between the coarsest and finest mesh. There appears to be convergence for the three finest meshes, with a maximum variation in the stress and risk ratio values of 3.4 and 2.8% respectively. In a similar fashion to the modulus data, there was a corresponding increase in the peak values of stress and risk ratio as the mesh was refined.

Table 5.4. Mean and peak values of Young's modulus, von Mises stress and risk ratio in the volume analysed (2-mm layer). The last three columns give a rough description of the risk ratio distribution in the layer of elements studied.

Elem. Size	Modulus (MPa)		von Mises (MPa)		Risk Ratio (R) (%)			60<R<80	80<R<100	R>100
(mm)	mean	peak	mean	peak	mean	median	peak	(% vol)	(% vol)	(% vol)
3.0	214.1	3011	1.027	14.3	47.0	38.7	265.4	9.8	5.9	8.6
2.0	209.4	3434	1.086	17.6	49.3	40.8	289.4	12.5	8.6	7.2
1.4	212.6	6655	1.237	25.9	58.3	49.9	325.2	15.4	10.8	12.4
1.0	213.7	5454	1.270	33.3	59.1	51.9	410.2	16.1	10.2	13.8
0.8	213.4	9310	1.228	55.4	57.5	49.6	858.9	16.8	9.4	11.6

Let us now concentrate on the risk ratio distribution within the volume of interest. In Table 5.4 (last three columns on the right) it can be observed that, from the elements within the 2-mm layer examined, the portion of volume that presented risk ratios in the bands of 60% – 80%, 80% – 100% and more than 100% seemed to have converged, as the values obtained from the three finest meshes show little variations between them. Conversely, the meshes with element sizes of 2 and 3 mm produced very different values from those corresponding to the other meshes. In Figure 5.17 the elements were grouped in bands of 10% for the whole range of values of risk ratios found in the 2-mm layer of each model. In this graph, the same behaviour discussed above was observed, as the curves describing the risk ratio distribution in the layer of interest of the two

coarsest models substantially differ from the curves corresponding to the other three models.

Even though the mean values of the parameters studied showed clear convergence, their peak values kept increasing as the mesh density was refined (Table 5.4). For the Young's modulus, this behaviour was expected as Bonemat assigns the material properties to each element by averaging all the pixels related to it. In other words, the smaller the elements the higher the likelihood of capturing high intensity pixels without them being averaged with lower intensity pixels. This effect was then reflected in the peak von Mises values and consequently in the risk ratio (von Mises stress / ultimate compressive strength), which showed the same behaviour.

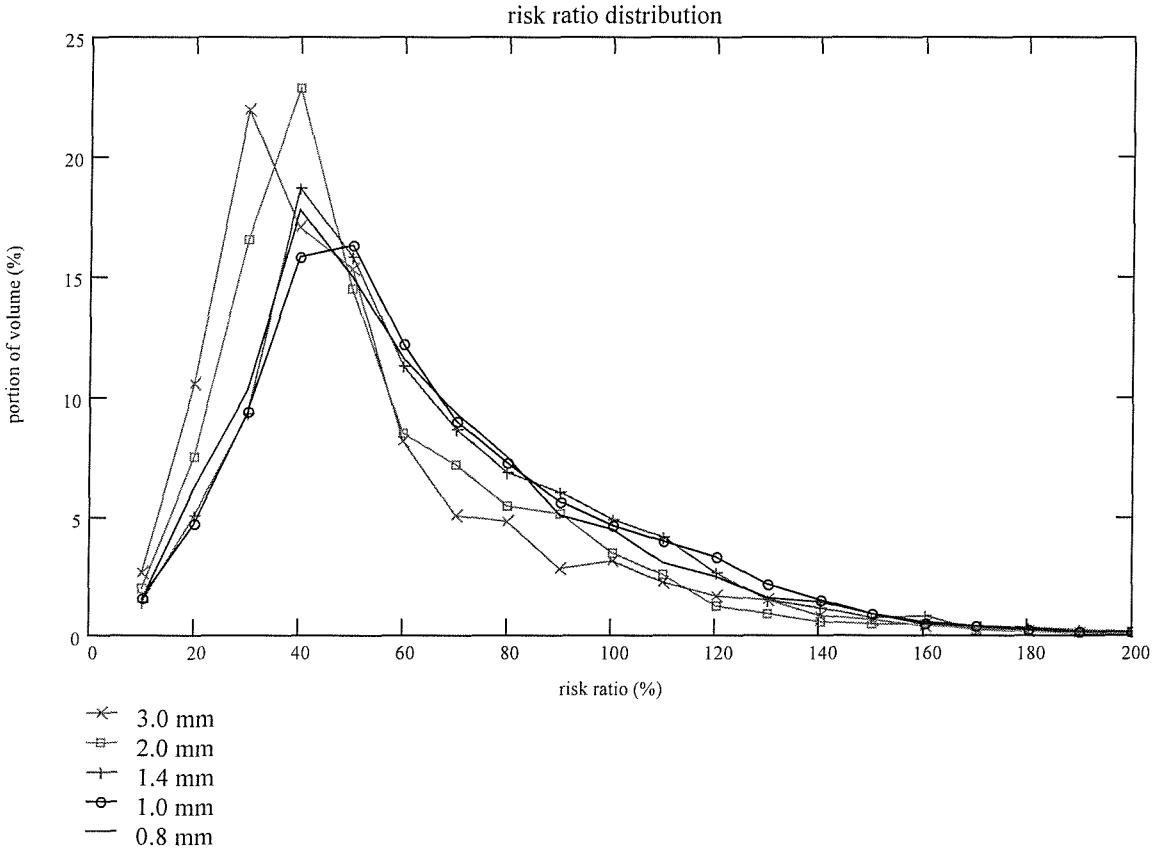

Figure 5.17. Risk ratio distribution in the volume of interest.

In general, Table 5.3 and Table 5.4 together with Figure 5.16 and Figure 5.17 show that convergence was achieved with the model using an element edge length of 1.4 mm. The mean values of stiffness, stress and risk ratio as well as the risk ratio distribution

showed a very stable performance or, in other words, with element sizes below 1.4 mm the stresses and risk ratios did not appear to be very sensitive to the mesh density.

5.5. DISCUSSION

In the foreseeable future, patient specific finite element models will be used to assess the performance of total joint replacements. The quality of patient-specific finite element models is dependent on the quality of the CT images, the assignment of the material properties and the mesh density. Despite various studies having used CT based FE analysis of bony structures, very few have explicitly verified convergence of either the assigned material properties or the resulting stress/strain distribution [26,155,164]. If the convergence of these parameters is not verified, the accuracy of a FE model may be uncertain. The objective of this study was to assess the accuracy of such models by testing the sensitivity of the assigned Young's modulus, von Mises stress and risk ratio to variations of the finite element size.

In section 0, the influence of the method to assign material properties to the model was examined. It was observed that when a logarithmic discretisation of material properties within the model was used instead of a linear discretisation, convergence of all variables of interest was achieved with considerably fewer different mechanical properties. In an analysis of an implanted proximal tibia, an accurate determination of stresses and material property distribution within the cancellous bone is required. The range of stiffness values found in the whole model can be significantly wide (50-23000 MPa), therefore the utilisation of a logarithmic ΔE is more appropriate, as it allows a finer discrimination of material properties for softer materials (cancellous bone), hence improving the accuracy only where it is needed. Even though convergence can also be achieved with the use of a linear ΔE, it requires significantly more different materials than the logarithmic distribution. A maximum number of 532 different material properties were used for the linear ΔE and yet no clear convergence was reached. In Figure 5.11 it can be perceived that, for a linear ΔE, all variables of interest were converging towards the same values obtained with logarithmic increments, with the difference that with the latter, an accuracy within 1% was reached with 304 material

properties, whereas with linear increments that level of accuracy is not reached at all in some cases. These results are comparable to those obtained by Zannoni *et al.* [164], who observed that for their model (distal femur), an accuracy of 1% in the strain energy could be achieved with 214 materials (linear ΔE). Therefore, it could be concluded that results are not only dependent on the number of material properties used, but also on the manner these material properties are distributed throughout the model. Furthermore, it was observed that the maximum difference between the material property assigned to a group and the "real" value corresponding to the elements contained in that group is so small that it is very unlikely to have any significant effect on the stress and risk ratio distributions. Hence, in terms of the results from the models, this method is deemed equivalent to assigning a unique material property to each element.

Section 5.4 examined the influence of the mesh density on the assigned material properties, the predicted stresses and risk ratios. It has been demonstrated that the assigned material properties were highly dependent on the element size. In certain areas of the resected tibial surface, there are rapid changes in modulus. Too coarse a mesh does not capture the subtle variations in the modulus distribution and in general gives highly erroneous modulus values. It was observed that unless there is convergence of the assigned material properties, convergence of the predicted stresses and risk ratios does not occur. To the authors' knowledge, no other study has examined the convergence of the assigned materials as a function of the mesh density, and as this study has shown, this is critical to ensure an accurate prediction of other parameters of interest.

In this study, the pixel size of the CT data was 0.468 x 0.468 mm with a slice thickness of 1 mm in the region of interest. An adequate discretisation of the material properties was only achieved when the element size approached the size of the slice thickness, i.e. when elements had an edge length of approximately 1 – 1.5 mm. Above this size, the mesh was unable to capture the rapid variations in modulus that occurred. This is due to the internal averaging of the pixel intensities during the assignment of material properties to an element. Therefore, it is recommended that in order to obtain convergence in the assigned material properties, the element size should be chosen to be similar to the pixel size of the CT scan.

Convergence was assessed at two levels, locally by examining variations at the nodal points and globally, by examining the mean and peak values within a pre-defined volume. At the local level, convergence of modulus was only achieved with an element edge length of 1.0 mm or smaller. Convergence of the stress and risk ratio was only achieved once the modulus distribution had also converged. At the global level, the mean modulus values and general distribution of the modulus appeared to have converged for all mesh densities. Even though the modulus distribution had converged, convergence of the mean stress and risk ratio values was only achieved with element edge lengths of 1.4 mm or less. Thus, it would appear that at a local level, a finer mesh is required to gain convergence than at a global level. This highlights the need for performing adequate convergence checks, which are appropriate to the type of analysis being performed. If nodal values (e.g. nodal stresses) are examined, performing a convergence study of a global parameter, such as the mean stress or the strain energy within a given volume, may not be adequate.

A limitation of this study is that linear tetrahedral elements were used. It is an accepted fact that these elements have poor performance and may not accurately predict the stresses in regions with a large stress gradient. However, the conclusions of this study, with regards to gaining convergence of the assigned material properties remain valid. The majority of the material assignment programs assign the modulus to the element; therefore, if second order tetrahedral elements were used instead of linear ones, in order to obtain the same modulus distribution, the same element size (edge length) would still be required. These statements seem to contradict the findings reported by Polgar *et al.* [117], who obtained better results using larger second order tetrahedral elements instead of smaller linear ones. They observed that using the same number of degrees of freedom, second order tetrahedral meshes produced a notably more stable solution. However, they used a model with a uniform material property throughout the whole volume. In this study, a heterogeneous material property distribution in the bone was used. Therefore, the concept of using larger but higher order elements would no longer be valid, as small element sizes would be required in order to achieve convergence of the Young's modulus distribution across the model of the tibia.

This study has shown that accurate assignment of the material properties is critical in achieving convergence of other parameters such as stress and risk ratio. If convergence of the assigned material properties is not achieved, errors are then propagated through to

other parameters of interest. There is no evidence of previous studies demonstrating that the assigned material properties of models of bony structures are influenced by the mesh density, as shown here.

CHAPTER 6

INTER-PATIENT EVALUATION OF STRESSES IN PROXIMAL IMPLANTED TIBIAE

Previous studies have suggested that implant migration is directly related to mechanical factors (section 3.7). It has been demonstrated that early migration can predict the risk of tibial component loosening, as it has been shown that even though loosening is detected several years after surgery, it is in fact a continuous process that begins shortly after the arthroplasty [134] (see section 3.5.4). Furthermore, it has been found that inducible displacements are strongly correlated with permanent migration [63,148]. Fukuoka *et al.* [47] have demonstrated that future migration of the tibial component can be predicted as early as at the time of surgery by observing the inducible displacements (specifically lift-off) produced by applying a force directly to the implant during surgery. Moreover, Taylor *et al.* [142] have suggested that cancellous bone stresses are correlated with tibial component migration, as they demonstrated that higher stresses are observed in finite element models that include implants that usually show higher rates of failure due to mechanical loosening.

Based on the above statements, there is clear evidence that inducible displacements, migration and implant loosening are closely related to the initial mechanical environment of the implant. Hence, the purpose of the work described in this chapter was to investigate whether the clinical performance of proximal implanted tibiae can be predicted by means of finite element models that include patient specific data, such as bone material properties and geometry, patient's weight and component alignment. Data from four different patients were included in the analysis. Migration data of the patients, obtained by means of RSA, were used to assess the clinical outcome of the prosthesis and compare it with the results obtained from patient-specific finite element models. It should be mentioned that to date, there have been no studies that have performed a direct comparison between the results from patient-specific FE models and migration or any other clinical data obtained from the same patients.

6.1. MATERIALS AND METHODS

Finite element models of four proximal implanted tibiae were analysed. The models were created from quantitative computed tomography (QCT) data of patients prior to total knee arthroplasties at the University Hospital Lünd Sweden, by Prof. Leif Ryd. In all patients, the type of prosthesis implanted was the Howmedica-Crucifix knee replacement. The fixation method used, as well as the sex and age of each patient are outlined in Table 6.1.

Table 6.1. Fixation method used in each patient.

Patient Number	Sex	Age (years)	Fixation Method
1	F	67	Non-cemented. Hydroxyapatite coated
2	F	67	Non-cemented. Press fit.
3	M	70	Non-cemented. Press fit.
4	F	81	Cemented.

The immediate post-operative situation was modelled by assuming frictionless contact between the tibia and the tibial plateau for patients 1, 2 and 3. A second model was created for patient 1 in order to analyse a bonded interface between the tibial tray and the bone. The purpose of examining this model was to simulate the situation in which the hydroxyapatite coating had become completely osseointegrated. In the second model for patient 1, the stem-bone interface was modelled as de-bonded and frictionless as the hydroxyapatite coating was applied only under the tibial tray. In the remainder of this chapter, the bonded and de-bonded models of patient 1 will be referred to as patient 1-B and patient 1-DB respectively.

The model corresponding to patient 4 included a 2-mm cement mantle between the tibial tray and the bone. The cement-implant and cement-tibia interfaces were simulated as perfectly bonded. The interface between the bone and the stem was simulated as de-bonded and frictionless in this model as well.

6.1.1. Tibial tray alignment

Post-operative X-ray images in both sagittal and frontal planes were used to determine

the vertical tibial plateau position and alignment relative to the tibia in each patient. The angles of the resected surface in both sagittal and frontal planes of each patient are shown in Table 6.2 and Figure 6.1.

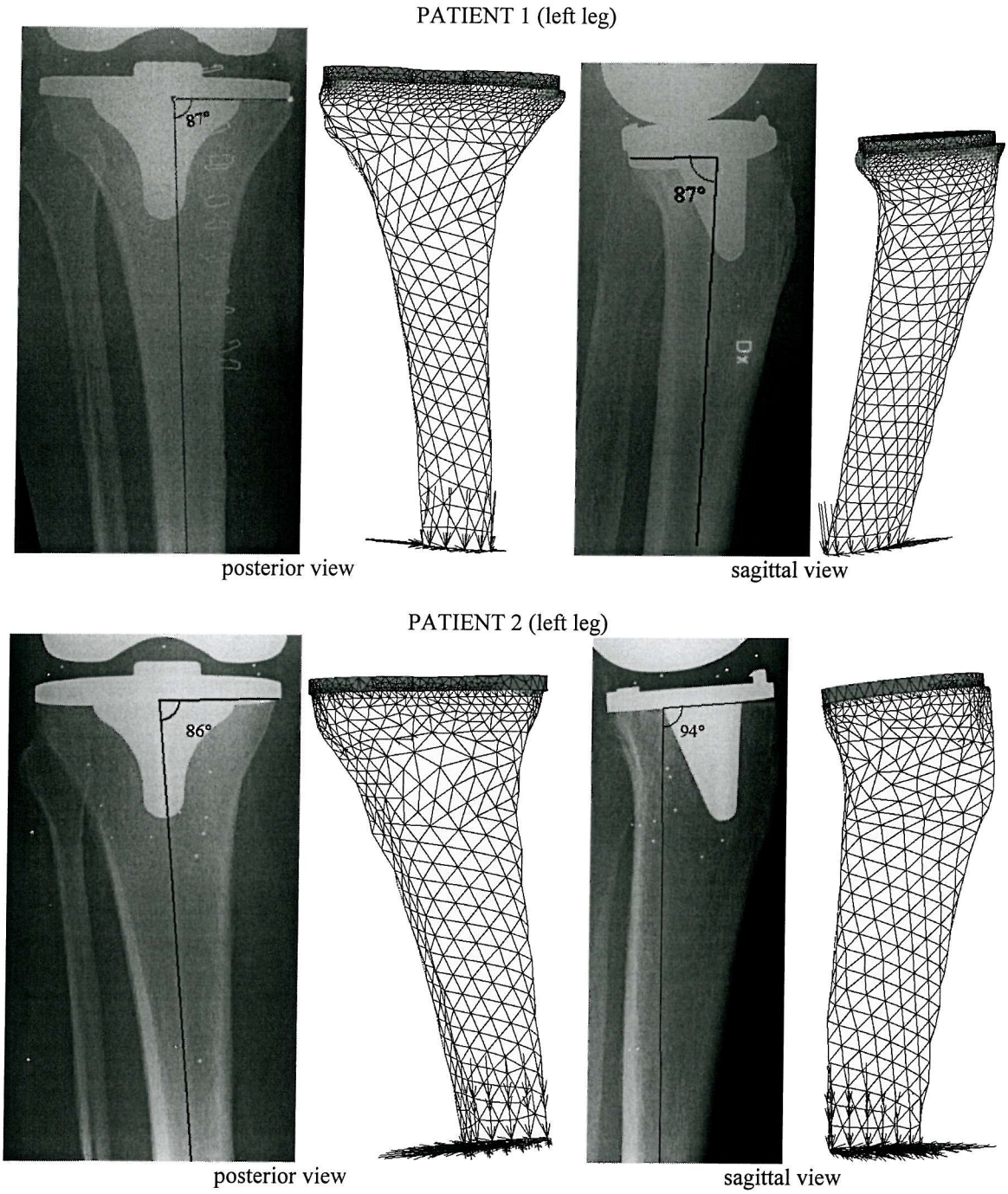

Figure 6.1. Frontal and sagittal angles of the resected plane of the tibia in each patient. Post-operative X-ray images (left) and FE models generated (right).

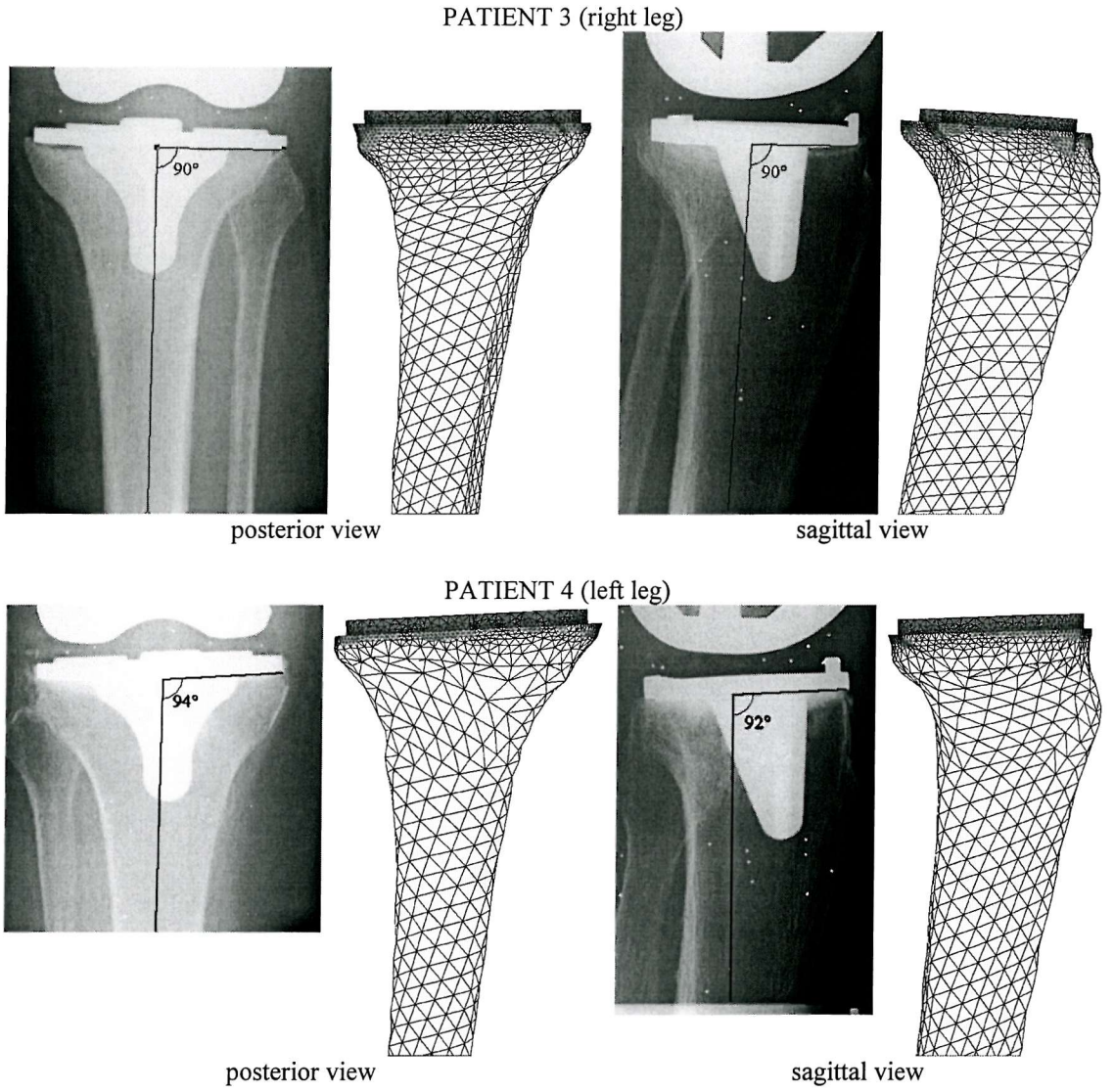

Figure 6.1 (continued). Frontal and sagittal angles of the resected plane of the tibia in each patient. Post-operative X-ray images (left) and FE models generated (right).

These angles were measured with reference to an axis aligned with the long axis of the bone. This axis was defined, as accurately as possible, directly on the sagittal and frontal X-ray images. In Figure 6.1, the models obtained for each patient are compared with the post-operative X-ray images.

Table 6.2. Angle of the resected plane of the tibia. Angles are expressed as deviation from a plane perpendicular to the long axis of the bone.

Patient No	Frontal Plane Angle	Sagittal Plane Angle
1	3° medially	3° posteriorly
2	4° medially	4° posteriorly
3	0°	0°
4	4° laterally	2° posteriorly

Even though a special effort was made to reproduce the angles as accurately as possible, the low quality of the X-rays and the lack of clear anatomic landmarks to base the measurements on, led to a level of uncertainty of one or two degrees for the tibial cut angle and of one or two millimetres for the vertical position of the implant. Additionally, from the X-ray images, it was virtually impossible to determine the angle about the long axis of the bone at which the prostheses were positioned. In chapter 4 [116], the effect of the tibial tray alignment on the stresses was extensively discussed. It was demonstrated that this parameter is significant in this type of model, as it influences the predicted stresses within the bone.

Meshes of linear tetrahedral elements were created in I-DEAS Master Series 7 for both bone and implant. Based on the study described in chapter 5, it was concluded that an element edge length of 1.4 mm on the contact surfaces is appropriate to properly describe the material property distribution for this type of analysis. The mesh of the implant was created in such a way that it perfectly matched that of the bone at the bone-implant interface, as it was noticed that this configuration produced more stable results.

The Bonemat program was used to assign the material properties on an element-by-element basis (chapter 5). The correlations to convert the values from Hounsfield Units to bone apparent density and subsequently to Young's modulus are defined in chapter 5 (equations 5.1 and 5.2). Table 6.3 displays the average and maximum values of Young's modulus in the 2-mm layer at the proximal end of each bone model. It should be noticed that patient 4 shows significantly lower mechanical properties (mean Young's modulus of 145.1 MPa), as compared to the other three patients studied here. Specifically, as opposed to the other three patients, the medial compartment has a lower mean stiffness than the lateral compartment. In fact, this deficiency was detected by the surgeon at the time of surgery and it was considered necessary to use PMMA cement to fix the tibial component to the bone. Even though the mean Young's modulus of the medial compartment is higher than that of the lateral compartment for the other three patients, the ratio between them varies substantially, with values of 3.5:1, 1.3:1 and 1.9:1 for patients 1, 2 and 3 respectively.

Six different load cases were analysed for all the models. In all cases, the loads were applied on nodes situated on two circular patches of 10 mm in diameter, artificially created for this purpose on the top surface of the tibial tray (Figure 6.2). In all models,

the element edge length on the top surface of the tibial tray was set to 4 mm; hence, the number of nodes where the loads were applied did not vary between the models.

Table 6.3. Young's modulus values in the proximal tibia (volume of interest).

Patient Number	Modulus (MPa)			
	mean values			peak
	entire volume	medial compartment	lateral compartment	
1	267.8	405.4	115.2	12850
2	212.6	263.8	195.8	6655
3	241.7	313.8	164.6	10090
4	145.1	133.4	157.6	13400

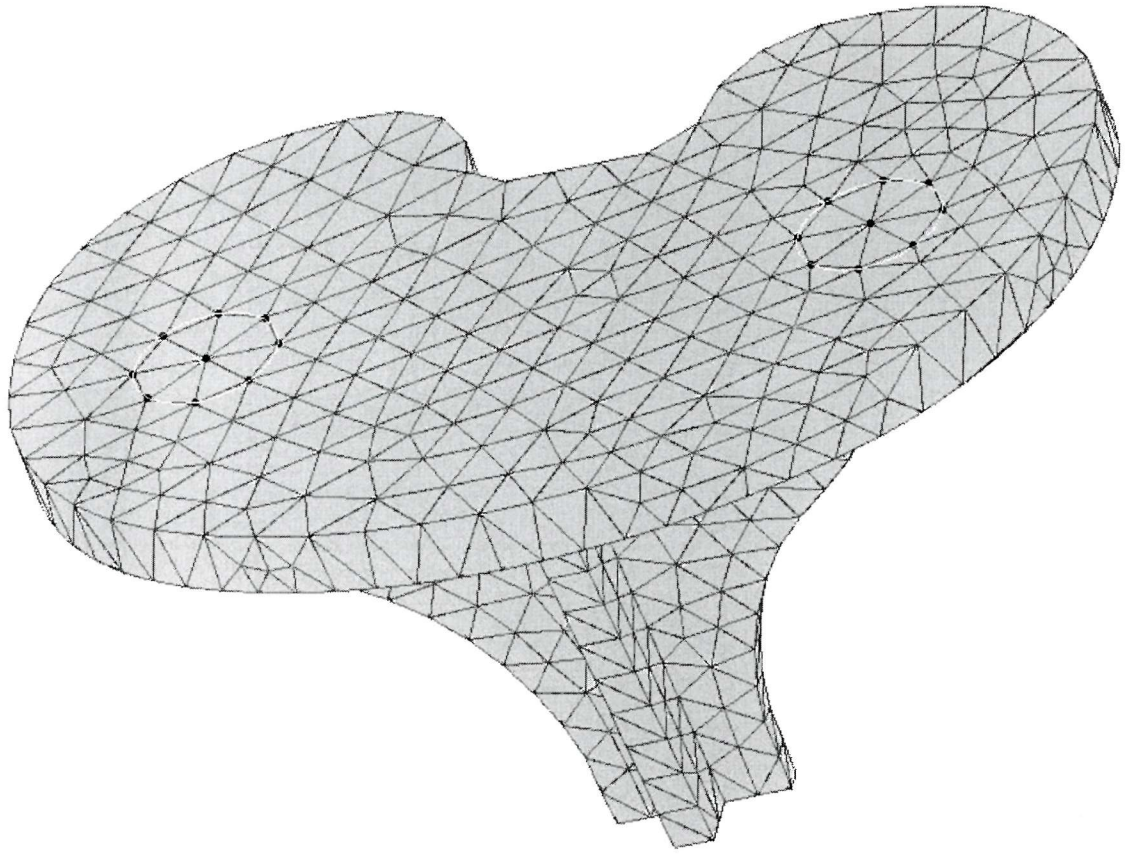

Figure 6.2. Nodes used to apply the external loads.

The different load cases examined here are described in Table 6.4. Load cases 1, 2, 3 and 4 consist only of axial forces equivalent to three times the patient's body weight (Table 6.5), whereas load cases 5 and 6 also included antero-posterior forces and

torques. Since in general, the load distribution between medial and lateral condyles varies significantly between patients, load cases 1 through 4 were selected to cover the whole range of possible load distributions, varying between medial unicondylar (load case 1) to lateral unicondylar (load case 4). Load cases 5 and 6 were selected in an attempt to model a more realistic load case that comprises loads in different directions applied simultaneously. The magnitude of the loads used in load cases 5 and 6 were obtained from ISO/DIS 14243-1 [75], taking the values corresponding to the percentage of gait cycle (50%) that produces the highest torque.

Table 6.4. Loads cases examined.

Load Case	Description
1	Pure axial uni-condylar load. Medial condyle 100%.
2	Pure axial bi-condylar load. Medial condyle 60%. Lateral condyle 40%.
3	Pure axial bi-condylar load. Medial condyle 40%. Lateral condyle 60%.
4	Pure axial, uni-condylar load. Lateral condyle 100%.
5	Axial bi-condylar load (medial 60%, lateral 40%). Antero-posterior force. Torque.
6	Axial uni-condylar load (medial 100%). Antero-posterior force. Torque

The loads applied in each model are depicted in detail in Table 6.5 (both models created for patient 1 had the same loads applied). In all cases, the distal end of the tibia was rigidly constrained. It should be noted that the patients were sorted by their weight, patient 1 being the heaviest and patient 4 the lightest.

Table 6.5. Loads applied in each model.

		Load cases 1,2,3,4	Load cases 5,6		
Patient Number	Body Weight (kg)	Pure Axial (N)	Axial (N)	Antero-Posterior* (N)	Torque** (N·m)
1	135	3969.0	3036.7	272.5	9.8 (c)
2	115	3381.0	2586.8	232.1	8.3 (c)
3	89	2616.6	2002.0	179.6	6.4 (cc)
4	74	2175.6	1664.6	149.4	5.3 (c)

* This force points posteriorly

** The torque is in the toe-in orientation, or (c) Clockwise or (cc) Counter clockwise.

All analyses were carried out in MARC 2000.

In the following section, the results from all the models are presented separately for each load case analysed. Mean and peak values of the von Mises stress and risk ratio as well as the percentage bone volume with risk ratios exceeding 100% are reported for the volume of interest (2-mm layer in the proximal tibia). The percentage of volume with

risk ratios exceeding 100% will be referred to as **PVFB** (Percentage Volume of Failing Bone) in the rest of this chapter. Images showing the risk ratio distribution on the resected surface of the proximal tibia are also included. As mentioned in section 3.7, it has been suggested that cancellous bone stresses are correlated with implant migration. Figures representing the contact areas for the three de-bonded models were also incorporated in order to show the portion of bone that separates from the prosthesis due to lift-off, especially in the unicondylar load cases. This parameter has been found to be strongly correlated with tibial component loosening [47] (section 3.5.4). The relative motion between the nodes on both bodies (implant and bone) located on the periphery of the initial contact area was reported for the three de-bonded models subjected to each load case. These displacements, expressed as implant lift-off (displacements perpendicular to the resected surface of the bone) and sliding (tangential displacements on the resected surface of the bone), were examined, as a strong correlation between inducible displacements (micromotions) and implant migration has been previously reported [63,148].

6.2. RESULTS

It should be noted that the von Mises stresses reported here are not very significant for this type of study as the supporting bone has a heterogeneous material property distribution. The von Mises stress alone is not enough to indicate whether the bone is likely to fail, hence it is only included in the following tables (Tables 6.7 to 6.8) as a reference. For this reason, the risk ratio parameter, which considers both stress and bone strength, was deemed more appropriate for this study (see section 5.2).

6.2.1. Load case 1 (pure axial, 100% medial condyle)

This load case produced the highest risk ratios in the patient 1-DB model, which showed a mean value 120% higher than its bonded counterpart (Table 6.6). Patient 4 was observed to be particularly sensitive to this load case, as it produced a mean value similar to that observed in patient 1-B, even though patient 1 has a body weight 82% higher than patient 4. Patient 2 showed lower mean risk ratio values followed by patient 3 which produced the lowest mean risk ratio of all the models. The same ranking was found from the median risk ratio. On the other hand, the portion of volume undergoing

risk ratios exceeding 100% produced a slightly different ranking, as the values corresponding to patient 1-B, patient 2 and patient 4 are very similar (Table 6.6). According to this parameter, patient 1-DB is still, by far, the model that presents the highest likelihood of failure, with 52.1% of the proximal volume showing risk ratios greater than 100%, whereas patient 3 shows the lowest portion of volume likely to fail (only 5.4 %).

Table 6.6. Von Mises stress and risk ratio values for the volume of interest. Load case 1.

patient	von Mises (MPa)		risk ratio (%)			PVFB
number	mean	peak	mean	median	peak	(%)
1-B	1.501	43.7	65.0	60.1	250.8	18.8
1-DB	2.880	73.1	143.2	109.9	1703.6	52.1
2	1.495	50.5	57.9	46.2	637.4	20.5
3	0.942	17.5	38.8	27.9	548.8	5.4
4	0.862	30.0	70.9	71.9	212.6	19.9

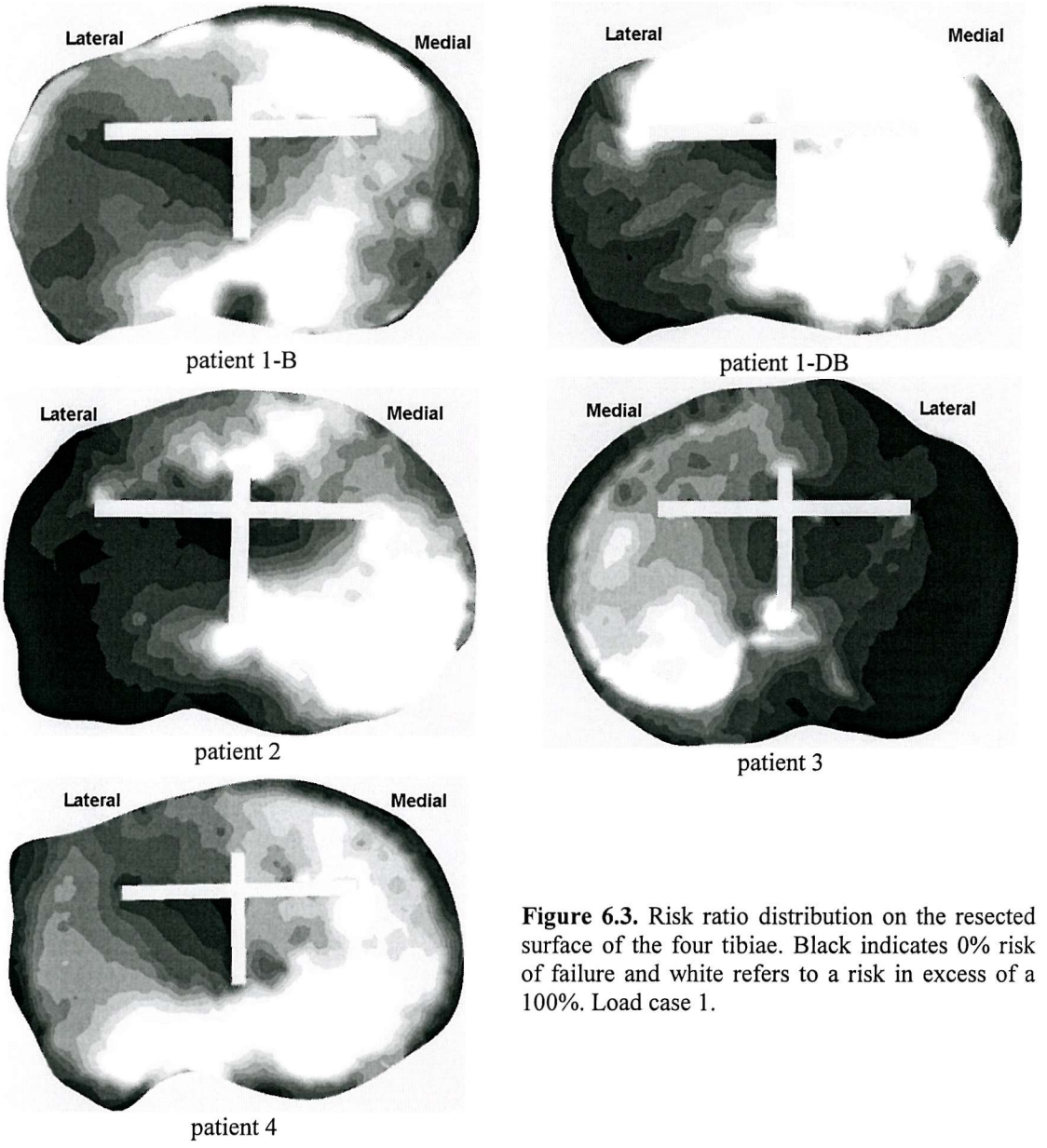

Figure 6.3. Risk ratio distribution on the resected surface of the four tibiae. Black indicates 0% risk of failure and white refers to a risk in excess of a 100%. Load case 1.

In Figure 6.3, it can be observed that under these loading conditions, the maximum risk ratios in patient 1-B are observed around the antero-medial and posterior-medial regions of the proximal tibia. When the bone-prosthesis interface is modelled as de-bonded (patient 1-DB), these values of risk ratio are significantly higher. In the rest of the models, the highest values of risk ratio are found around the posterior-medial side of the resected surface of the bone. In particular, patient 4 shows a significant portion of volume undergoing high risk ratios in the posterior aspect of the bone.

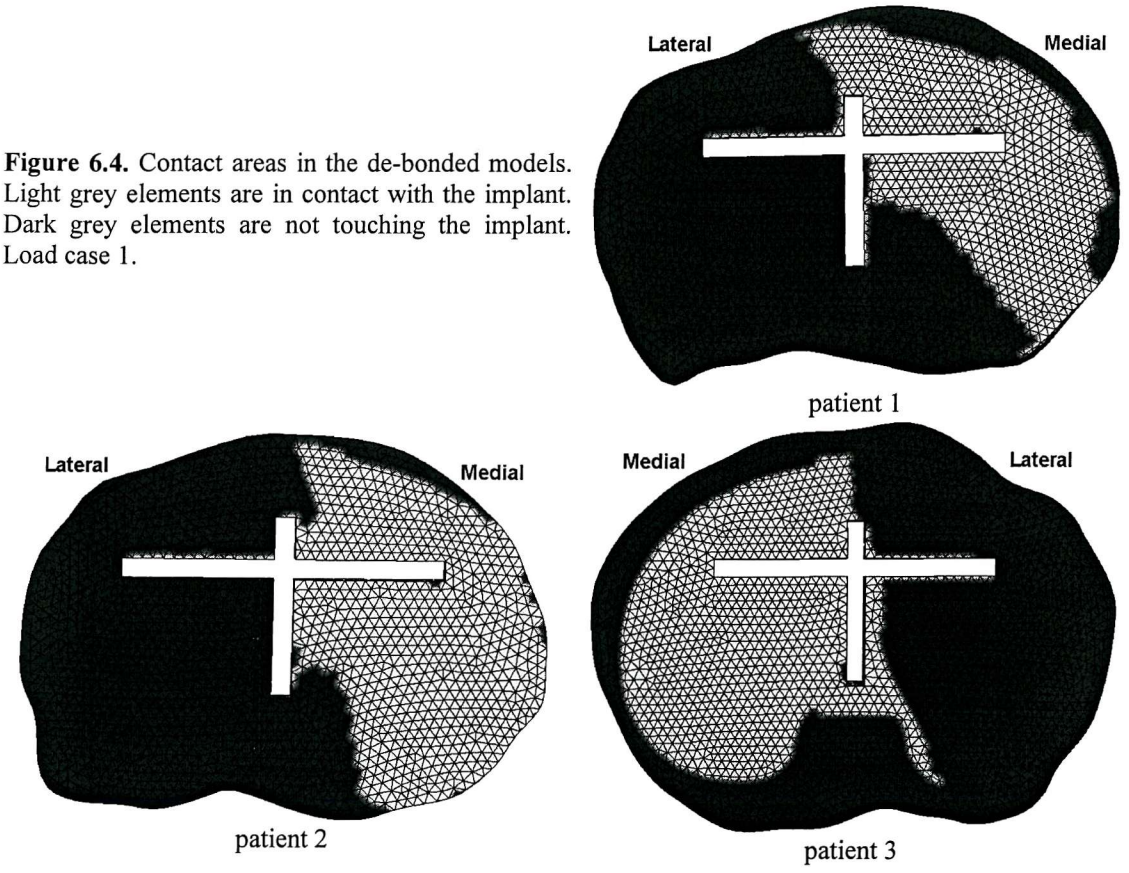

Figure 6.4. Contact areas in the de-bonded models. Light grey elements are in contact with the implant. Dark grey elements are not touching the implant. Load case 1.

As it can be seen in Figure 6.4, a substantial area of the resected surface of the bone (virtually the entire lateral aspect) is not in contact with the prosthesis. This amount of lateral lift-off was expected, as the load case is not balanced between the condyles. It should be noticed that the heavier the patient is (Table 6.5), the smaller is the region of bone that stays in contact with the prosthesis. This phenomenon is further illustrated in Figure 6.5-b, where significant lift-off values can be observed in the lateral aspect of the implant whereas the medial aspect stays in contact with the bone. The sliding micromotion (Figure 6.5-a) in patients 2 and 3 was higher in the lateral and posterior aspects of the tibial tray, as compared to the medial aspect. Nonetheless, this phenomenon was not present in patient 1, which showed similar levels of micromotions in both medial and lateral sides.

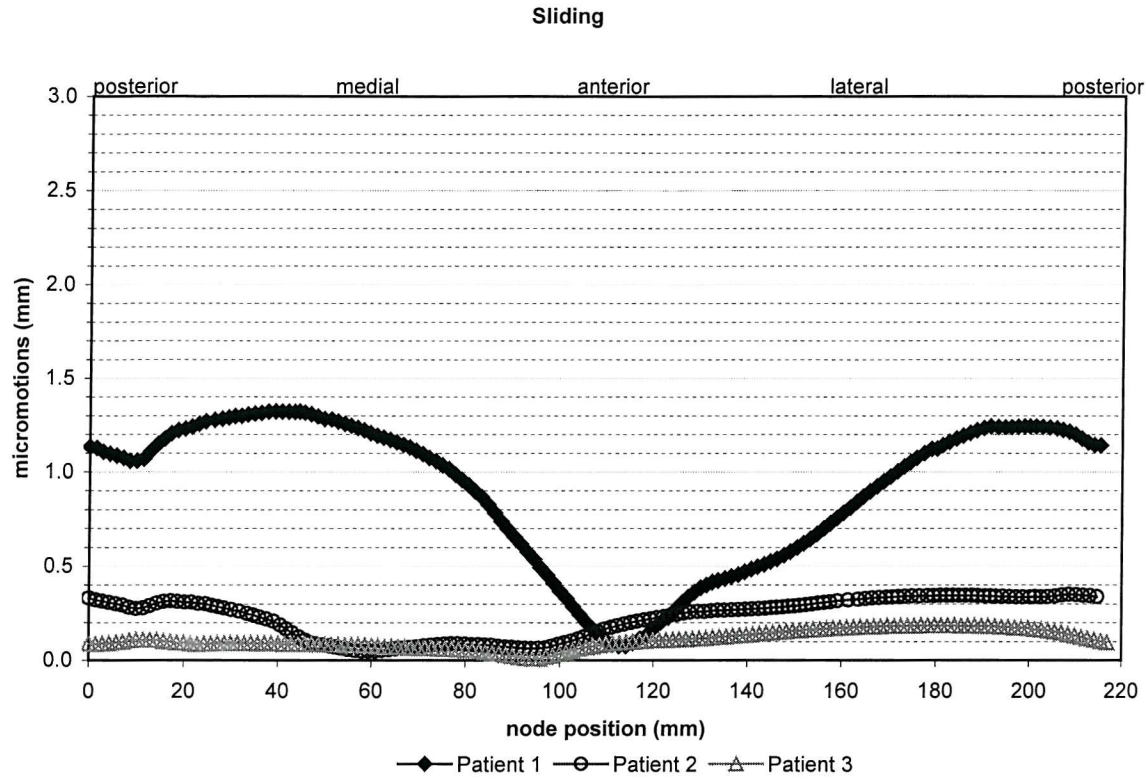

(a)

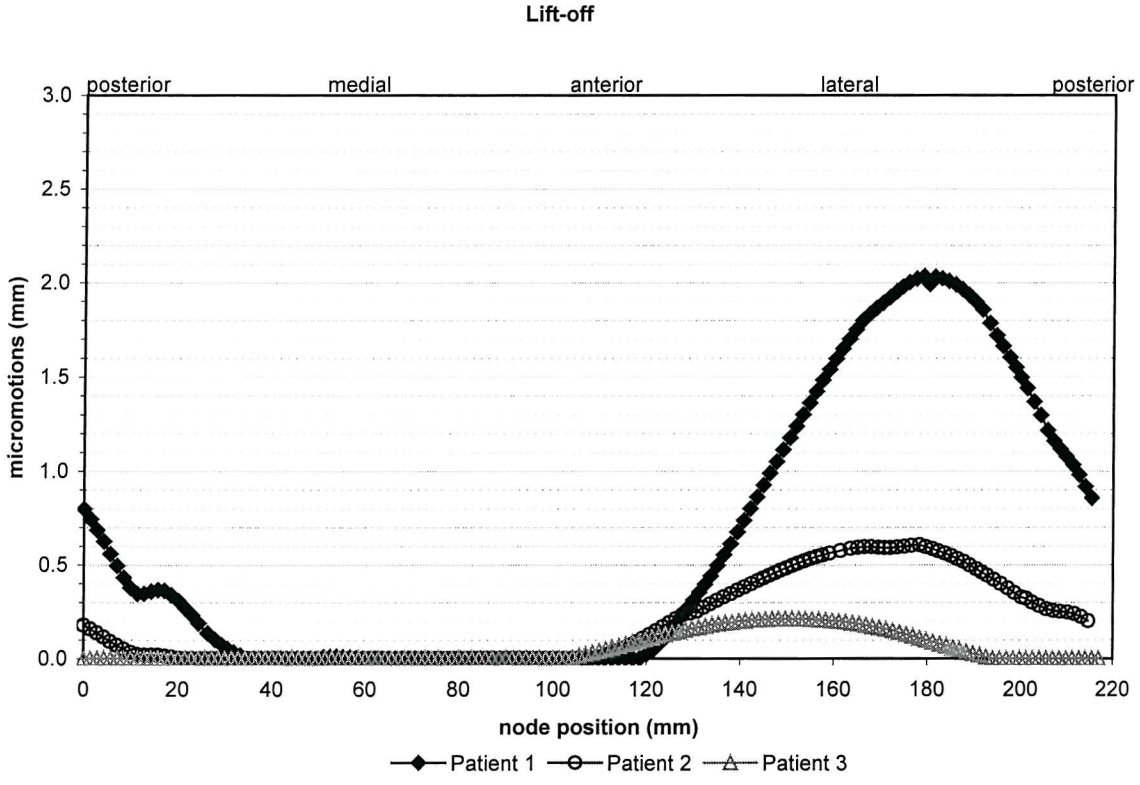

(b)

Figure 6.5. Relative motion between bone and implant calculated for the nodes located on the contour of the contact area between tibia and tibial plateau. (a) Sliding. (b) Lift off. Load Case 1.

Notice that patient 1-DB (heaviest patient) produced significant higher values of micromotion than those observed in patient 2 and patient 3 (lowest body weight of all three de-bonded models), which showed the lowest values of implant micromotion. The maximum values of lift-off resulting from this load case were 2.04, 0.61 and 0.21 mm for patients 1-DB, 2 and 3 respectively, whereas the maximum sliding observed was 1.14, 0.35 and 0.19 mm for patients 1, 2 and 3 respectively.

6.2.2. **Load case 2** (pure axial, 60% medial condyle, 40% lateral condyle)

The mean risk ratio values reported in Table 6.7 show that the de-bonded version of patient 1 is more likely to fail than any other patient under these loading conditions. Patient 2 shows the second highest mean risk ratios, followed closely by patient 1-B and patient 3. Patient 4 shows the lowest risk ratios of all five models subjected to this load case. The same ranking was produced by the median risk value, only that the differences between the models are smaller; in fact, patient 1-B and patient 3 show the same median risk ratio. The highest value of PVFB was again found in patient 1-DB, followed by, at a much lower level, patient 2, patient 1-B and patient 3. Patient 4 presented virtually no elements in the volume of interest with risk ratios that exceeded 100%.

Table 6.7. Von Mises stress and risk ratio values for the volume of interest. Load case 2.

patient	von Mises (MPa)		risk ratio (%)			PVFB
number	mean	peak	mean	median	peak	(%)
1-B	1.007	26.8	55.1	47.0	335.8	8.5
1-DB	1.654	35.8	107.0	73.5	934.9	40.3
2	1.180	24.2	60.2	55.2	388.2	13.9
3	0.800	20.1	50.4	47.0	305.6	7.4
4	0.478	16.4	39.7	41.6	104.6	0.0

In Figure 6.6, it can be observed that in patient 1 (both bonded and de-bonded models) higher risk ratios are found in the anterior aspect of the bone. Patient 2 presents a significant portion of bone in the posterior and anterior regions with risk ratios over 100%. Patient 3 presents a concentration of high risk ratios in the anterior-lateral and posterior-lateral aspects of the tibia. In agreement with the values observed in Table 6.7 for patient 4, almost no elements with risk ratios greater than 100% can be seen in Figure 6.6 (white regions). In the latter model, the maximum values of risk ratios are observed around the posterior-medial region of the resected surface of the bone.

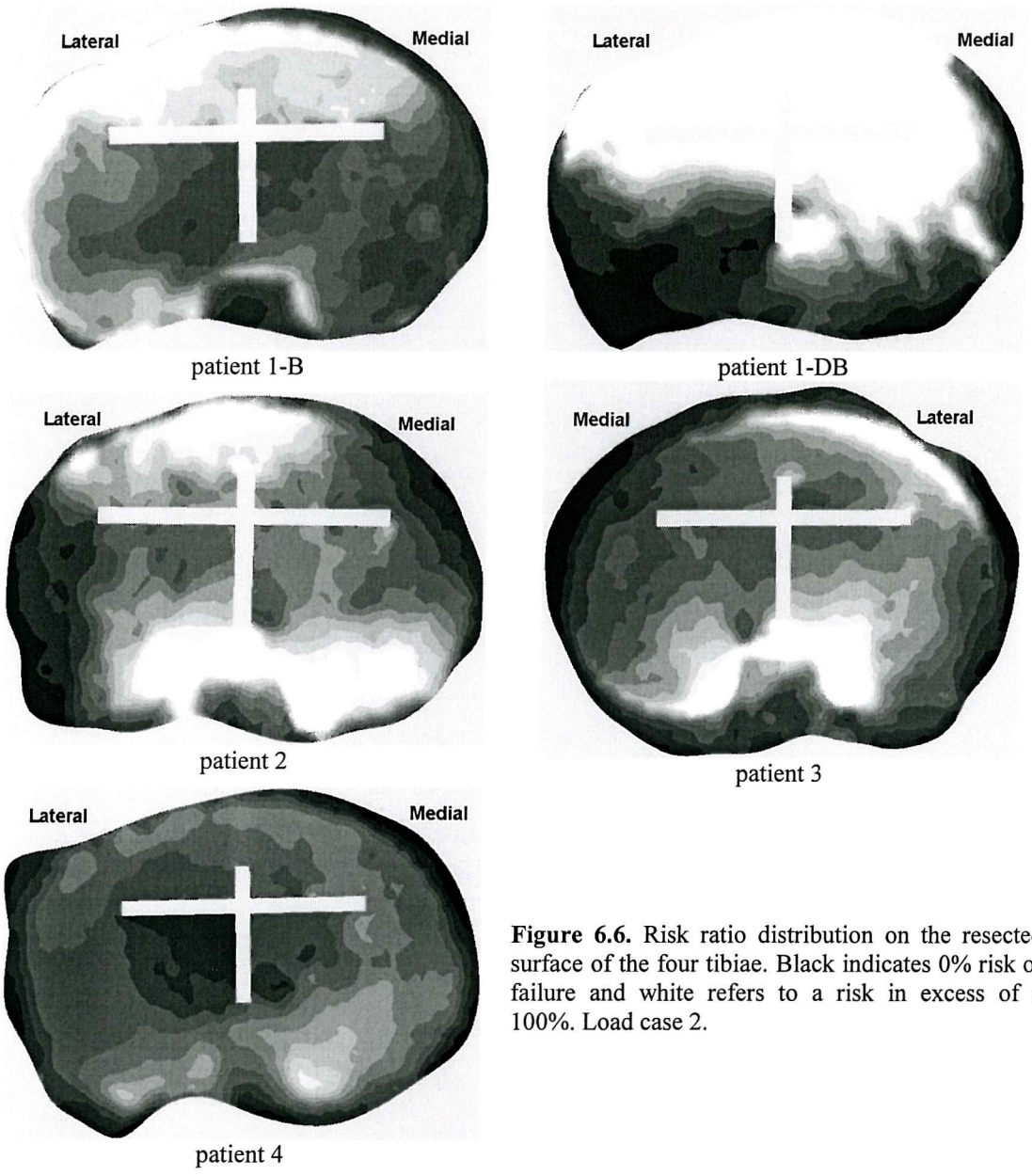

Figure 6.6. Risk ratio distribution on the resected surface of the four tibiae. Black indicates 0% risk of failure and white refers to a risk in excess of a 100%. Load case 2.

In Figure 6.7, it can be observed that despite the loads being relatively balanced between both condyles, in patient 1 there was a significant lift-off of the implant in the posterior side. This is due to the loads being applied slightly towards the front aspect of the implant (Figure 6.2). Nevertheless, virtually no lift-off was observed in the other two de-bonded models. This was corroborated in Figure 6.8-b, which shows a maximum lift-off of 0.32 mm for patient 1, whereas patients 2 and 3 show no lift-off at all.

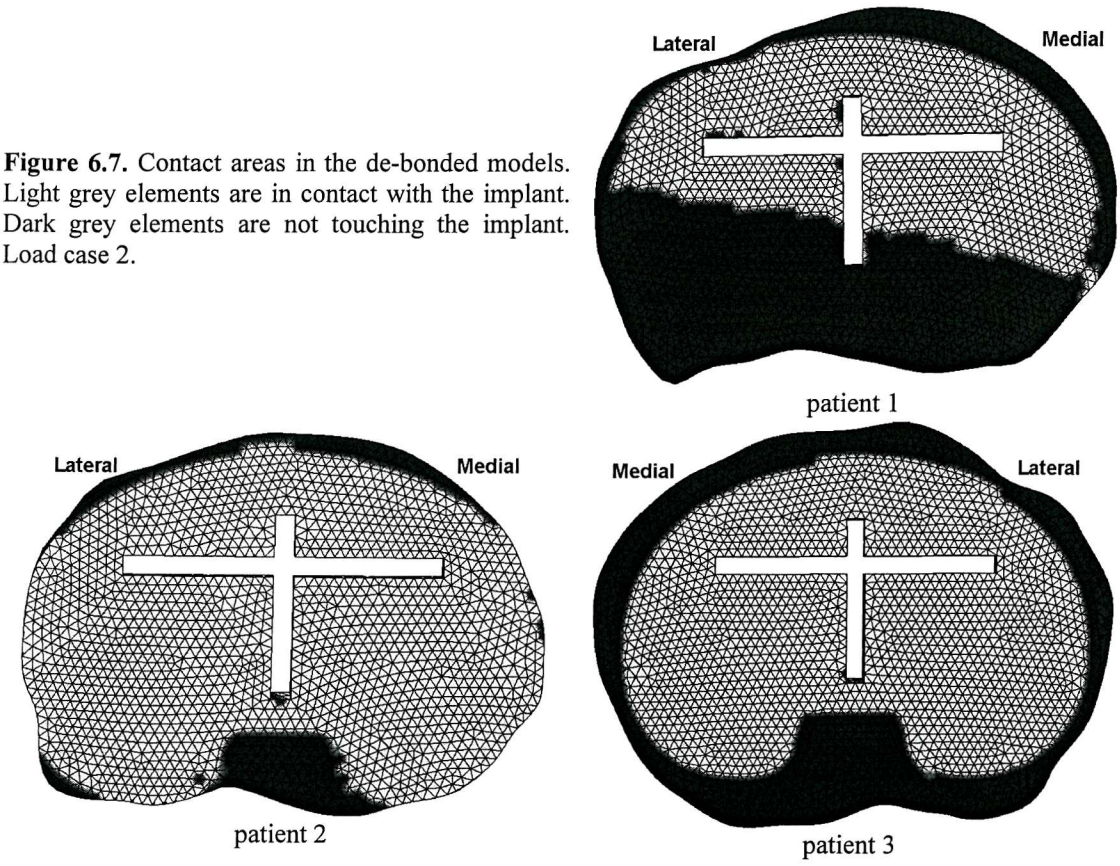

Figure 6.7. Contact areas in the de-bonded models. Light grey elements are in contact with the implant. Dark grey elements are not touching the implant. Load case 2.

The micromotions displayed in Figure 6.8 correlate with the contact areas observed in Figure 6.7, as patient 1 shows significantly higher sliding (maximum of 0.62 mm) as compared to those observed in patient 2 and 3 (maximum of 0.16 and 0.15 mm respectively). Furthermore, it can be noticed that for patient 1, since a higher percentage of the total load is applied on the medial side of the tibial plateau, the lift-off is higher in the lateral condyle (maximum of 0.32 mm), whereas the sliding is higher on the medial side.

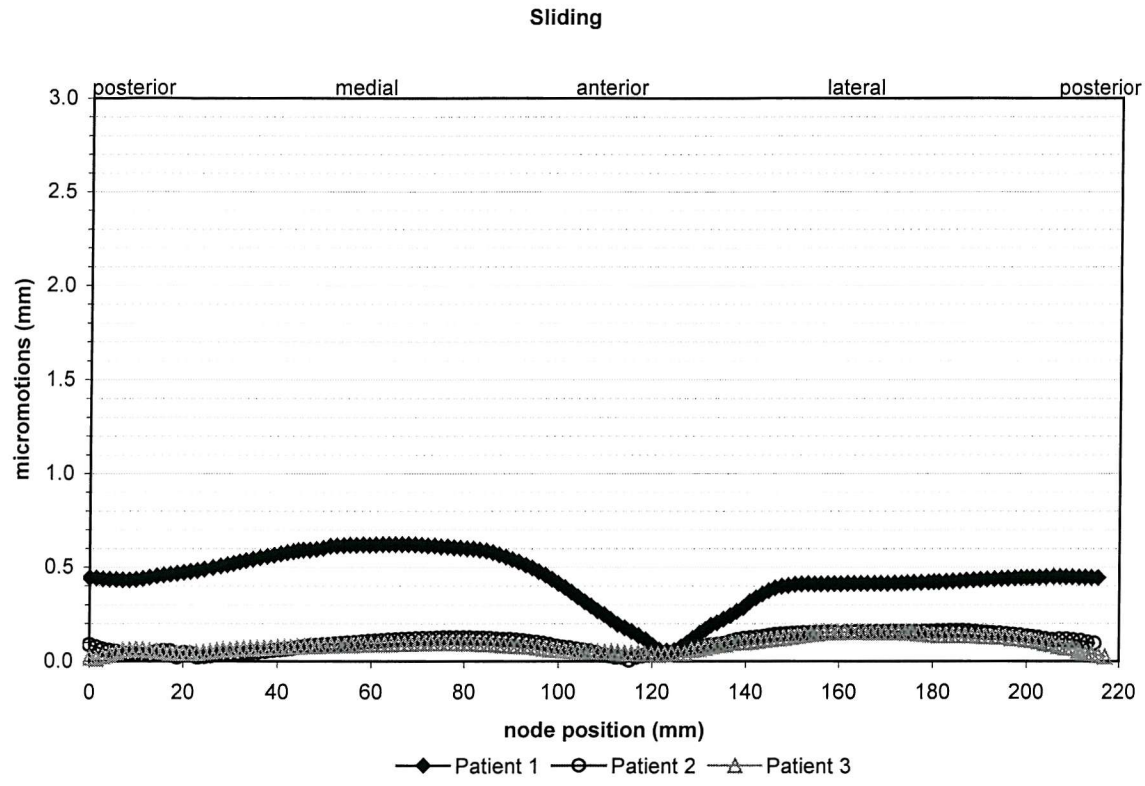

(a)

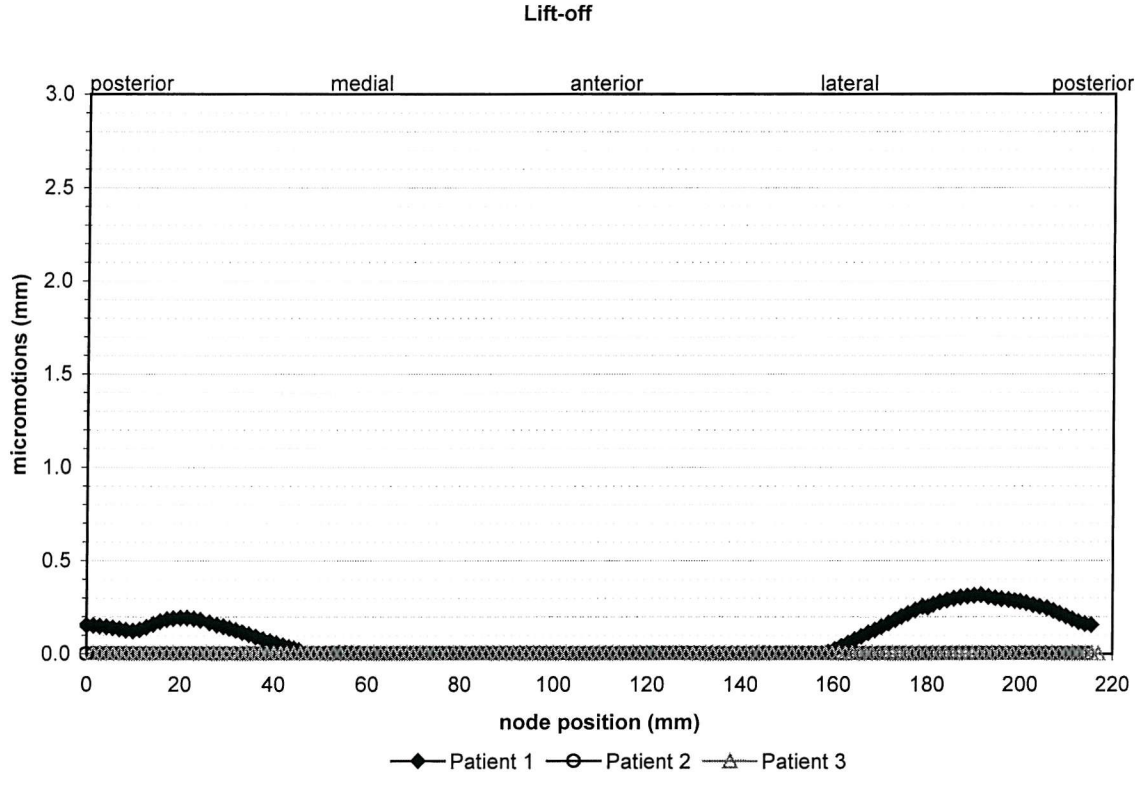

(b)

Figure 6.8. Relative motion between bone and implant calculated for the nodes located on the contour of the contact area between tibia and tibial plateau. (a) Sliding. (b) Lift off. Load Case 2.

6.2.3. **Load case 3** (pure axial, 40% medial condyle, 60% lateral condyle)

Table 6.8. Von Mises stress and risk ratio values for the volume of interest. Load case 3.

patient	von Mises (MPa)		risk ratio (%)			PVFB
number	mean	peak	mean	median	peak	(%)
1-B	1.028	19.6	64.1	56.5	470.6	21.2
1-DB	1.264	12.3	97.0	84.1	956.0	40.2
2	1.221	30.1	72.3	61.4	432.5	26.2
3	0.799	27.1	61.2	53.8	409.5	19.3
4	0.450	18.3	39.5	38.4	127.2	0.4

In this load case, the ranking in terms of the mean and median risk ratios, as well as the PVFB, is the same as that produced by load case 2 (section 6.2.2). In other words, patient 1-DB presents the highest values of the mean and median risk ratio, as well as PVFB, followed by patient 2, patient 1-B, patient 3 and patient 4 (Table 6.8). However, since in this load case the applied loads are weighted towards the lateral condyle and considering that the supporting bone on this region has generally lower mechanical properties (Table 6.3), the resultant risk ratios for patients 1, 2 and 3 are slightly higher that those found in load case 2 (Table 6.9). On the other hand, patient 4 shows slightly lower values of risk ratios as compared to load case 2. This behaviour was expected, as in patient 4 the medial compartment has lower mechanical properties than the lateral compartment (Table 6.3).

In Figure 6.9, it can be observed that the regions of high risk ratio concentrations are shifted towards the lateral side in all models. In this load case, higher stresses are found on the lateral side in both models of patient 1 (bonded and de-bonded). It should be noticed that like the rest of the load cases, the risk ratio distributions are similar in both bonded or de-bonded models of patient 1, with the difference that in the de-bonded model, risk ratio values are generally higher that in the bonded model. Both patient 2 and 3 show similar risk ratio distributions, as in both cases high values of this parameter are observed in the anterior-lateral and posterior-lateral regions of the resected surface. As mentioned above, patient 4 displays very small regions with risk ratios greater than 100% (regions in white), which are found on the lateral aspect of the resected surface of the proximal tibia.

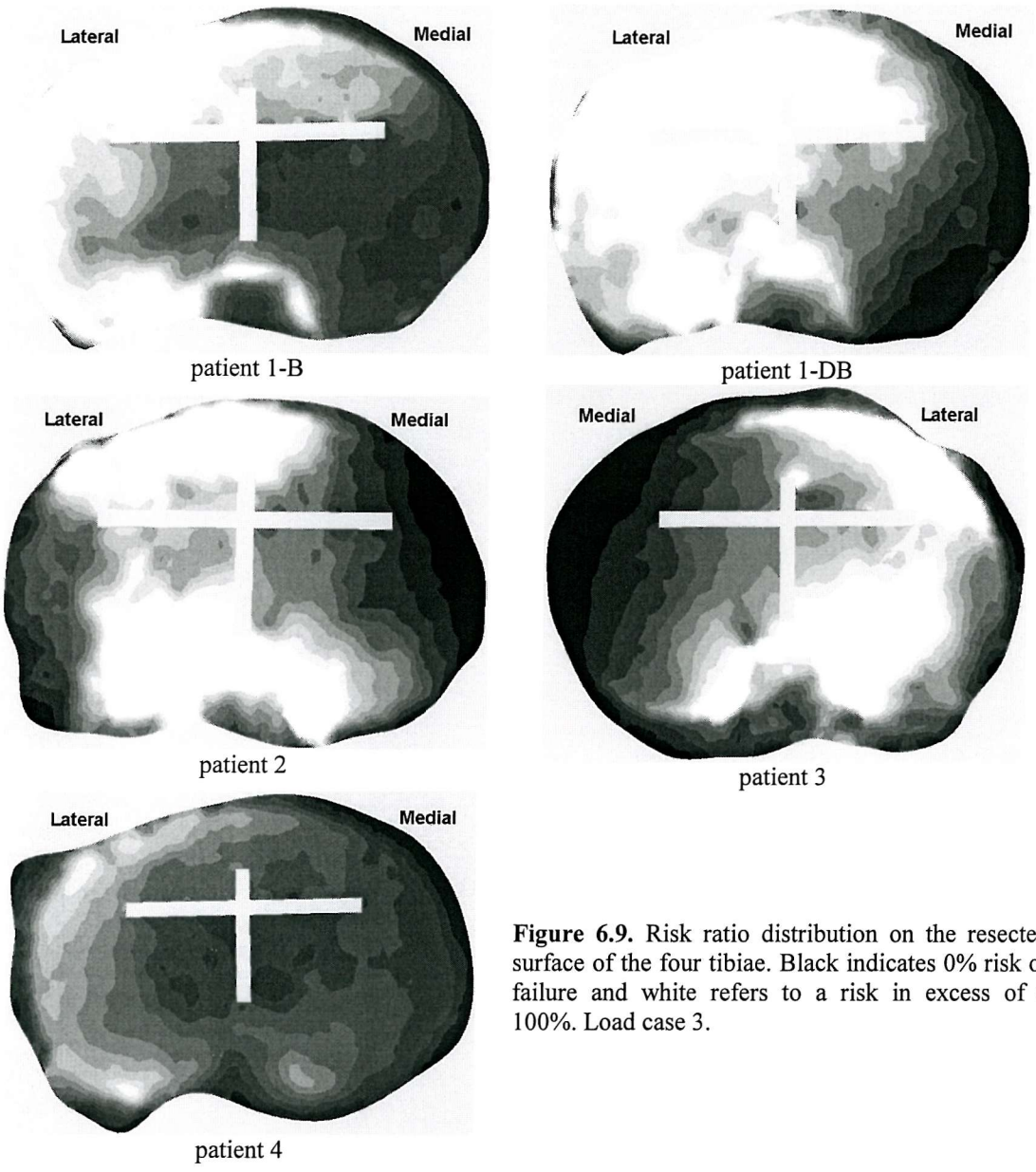

Figure 6.9. Risk ratio distribution on the resected surface of the four tibiae. Black indicates 0% risk of failure and white refers to a risk in excess of a 100%. Load case 3.

The contact areas resulting in this load case (Figure 6.10) show that there is virtually no lift-off in any of the three models analysed, hence all of the micromotion observed was in the form of sliding of the implant on the resected surface of the bone (Figure 6.11). There are only few elements around the anterior-medial aspect of patients 2 and 3 and posterior-medial aspect of patient 1, which separate from the prosthesis. Since the loads are weighted towards the lateral condyle, the medial side was expected to present the weakest contact (i.e. lowest contact pressure).

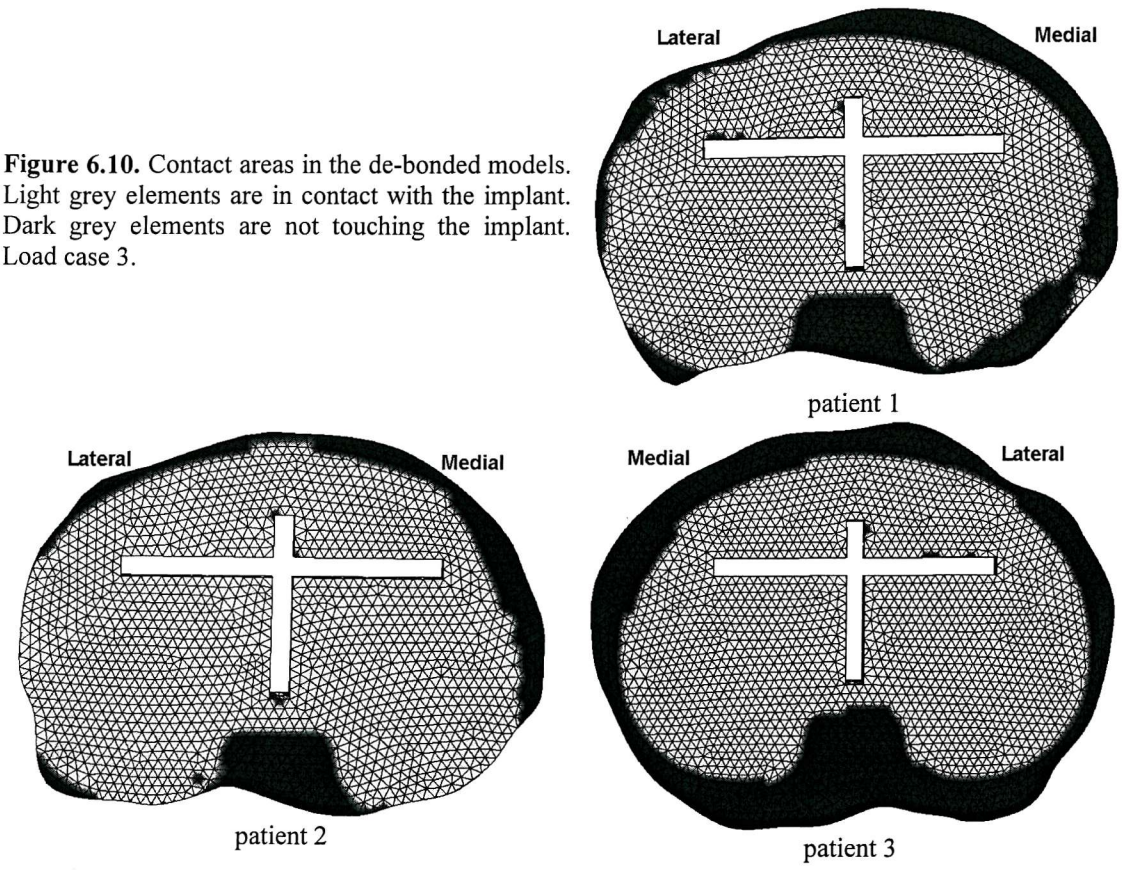

Figure 6.10. Contact areas in the de-bonded models. Light grey elements are in contact with the implant. Dark grey elements are not touching the implant. Load case 3.

In Figure 6.11, the micromotions observed in patient 1-DB are significantly higher than those observed in patients 2 and 3. Comparing load cases 2 and 3, the maximum micromotions produced with this load case are similar to those produced with load case 2 (Figure 6.8), except for the fact that some lift-off was observed in patient 1 with load case 2 and not with load case 3. The maximum values observed here where 0.55, 0.19 and 0.19 mm for patients 1, 2 and 3 respectively.

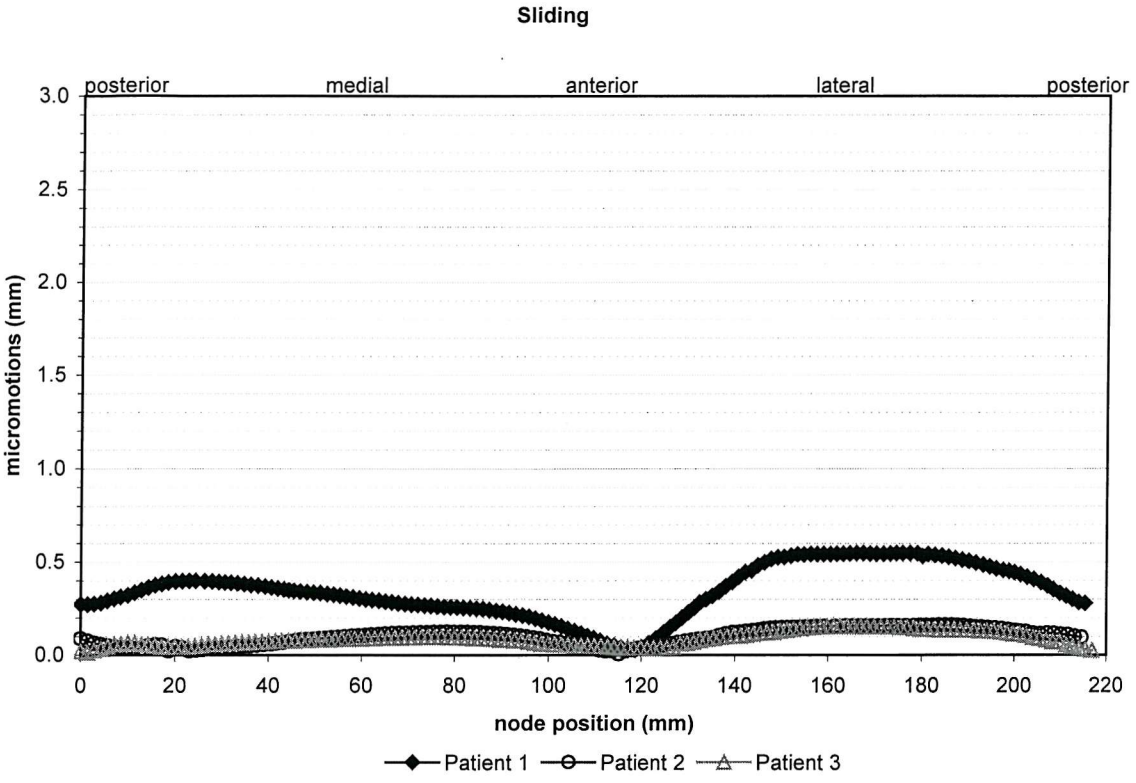

Figure 6.11. Relative motion between bone and implant calculated for the nodes located on the contour of the contact area between tibia and tibial plateau (pure sliding). Load Case 3.

6.2.4. **Load case 4** (pure axial, 100% lateral condyle)

Table 6.9. Von Mises stress and risk ratio values for the volume of interest. Load case 4.

patient	von Mises (MPa)		risk ratio (%)			PVFB
number	mean	peak	mean	median	peak	(%)
1-B	1.588	21.9	104.0	87.0	801.8	45.4
1-DB	2.578	84.4	205.6	171.3	3725.6	60.9
2	2.563	84.2	153.8	125.6	2083.7	57.5
3	1.615	56.9	122.2	91.7	2085.0	47.8
4	0.613	34.3	54.8	38.3	203.1	22.8

For this load case, the ranking between models changes with respect to the previous load cases analysed. The highest values of mean and peak risk ratio, as well as the PVFB, are again produced by patient 1-DB, followed by patient 2, patient 3 and patient 1-B (Table 6.9). Finally, patient 4 is again the model that produced the lowest values of risk ratio. In general, the risk ratio values generated with a lateral uni-condylar load case (load case 4) are greater than those produced by a medial uni-condylar load (load case 1). This result was also expected for the reasons explained in the previous section, which is that the supporting bone on this condyle is generally weaker than the bone on the medial condyle. This phenomenon is reflected in Figure 6.12, as the regions of high risk ratio observed here are by far the largest of all load cases analysed. In Figure 6.12, it can be observed that the whole of the lateral side of the resected surface presents risk ratios above 100%, even in patient 4, which is the model subjected to the smallest loads.

These extreme, unbalanced loading conditions produced an expected significant lift-off of the prosthesis on the lateral aspect, observed in all three de-bonded models (Figure 6.13). In Figure 6.14-a, it can be seen that the sliding micromotions of all three models are high. In particular patient 1, showed a maximum implant sliding of 1.86 mm, whereas this value was 1.22 mm and 0.88 mm for patients 2 and 3 respectively. In all three models, the maximum relative motion of the implant was observed on nodes located on the medial aspect of the implant. The values displayed in Figure 6.14-b, clearly show that significant lift-off was observed in the medial aspect of the implant in all models, reaching peak values of 2.88, 2.40 and 1.86 mm for patients 1, 2 and 3 respectively.

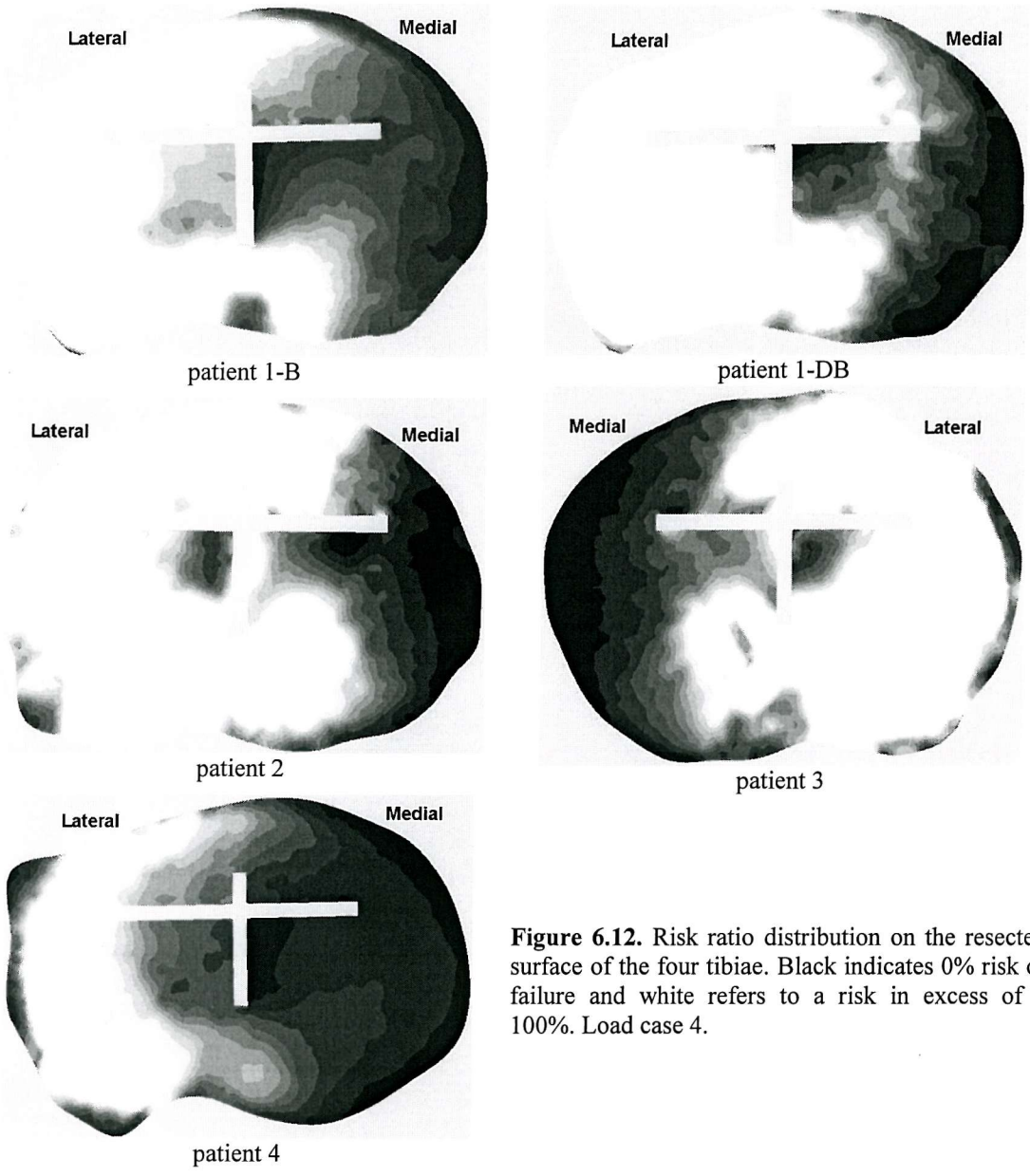

Figure 6.12. Risk ratio distribution on the resected surface of the four tibiae. Black indicates 0% risk of failure and white refers to a risk in excess of a 100%. Load case 4.

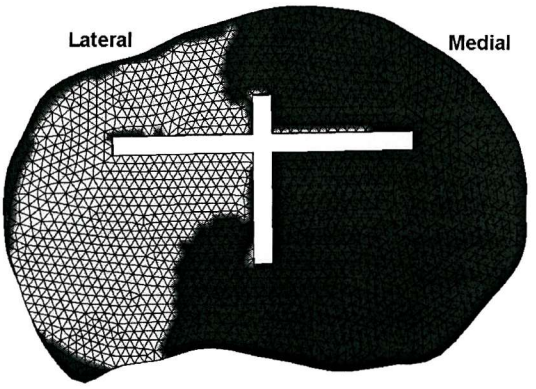

patient 1

Figure 6.13. Contact areas in the de-bonded models. Light grey elements are in contact with the implant. Dark grey elements are not touching the implant. Load case 4.

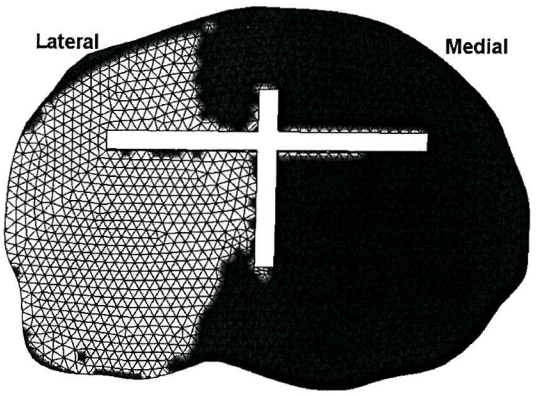

patient 2

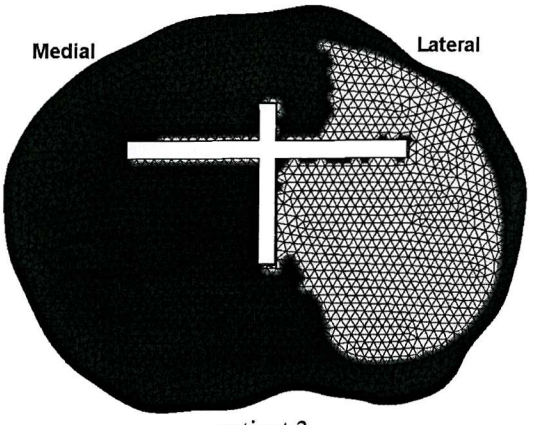

patient 3

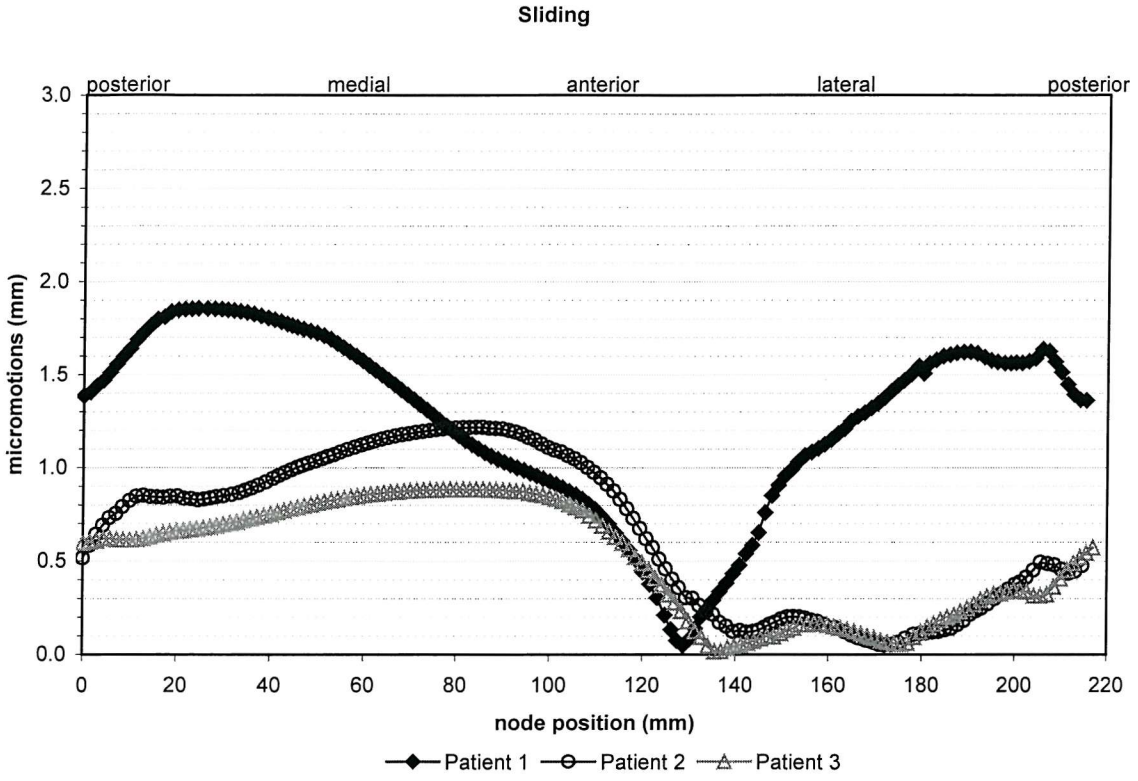

(a)

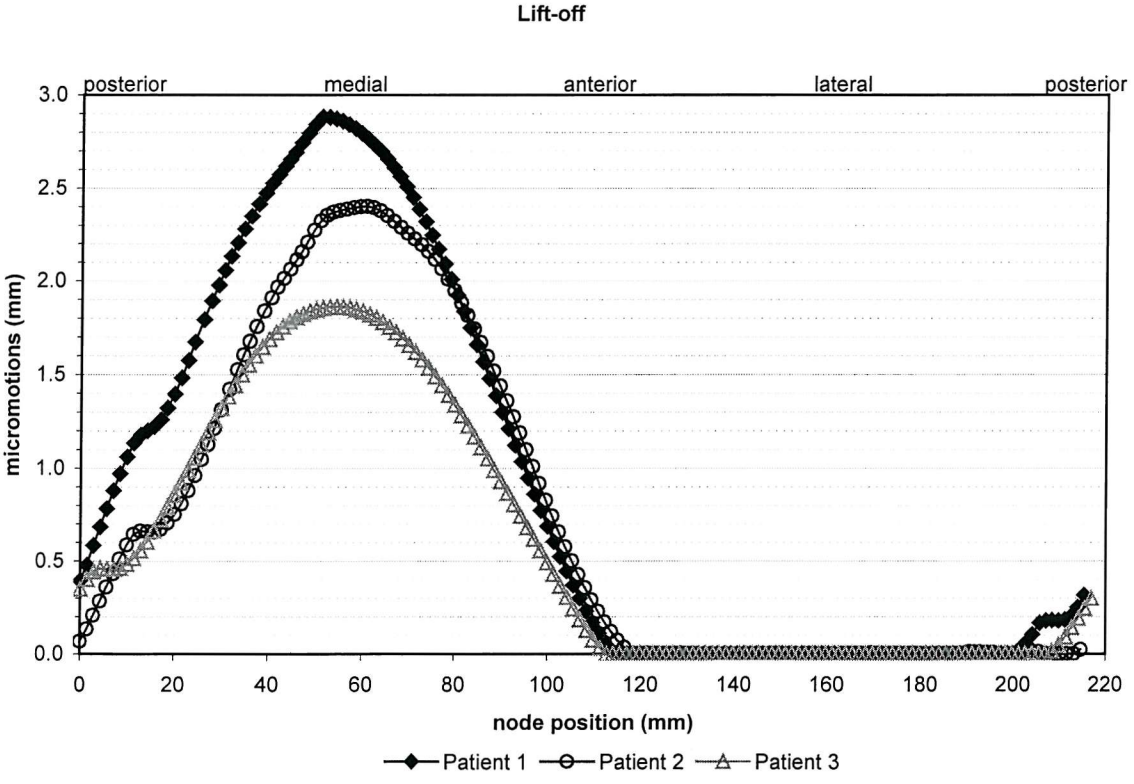

(b)

Figure 6.14. Relative motion between bone and implant calculated for the nodes located on the contour of the contact area between tibia and tibial plateau. (a) Sliding. (b) Lift off. Load Case 4.

6.2.5. Load case 5 (axial + torque + AP force, 60% medial, 40% lateral)

Table 6.10. Von Mises stress and risk ratio values for the volume of interest. Load case 5.

patient	von Mises (MPa)		risk ratio – R (%)			PVFB
number	mean	peak	mean	median	peak	(% Vol)
1-B	0.750	20.1	37.6	36.0	212.8	1.6
1-DB	1.106	16.1	68.6	61.8	873.4	19.9
2	0.997	34.1	50.3	43.6	528.0	7.5
3	0.689	26.9	44.5	38.8	615.9	5.5
4	0.365	12.4	30.4	30.1	91.8	0.0

The risk ratio distributions obtained here are similar to that obtained with load case 2, but in general the magnitude of risk ratio values is smaller in this case. The ranking between models is very similar to load case 2, as the maximum values of mean and median risk ratios, as well as the PVFB, are found again in patient 1-DB, followed by patient 2, patient 3, patient 1-B and finally finding the lowest values of these parameters in patient 4 (Table 6.10). The similarity with load case 2 can be appreciated when Figure 6.15 is compared with Figure 6.6, as the regions with high risk ratio concentrations are found in the same positions here for each model, with the difference that in general, the risk ratio values are lower (the grey tones in Figure 6.15 are darker). Similar to the risk ratio distribution obtained from load case 2, the maximum risk ratio values in patient 1 (both bonded and de-bonded models) are found around the anterior-lateral region of the tibia and around the region in contact with the posterior edge of the implant. In patients 2 and 3, maximum risk ratios were observed in the same regions (anterior-lateral and posterior). Patient 4 presents the highest risk ratios around the posterior-medial region of the resected surface of the tibia.

Additionally, in Figure 6.15, small regions of high risk ratio concentration can be seen around the medial, lateral and posterior ends of the "cross". The latter regions result from the torque applied in this load case, as they clearly appear to be a reaction to the internal torque included in this load case (Table 6.5). These regions can be clearly appreciated in the de-bonded models (patients 1-DB, patient 2 and patient 3) in Figure 6.15.

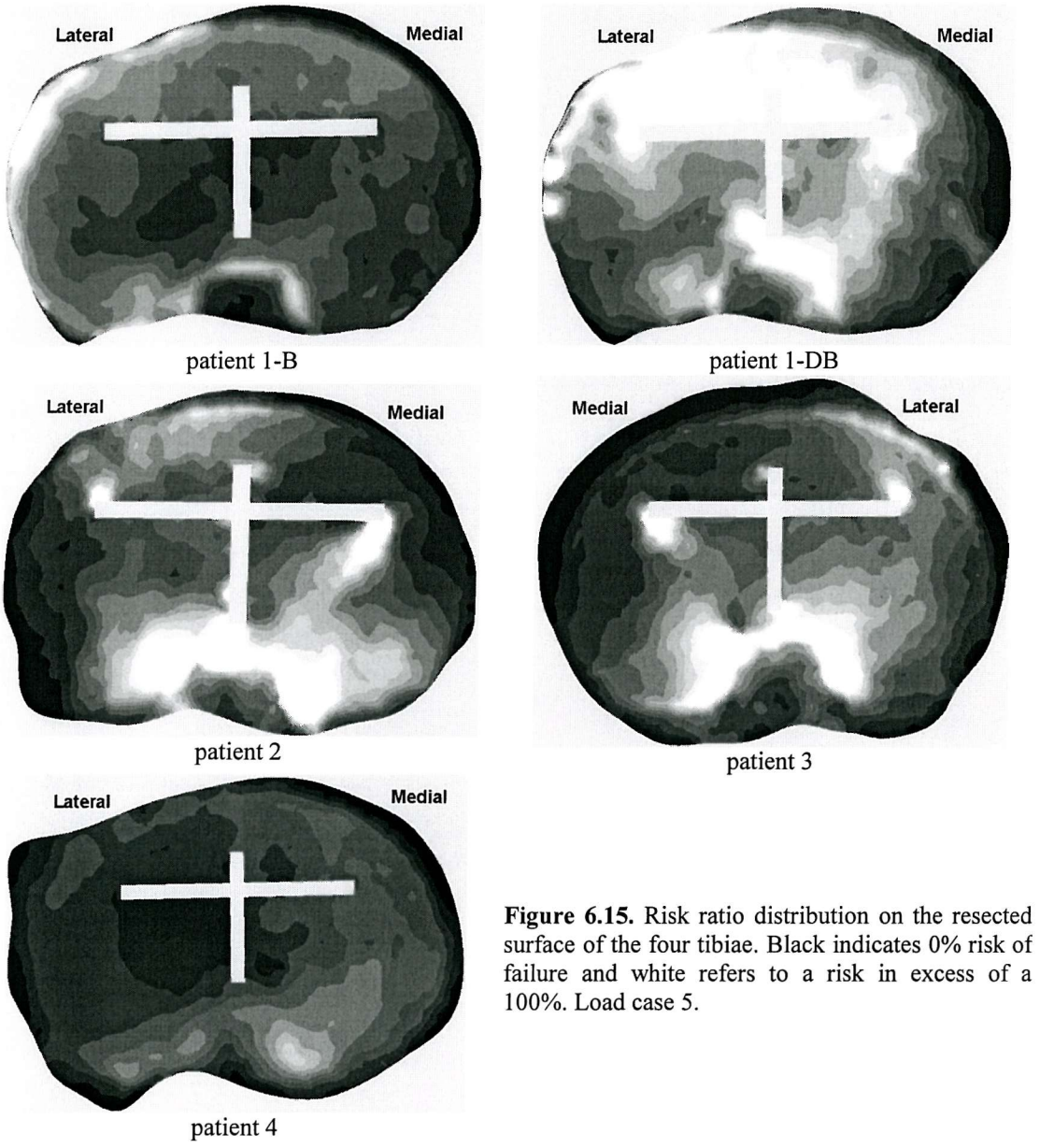

Figure 6.15. Risk ratio distribution on the resected surface of the four tibiae. Black indicates 0% risk of failure and white refers to a risk in excess of a 100%. Load case 5.

The contact areas observed in Figure 6.16 suggest that there was virtually no lift-off of the tibial component under these loading conditions. This result was expected, as the axial loads in this load case (which are believed to be responsible for the implant lift-off) are smaller than those of load case 2. With load case 2 there was only some lift-off in the posterior aspect of the implant for patient 1-DB, whereas patients 2 and 3 showed no lift-off either with load case 2 or 3.

The sliding micromotions observed in Figure 6.17-a are similar to those produced by load case 2, with maximum values of 0.53, 0.35 and 0.31 mm for patient 1-DB, patient 2 and patient 3. It can be seen that the torque included in this load case increases the

sliding of the implant with respect to load case 2 for patients 2 and 3, but not in patient 1. In patient 1, the maximum sliding was found in the lateral side, as opposed to the medial side in load case 2 (Figure 6.17 and Figure 6.8-a respectively). For this patient, the effect of the axial force seemed to dominate the sliding in the medial side (higher sliding with load case 2), whereas the effect of the torque was predominant in the lateral aspect, as higher sliding was observed on this side for load case 5 as compared to load case 2.

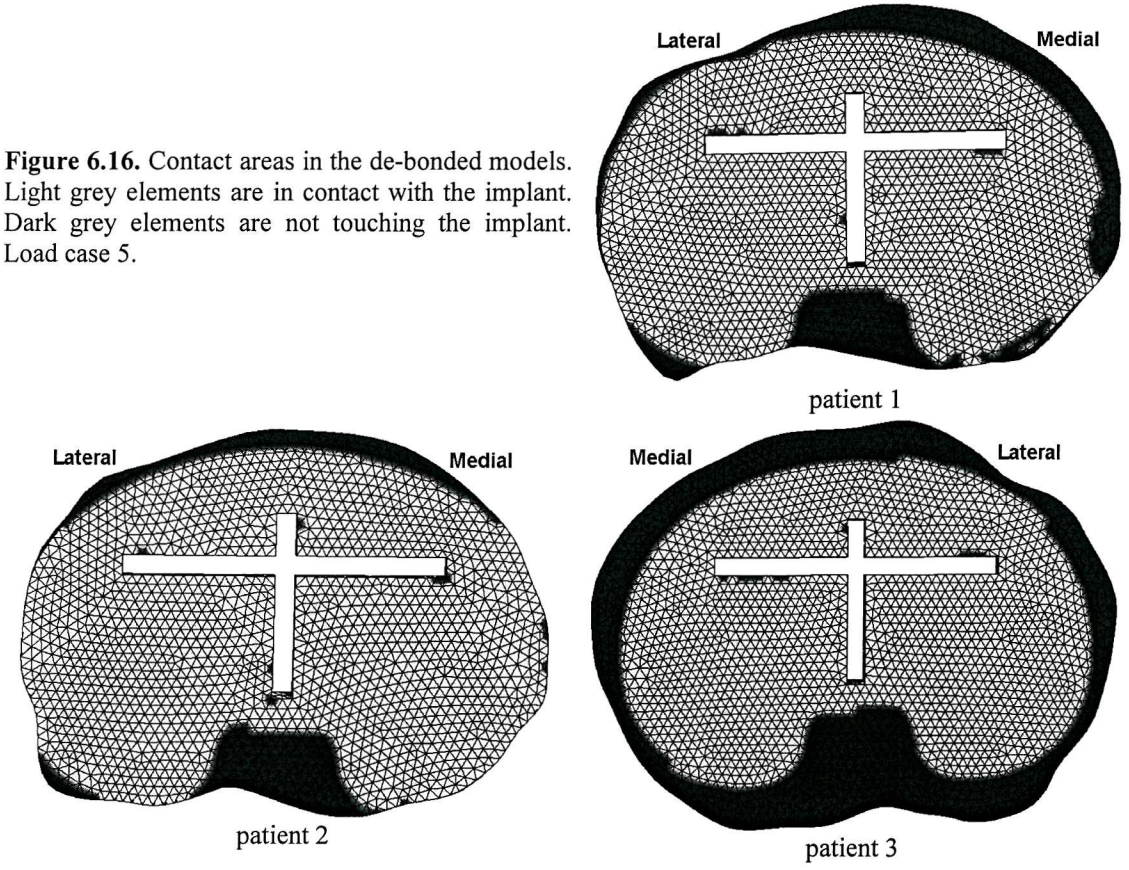

Figure 6.16. Contact areas in the de-bonded models. Light grey elements are in contact with the implant. Dark grey elements are not touching the implant. Load case 5.

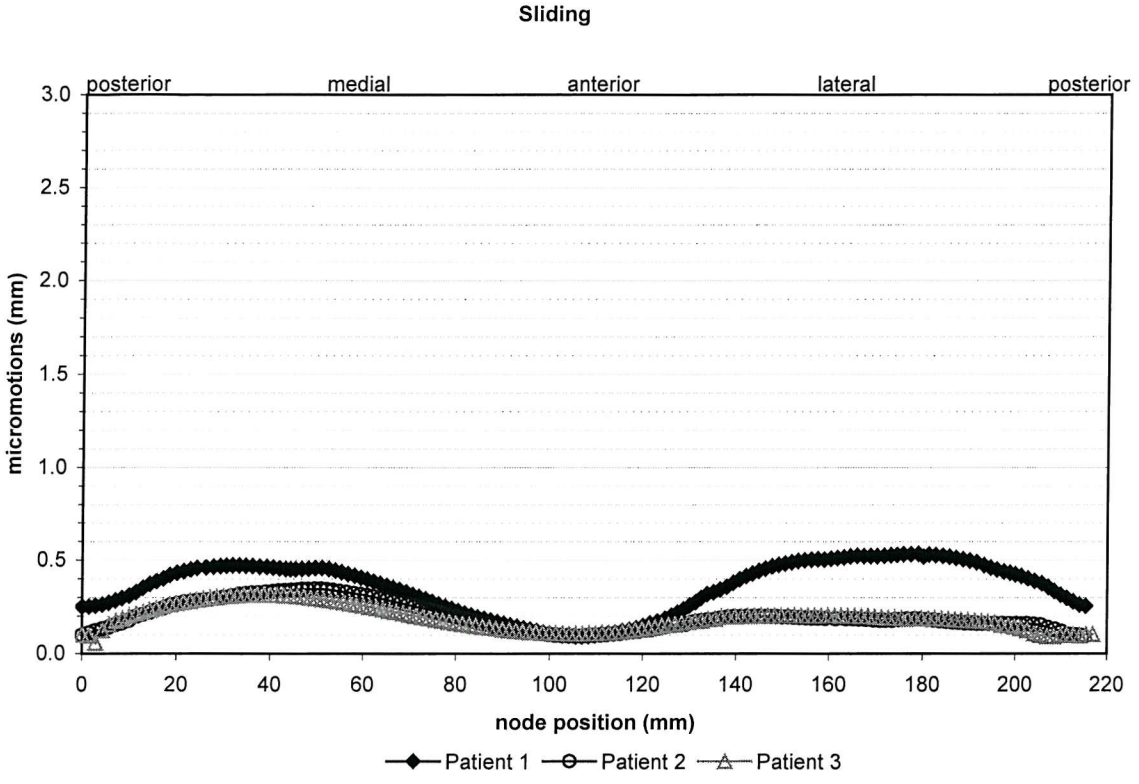

Figure 6.17. Relative motion between bone and implant calculated for the nodes located on the contour of the contact area between tibia and tibial plateau (pure sliding). Load Case 5.

6.2.6. Load case 6 (axial + torque + AP force, 100% medial)

Table 6.11. Von Mises stress and risk ratio values for the volume of interest. Load case 6.

patient	von Mises (MPa)		risk ratio (%)			PVFB
number	mean	peak	mean	median	peak	(%)
1-B	1.028	31.6	41.6	37.1	174.3	1.4
1-DB	1.731	30.8	78.7	71.3	862.7	37.8
2	1.137	48.8	42.5	31.2	754.9	12.3
3	0.813	32.5	36.7	27.0	544.7	4.8
4	0.601	17.4	49.6	51.0	138.5	4.3

The mean and median values of risk ratio found in Table 6.11 produced a similar ranking as that observed in load case 1, which consists of a medial uni-condylar axial force of a larger magnitude than the axial component applied in this load case. The highest value of medial risk ratio was found in patient 1-DB followed by patient 4, which seems to be particularly sensitive to unbalanced medial forces, as both medial uni-condylar load cases (load cases 1 and 6) produce significantly high risk ratios on this model. Patients 1 bonded and 2 presented virtually the same median risk ratio whereas patient 3 shows a lower value of this parameter. The median risk ratio produced nearly the same comparative ranking, with patient 1-DB showing the highest value, followed by patient 4, patient 1-B, patient 2 and patient 3 with the smallest median risk ratio. The PVFB produced a different ranking, as even though patient 1-DB was the model that presented the highest value, the second highest value of PVFB was found in patient 2, whereas patients 3 and 4 had nearly the same PVFB. With this load case, patient 1-B was the model that showed the lowest PVFB.

Also in this load case, the risk ratio distributions observed in Figure 6.18 were similar to those yielded with load case 1 (Figure 6.3), only with lower magnitudes. Both models of patient 1 (bonded and de-bonded) present the maximum risk ratios on the medial condyle. Patients 2, 3 and 4 showed the maximum values of risk ratio around the posterior part of the medial condyle. This type of distribution was expected as the axial load was on the medial side. Similarly to load case 5, the de-bonded models (patient 1-DB, patient 2 and patient 3) presented high risk ratio concentration zones at the ends of

the cross (Figure 6.18). This again is clearly the result of applying a toe-in torque on the implant.

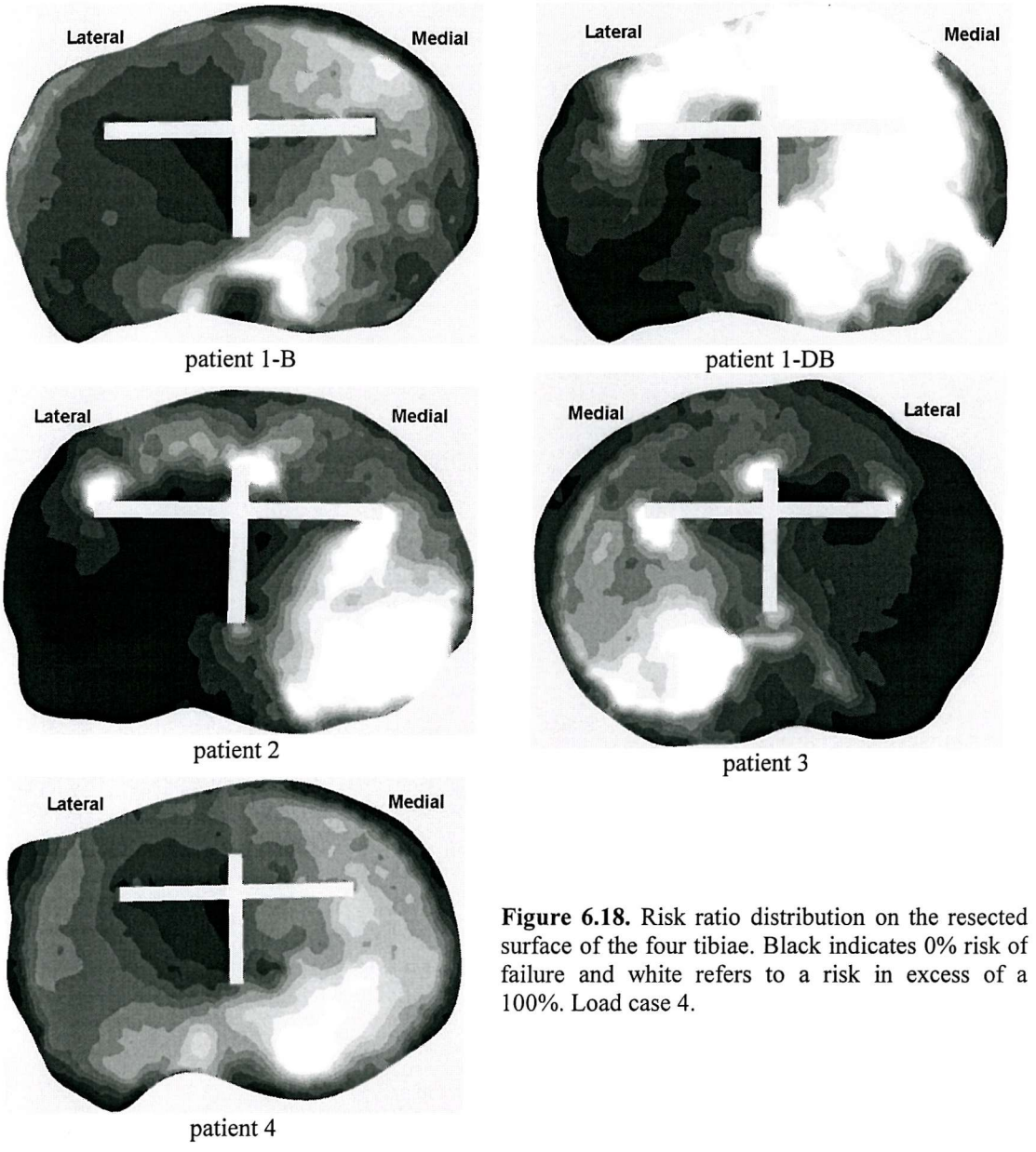

Figure 6.18. Risk ratio distribution on the resected surface of the four tibiae. Black indicates 0% risk of failure and white refers to a risk in excess of a 100%. Load case 4.

Even though the axial loads used in this load case are lower than those in load case 1, there is still a significant lateral lift-off of the implant (Figure 6.19 and Figure 6.20-b). The shape of the areas that stay in contact (light grey) are similar to those observed in load case 1 (Figure 6.4). Nevertheless, the values of lift-off of the implant were lower in this case as compared to load case 1 (Figure 6.20-b and Figure 6.5-b respectively), with maximum values of lateral lift-off of 1.01, 0.31 and 0.20 mm for patients 1, 2 and 3 respectively, for this load case. This phenomenon was also expected, as the lower axial

loads are likely to produce lower tilting of the implant. The sliding observed with this load case for patients 2 and 3 (with maximum values of 0.36 and 0.32 respectively) are slightly higher as compared to load case 1, whereas patient 1 shows significantly lower sliding values (maximum of 0.51 mm) than those produced by load case 1 (Figure 6.20-a and Figure 6.5-a for load cases 6 and 1 respectively). As noted in section 6.2.5, the sliding motion of the implant in patient 1 seems to be more sensitive to the magnitude of the axial load than the presence of torque. On the other hand, in patients 2 and 3 the torque included in this load case seemed to be dominant over the axial load in terms of sliding.

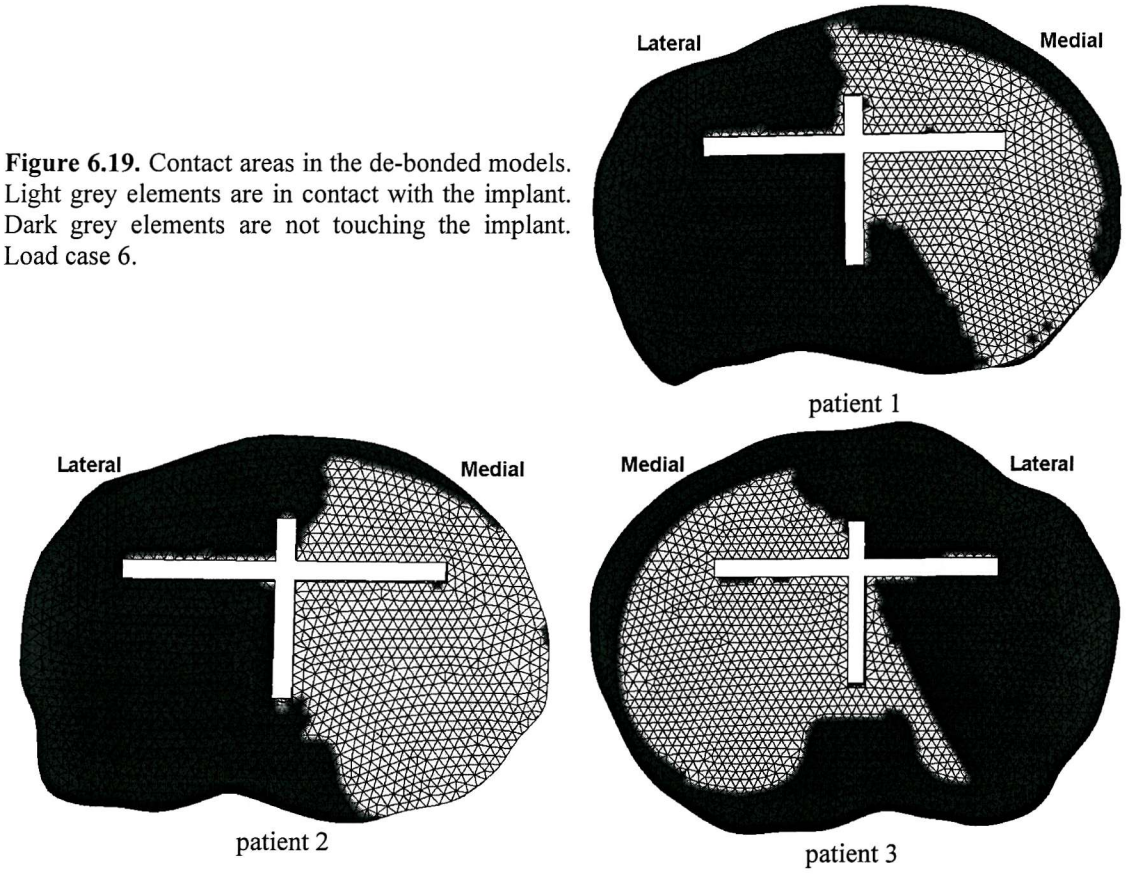

Figure 6.19. Contact areas in the de-bonded models. Light grey elements are in contact with the implant. Dark grey elements are not touching the implant. Load case 6.

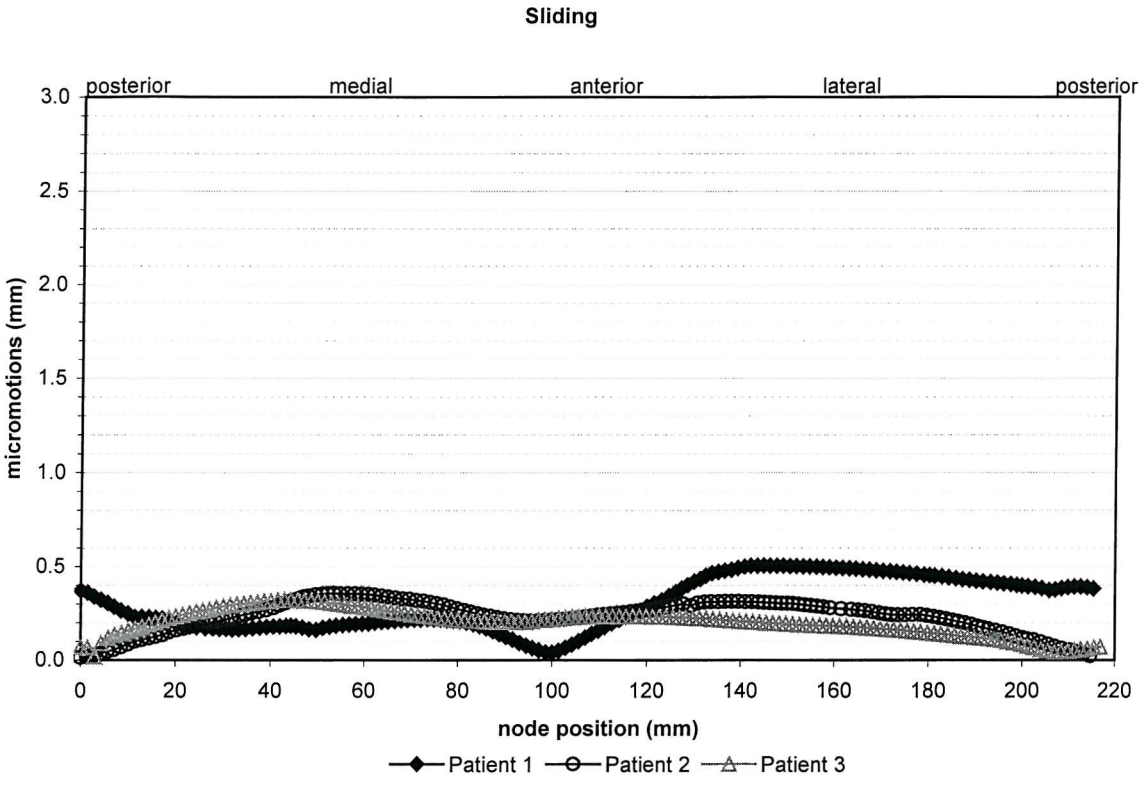

(a)

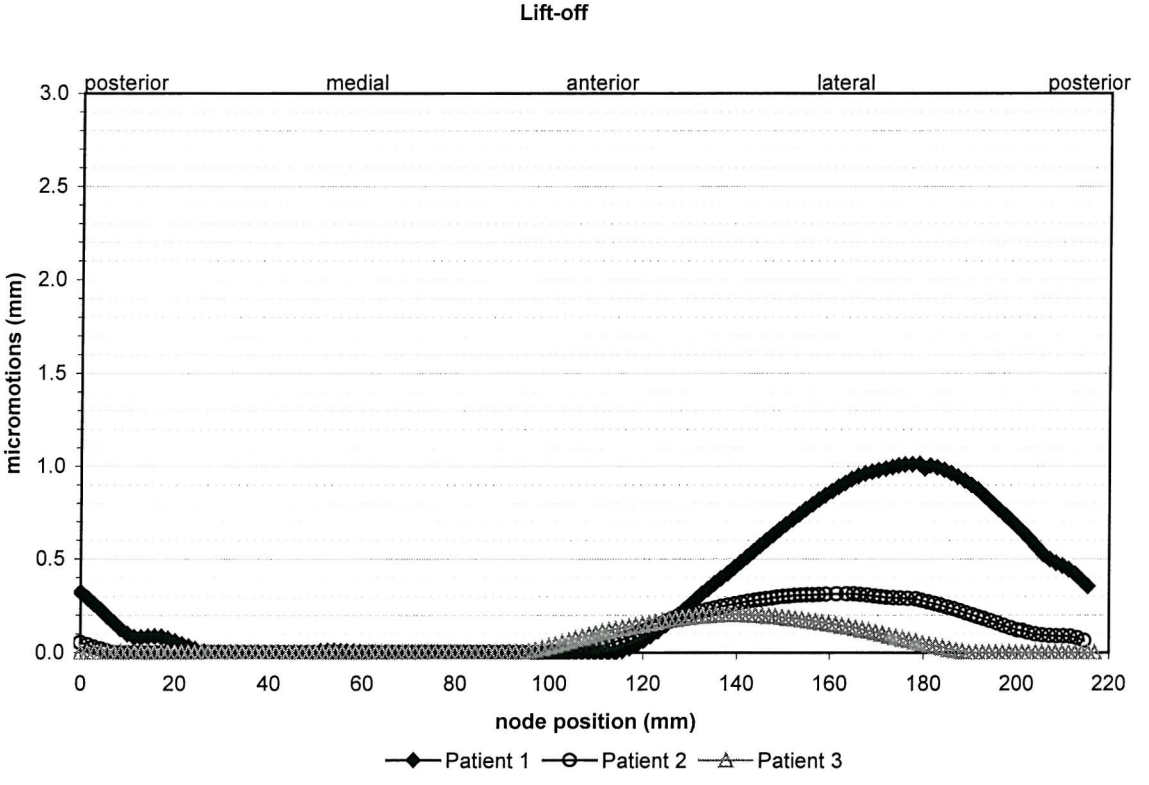

(b)

Figure 6.20. Relative motion between bone and implant calculated for the nodes located on the contour of the contact area between tibia and tibial plateau. (a) Sliding. (b) Lift off. Load Case 6.

6.2.7. Global results

Figures 6.21, 6.22 and 6.23 show the mean and median risk as well as the PVFB respectively, for all the models and all the load cases analysed. These graphs represent a summary of the results presented and commented on above (sections 6.2.1 to 6.2.6), giving an overview of the general condition of the five models for all the load cases. It should be noticed that in general, the highest risk ratios were observed in patient 1-DB, however, when the interface between implant and bone is modelled as bonded, the risk ratios drop significantly. The mean risk ratio of this model was lower than that of patient 2 when subjected to load cases 2, 3, 4, 5 and 6, but higher than that observed in patient 3 for load cases 1, 2, 3 and 6. On the other hand, if the PVFB is considered as a comparative parameter, patient 1-B showed lower values than patient 2 for all load cases, whereas these values were higher than those observed in patient 3 for load cases 1, 2 and 3. For all load cases, patient 2 presented higher values of risk ratio than patient 3. Patient 4 showed the lowest risk ratio levels for all but two load cases, with load cases 1 and 6 (medial uni-condylar loads) seeming to have a particularly negative effect on this model.

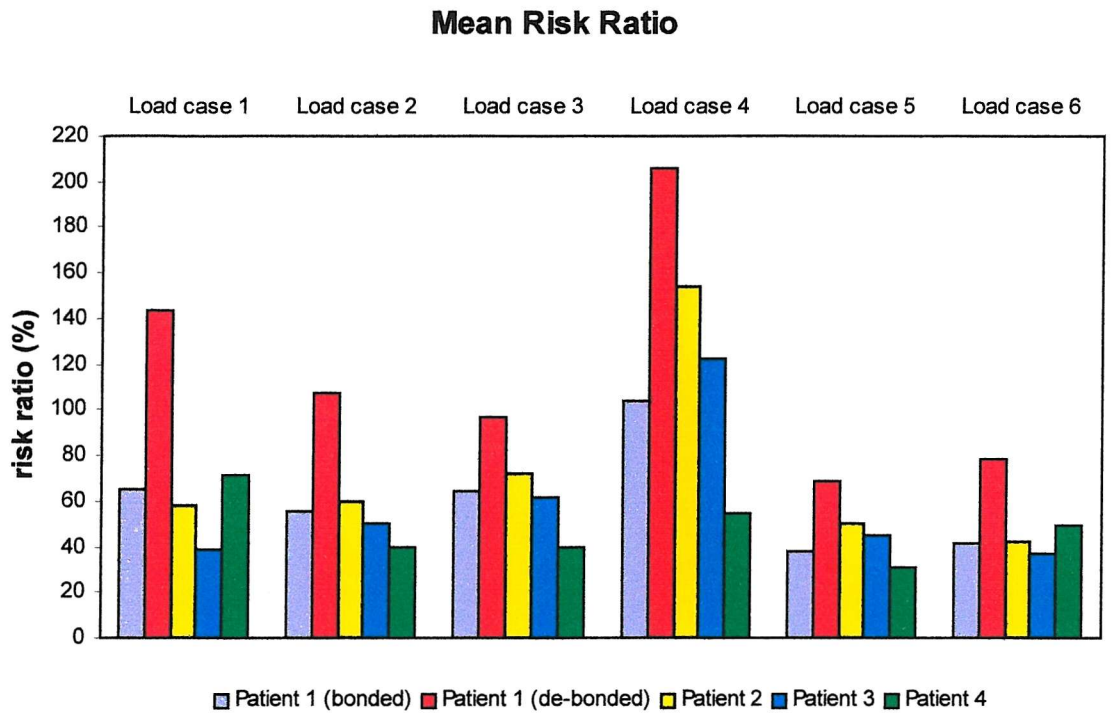

Figure 6.21. Mean value of risk ratio for the volume of interest.

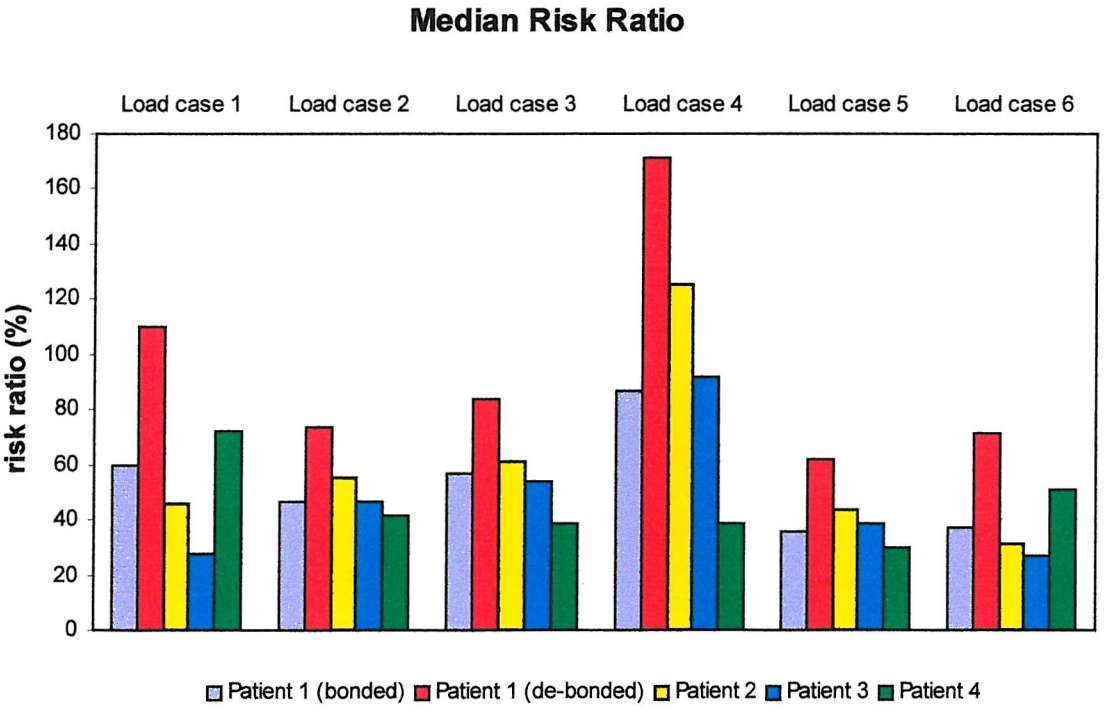

Figure 6.22. Median value of risk ratio for the volume of interest.

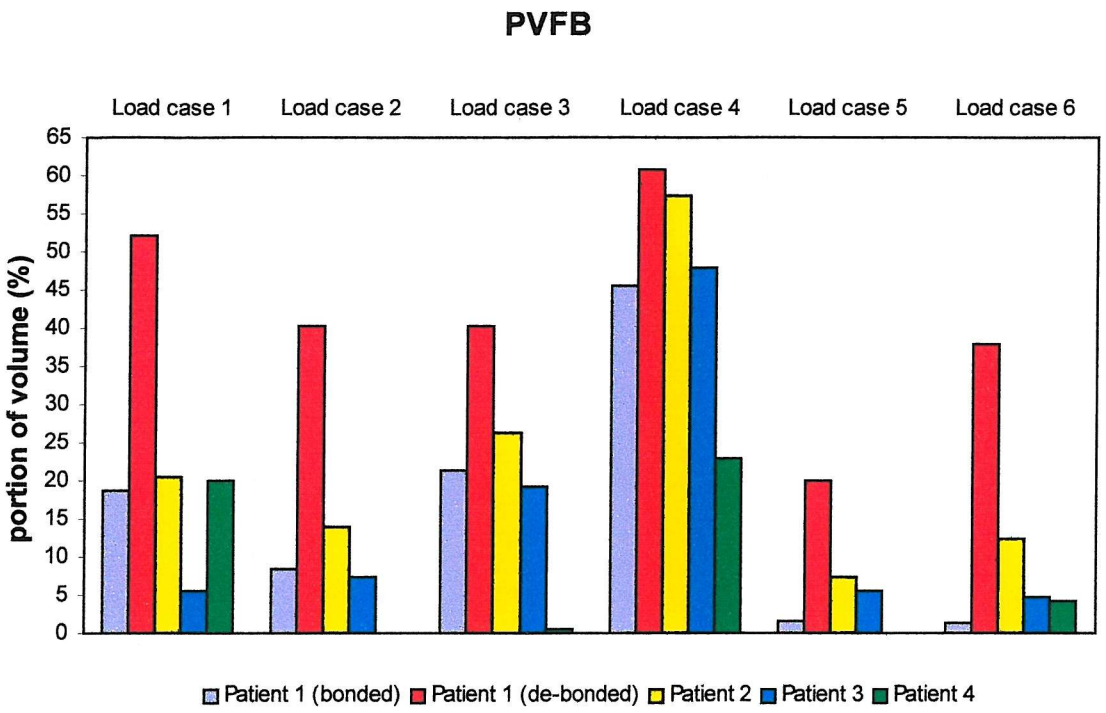

Figure 6.23. Percentage of the volume of interest with risk ratio exceeding 100% (PVFB) for all load cases.

6.2.8. Measured migrations

The four patients analysed here were followed after surgery by means of RSA (performed at University Hospital Lünd - Sweden). Table 6.12 shows the rotation angles, translations and the maximum total point motion (MTPM) of the four implants, measured six weeks, three months and one year after surgery (measurements corresponding to six weeks and three months were not obtained for patient 1 and 3 respectively).

The values presented in Table 6.12 indicate that the tibial components in patients 2 and 3 are very likely to undergo mechanical loosening, as both prostheses show substantial subsidence (2.1 and 3.8 mm respectively) and large rotation angles at one year after implantation, with MTPM values of 4.3 and 4.9 mm respectively). On the other hand, the prostheses implanted in patients 1 and 4, which were HA coated and cemented respectively (only underneath the tibial plateau), showed significantly lower

displacements and rotations as compared to patients 2 and 3 (MTPM of 1.1 and 0.6 mm for patients 1 and 4 respectively).

Table 6.12. Measured migrations

	time of measurement	rotations (deg) X	Y	Z	translations (mm) X	Y	Z	MTPM
Patient 1	6 weeks	—	—	—	—	—	—	—
	3 months	-0.8	0.4	0.3	-0.3	-0.2	-0.2	0.7
	1 year	-1.4	0.0	0.4	-0.2	-0.4	-0.6	1.1
Patient 2	6 weeks	-1.8	1.2	-1.0	0.0	-1.1	-0.5	2.2
	3 months	—	—	—	—	—	—	—
	1 year	-4.2	3.4	-1.2	-0.1	-2.1	-0.5	4.3
Patient 3	6 weeks	-1.9	-1.8	-1.6	0.5	-2.7	0.6	4.4
	3 months	-0.8	-1.8	-1.4	0.4	-3.3	0.5	3.8
	1 year	1.1	-2.0	-0.6	0.3	-3.8	1.3	4.9
Patient 4	6 weeks	0.4	0.0	-0.1	-0.1	-0.1	0.2	0.4
	3 months	0.3	0.1	-0.1	0.0	-0.1	0.0	0.3
	1 year	0.4	-0.2	-0.3	0.3	-0.2	0.3	0.6

The convention that RSA has adopted is that values are positive if:

Anterior aspect moves downwards (rotation about transverse x-axis)
Anterior aspect moves outwards or toe-out (rotation about vertical y-axis)
Medial aspect moves downwards (rotation about sagittal z-axis)

Prosthesis moves laterally (translation along transverse x-axis)
Prosthesis moves upwards (translation along vertical y-axis)
Prosthesis moves anteriorly (translation along sagittal z-axis)

Figure 6.24 displays a graphic summary of the information shown in Table 6.12. The arrows coloured in red represent the components of migration with excessive values. It can be observed that the red coloured arrows only appear on the figures corresponding to patients 2 and 3, as patients 1 and 4 showed low migration values. Patient 2 showed a significant subsidence (downward motion) of the implant, especially on the posterior side, producing a severe rotation around the transverse axis of 4.1 degrees. Additionally, the tibial component of this patient displayed a high external rotation angle (3.4 degrees) around the vertical axis. On the other hand, patient 3 did not show rotations so high as those observed in patient 2, with an angle around the transverse axis (sagittal view) of 1.1 degrees and around the vertical axis of 2.0 degrees (internally). Nevertheless, the translation values observed in this implant were significantly high, with a subsidence of 3.8 mm and an anterior motion of 1.3 mm.

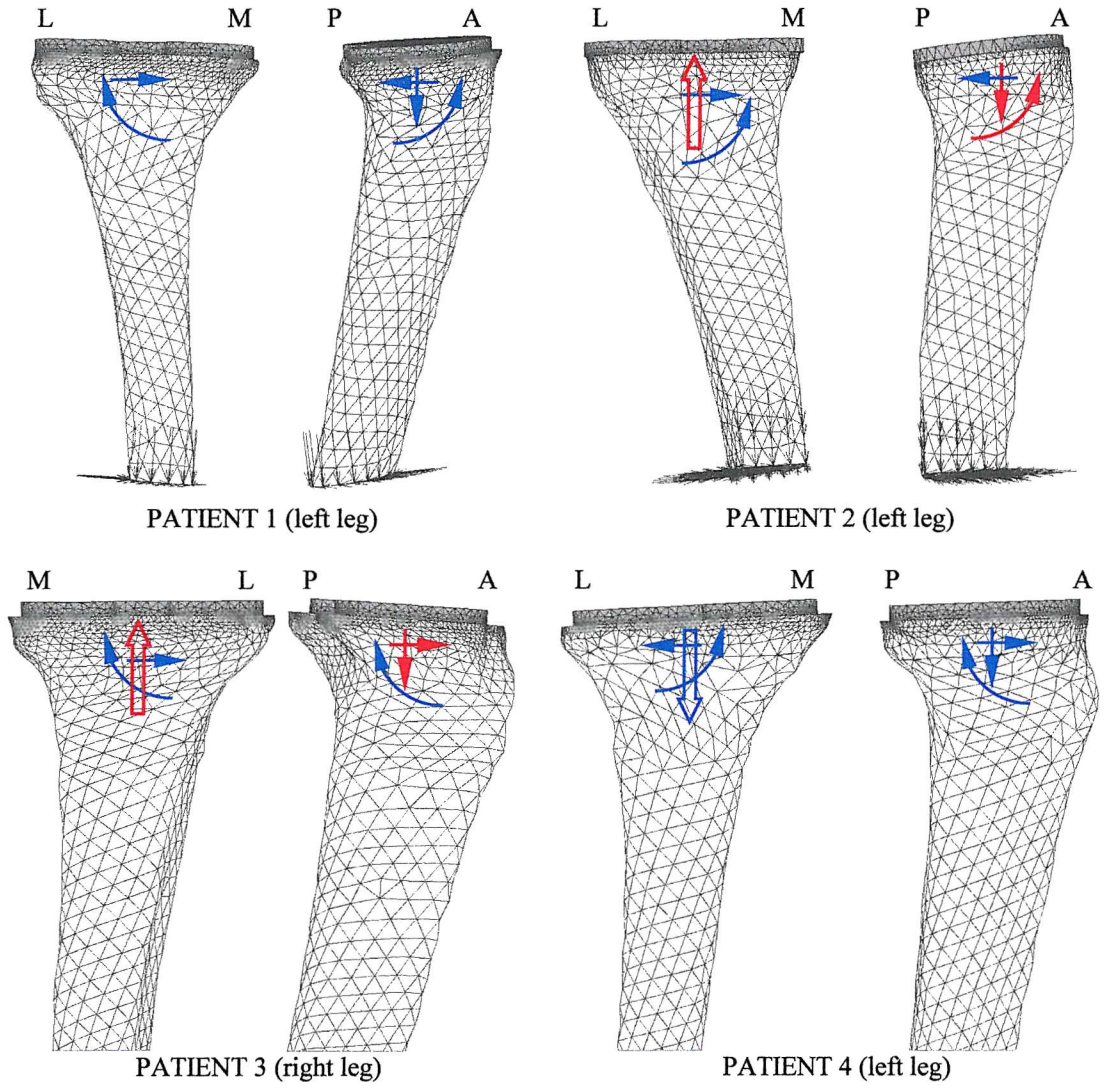

Figure 6.24. Direction of the migration of the implants at one year after surgery.

6.2.9. Comparison of results with RSA data

It should be noted that according to the migration values of the patients studied, which were obtained by means of RSA (Table 6.12) for a period of one year after surgery, a different load case for each patient is necessary to properly describe the real loads in each knee, as the migrations observed in all patients are different (Figure 6.24). In other words, it does not make sense to compare the risk ratios of all patients undergoing the same load case; instead, each patient should be modelled with a specific load case that

best suits it. Since it was out of the scope of this thesis to study the kinematics of the knees analysed here, out of the six load cases examined, one of them was selected as most appropriate for each patient, based on the migration data shown in Table 6.12 and Figure 6.24. Since the main difference between the load cases studied in this chapter was the distribution of axial forces between the medial and lateral condyles, special attention was paid to the varus-valgus rotation (Z axis in Table 6.12). Therefore, load case 2 (medial bi-condylar) was deemed as most appropriate for patient 1, as the implant rotated 0.4 degrees medially. Load case 3 (lateral bi-condylar) would suit patients 2, 3 and 4, as they showed rotations of 1.2, 0.6 and 0.3 degrees respectively, toward the lateral side. The unicondylar load cases were not selected for this analysis as they produced substantial tilts of the prostheses that were not observed in the RSA study of the patients. It should be mentioned that the selection of the most appropriate load case for each patient by this method is strongly dependant on the personal appreciation of the analyst and hence, it can be argued that different load cases may suit better the patients analysed here.

Based on the low migration values observed in patient 1 during the first post-operative year, which suggests that osseointegration has been achieved, it was considered that the bonded model of patient 1 (patient 1-B) would more accurately simulate the actual clinical situation. Therefore, the de-bonded model of patient 1 (patient 1-DB) was not considered for this part of the analysis.

Figure 6.25 displays the mean risk, median risk and PVFB for the load cases proposed above for each patient. It can be observed that the patients that show the highest likelihood of failure are patients 2 and 3. This fact correlates with the clinical results obtained from the one-year follow-up performed, as patients 2 and 3 show extremely high implant migration as compared to the other two patients included in this study. Patients 1 exhibited lower values of risk ratio followed by patient 4 which showed the lowest risk ratios in the proximal tibia as compared to the other three patients, hence suggesting that this patient is the least likely to present failure due to mechanical loosening. It can be observed that if either mean and median risk ratios are used as a comparative parameter, the values corresponding to patient 1 are only 11% and 15% lower respectively, suggesting that patient 1 may not be performing noticeably better that patient 3. Nonetheless, if the PVFB is used to compare the models, it can be clearly observed that patients 2 and 3 are performing significantly worse that patients 1 and 4,

as the amount of bone undergoing risk ratios higher than 100% in patient 3 is 127% higher than the value corresponding to patient 1. Patient 2 presents an even higher PVFB value than that of patient 3 whereas patient 4 shows a PVFB of only 0.4 % (the lowest of all models). The physical significance of this parameter should be emphasised, as it represents the proportion of supporting bone that is likely to fail.

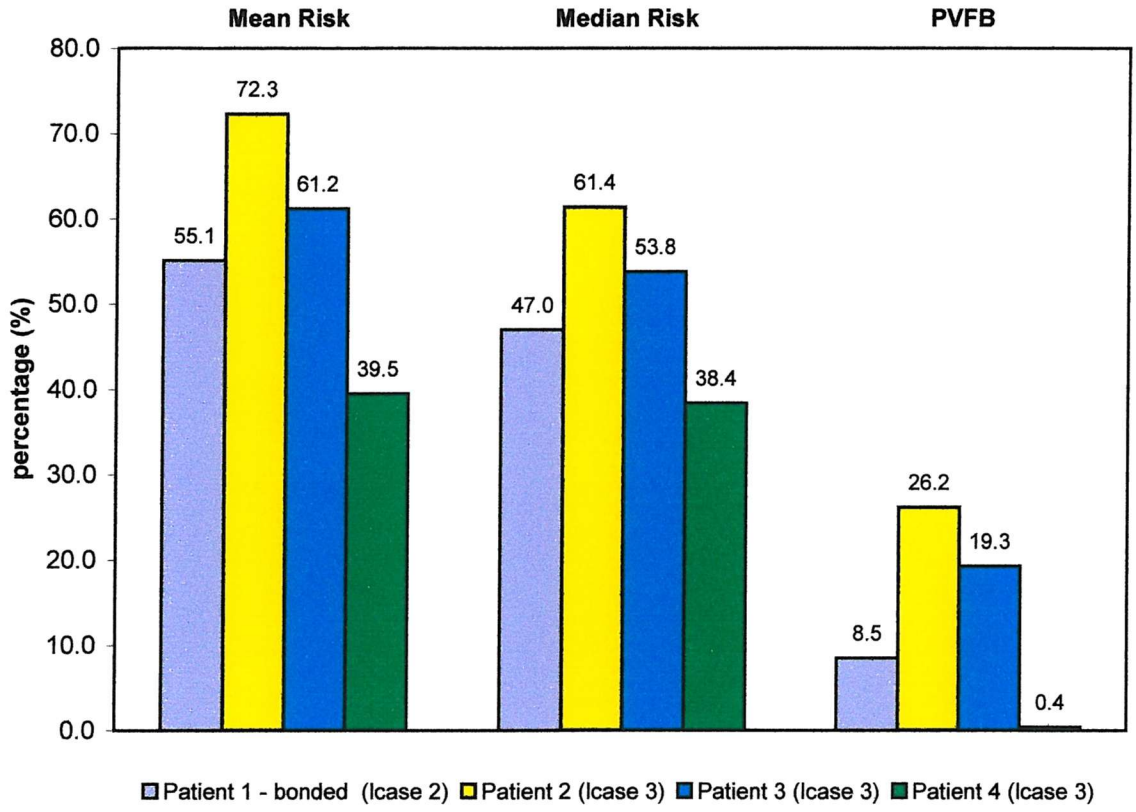

Figure 6.25. Mean risk ratio, median risk ratio and PVFB, using the most appropriate load case for each model.

The micromotion could not be included in this section as the bone-implant interfaces for patients 1 and 4 were modelled as perfectly bonded in the finite element study. In other words, the relative displacement between the two contact bodies (bone and implant) was restrained for these two models. However, it should be mentioned that the micromotion values observed in patient 1-DB were considerably higher than those seen in patients 2 and 3 with all six load cases (sections 6.2.1 to 6.2.6). Nonetheless, the migration data obtained for this patient indicate that the use of hydroxyapatite for this patient was crucial, as it seemed to have promoted osseointegration.

6.3. DISCUSSION

The purpose of this study was to evaluate the power of patient specific finite element analysis to predict tibial component migration. Data from four different patients were used in order to create the models of the proximal implanted tibia immediately after surgery (section 6.1). However, since there was no knowledge about the real loads present in the knees studied, six different load cases were analysed with the aim of comparing the risk of failure (risk ratio) produced in each model with each load case.

It was observed that in general, the risk ratio distribution on the resected surface of the tibia was the expected response to the load cases applied, as the maximum values of this parameter appeared underneath the location of the forces (e.g. maximum risk ratios are found in the medial condyle when the forces are unbalanced towards the medial side of the implant). It was also observed that lower risk ratios are obtained with medial load cases than with lateral forces. This phenomenon was to be expected as in general it has been found that the mechanical properties of the cancellous bone are higher in the medial compartment than in the lateral compartment [43] (Table 6.3). This situation was clearly seen in Figure 6.3, Figure 6.12 (load cases 1 and 4 respectively) and Figure 6.21, where it can be appreciated how the lateral uni-condylar force (load case 4) generated appreciable larger areas of risk ratios exceeding 100% (represented in white) than those generated by the medial uni-condylar load (load case 1). The PVFB was lower for load case 1 than load case 4 even in patient 4 where the mechanical properties of the medial compartment were slightly lower than those of the lateral compartment.

Another important finding of this study was the significant difference in risk ratio observed between the bonded and de-bonded models of patient 1, with the values corresponding to the de-bonded models being up to 120 % greater than those of the bonded models (load case 1). The results obtained for this patient suggest that shortly after surgery it is not advisable for the patient to fully load the prosthetic joint, as at that stage, excessive stresses on the supporting cancellous bone and substantial implant displacements may be generated. As a matter of fact, generally the post operative regime used for cementless devices is different than that used for cemented implants. Patients that have been implanted with cemented prostheses are allowed to fully load the prosthetic joint soon after surgery, whereas cementless implants undergo long periods of partial-weight bearing. This is done in order to improve the chance of

osseointegration by keeping the inducible displacements of the implant to a minimum. Previous studies have demonstrated that high values of micromotion of the tibial component make it difficult for osseointegration of the bone into the prosthesis to be achieved [13]. Furthermore, extreme values of risk ratio may cause the failure of portions of cancellous bone in some localised areas allowing the prosthesis to subside into the host bone. On the other hand, once good fixation has developed between the bone and the implant, the risk ratio values at the interface decreased considerably, decreasing the likelihood for the prosthesis to exhibit further migration. The migration values obtained for patient I suggest that good bonding was developed between the prosthesis and the supporting bone. It has been previously demonstrated that hydroxyapatite promotes faster and better osseointegration as compared to press-fit devices [13,113,115,121]. Previous RSA studies demonstrated that HA coated implants show lower and more stable migration than press-fit implants (see section 3.5.4.1), and when compared with cemented devices, HA coated prosthesis present equivalent clinical performance. The migration values observed for this implant (patient 1) are similar to the values reported in the literature for clinical successful cases (0.5–1.25 mm at one year after surgery – Table 3.1), suggesting that this prosthesis is likely to show little migration in the future [134].

The risk ratios obtained for patients 2 and 3 ranked as the highest when each model was analysed with its appropriate load case, assuming that good implant fixation has developed in patient 1 (Figure 6.25). This correlates with the migration data displayed in Table 6.12, which shows excessive values for these two patients, suggesting that they are both likely to become loose in the future. The migration values at one year observed for these two patients (MTPM of 4.3 and 4.9 mm) are clearly excessively high when compared with the normal values reported in the literature for uncemented devices (typically mean values of 1.0–2.0 mm at one year – Table 3.1), suggesting that the implants will become loose in the near future.

The results obtained for the cemented prosthesis (patient 4) correlate with the migration values corresponding to this patient, as they were the lowest of all four patients studied (Table 6.12). These results also correlate with previous clinical data, which reported low migration values for cemented implants in the first post-operative year (typically mean migration around 0.5–1.0 mm at one year – Table 3.1), as well as presenting low incidence of short term failure due to mechanical loosening [56]. It should be noted that

the reduced body weight of this patient (Table 6.5) does not necessarily mean that this is the reason why such low risk ratios were generated in this model, as this patient also had the poorest mechanical bone properties (Table 6.3), i.e. the lowest value of compressive strength of bone. These results also correlate with those of Taylor *et al.* [142] who found that out of the models that they analysed, the cemented device produced lower cancellous bone stresses as compared to uncemented implants.

It has been found that relative displacements greater than 150 μm produce a negative effect in terms of osseointegration [13]. In animal models, it has been observed that micromotions exceeding this value promote the formation of fibrous tissue at the bone-implant interface. In general, metal backed tibial components show inducible displacements in the order of 0.5-0.8 mm [63,148]. For most of the load cases studied here, the micromotions exceeded by far the values mentioned above. This indicates that in the patients modelled here, osseointegration could not be achieved naturally under these conditions, especially in patient 1-DB, which showed significantly higher values of micromotion. With these levels of micromotion, natural osseointegration is unlikely to happen. It is believed that hydroxyapatite was critical for patient 1, as the migration data corresponding to this patient suggests that osseointegration was achieved. All this indicates that hydroxyapatite may act as a drug that stimulates bone ingrowth even in an adverse mechanical environment. The above observations are in line with previous clinical studies that reported lower migration levels for HA coated implants as compared to plain porous devices (see section 3.5.4.1). On the other hand, even though patients 2 and 3 (press-fit implants) showed lower micromotions than patient 1-DB, the RSA data imply that osseointegration did not take place in those two patients, as they exhibited excessive migration values.

The results from this work could not be directly compared with other FE studies previously published, as none of them includes patient-specific data and in general, regions with uniform material properties are used to represent the bone instead (section 3.6). Nonetheless, it was observed that the risk ratio values obtained here are higher than those reported by Taylor *et al.* [142], who observed a maximum risk of failure of 149.3% in a model that included an uncemented all-polyethylene prosthesis, subjected to a medial uni-condylar load case. A similar load case was examined in this study (load case 1) and produced peak risk ratios as high as 1703.6% for patient 1-DB. Specifically,

load case 4 (lateral uni-condylar) produced extreme values of peak risk ratios, varying from 203.1% in patient 4 to 3725.6% in patient 1-DB, as well as generating significant proportions of bone with risk ratios exceeding 100% (Table 6.9). It is believed that these values are unlikely to occur in reality, suggesting that the method used to calculate the risk ratio overestimates this parameter. However, since the risk ratio was calculated in the same way throughout the study, the ranking order between the different models will not be affected by this error. It should be noticed that one way of reducing this problem would be to use a different correlation between compressive strength and apparent density that produces higher values of strength (hence, lower risk ratios).

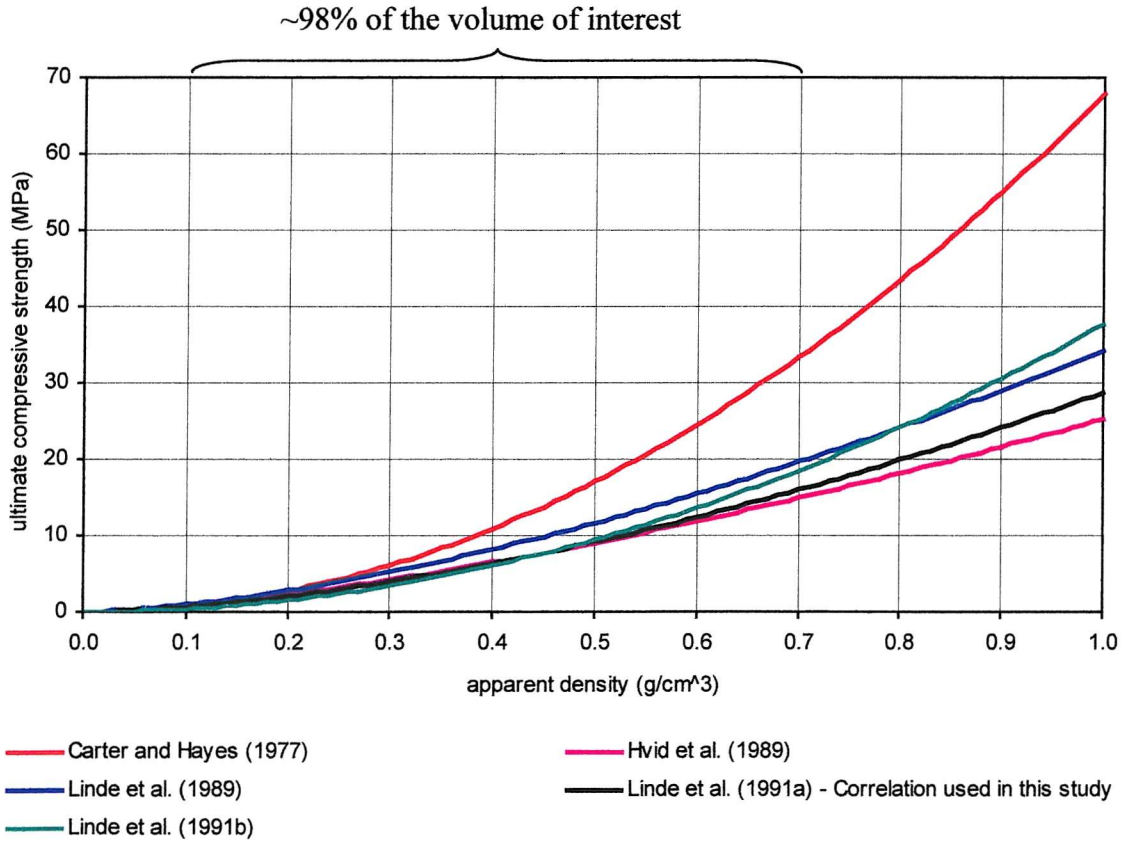

Figure 6.26. Correlations of compressive strength vs. apparent density in the proximal tibia (based on the values shown in Table 1.4)

In Figure 6.26, five different strength – density correlations obtained from the literature (Table 1.4) are plotted. It can be observed that the correlation proposed by Carter and Hayes [23] provides higher values of strength as compared to those produced by the

correlation used in this study (Linde *et al.* 1991a [94]). In the four models analysed here, the majority of the volume of interest displayed density values between 0.1 and 0.7 g/cm^3; and the difference between the correlations proposed by Cater and Hayes [23] and Linde *et al.* ranges from 6% (for a density of 0.1 g/cm^3) and 109 % (for a density of 0.7 g/cm^3). In other words, if the correlation proposed by Carter and Hayes [23] were used, the risk ratios would decrease according to the magnitude of the apparent density of the bone.

The migration process of an implant can be divided in two phases. During the initial phase, which is usually observed within the first six post-operative months, large implant migration values are thought to be a result of the prosthesis settling into necrotic cancellous bone (caused by a combination of thermal and mechanical damage during surgery). Despite having similar mechanical properties to living bone, necrotic bone has no regeneration capabilities, which are necessary to repair the damage caused by a foreign body (i.e. implant) [141]. During the second phase, lower rates of migration are observed. These rates are believed to be related to the ability of the supporting cancellous bone to repair the damage as it occurs. If repair is slower than damage, then it is likely that migration continues, though at slower rates than in phase one. Migration ceases only if the repair rates equal or exceed the rates of damage [141]. The high portions of bone exhibiting extreme values of risk ratio that were observed here in some load cases can be related to the initial phase of migration. In this study, the immediate postoperative situation was modelled, hence the remodelling capabilities of the bone were not accounted for in the analysis. The results support the above hypothesis, as in some places, the risk ratio values were sufficiently high to cause the static failure of the supporting cancellous bone, which would result in rapid early migration.

In addition to the points discussed above, this study has the following limitations:

- The cancellous bone was assumed to be isotropic, whereas it has been demonstrated to be transversely isotropic in the proximal tibia [8]. Rakotomanana *et al.* [119] observed that in their models, anisotropy has a significant effect at the bone-implant interface, as it overestimates the axial compressive stresses by up to 40%. Once more, this limitation is not thought to affect the comparative ranking order between models.

- There was absolutely no knowledge about the real kinematics or the loads occurring in the knees modelled in this study; hence, none of the load cases analysed here allow a direct correlation between the results from this study and the measured migrations. However, from section 6.2.9, it can be concluded that a coarsely approximated load case is already capable of predicting whether an implant is more or less likely to become loose as compared to another implant.

- The effect of friction at the bone-implant interface was not considered in any of the de-bonded models. Previous works [44,146] have demonstrated that when friction is included, the micromotions are significantly reduced, and so are the stresses at the interface. This suggests that the de-bonded models analysed here represent the worst case scenario, as the implant micromotion as well as the stresses (and consequently the risk ratios) at the interface between bone and implant are overestimated with respect to the real situation (where friction is present).

- An uncertainty of 1-2 mm and 1-2 degrees in the positioning of the implant with respect to the host bone was present in this study, due to the lack of clear land marks and the low quality of the post-operative X-rays, which were used to determine the tibial component location and orientation in the models.

There have been several finite element studies in biomechanics (including analyses on the hip, knee and other joints), however these have not been used to predict clinical performance. In particular, numerous finite element studies have been performed on the hip joint but in general, they have been used as a comparative tool, in which either the effects of different implants or loading conditions have been assessed within the same model or the results have been compared with in-vitro data, but none of these studies has shown any correlation with clinical data of the same patients used to generate the models.

As discussed in section 3.6, despite the fact that tibial component loosening is by far the major cause of total knee replacement failure (section 3.5.1), the use of finite element to analyse proximal implanted tibiae has been limited (see section 3.6). In general, the results obtained from the models, often based on the analysis of one single bone, have been assumed to be applicable to the whole patient population. A number of 2D studies

have been performed but only one of them used a heterogeneous material property distribution obtained from the QCT data [49]. However, apart from the limitations related to the analysis of a 3D structure by means of an approximated 2D model, they used only 17 different material properties throughout the bone. Additionally, they did not compare their results with any clinical post-operative data obtained from the patients used to build the models. The quality of the 3D models examined to date has been relatively poor. Most studies carried out comparative parametric analyses between their models and assume uniform regions of material properties. Only a few studies [83,146] have included a heterogeneous material property distribution within the bone, however these data were not obtained from specific patients but from experimental works, hence performing general studies and not patient-specific analyses. Kerner *et al.* [84] analysed patient-specific finite element models of the proximal implanted femurs to simulate bone remodelling and to predict bone resorption in correlation to stress shielding. Even though they validated their models with clinical data (densitometry measurements), this type of study does not predict the mechanical factors related to component loosening (stress, risk ratio, micromotions), as the stress shielding is not a predictor of clinical performance. Taylor *et al.* [142] performed a 3D finite element analysis of proximal implanted tibia models that included only a few regions of uniform material properties within the bone. They used the data obtained from a cadaveric specimen to build their models, and generalised their results to the whole patient population. They found a good correlation between the predicted cancellous bone stresses and clinical migration and survivorship data, as the implants generating the lowest cancellous bone stresses were those found to present the lowest migration and revision rates. Nonetheless, their models were not created from patient-specific data, hence they cannot be used as a predictor of implant loosening.

As opposed to all the finite element studies performed in general in biomechanics, the models analysed here simulate the mechanical situation of four specific patients and correlate the results from the models with the implant migrations measured during the first post-operative year. The fact that the models analysed here correlate with the RSA data obtained from the patients examined, implies that this type of analysis can potentially be used as a predictor of implant loosening, as RSA is the only clinical tool that has been demonstrated to be capable of predicting component loosening (see section 3.5.4).

In general, it can be concluded that as long as an appropriate load case is used in the models, patient-specific finite element analysis is capable of predicting the future behaviour of the tibial component by examining the risk ratios in the supporting cancellous bone. The results obtained from the finite element models analysed here produced a ranking order between patients that correlated well with the clinical data obtained for the same patients by means of RSA. As explained above, this is the first time that finite element models include patient-specific data of a number of patients, and that the results from them are compared with the migration data obtained from the patients examined. Furthermore, good correlation was observed between the results from the models and the clinical data, as the same ranking order between patients produced by the RSA measurements was observed in the finite element models.

6.4. CONCLUSIONS

The main conclusions drawn from this study are that:

- Extremely high values of risk ratio in the supporting bone of proximal implanted tibiae were observed when the interface between bone and implant was modelled as de-bonded and frictionless (simulating press-fit prostheses).
- A significant decrease of the risk ratios was observed in the bonded model of patient 1 (simulating an osseointegrated HA coated implant) as compared to its de-bonded counterpart.
- The cemented prosthesis produced the lowest values of risk ratio in the proximal tibia, as compared with the other three models analysed in this study.
- Good correlation was observed between the results from the finite element models of four patients and the migration data corresponding to the same patients.
- In general the use of the same load case for all the patients does not produce a valid comparison between patient-specific finite element models and clinical migration data. Instead, it is necessary to apply a load case that describes (at least in an approximate manner) the kinematics of the knee modelled.

- Even though the method used here is still not capable of predicting the clinical performance of a tibial component (as prior knowledge of the direction of implant migration is required), good correlation between patient-specific finite element analysis and migration data has been demonstrated for the first time.

CHAPTER 7
CONCLUDING COMMENTS AND RECOMMENDATIONS FOR FUTURE WORK

In general, this thesis is intended to study the cancellous bone stresses and risk ratios at the interface between the tibial component of a TKR and the host bone. Aseptic loosening of tibial trays has been found to be the major cause of failure of total knee replacements (section 3.5.1). It has been observed that prosthesis mal-alignment is closely related to tibial component loosening (section 3.5.2). In previous clinical investigations [56,134], a strong correlation between early migration and aseptic loosening of the tibial component has been found. Additionally, previous finite element analyses have suggested that cancellous bone stresses are correlated with implant migration (section 3.7).

Based on the above statements, as a first step, a finite element study was performed in order to analyse the influence of tibial component alignment upon the stresses on the resected surface of the tibia (Chapter 4). It was observed that the tibial component alignment noticeably affects the bone-implant stresses, as a difference of 93% in the average stresses on the medial compartment was observed between the models with a PA angle of 10^{o} valgus and 10^{o} varus respectively. The results obtained suggest that the more the tibial tray is tilted into valgus, the lower are the cancellous bone stresses at the bone-implant interface. Valgus angles as large as 10 degrees were examined. Even though the results suggest that this configuration would perform better (i.e. it produces lower stresses), the interrelation with other factors, such as joint kinematics, was not included in this study. Moreover, such excessive valgus angles are not recommended, as they are likely to have a negative effect on the kinematics of the joint, resulting in considerable problems in the clinical performance of the prosthesis. Despite the limitations of this study (section 4.3), the results from the finite element analysis correlate with clinical studies (section 3.5.2) that have reported that alignments of a few degrees of valgus show lower rates of failure due to component loosening. This correlation with clinical data further supports the hypothesis proposed by Taylor *et al.*

[142], who suggested that the cancellous bone stresses are correlated with the aseptic loosening of the tibial component.

Even though finite element modelling has been extensively used in biomechanics, to date, the studies performed on proximal implanted tibiae are very poor as compared to those performed on proximal implanted femurs (section 3.6). In Chapter 5, patient-specific finite element models of a proximal implanted tibia were analysed. The accuracy of the methods used here were extensively examined by performing an in-depth convergence study of the method of assigning material properties, as well as the mesh density, in order to evaluate the effect of these parameters on the predicted risk ratio within the cancellous bone. This study was used to define the appropriate characteristics that a finite element model of this specific problem should have. Firstly, the influence of the number of material properties assigned to the bone model and the manner in which they are distributed was analysed in section 5.3. It was concluded that convergence of the Young's modulus, the von Mises stress and the risk ratio on the resected surface of the tibia was reached for a number of material properties of around 500, using Young's modulus increments that increased logarithmically with the Young's modulus value assigned to each group. By using a logarithmic increment of the Young's modulus, a better discretisation of material properties was obtained in the proximal tibia (as it is basically composed of softer bone), whereas greater increments were used for high stiffness values (cortical bone). If a constant Young's modulus increment were used, a higher number of material groups would be needed to achieve convergence of the parameters of interest. Furthermore, for the region of interest (proximal tibia), it was observed that the maximum difference between the material property assigned to a group and the "real" value corresponding to the elements contained in that group is so small that it is very unlikely to have any significant effect on the predicted stress and risk ratio distributions. Hence, this method is considered equivalent to assigning a unique material property to each element.

Once an acceptable method for assigning the material properties was obtained, the next step of this study (section 5.4) was to examine the effect of the mesh density on the Young's modulus, von Mises stress and risk ratio for the same model studied in section 5.3. Convergence was assessed at both local and global levels, by examining the mean and peak values within a pre-defined volume. At the local level, convergence of the modulus was only achieved with a minimum element size of 1.0 mm. Convergence of

the stress and risk ratio was only reached once the modulus distribution had also converged. At the global level, the mean modulus values and general distribution of the modulus seemed to have converged for all mesh densities. Nevertheless, an element size of 1.4 mm or smaller was required to reach convergence of the stress and risk ratios. Hence, it was observed that convergence at a local level requires a finer mesh than convergence at a global level. This emphasizes the importance of performing appropriate convergence checks for each type of analysis. In other words, if nodal values are examined, a convergence analysis performed at a global level (e.g. strain energy or mean von Mises stress) may not be adequate. The CT scan data used here included a pixel size of 0.468 x 0.468 mm and a separation between slices of 1 mm in the proximal region of the tibia. Adequate discretisation of the material property distribution was obtained with element sizes of 1 or 1.4 mm, which is comparable to the slice thickness. With grater element sizes, the mesh was unable to capture steep gradients of Young's modulus. This was thought to be caused by the averaging of pixel intensity values performed during the assignment of material properties to the elements. Based on this, it is recommended the use of element sizes similar to the maximum voxel dimension (in this case the voxel size was 0.468 x 0.468 x 1 mm) of the CT data. The main conclusion drawn here was that accurate assignment of the material properties is critical in achieving convergence of other parameters such as stress and risk ratio. The errors produced by using a non-converged material property distribution, are reflected and even magnified in other parameters of interest, such as the von Mises stress and risk ratio. There has been found no evidence of previous studies discussing the effect that the mesh density has upon the material property distribution, as was demonstrated here.

Based on the findings reported by Taylor *et al.* [142] and Fukuoka *et al.* [47], the last part of this thesis (chapter 6) consisted of assessing the power of finite element analysis to predict implant loosening. For this purpose, models of proximal implanted tibiae were created based on the results obtained from the convergence study performed in chapter 5 and including patient specific data (body weight, material properties and component alignment) obtained from four patients that were followed-up using RSA for a period of one year after implantation. The von Mises stresses and risk ratios in the proximal end of the implanted tibia, as well as implant micromotions were calculated for each patient, subjected to six different loading conditions. The results from the study were compared with the migration over the first post-operative year obtained for each patient by means

of RSA (study performed at University Hospital Lünd – Sweden). Different fixation methods were used between the tibial component and the host bone. The prosthesis used for patient 1 was hydroxyapatite coated underneath the tibial plateau only (the stem was not HA coated), in patient 2 and 3 the prostheses were press-fitted into the tibiae and in patient 4 the tibial component was cemented to the bone (no cement was used around the stem). Two different models were analysed for patient 1, in order to simulate the immediate post-operative situation (de-bonded model) and the condition in which osseointegration had occurred between bone an implant (bonded model).

It was observed that in general, lower risk ratios were obtained with medial load cases than with lateral forces. This phenomenon was to be expected as it has been found that the mechanical properties of the cancellous bone are generally higher in the medial compartment than in the lateral compartment [43]. This situation was clearly seen here, as the lateral uni-condylar load case generated appreciable larger volumes of bone experiencing risk ratios exceeding 100% than those generated by the medial uni-condylar load.

Considerable difference in the risk ratios was observed between the bonded and de-bonded models of patient 1, as the values of risk ratio of the de-bonded model were up to 120% higher than those corresponding to the bonded model (lad case 1). This suggests that shortly after surgery (and until osseointegration is achieved), the patient should not fully load the operated limb, as under these conditions, excessive stresses and micromotions can be generated in the supporting cancellous bone. It has been previously demonstrated that excessive values of micromotions inhibit the growth of the bone onto the implant (osseointegration). Additionally, high values of risk ratio may result in the failure of some localised areas of the supporting bone, allowing the prosthesis to subside into the supporting bone. On the other hand, once good bonding between bone and implant is achieved, the risk ratio values at the interface are significantly lower, resulting in the prosthesis being less likely to experience high migration. Clinical measurements (RSA) performed on this patient suggest that osseointegration has been achieved, as the tibial component shows migration values comparable to other successful HA coated implants previously reported [13,113,115,121], suggesting that this prosthesis is likely to show little migration in the future [134].

When each patient was analysed with its appropriate load case, patients 2 and 3 presented the highest values of risk ratio. This correlates with the clinical migration data obtained for these two patients, which show excessively high values as compared to successful press-fit devices previously reported, suggesting that these two tibial components are likely to become loose in the near future.

Patient 4 (cemented implant) showed the lowest values of risk ratio as compared to the other three patients studied. This correlates with the RSA data obtained for this patient over the first post-operative year, as it produced the lowest migration of all patients included in this study. Additionally, the results from this patient are in line with previously reported clinical data, which showed low migration values for cemented prostheses during the first year after surgery, as well as low incidence of short-term mechanical loosening. It should be mentioned that the low risk ratio values observed for this patient were not a direct result of the low magnitude of the load supported by the implant (due to the low body weight of patient 4), as the mechanical properties of the supporting bone also were considerably lower than those of the other three patients (i.e. lower values of Young's modulus and compressive strength). The results obtained for patient 4 also correlate with a previous finite element analysis performed by Taylor *et al.* [142], who observed that the cemented implant included in their study exhibited lower cancellous bone stresses than the uncemented devices.

Despite the fact that tibial component loosening is the major cause of implant loosening, finite element studies of the proximal implanted tibia are few and coarse as compared to those performed on the proximal implanted femur (hip prostheses). In general, previous finite element studies of the implanted tibia have been used to compare the results with similar models in order to assess the effect of parameters of interest, such as component design, fixation method and friction at the bone-implant interface. Nevertheless, the results have usually been obtained for specific models and assumed to be applicable in general to the whole patient population. The geometries and material properties assigned to the models have usually been acquired from experimental data obtained from healthy bone samples or from one single patient, but the possibility that the results obtained from these models may only be valid for the patients or the bone samples used to generate the models has never been discussed. Clinical studies have demonstrated that implant designs, component alignment, and fixation methods do not produce the same effects in all patients, hence suggesting that the results obtained from finite

element models may not be applicable in general for all patients. In this study, each model was entirely created from data obtained from four specific patient, and the results from the finite element analysis were compared with clinical data corresponding to the same patients.

In particular, the material property assignment observed in previous FE models has been very poor, as most studies assume a few regions of uniform material properties within the bone, when in reality, it is well know that bone presents a heterogeneous material property distribution. Only few studies [83,146] have included heterogeneous material property distributions within the bone, however these data were not obtained from specific patients but from experimental works, hence resulting in general studies and not patient-specific analyses. Huiskes *et al.* [67] analysed patient-specific finite element models of the proximal implanted femurs to simulate bone remodelling and to predict bone resorption in correlation to stress shielding. Even though they validated their models with clinical data (densitometry measurements), stress shielding has yet to be demonstrated to be correlated to component loosening (stress, risk ratio, micromotions). Taylor *et al.* [142] performed a 3D finite element analysis of a proximal implanted tibia created from data obtained from one specific patient, but their models included only five regions of uniform material properties within the bone. They found a good correlation between the predicted cancellous bone stresses and the clinical data, as the implants generating the lowest cancellous bone stresses are those found to present the lowest migration and revision rates. Nonetheless, their models were not created in full from patient-specific data, as they did not consider the material properties, body weight or implant alignment of the patient, hence they cannot be used as a predictor of implant loosening. Moreover, they compared the results from one model to a larger patient population (previous clinical data).

On the other hand, the models analysed here simulate the mechanical characteristics of four patients and correlate the results from the finite element analysis with the migration of the same four patients. RSA is the only clinical tool that has been demonstrated to be capable of predicting component loosening (see section 3.5.4), hence the correlation found between the models and the RSA data suggests that this type of analysis can be used as a predictor of implant loosening.

Finally, it was concluded that as long as an appropriate load case (according to the kinematics of the specific knee) is used in the models, patient-specific finite element analysis is capable of predicting the future behaviour of tibial components by examining the risk ratios in the supporting cancellous bone. The results obtained from the finite element models analysed here produced a ranking order between patients that correlated well with the clinical data obtained for the same patients by means of RSA. This is the first time that finite element models of the proximal implanted tibia include patient-specific data of a number of patients, and that the results are compared with the RSA data obtained for the same patients. In addition, good correlation was observed between the results from the finite element models and the clinical data, as the same ranking order between patients produced by the RSA measurements was observed in the finite element models.

The work performed in this thesis may be viewed as a pilot study to assess the parameters that should be considered to perform a large scale patient-specific finite element analysis including data from several patients. The pre-processing method used here to create patient-specific models of the proximal implanted tibiae only takes about two days per patient. If the appropriate pre-operative data is available (CT scans including calibration bars used to determine the material properties), by means of the method presented here and including the improvements mentioned above, it is possible to perform the same study on a large number of patients in order to further validate the predictive power of FE. Patient specific finite element analysis can also be used to foresee or minimise the likelihood of failure of the prostheses even before implantation. For instance, it could be used optimise the selection of the prosthesis model, fixation type and component alignment that best suits each patient, potentially leading to the design of customised prostheses based on the characteristics of each patient (bone quality, activity levels, weight, kinematics). It should be mentioned that currently, the above parameters are entirely controlled by the surgeon, who can exhaustively examine the knee to be implanted only at the time of surgery. Hence, the success of the implant is very much dependent on visual inspection and assessment by the surgeon, meaning that if the surgeon is not sufficiently experienced the operation may not have the best outcome possible, incurring in the risk of facing future prosthesis complications due to an inappropriate selection of the above parameters (implant design and size, component alignment and fixation method). Hence, patient-specific finite element analysis may

become a valuable preoperative planning tool that can assist the surgeon in predicting the set of parameters that would produce the best clinical result, as well as foreseeing potential complications that might occur during surgery.

FUTURE WORK

Further improvements can be implemented in the models analysed in this thesis in order to increase the accuracy (and hence the predictive power) of patient-specific finite element analysis.

Friction between two contacting bodies is always present in reality and specifically, between the tibial component and the host bone. It has been demonstrated that both micromotions and stresses in the interface between the contacting bodies are significantly reduced when friction is included in the models [44,146]. Therefore, it is recommended that this parameter be considered in future analyses.

For future models it is important to take into account the kinematics of the patient, as it was demonstrated (chapter 6) that each model should be subjected to a load case that at least resembles the real loads in the knee, if the results from FE are to be compared with the clinical data. Furthermore, in order to make the study more realistic and hence, more accurate, dynamic loads should be applied instead of static ones. Godest *et al.* [51] have simulated the variable loads acting in a knee joint replacement during a gait cycle by means of explicit finite element analysis. They compared their results with experimental data and concluded that the kinematics and stresses present in a knee joint replacement can be predicted with a relatively low computational cost. This type of analysis should be performed in the future in order to determine more realistic load cases to be applied on models of the proximal implanted tibia.

In this thesis, the risk ratios resulting from immediate post-operative conditions were correlated with migration data measured at one year after surgery. A more complex analysis would consider the plastic deformation or accumulated damage of the supporting bone as well as including remodelling of the cancellous bone in order to simulate and predict migration directly from the finite element models. If migration could be simulated in patient-specific models, the results would be capable of predicting

future implant loosening as it has been demonstrated that migration measurements using RSA can predict during the first two post-operative years, the risk of failure due to component loosening at five or more years after surgery, with a reliability of 85% [134]. It should be mentioned, that to date RSA has been the only clinical tool to show predictive capabilities in terms of implant loosening. Undoubtedly, the complexity involved in the simulation of remodelling would increase considerably the computational cost to solve the models.

REFERENCES

1. Adalberth G, Nilsson KG, Bystrom S, Kolstad K and Milbrink J. "Low-conforming all-polyethylene tibial component not inferior to metal-backed component in cemented total knee arthroplasty - Prospective, randomized radiostereometric analysis study of the AGC total knee prosthesis". Journal of Arthroplasty. 15: 6, 783-792, (2000).

2. Ahmed AM, Tissakht M, Shrivastava SC and Chan K. "Dynamic stress response of the implant/cement interface: an axisymmetric analysis of a knee tibial component". J Orthop Res. 8: 3, 435-47., (1990).

3. Akil M and Amos RS. "ABC of Rheumatology. Rheumatoid Arthritis--I: Clinical Features and Diagnosis". Bmj. 310: 6979, 687-590, (1995).

4. Albrektsson BE, Ryd L, Carlsson LV, Freeman MA, Herberts P, Regner L and Selvik G. "The effect of a stem on the tibial component of knee arthroplasty. A roentgen stereophotogrammetric study of uncemented tibial components in the Freeman-Samuelson knee arthroplasty". J Bone Joint Surg [Br]. 72: 2, 252-8, (1990).

5. Albrektsson BE, Carlsson LV, Freeman MA, Herberts P and Ryd L. "Proximally cemented versus uncemented Freeman-Samuelson knee arthroplasty. A prospective randomised study". J Bone Joint Surg [Br]. 74: 2, 233-8, (1992).

6. Allardyce T, Scuderi G and Insall J. "Long - term results of cemented total knee replacement". Bombay Hospital Journal. July: (1996).

7. Ashman RB, Cowin SC, Van Buskirk WC and Rice JC. "A continuous wave technique for the measurement of the elastic properties of cortical bone". J Biomech. 17: 5, 349-61, (1984).

8. Ashman RB, Rho JY and Turner CH. "Anatomical variation of orthotropic elastic moduli of the proximal human tibia". J Biomech. 22: 8-9, 895-900, (1989).

9. Bargren J, Blaha J and Freeman M. "Alignment in total knee arthroplasty. Correlated biomechanical and clinical observations.". Clin Orthop. 173: Mar, 178-83., (1983).

10. Bartel DL, Burstein AH, Santavicca EA and Insall JN. "Performance of the tibial component in total knee replacement". J Bone Joint Surg [Am]. 64: 7, 1026-33, (1982).

11. Beaupre GS, Vasu R, Carter DR and Schurman DJ. "Epiphyseal-based designs for tibial plateau components--II. Stress analysis in the sagittal plane". J Biomech. 19: 8, 663-73, (1986).

12. Behrens JC, Walker PS and Shoji H. "Variations in strength and structure of cancellous bone at the knee". J Biomech. 7: 3, 201-7, (1974).

13. Bellemans J. "Osseointegration in porous coated knee arthroplasty. The influence of component coating type in sheep". Acta Orthop Scand Suppl. 288: 1-35., (1999).

14. Bentzen SM, Hvid I and Jorgensen J. "Mechanical strength of tibial trabecular bone evaluated by X-ray computed tomography". J Biomech. 20: 8, 743-52, (1987).

15. Bergmann G, Deuretzbacher G, Heller M, Graichen F, Rohlmann A, Strauss J and Duda GN. "Hip contact forces and gait patterns from routine activities". J Biomech. 34: 7, 859-71., (2001).

16. Bertin KC, Freeman MA, Samuelson KM, Ratcliffe SS and Todd RC. "Stemmed revision arthroplasty for aseptic loosening of total knee replacement". J Bone Joint Surg [Br]. 67: 2, 242-8, (1985).

17. Bryan R and Rand J. "Revision total knee arthroplasty". Clin Orthop. 170: Oct, 116-22, (1982).

18. Burstein AH, Reilly DT and Martens M. "Aging of bone tissue: mechanical properties". J Bone Joint Surg [Am]. 58: 1, 82-6, (1976).

19. Cameron HU and Hunter GA. "Failure in total knee arthroplasty: mechanisms, revisions, and results". Clin Orthop: 170, 141-6, (1982).

20. Campbell B. "Thrombosis, phlebitis, and varicose veins [editorial] [see comments]". Bmj. 312: 7025, 198-9, (1996).

21. Carlsson LV, Albrektsson BE, Freeman MA, Herberts P, Malchau H and Ryd L. "A new radiographic method for detection of tibial component migration in total knee arthroplasty". J Arthroplasty. 8: 2, 117-23, (1993).

22. Carter DR and Hayes WC. "Bone compressive strength: the influence of density and strain rate". Science. 194: 4270, 1174-6, (1976).

23. Carter DR and Hayes WC. "The compressive behavior of bone as a two-phase porous structure". J Bone Joint Surg [Am]. 59: 7, 954-62, (1977).

24. Carter DR and Spengler DM. "Mechanical properties and composition of cortical bone". Clin Orthop: 135, 192-217, (1978).

25. Carter DR, Schwab GH and Spengler DM. "Tensile fracture of cancellous bone". Acta Orthop Scand. 51: 5, 733-41, (1980).

26. Cattaneo PM, Dalstra M and Frich LH. "A three-dimensional finite element model from computed tomography data: a semi-automated method". Proc Inst Mech Eng [H]. 215: 2, 203-13., (2001).

27. Charras GT and Guldberg RE. "Improving the local solution accuracy of large-scale digital image-based finite element analyses". J Biomech. 33: 2, 255-9., (2000).

28. Cheal EJ, Hayes WC, Lee CH, Snyder BD and Miller J. "Stress analysis of a condylar knee tibial component: influence of metaphyseal shell properties and cement injection depth". J Orthop Res. 3: 4, 424-34, (1985).

29. Cheal EJ, Spector M and Hayes WC. "Role of Loads and Prosthesis Material Properties On the Mechanics of the Proximal Femur After Total Hip-Arthroplasty". Journal of Orthopaedic Research. 10: 3, 405-422, (1992).

30. Ciarelli M, Goldstein S, Dickie D, Ku J, Kapper M, Stanley J, Flynn M and Mathews L. "Experimental determination of the orthogonal mechanical properties, density and distribution of human trabecular bone from major metaphyseal regions utilizing materials testing and computed tomography". Transactions of the Orthopedic Research Society: 42, (1986).

31. Cooke T, Kelly B and Li J. "Prosthetic reconstruction of the arthritic knee: considerations for limb alignment, geometry of soft tissue reconstruction". The Knee. 5: 165-174, (1998).

32. Coull R, Bankes MJK and Rossouw DJ. "Evaluation of tibial component angles in 79 consecutive total knee arthroplasties". Knee. 6: 4, 235-237, (1999).

33. Davy DT, Kotzar GM, Brown RH, Heiple KG, Goldberg VM, Heiple KG, Jr., Berilla J and Burstein AH. "Telemetric force measurements across the hip after total arthroplasty". J Bone Joint Surg Am. 70: 1, 45-50., (1988).

34. Dawson JM and Bartel DL. "Consequences of an interference fit on the fixation of porous-coated tibial components in total knee replacement". J Bone Joint Surg Am. 74: 2, 233-8., (1992).

35. Diduch DR, Insall JN, Scott WN, Scuderi GR and Font-Rodriguez D. "Total knee replacement in young, active patients. Long-term follow-up and functional outcome". J Bone Joint Surg Am. 79: 4, 575-82, (1997).

36. Dieppe P. "Osteoarthritis: time to shift the paradigm. This includes distinguishing between severe disease and common minor disability [editorial]". Bmj. 318: 7194, 1299-300, (1999).

37. Douek P, Pinaudeau D and Amiel M. "Tomodensitométrie X. Principes. Technologie. Caractéristiques de l'imagerie (1ere partie).". Feuillets de Radiologie. 72: 4, 221-230, (1987).

38. Ducheyne P, Heymans L, Martens M, Aernoudt E, de Meester P and Mulier JC. "The mechanical behaviour of intracondylar cancellous bone of the femur at different loading rates". J Biomech. 10: 11/12, 747-62, (1977).

39. Ecker ML, Lotke PA, Windsor RE and Cella JP. "Long-term results after total condylar knee arthroplasty. Significance of radiolucent lines". Clin Orthop: 216, 151-8, (1987).

40. Engh GA, Dwyer KA and Hanes CK. "Polyethylene wear of metal-backed tibial components in total and unicompartmental knee prostheses". J Bone Joint Surg [Br]. 74: 1, 9-17, (1992).

41. Esses SI, Lotz JC and Hayes WC. "Biomechanical properties of the proximal femur determined in vitro by single-energy quantitative computed tomography". J Bone Miner Res. 4: 5, 715-22, (1989).

42. Ewald FC and Walker PS. "The current status of total knee replacement". Rheum Dis Clin North Am. 14: 3, 579-90, (1988).

43. Finlay JB, Bourne RB, Kraemer WJ, Moroz TK and Rorabeck CH. "Stiffness of bone underlying the tibial plateaus of osteoarthritic and normal knees". Clin Orthop: 247, 193-201., (1989).

44. Forcione A and Shirazi-Adl A. "Biomechanical analysis of a porous-surfaced knee implant: a finite element contact problem with nonlinear friction.". CSME Mechanical Engineering Forum 1990: 19-24, (1990).

45. Freeman M, Samuelson K and Bertin K. "Freeman-Samuelson total arthroplasty of the knee". Clin Orthop. 192: Jan-Feb, 46-58, (1985).

46. Freeman M. "Principles of total knee replacement: The Freeman/Samuelson arthroplasty". Bombay Hospital Journal. July: (1996).

47. Fukuoka S, Yoshida K and Yamano Y. "Estimation of the migration of tibial components in total knee arthroplasty". J Bone Joint Surg (Br). 82-B: 222-227, (2000).

48. Galante J, Rostoker W and Ray RD. "Physical properties of trabecular bone". Calcif Tissue Res. 5: 3, 236-46, (1970).

49. Garg A and Walker PS. "The effect of the interface on the bone stresses beneath tibial components". J Biomech. 19: 12, 957-67., (1986).

50. Genant HK, Wilson JS, Bovill EG, Brunelle FO, Murray WR and Rodrigo JJ. "Computed tomography of the musculoskeletal system". J Bone Joint Surg [Am]. 62: 7, 1088-101, (1980).

51. Godest AC, Beaugonin M, Haug E, Taylor M and Gregson PJ. "Simulation of a knee joint replacement during a gait cycle using explicit finite element analysis". Journal of Biomechanics: (In press).

52. Goldstein SA, Wilson DL, Sonstegard DA and Matthews LS. "The mechanical properties of human tibial trabecular bone as a function of metaphyseal location". J Biomech. 16: 12, 965-9, (1983).

53. Goldstein SA. "The mechanical properties of trabecular bone: dependence on anatomic location and function". J Biomech. 20: 11-12, 1055-61, (1987).

54. Goodfellow J. "Knee prostheses--one step forward, two steps back [editorial]". J Bone Joint Surg [Br]. 74: 1, 1-2, (1992).

55. Goodman S and Lidgren L. "Polyethylene wear in knee arthroplasty. A review". Acta Orthop Scand. 63: 3, 358-64, (1992).

56. Grewal R, Rimmer MG and Freeman MA. "Early migration of prostheses related to long-term survivorship. Comparison of tibial components in knee replacement". J Bone Joint Surg [Br]. 74: 2, 239-42, (1992).

57. Hampton KK and Preston FE. "ABC of clinical haematology. Bleeding disorders, thrombosis, and anticoagulation". Bmj. 314: 7086, 1026-9, (1997).

58. Hansson TH, Keller TS and Panjabi MM. "A study of the compressive properties of lumbar vertebral trabeculae: effects of tissue characteristics". Spine. 12: 1, 56-62, (1987).

59. Hayes W, Vichnin H and Lotke P. "Parametric finite element studies of tibial component fixation in the total condylar knee prosthesis". Biomechanics symposium, ASME. W. Van Buskirk. New York: 63-66, (1979).

60. Hayes W. "Biomechanics of cortical and trabecular bone: implications for assesment of fracture risk.". Basic Orthopaedic Biomechanics. V. Mow and W. Hayes, Raven Press: (1991).

61. Hilding M, Asplund S, Bäckbro B and Ryd L. "Alignment accuracy by two different instrumentation systems in total knee arthroplasty". The American Journal of Knee Surgery. 6: 4, (1993).

62. Hilding MB, Lanshammar H and Ryd L. "A Relationship between Dynamic and Static Assessments of Knee- Joint Load - Gait Analysis and Radiography before and after Knee Replacement in 45 Patients". Acta Orthopaedica Scandinavica. 66: 4, 317-320, (1995).

63. Hilding MB, Yuan XH and Ryd L. "The Stability of 3 Different Cementless Tibial Components - a Randomized Radiostereometric Study in 45 Knee Arthroplasty Patients". Acta Orthopaedica Scandinavica. 66: 1, 21-27, (1995).

64. Hilding MB, Lanshammar H and Ryd L. "Knee joint loading and tibial component loosening". Journal of Bone and Joint Surgery-British Volume. 78B: 1, 66-73, (1996).

65. Hobatho M, Asman R, Darmana R and Morucci J. "Assesment of the elastic properties of human tibial cortical bone by ultrasonic measurements.". In vivo assesment of bone quality by vibration and wave propagation techniques. G. Van Der Perre, G. Lowet and A. Borgwardt. Leuven, ACCO: 45-56, (1991).

66. Hsu HP, Garg A, Walker PS, Spector M and Ewald FC. "Effect of knee component alignment on tibial load distribution with clinical correlation". Clin Orthop: 248, 135-44, (1989).

67. Huiskes R. "The Various Stress Patterns of Press-Fit, Ingrown, and Cemented Femoral Stems". Clinical Orthopaedics and Related Research: 261, 27-38, (1990).

68. Hungerford D, Kenna R and Haynes D. "Relevant Biomechanics of the Knee for Knee Replacements. W. a. Wilkins. Baltimore: (1984).

69. Hvid I and Hansen SL. "Trabecular bone strength patterns at the proximal tibial epiphysis". J Orthop Res. 3: 4, 464-72, (1985).

70. Hvid I. "Trabecular bone strength at the knee". Clin Orthop. 227: 210-21, (1988).

71. Hvid I, Bentzen SM, Linde F, Mosekilde L and Pongsoipetch B. "X-ray quantitative computed tomography: the relations to physical properties of proximal tibial trabecular bone specimens". J Biomech. 22: 8-9, 837-44, (1989).

72. Insall J, Scott WN and Ranawat CS. "The total condylar knee prosthesis. A report of two hundred and twenty cases". J Bone Joint Surg [Am]. 61: 2, 173-80, (1979).

73. Insall J and Dethmers D. "Revision of total knee arthroplasty". Clin Orthop. 170: Oct, 123-30, (1982).

74. Insall JN, Hood RW, Flawn LB and Sullivan DJ. "The total condylar knee prosthesis in gonarthrosis. A five to nine-year follow-up of the first one hundred consecutive replacements". J Bone Joint Surg [Am]. 65: 5, 619-28, (1983).

75. ISO/DIS.14243-1. "Implants for surgery - Wear of total knee joint prostheses - Part 1: Loading and displacement parameters for wear-testing machines with load control and corresponding environmental conditions for tests": (1999).

76. Jeffery R, Morris R and Denham R. "Coronal alignment after total knee replacement". J Bone Joint Surg [Br]. 73(5): Sep, 709-14, (1991).

77. Kapandji I. "The Physiology of the Joints, Churchill Livingstone. 2 (Lower Limb): (1987).

78. Kaplan SJ, Hayes WC, Stone JL and Beaupre GS. "Tensile strength of bovine trabecular bone". J Biomech. 18: 9, 723-7, (1985).

79. Kaufman KR, An KN, Litchy WJ, Morrey BF and Chao EY. "Dynamic joint forces during knee isokinetic exercise". Am J Sports Med. 19: 3, 305-16, (1991).

80. Keaveny TM and Hayes WC. "A 20-year perspective on the mechanical properties of trabecular bone". J Biomech Eng. 115: 4B, 534-42, (1993).

81. Keaveny TM and Bartel DL. "Fundamental Load-Transfer Patterns For Press-Fit, Surface- Treated Intramedullary Fixation Stems". Journal of Biomechanics. 27: 9, 1147-1157, (1994).

82. Keaveny TM, Wachtel EF, Ford CM and Hayes WC. "Differences between the tensile and compressive strengths of bovine tibial trabecular bone depend on modulus [see comments]". J Biomech. 27: 9, 1137-46, (1994).

83. Keja M, Wevers HW, Siu D and Grootenboer H. "Relative Motion at the Bone Prosthesis Interface". Clinical Biomechanics. 9: 5, 275-283, (1994).

84. Kerner J, Huiskes R, van Lenthe GH, Weinans H, van Rietbergen B, Engh CA and Amis AA. "Correlation between pre-operative periprosthetic bone density and post-operative bone loss in THA can be explained by strain-adaptive remodelling". J Biomech. 32: 7, 695-703., (1999).

85. Keyak JH and Skinner HB. "Three-dimensional finite element modelling of bone: effects of element size". J Biomed Eng. 14: 6, 483-9, (1992).

86. Kim W, Rand JA and Chao EYS. "Biomechanics of the Knee". Total Knee Arthroplasty. J. A. Rand. New York, Raven Press Ltd.: (1993).

87. Kotzar GM, Davy DT, Goldberg VM, Heiple KG, Berilla J, Heiple KG, Jr., Brown RH and Burstein AH. "Telemeterized in vivo hip joint force data: a report on two patients after total hip surgery". J Orthop Res. 9: 5, 621-33., (1991).

88. Lafortune MA, Cavanagh PR, Sommer HJd and Kalenak A. "Three-dimensional kinematics of the human knee during walking". J Biomech. 25: 4, 347-57, (1992).

89. Lewallen D, Bryan R and Peterson L. "Polycentric total knee arthroplasty. A ten-year follow-up study". J Bone Joint Surg [Am]. 66(8): Oct, 1211-8, (1984).

90. Lewis JL, Askew MJ and Jaycox DP. "A comparative evaluation of tibial component designs of total knee prostheses". J Bone Joint Surg [Am]. 64: 1, 129-35, (1982).

91. Lindahl O. "Mechanical properties of dried defatted spongy bone". Acta Orthop Scand. 47: 1, 11-9, (1976).

92. Linde F, Hvid I and Pongsoipetch B. "Energy absorptive properties of human trabecular bone specimens during axial compression". J Orthop Res. 7: 3, 432-9, (1989).

93. Linde F, Pongsoipetch B, Frich LH and Hvid I. "Three-axial strain controlled testing applied to bone specimens from the proximal tibial epiphysis". J Biomech. 23: 11, 1167-72, (1990).

94. Linde F, Norgaard P, Hvid I, Odgaard A and Soballe K. "Mechanical properties of trabecular bone. Dependency on strain rate". J Biomech. 24: 9, 803-9, (1991).

95. Lotke P and Ecker M. "Influence of positioning of prosthesis in total knee replacement". J Bone Joint Surg [Am]. 59(1): Jan, 77-9, (1977).

96. Lotz JC, Gerhart TN and Hayes WC. "Mechanical properties of trabecular bone from the proximal femur: a quantitative CT study". J Comput Assist Tomogr. 14: 1, 107-14, (1990).

97. Marieb E. "Human anatomy and physiology, Addison Wesley Longman, Inc: (1998).

98. Marks LW and Gardner TN. "The use of strain energy as a convergence criterion in the finite element modelling of bone and the effect of model geometry on stress convergence". J Biomed Eng. 15: 6, 474-6, (1993).

99. Martin RB and Atkinson PJ. "Age and sex-related changes in the structure and strength of the human femoral shaft". J Biomech. 10: 4, 223-31, (1977).

100. McBroom RJ, Hayes WC, Edwards WT, Goldberg RP and White AAd. "Prediction of vertebral body compressive fracture using quantitative computed tomography". J Bone Joint Surg [Am]. 67: 8, 1206-14, (1985).

101. McCalden RW, McGeough JA, Barker MB and Court-Brown CM. "Age-related changes in the tensile properties of cortical bone. The relative importance of changes in porosity, mineralization, and microstructure". J Bone Joint Surg Am. 75: 8, 1193-205, (1993).

102. McCaskie AW, Deehan DJ, Green TP, Lock KR, Thompson JR, Harper WM and Gregg PJ. "Randomised, prospective study comparing cemented and cementless total knee replacement - Results of press-fit condylar total knee replacement at five years". Journal of Bone and Joint Surgery-British Volume. 80B: 6, 971-975, (1998).

103. Moran CG and Horton TC. "Total knee replacement: the joint of the decade. A successful operation, for which there's a large unmet need [In Process Citation]". Bmj. 320: 7238, 820, (2000).

104. Moreland J. "Mechanisms of failure in total knee arthroplasty". Clin Orthop. 226: Jan, 49-64, (1988).

105. Morrison J. "The mechanics of the knee joint in relation to normal walking". J Biomech. 3(1): Jan, 51-61, (1970).

106. Murase K, Crowninshield RD, Pedersen DR and Chang TS. "An analysis of tibial component design in total knee arthroplasty". J Biomech. 16: 1, 13-22, (1983).

107. Nafei A, Nielsen S, Kristensen O and Hvid I. "The Press-Fit Kinemax Knee Arthroplasty - High Failure Rate of Noncemented Implants". Journal of Bone and Joint Surgery-British Volume. 74: 2, 243-246, (1992).

108. Natali AN and Meroi EA. "A review of the biomechanical properties of bone as a material". J Biomed Eng. 11: 4, 266-76, (1989).

109. Nelissen RG, Valstar ER and Rozing PM. "The effect of hydroxyapatite on the micromotion of total knee prostheses. A prospective, randomized, double-blind study". J Bone Joint Surg Am. 80: 11, 1665-72, (1998).

110. Newman J and Ackroyd C. "25 years of unicompartmental knee replacement with the St George Sled prosthesis". International Conference on Knee Replacement 1974-2024. London: 10-12, (1999).

111. Nigg B and Grimston S. "Bone". Biomechanics of the musculo-skeletal system. B. Nigg and W. Herzog. Chichester, John Wiley: (1999).

112. Nilsson KG and Karrholm J. "RSA in the assessment of aseptic loosening [editorial; comment]". J Bone Joint Surg Br. 78: 1, 1-3, (1996).

113. Nilsson KG, Karrholm J, Carlsson L and Dalen T. "Hydroxyapatite coating versus cemented fixation of the tibial component in total knee arthroplasty: prospective randomized comparison of hydroxyapatite-coated and cemented tibial components with 5-year follow-up using radiostereometry". J Arthroplasty. 14: 1, 9-20., (1999).

114. Norkin CC and Levangie PK. "Joint Structure& Function. A comprehensive analysis. Philadelphia, F. A. Davis Company. 1: (1992).

115. Önsten I, Nordqvist A, Carlsson AS, Besjakov J and Shott S. "Hydroxyapatite augmentation of the porous coating improves fixation of tibial components. A randomised RSA study in 116 patients". J Bone Joint Surg Br. 80: 3, 417-25., (1998).

116. Perillo-Marcone A, Barrett DS and Taylor M. "The importance of tibial alignment: finite element analysis of tibial malalignment". J Arthroplasty. 15: 8, 1020-7., (2000).

117. Polgar K, Viceconti M and O'Connor JJ. "A comparison between automatically generated linear and parabolic tetrahedra when used to mesh a human femur". Proceedings of the Institution of Mechanical Engineers Part H- Journal of Engineering in Medicine. 215: H1, 85-94, (2001).

118. Pugh JW, Rose RM and Radin EL. "Elastic and viscoelastic properties of trabecular bone: dependence on structure". J Biomech. 6: 5, 475-85, (1973).

119. Rakotomanana RL, Leyvraz PF, Curnier A, Heegaard JH and Rubin PJ. "A finite element model for evaluation of tibial prosthesis-bone interface in total knee replacement". J Biomech. 25: 12, 1413-24, (1992).

120. Rand JA and Fitzgerald RH, Jr. "Diagnosis and management of the infected total knee arthroplasty". Orthop Clin North Am. 20: 2, 201-10, (1989).

121. Regnér L, Carlsson L, Karrholm J and Herberts P. "Tibial component fixation in porous- and hydroxyapatite-coated total knee arthroplasty: a radiostereo metric evaluation of migration and inducible displacement after 5 years". J Arthroplasty. 15: 6, 681-9., (2000).

122. Reilly DT and Burstein AH. "Review article. The mechanical properties of cortical bone". J Bone Joint Surg [Am]. 56: 5, 1001-22, (1974).

123. Reilly DT, Burstein AH and Frankel VH. "The elastic modulus for bone". J Biomech. 7: 3, 271-5, (1974).

124. Reilly DT and Burstein AH. "The elastic and ultimate properties of compact bone tissue". J Biomech. 8: 6, 393-405, (1975).

125. Rho JY, Hobatho MC and Ashman RB. "Relations of mechanical properties to density and CT numbers in human bone". Med Eng Phys. 17: 5, 347-55, (1995).

126. Riggs BL, Wahner HW, Seeman E, Offord KP, Dunn WL, Mazess RB, Johnson KA and Melton LJd. "Changes in bone mineral density of the proximal femur and spine with aging. Differences between the postmenopausal and senile osteoporosis syndromes". J Clin Invest. 70: 4, 716-23, (1982).

127. Ritter M, Herbst S, Keating E and Faris P. "Radiolucency at the bone-cement interface in total knee replacement. The effects of bone-surface preparation and cement technique". J Bone Joint Surg Am. 76(1): Jan, 60-5, (1994).

128. Robertsson O. "The Swedish Knee Arthroplasty Register - Validity and Outcome". Department of Orthopaedics. Lund - Sweden, Lund University Hospital: 37, (2000).

129. Røhl L, Larsen E, Linde F, Odgaard A and Jørgensen J. "Tensile and compressive properties of cancellous bone". J Biomech. 24: 12, 1143-9, (1991).

130. Rohlmann A, Zilch H, Bergmann G and Kolbel R. "Material properties of femoral cancellous bone in axial loading. Part I: Time independent properties". Arch Orthop Trauma Surg. 97: 2, 95-102, (1980).

131. Ryd L, Lindstrand A, Rosenquist R and Selvik G. "Micromotion of conventionally cemented all-polyethylene tibial components in total knee replacements. A roentgen stereophotogrammetric analysis of migration and inducible displacement". Arch Orthop Trauma Surg. 106: 2, 82-8, (1987).

132. Ryd L, Albrektsson BE, Herberts P, Lindstrand A and Selvik G. "Micromotion of noncemented Freeman-Samuelson knee prostheses in gonarthrosis. A roentgen-stereophotogrammetric analysis of eight successful cases". Clin Orthop: 229, 205-12, (1988).

133. Ryd L and Linder L. "On the correlation between micromotion and histology of the bone-cement interface. Report of three cases of knee arthroplasty followed by roentgen stereophotogrammetric analysis". J Arthroplasty. 4: 4, 303-9, (1989).

134. Ryd L, Albrektsson BE, Carlsson L, Dansgard F, Herberts P, Lindstrand A, Regner L and Toksvig-Larsen S. "Roentgen stereophotogrammetric analysis as a predictor of mechanical loosening of knee prostheses". J Bone Joint Surg Br. 77: 3, 377-83, (1995).

135. Selvik G. "Roentgen stereophotogrammetry. A method for the study of the kinematics of the skeletal system". Acta Orthop Scand Suppl. 232: 1-51, (1989).

136. Snyder SM and Schneider E. "Estimation of mechanical properties of cortical bone by computed tomography". J Orthop Res. 9: 3, 422-31, (1991).

137. Stiehl JB, Dennis DA, Komistek RD and Crane HS. "In vivo determination of condylar lift-off and screw-home in a mobile-bearing total knee arthroplasty". Journal of Arthroplasty. 14: 3, 293-299, (1999).

138. Stone JL, Beaupre GS and Hayes WC. "Multiaxial strength characteristics of trabecular bone". J Biomech. 16: 9, 743-52, (1983).

139. Taylor M, Tanner K, Freeman M and Yettram A. "Finite element modelling - a predictor of implant survival?". Journal of Materials Science: Mat Medicine. 6: 808-812, (1995).

140. Taylor M, Tanner K, Freeman M and Yettram A. "Cancellous bone stresses surrounding the femoral component of a hip prosthesis: an elastic-plastic finite element analysis". Med Eng Phys. 17(7): Oct, 544-50, (1995).

141. Taylor M and Tanner KE. "Fatigue failure of cancellous bone: a possible cause of implant migration and loosening". J Bone Joint Surg Br. 79: 2, 181-2, (1997).

142. Taylor M, Tanner K and Freeman M. "Finite element analysis of the implanted proximal tibia: a relationship between the initial cancellous bone stresses and implant migration". J Biomech. 31(4): Apr, 303-10, (1998).

143. Tennant A, Fear J, Pickering A, Hillman M, Cutts A and Chamberlain MA. "Prevalence of knee problems in the population aged 55 years and over: identifying the need for knee arthroplasty". Bmj. 310: 6990, 1291-3, (1995).

144. Tew M and Waugh W. "Tibiofemoral alignment and the results of knee replacement". J Bone Joint Surg [Br]. 67(4): Aug, 551-6, (1985).

145. Thornhill T, Dalziel R and Sledge C. "Alternatives to arthrodesis for the failed total knee arthroplasty". Clin Orthop. 170: Oct, 131-40, (1982).

146. Tissakht M, Eskandari H and Ahmed AM. "Micromotion Analysis of the Fixation of Total Knee Tibial Component". Computers & Structures. 56: 2-3, 365-375, (1995).

147. Toksvig-Larsen S, Magyar G, Onsten I, Ryd L and Lindstrand A. "Fixation of the tibial component of total knee arthroplasty after high tibial osteotomy: a matched radiostereometric study". J Bone Joint Surg Br. 80: 2, 295-7., (1998).

148. Toksvig-Larsen S, Ryd L and Lindstrand A. "Early inducible displacement of tibial components in total knee prostheses inserted with and without cement: a randomized study with roentgen stereophotogrammetric analysis". J Bone Joint Surg Am. 80: 1, 83-9, (1998).

149. Van Rietbergen B, Muller R, Ulrich D, Ruegsegger P and Huiskes R. "Tissue stresses and strain in trabeculae of a canine proximal femur can be quantified from computer reconstructions". J Biomech. 32: 4, 443-51., (1999).

150. Vasu R, Carter DR, Schurman DJ and Beaupre GS. "Epiphyseal-based designs for tibial plateau components--I. Stress analysis in the frontal plane". J Biomech. 19: 8, 647-62, (1986).

151. Walker P. "Review of the 1974 conference and design forms of knee replacement". International Conference on Knee Replacement 1974-2024. London: 2-8, (1999).

152. Walker PS. "Design of a knee prosthesis system". Acta Orthop Belg. 46: 6, 766-75, (1980).

153. Walker PS. "Requirements for successful total knee replacements. Design considerations". Orthop Clin North Am. 20: 1, 15-29, (1989).

154. Walker PS and Sathasivam S. "Design forms of total knee replacement". Proc Inst Mech Eng [H]. 214: 1, 101-19, (2000).

155. Weinans H, Sumner DR, Igloria R and Natarajan RN. "Sensitivity of periprosthetic stress-shielding to load and the bone density-modulus relationship in subject-specific finite element models". J Biomech. 33: 7, 809-17., (2000).

156. Whiteside L. "Cementless Total Knee Arthroplasty". Total Knee Arthroplasty. J. Rand. New York, Raven Press Ltd: 329-347, (1993).

157. Willert HG, Ludwig J and Semlitsch M. "Reaction of bone to methacrylate after hip arthroplasty: a long-term gross, light microscopic, and scanning electron microscopic study". J Bone Joint Surg [Am]. 56: 7, 1368-82, (1974).

158. Williams JL and Lewis JL. "Properties and an anisotropic model of cancellous bone from the proximal tibial epiphysis". J Biomech Eng. 104: 1, 50-6, (1982).

159. Winemaker MJ, Beingessner DM and Rorabeck CH. "Revision total knee arthroplasty: should tibial stems be cemented or uncemented?". Knee. 5: 3, 175-181, (1998).

160. Wolff J. "Das Gesetz der Transformation der Knochen. Berlin, Hirchwild: (1882).

161. Wolheim F. "Rheumatoid Arthritis - the clinical picture". Oxford Textbook of Rheumatology. P. Maddison, D. Isenberg, P. Woo and D. Glass, Oxford university press: (1993).

162. Yamada H. "Strength of Biomechanical Materials. F. Evans and F. Gaynor. Baltimore, Maryland, Williams & Wilkins: 49, (1970).

163. Yuan X. "Accuracy anlaysis of RSA and develpment of roentgen single-plane photogrammetric analysis". Department of Orthopaedics. Lund, Sweden, Lund University: (1999).

164. Zannoni C, Mantovani R and Viceconti M. "Material properties assignment to finite element models of bone structures: a new method". Med Eng Phys. 20: 10, 735-40., (1998).

165. Zernicke R and Judex S. "Adaptation of biological materials to excercise, disuse and aging". Biomechanics of the Musculo-Skeletal System. B. Nigg and W. Herzog, Wiley: 189-198, (1995).

APPENDIX A

THE IMPORTANCE OF TIBIAL ALIGNMENT: FINITE ELEMENT ANALYSIS OF TIBIAL MALALIGNMENT

A. Perillo-Marcone[1], M. Taylor[1], D. S. Barrett[2]

[1]School of Engineering Sciences, University of Southampton, Highfield, Southampton, SO17 1BJ, UK

[2]Department of Orthopaedics, Southampton University Hospital, Tremona Road, Southampton, SO16 6YD. UK.

(Published in Journal of Arthroplasty)

The Journal of Arthroplasty Vol. 15 No. 8 2000

The Importance of Tibial Alignment

Finite Element Analysis of Tibial Malalignment

A. Perillo-Marcone, BEng, MSc,* D. S. Barrett, BSc, FRCS† and M. Taylor, BEng, MSc, PhD*

Abstract: The influence of the tibial plateau orientation on cancellous bone stress was examined by finite element analysis for a cemented device. The objectives of the study were i) to examine the effect of the plateau-ankle angle on the cancellous bone stress, ii) to analyze the significance of the anteroposterior angles of the tibial component on these stresses, and iii) to compare the finite element predictions with clinical data. In general, positioning the tibial plateau in valgus resulted in lower cancellous bone stresses. These results support previous clinical studies, which suggest that overall alignment in valgus results in lower migration rates and lower incidence of loosening. **Key words:** tibial tray alignment, cancellous bone stress, finite element analysis.

Aseptic loosening of the tibial component is a major cause of failure in total knee arthroplasties [1–6]. Many clinical studies have suggested that alignment of the limb is crucial. Knee alignment comprises various parameters [7]. In the frontal plane, there are 4 parameters (Fig. 1): i) Hip-knee-ankle (HKA) angle, which is the angle between the mechanical long axes of the femur and tibia; ii) condylar-hip (CH) angle, defined as the orientation of the mechanical axis of the femur with respect to the tangent of the outline of the femoral condyles; iii) plateau-ankle (PA) angle, which is defined as the angle between the tibial plateau and the mechanical axis of the tibia; and iv) condylar-plateau angle, which is the angle between the knee joint surfaces. In the sagittal plane, there also is the anteroposterior (AP) angle, which is the angle of the tibial plateau with respect to the mechanical axis of the bone. The CH, PA, and AP angles are expressed as deviations from 90°. With the exception of the AP angle, these angles are assumed positive when they are in the valgus direction and negative if they are in the varus direction. The AP angle is assumed positive if the tibial plateau is tilted backward.

Various studies have examined the influence of overall knee alignment on the performance of total knee joint arthroplasty [7–10] using the HKA angle. Lotke and Ecker [11] observed a significant correlation between the positioning of the prosthesis, clinical performance, and the radiographic index. The radiographic index evaluates the knee in terms of overall alignment as well as the tibial and femoral component positioning separately. This index includes PA angles of ±10°. In the study by Lotke and Ecker [11], it was suggested that the ideal position for the tibial component is perfectly horizontal in both planes (perpendicular to the longer axis of the tibia), although this assumption was not supported by any results. After studying 70 knees before and

*From the *School of Engineering Sciences, University of Southampton; and †Department of Orthopaedics, Southampton University Hospital, Southampton, United Kingdom.*

Submitted November 25, 1999; accepted July 15, 2000.

Funds were received from CONICIT and Universidad Simón Bolívar, Venezuela, in support of the research material described in this article.

Reprint requests: A. Perillo-Marcone, School of Engineering Sciences, University of Southampton, Highfield, Southampton SO17 1BJ, UK.

0883-5403/00/1508-0014$10.00/0
doi:10.1054/arth.2000.17941

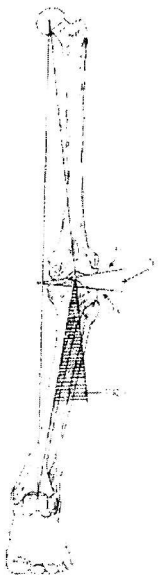

Fig. 1. Frontal view of the left leg with the knee fully extended. (From Cooke et al [20], with permission from Elsevier Science.)

after surgery (1–3 years' follow-up), Lotke and Ecker [11] concluded that generally there is a strong correlation between good positioning of the prosthesis and good clinical results. Although these authors evaluated each component individually, all these values were summed to produce only one radiographic score per knee, and the latter was compared with the clinical performance.

To assess factors that influence loosening, specific measurements of the alignment of the femoral and tibial component, relative to the femur and tibia, are needed. If the incidence of tibial component loosening is higher than for the femoral component, it could be argued that the orientation of the tibial component (PA and AP angles) is important. Only two studies have examined this argument. Hilding et al [12] compared two different interoperative alignment systems, and although 1 system was proved to be more accurate than the 1 traditionally used, it produced surgical error. Hilding's study included 45 knees with gonarthrosis. The ideal angle of the tibial component was assumed to be 3° of varus in the frontal plane and perfectly horizontal in the sagittal plane. The error in the frontal plane (PA angle) was found to be ±4° from the ideal position, whereas the maximum error detected in the sagittal plane was a posterior slope of 8°. Coull et al [13] evaluated 79 total knee arthroplasties to assess the alignment of the tibial component. They reported a mean PA angle of 86.88° (in varus), with 38 knees (48%) having a PA angle <86.88°. These knees were expected to show a poor performance. The PA angles observed in Coull's study ranged from 81° to 96°, representing a significant deviation from the mean value. Both of these studies showed that significant errors in tibial component alignment can occur.

Relatively few finite element analyses of the implanted proximal tibia have been carried out. Three-dimensional finite element studies have been performed mostly on cemented tibial components [14–18]. It has been shown that all-polyethylene tibial components produce high stresses within the supporting bone. These stresses can be reduced by addition of metal backing [14,16,17]. The addition of a central stem and a fixation with cement further reduces the cancellous bone stresses [17]. All of these finite element analyses have assumed perfect alignment of the prosthesis, that is, PA = AP = 0°. To our knowledge, no analytic or experimental study has examined the influence of orientation of the tibial tray on the cancellous bone stresses. The purposes of this investigation were to i) examine the effect of the PA angle on the cancellous bone stress (malpositioning of the tibial component), ii) analyze the significance of the anteroposterior angles of the tibial component on these stresses, and iii) correlate these findings with clinical data.

Materials and Methods

A three-dimensional finite element model of a proximal right tibia was generated based on a set of serial transverse computed tomography scans of a

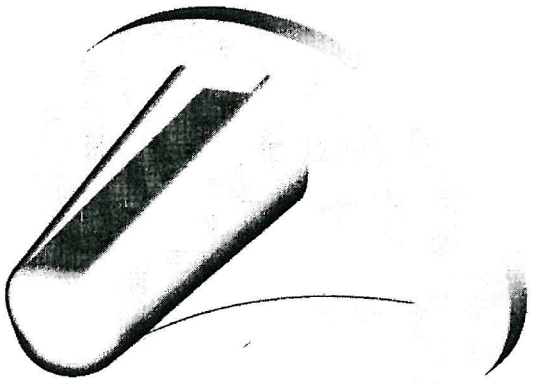

Fig. 2. Tibial component of the Dual Bearing Knee system.

1022 The Journal of Arthroplasty Vol. 15 No. 8 December 2000

Table 1. Material Properties of the Implanted Tibia

Material	Modulus (GPa)	Poisson Ratio	Ultimate Compressive Strength (MPa)
Diaphyseal cortical bone	17.0	0.29	—
Metaphyseal cortical bone	5.0	0.29	—
Medial cancellous bone	0.4	0.29	6.0
Intercondylar cancellous bone	0.1	0.29	1.5
Lateral cancellous bone	0.3	0.29	4.0
Metal (titanium)	110.0	0.33	—
Cement	2.0	0.30	—

From Taylor et al [19], with permission.

cadaveric specimen [19]. The tibia was implanted with a flanged-type tibial plateau (Dual Bearing Knee, MMT Ltd, Birmingham, UK) as shown in Fig. 2. The various material properties used in the model are listed in Table 1 [19]. The tibia was divided into five different regions—diaphyseal and metaphyseal cortical bone and medial, intercondylar, and lateral cancellous bone. The cemented fixation was modeled by adding a 1-mm layer of cement covering the top surface of the tibia in its entirety. No cement was considered around the stem or the flanges; however, the metal–cancellous bone interface was modeled as bonded. All materials were assumed isotropic, homogeneous, and linear elastic. The ultimate compressive strength of the medial cancellous bone was assumed to be 6.0 MPa [19].

The proximal tibia was resected at the 7 different PA angles [20], as shown in Fig. 3 (0°, ±2.5°, ±5°, and ±10°). From previous investigations [12], it was observed that because alignment depends on the surgeon's expertise as well as on the accuracy of the instruments used for this purpose, errors of ±5° in the PA angle could be present. An extreme case of ±10° was chosen as the worst possible case because these values were present in the Lotke scoring system [11]. Two AP angles were included in the analysis—neutral (0°) and 7° posterior slope.

A uniformly distributed unicondylar load of 2.2 kN was applied on a circular patch, 10 mm in diameter, in the center of the medial condyle in the same direction as the long axis of the tibia in all cases (Fig. 3). A unicondylar load was used to represent the worst-case scenario. Stiehl et al [21] showed that 18 of 20 patients analyzed using fluo-

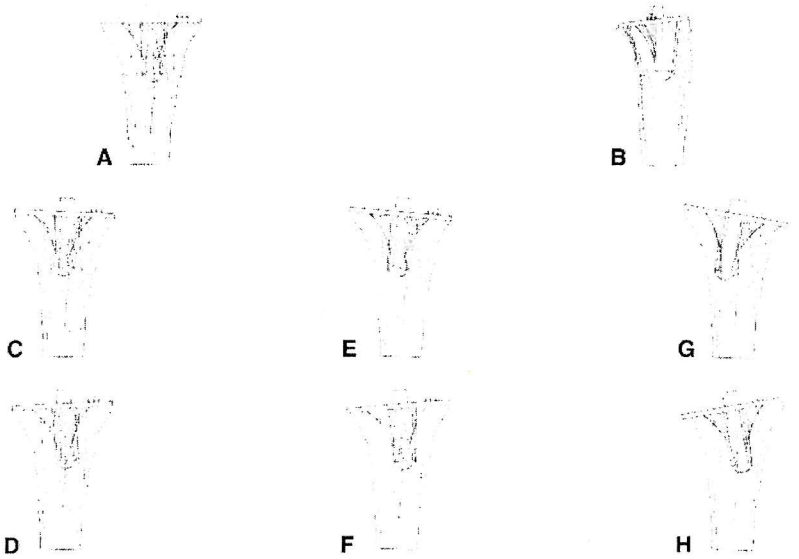

Fig. 3. Frontal view of the tibial plateau positions analyzed (except for B, which is viewed laterally). (A) 0°; (B) 7° posterior; (C) 2.5° varus; (D) 2.5° valgus; (E) 5° varus; (F) 5° valgus; (G) 10° varus; (H) 10° valgus.

Table 2. Number of Elements and Nodes Used in Each Model

Plateau-Ankle Angle (°)	No. Elements	No. Nodes
10 varus	31,865	45,943
5 varus	28,437	41,265
2.5 varus	35,145	50,861
0	32,349	46,432
2.5 valgus	41,294	59,108
5 valgus	34,054	48,422
10 valgus	29,792	42,637
7 posterior	43,711	61,959

roscopy exhibited significant lift-off at 1 point of the gait cycle (heel-strike), subjecting the tibia to unicondylar loading. This load represents the maximum force transmitted by the joint during the gait cycle for a 75-kg person (3 × body weight) [22]. To simplify the analysis, the polyethylene insert was not considered in the models, and the force was exerted directly on the tibial plateau. The distal end of the tibia was rigidly constrained. All analyses were performed using I-DEAS Master Series 6. Tetrahedral second-order (10-noded) elements (SDRC, Cincinnati, OH) were used in all models. A convergence analysis of the mesh refinement was performed with the implant in the neutral position (PA = AP = 0°). The refinement was carried out only on the surface of interest (medial compartment–cement interface) until the average stress on that surface was observed to converge to a constant value. The element size found to be most suitable for this study (1-mm edge length) was used in the rest of the models. The total number of elements and nodes used by each model are listed in Table 2.

Migration and the subsequent aseptic loosening of tibial trays is thought to be due to fatigue failure of the supporting cancellous bone [23]. This fatigue failure is a result of excessive compressive stresses occurring at the bone–implant interface. For the purpose of this study, the minimum principal stresses (ie, the largest compressive stress component) have been reported. For migration to occur, global failure of the underlying cancellous bone is required. In a similar fashion to Bartel et al [14] and Taylor et al [19], the average cancellous bone stresses in the medial compartment have been reported as a percentage of the ultimate compressive strength. This percentage represents the risk factor for global failure of the supporting cancellous bone.

Results

The stress distribution on the cancellous bone in the different models (varus-valgus angles and posterior angle) is shown in Fig. 4. Regardless of the orientation of the implant, the maximum cancellous bone stresses always appeared in the medial compartment. From 10° of valgus to neutral, the load-bearing area of the medial condyle remains relatively constant. From neutral to 10° of varus, however, the load-bearing area tends to decrease. In general, the peak cancellous bone stresses occurred at the medial-anterior rim of the resected surface in all of the models and varied from 9.27 MPa at neutral position to 3.78 MPa at 10° of valgus. There was a general trend for the peak cancellous bone stresses to increase as the position of the prosthesis was rotated from valgus into varus. There was some variability in the peak cancellous bone stresses, and this was thought to be due to local variations in the degree of cortical bone contact present in each model.

The average cancellous bone stresses occurring in each model are shown in Table 3. A general trend in the stresses was observed, suggesting that the more tilted to valgus the tibial plateau, the lower the stresses on the resected surface. First, we concentrate the analysis on the range of PA angles in which prostheses are implanted most commonly (5° varus to 5° valgus). In the range from 5° valgus to 2.5° varus, there is a 9% increase in the average cancellous bone stresses. Increasing the varus angle from 2.5° to 5° resulted in a substantial increase of 41% in the average stress on the medial resected surface. Comparing both extreme cases (±10°), the average cancellous bone stresses on the surface of the model in varus are nearly double that of the model in valgus. The posterior slope–implanted prosthesis (Fig. 4A) generated stresses 9% greater than those observed in the implant in a neutral position (Fig. 4B). The predicted risk of global failure in all models ranged from 22% in 10° valgus to 42% in 10° varus.

Discussion

The aim of this study was to examine the influence of the orientation of the tibial tray on the cancellous bone stresses because they are believed to relate most closely to migration and aseptic loosening [19,23–25]. The lowest stress and lowest risk of cancellous bone failure were obtained when the tibial tray was oriented in valgus. According to the tendency observed, the larger this valgus tilt, the lower the stresses within the cancellous bone. In this study, the varus-valgus angle referred to is the PA angle (Fig. 3). Between 10° of valgus and 2.5° of varus, there was only a 9% increase in the

1024 The Journal of Arthroplasty Vol. 15 No. 8 December 2000

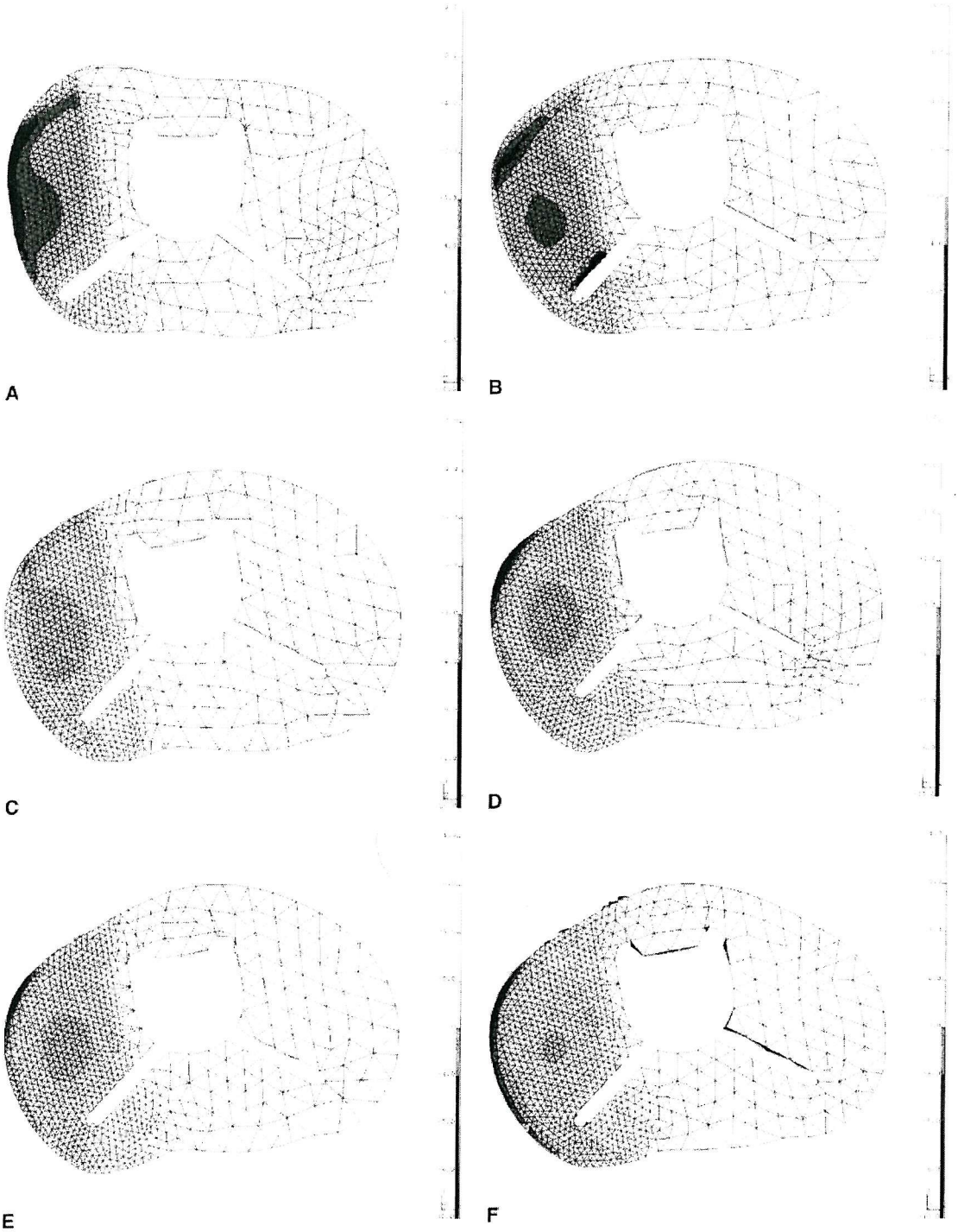

Fig. 4. Minimum principal cancellous bone stresses at the bone–implant interface for (A) 0°; (B) 7° posterior; (C) 2.5° varus; (D) 2.5° valgus; (E) 5° varus; (F) 5° valgus. (*Figure continues.*)

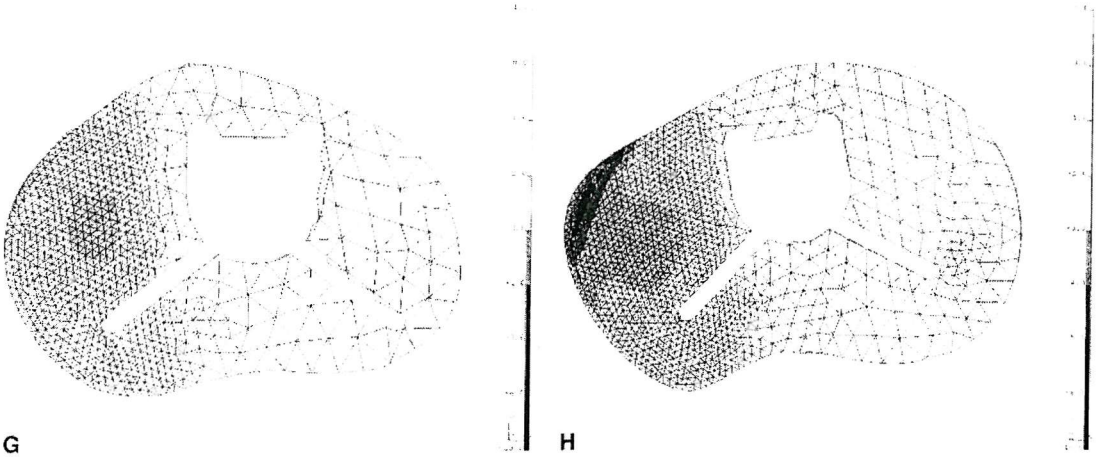

Fig. 4. *(Continued.)* (G) 10° varus; (H) 10° valgus.

global risk of cancellous bone failure. Increasing the varus angle by a further 2.5° produced a significant increase (41%) in potential risk for cancellous bone failure, however. This increase in risk was due to the reduction of the available load-bearing area on the higher-strength medial cancellous bone: The same load was being spread over a smaller area, leading to a significant elevation in the predicted cancellous bone stresses.

Many implant designs are available that include a posterior slope. To our knowledge, no experimental or clinical work has been performed to examine the influence of the PA angle on the likely performance of a tibial tray. This study has shown that the introduction of a posterior slope produces a marginal increase (9%) in the global risk for cancellous bone failure. This finding agrees with the score system used by Lotke and Ecker [11], which assumes that the optimal position of the tibial plateau is horizontal in both planes.

Table 3. Average Cancellous Bone Stress on the Medial Compartment

Plateau-Ankle Angle (°)	Stress (MPa)
10 varus	2.527
5 varus	2.398
2.5 varus	1.700
0	1.652
2.5 valgus	1.569
5 valgus	1.555
10 valgus	1.306
7 posterior	1.806

Comparison of these results with previous finite element studies is not easy because most of them used different bone and prosthesis geometries, material properties, and load conditions. Most studies performed previously employed bicondylar load cases [15,26,27], and they reported relatively low compressive cancellous bone stresses, of the order of 2 MPa. Taylor et al [19] analyzed a similar unicondylar load case and used the same tibial geometry and material properties and reported stresses of magnitudes comparable to those reported here. In the present study, the maximum risk of global cancellous bone failure of 42% was observed at 10° of varus, whereas the minimum of 22% was observed with the tibial tray oriented in 10° of valgus. These values are marginally lower than those of Taylor et al [19], who also predicted a maximum of 42% risk of global failure for a cemented, stemmed, metal-backed prosthesis as well as for a metal-backed tibial tray, assuming the same ultimate compressive strength for the medial cancellous bone. Slightly higher risks of global failure were observed for an all-polyethylene prosthesis (50%), however. Lewis et al [16] found a risk of global failure of 13% to 21% for 3 different cemented prostheses with bicondylar load conditions. Using similar load conditions, Bartel et al [14] reported risks of global failure of 9% to 33% for many cemented, metal-backed, and all-polyethylene prostheses. In these studies, ultimate compressive strength values of 11 MPa and 18.3 MPa were assumed. In the present study, a lower ultimate compressive strength was assumed because it was believed to be closer to the experimen-

tal values reported for human tibial cancellous bone [28,29].

This study has many limitations, including the cancellous bone being divided into three distinct isotropic regions as opposed to being transversely isotropic and heterogeneous. The influence of these limitations is discussed in depth by Taylor et al [19]. Also, extreme varus and valgus angles of 10° were examined. It is accepted that these angles are unlikely to be achieved in surgery because they would affect many other parameters, including the kinematics of the replaced joint, and cause potential patellar instability. To be positioned in such large varus-valgus angles, the tibial tray had to be displaced medially or laterally to avoid contact or penetration of the stem with the cortex of the medullar cavity and provide adequate coverage of the resected surface.

Another important limitation of this study is that the load was applied only to the medial condyle. Different loading situations may have resulted in different stresses and different conclusions. This loading condition may not be an appropriate assumption when large valgus angles are analyzed (10°) because under these circumstances, the load may not be transmitted through the medial condyle as it was assumed. Consequently, although the finite element models studied showed lower cancellous bone stresses with large valgus tibial cuts, excessive valgus orientation of the tibial tray still may lead to significant clinical complications.

Despite its limitations, this study supports the clinical findings in the literature. Various clinical studies have shown that the orientation of the components of total knee arthroplasty has a crucial effect on the performance of the replaced joint [7–10,30,31]. In general, these investigations suggest that HKA angles of a few degrees in valgus minimize the possibility of failure and that varus orientations lead to a higher risk of failure. This study has shown that varus orientation of the tibial plateau tends to increase the risk of cancellous bone failure, whereas valgus orientation of the prosthesis reduces the risk of failure. This study further supports the hypothesis proposed by Taylor et al [23] that implant migration and aseptic loosening is a result of the progressive failure of the supporting cancellous bone.

References

1. Bryan R, Rand J: Revision total knee arthroplasty. Clin Orthop 170:116, 1982
2. Cameron H, Hunter G: Failure in total knee arthroplasty: mechanisms, revisions, and results. Clin Orthop 170:141, 1982
3. Freeman M, Samuelson K, Bertin K: Freeman-Samuelson total arthroplasty of the knee. Clin Orthop 192:46, 1985
4. Insall J, Dethmers D: Revision of total knee arthroplasty. Clin Orthop 170:123, 1982
5. Moreland J: Mechanisms of failure in total knee arthroplasty. Clin Orthop 226:49, 1988
6. Thornhill T, Dalziel R, Sledge C: Alternatives to arthrodesis for the failed total knee arthroplasty. Clin Orthop 170:131, 1982
7. Bargren J, Blaha J, Freeman M: Alignment in total knee arthroplasty: correlated biomechanical and clinical observations. Clin Orthop 173:178, 1983
8. Jeffery R, Morris R, Denham R: Coronal alignment after total knee replacement. J Bone Joint Surg Br 73:709, 1991
9. Tew M, Waugh W: Tibiofemoral alignment and the results of knee replacement. J Bone Joint Surg Br 67:551, 1985
10. Lewallen D, Bryan R, Peterson L: Polycentric total knee arthroplasty: a ten-year follow-up study. J Bone Joint Surg Am 66:1211, 1984
11. Lotke P, Ecker M: Influence of positioning of prosthesis in total knee replacement. J Bone Joint Surg Am 59:77, 1977
12. Hilding M, Asplund S, Bäckbro B, et al: Alignment accuracy by two different instrumentation systems in total knee arthroplasty. Am J Knee Surg 6, 158 1993
13. Coull R, Bankes MJK, Rossouw DJ: Evaluation of tibial component angles in 79 consecutive total knee arthroplasties. Knee 6:235, 1999
14. Bartel DL, Burstein AH, Santavicca EA, et al: Performance of the tibial component in total knee replacement. J Bone Joint Surg Am 64:1026, 1982
15. Cheal EJ, Hayes WC, Lee CH, et al: Stress analysis of a condylar knee tibial component: influence of metaphyseal shell properties and cement injection depth. J Orthop Res 3:424, 1985
16. Lewis JL, Askew MJ, Jaycox DP: A comparative evaluation of tibial component designs of total knee prostheses. J Bone Joint Surg Am 64:129, 1982
17. Murase K, Crowninshield RD, Pedersen DR, et al: An analysis of tibial component design in total knee arthroplasty. J Biomech 16:13, 1983
18. Rakotomanana RL, Leyvraz PF, Curnier A, et al: A finite element model for evaluation of tibial prosthesis-bone interface in total knee replacement. J Biomech 25:1413, 1992
19. Taylor M, Tanner K, Freeman M: Finite element analysis of the implanted proximal tibia: a relationship between the initial cancellous bone stresses and implant migration. J Biomech 31:303, 1998
20. Cooke T, Kelly B, Li J: Prosthetic reconstruction of the arthritic knee: considerations for limb alignment, geometry of soft tissue reconstruction. Knee 5:165, 1998
21. Stiehl JB, Dennis DA, Komistek RD, et al: In vivo

determination of condylar lift-off and screw-home in a mobile-bearing total knee arthroplasty. J Arthroplasty 14:293, 1999
22. Morrison J: The mechanics of the knee joint in relation to normal walking. J Biomech 3:51, 1970
23. Taylor M, Tanner KE: Fatigue failure of cancellous bone: a possible cause of implant migration and loosening. J Bone Joint Surg Br 79:181, 1997
24. Taylor M, Tanner K, Freeman M, et al: Finite element modelling—a predictor of implant survival? Journal of Materials Science: Mat Medicine 6:808, 1995
25. Taylor M, Tanner K, Freeman M, et al: Cancellous bone stresses surrounding the femoral component of a hip prosthesis: an elastic-plastic finite element analysis. Med Eng Phys 17:544, 1995
26. Beaupre GS, Vasu R, Carter DR, et al: Epiphyseal-based designs for tibial plateau components. II: stress analysis in the sagittal plane. J Biomech 19: 663, 1986
27. Vasu R, Carter DR, Schurman DJ, et al: Epiphyseal-based designs for tibial plateau components. I: stress analysis in the frontal plane. J Biomech 19:647, 1986
28. Hvid I: Trabecular bone strength at the knee. Clin Orthop 227:210, 1988
29. Røhl L, Larsen E, Linde F, et al: Tensile and compressive properties of cancellous bone. J Biomech 24: 1143, 1991
30. Ritter M, Herbst S, Keating E, et al: Radiolucency at the bone-cement interface in total knee replacement: the effects of bone-surface preparation and cement technique. J Bone Joint Surg Am 76:60, 1994
31. Ecker ML, Lotke PA, Windsor RE, et al: Long-term results after total condylar knee arthroplasty: significance of radiolucent lines. Clin Orthop 216:151, 1987

APPENDIX B

ASSESSMENT OF THE QUALITY OF QCT-BASED FE MODELS OF PROXIMAL IMPLANTED TIBIAE

A. Perillo-Marcone[1], A. Alonso-Vazquez[1,2], M. Taylor[1]

[1]School of Engineering Sciences, University of Southampton, Highfield, Southampton, SO17 1BJ, UK

[2] Department of Orthopaedics, University Hospital in Lund, S22185 Lund, Sweden

(Submitted to Journal of Biomechanics and currently under review)

NOTATION

- FE: Finite Element
- FEA: Finite Element Analysis
- BW: Body Weight (kg)
- CT: Computed Tomography
- QCT: Quantitative Computed Tomography
- HU: Hounsfield Units
- E: Young's modulus (MPa)
- ΔE: Young's modulus increment (MPa)
- ρ: apparent density (g/cm^3)
- σ_u: ultimate compressive strength (MPa)

ABSTRACT

Three-dimensional, QCT based finite element models of a proximal implanted tibia were analysed in order to assess the effect of the material property discretisation on the stress distribution in the bone. The mesh was refined on the contact surfaces (matched meshes) with element sizes of 3, 2, 1.4, 1 and 0.8 mm. The same loading conditions were used in all models (bi-condylar load: 60% medial, 40% lateral).

Significant variations were observed in the modulus distributions between the coarsest and finest mesh densities. Poor discretisation of the material properties also resulted in poor correlations of the stresses and risk ratios between the coarsest and finest meshes. Little difference in Young's modulus, von Mises stress and risk ratio distributions were observed between the three finest models; hence it was concluded that for this particular case an element size of 1.4 mm on the contact surfaces was enough to properly describe the stiffness, stress and risk ratio distributions within the bone. It was concluded that unless there is convergence in the Young's modulus distribution, convergence of the stress field or of other parameters of interest will not occur either.

INTRODUCTION

In orthopaedics biomechanics, finite element analysis (FEA) is still only a comparative tool. The predictive capabilities of FEA can only be evaluated by performing prospective clinical trials in conjunction with patient specific FE modelling. Advances in image analysis tools and mesh generation software now make it possible to combine clinical and FE studies.

The quality of patient-specific finite element models is dependent on three parameters: the quality of the computed tomography (CT) images; the assignment of material properties to the mesh and the mesh density. In previous studies, quantitative computed tomography (QCT) has been used for the generation of FE models with a heterogeneous material distribution throughout the bone (Keyak and Skinner, 1992; Zannoni et al., 1998; van Rietbergen et al., 1999; Charras and Guldberg, 2000; Weinans et al., 2000; Cattaneo et al., 2001). There are essentially two methods to generate QCT-based FE models, which consist of: (a) generating finite elements from the voxels of the CT scan dataset (Keyak and Skinner, 1992; van Rietbergen et al., 1999; Charras and Guldberg, 2000; Weinans, et al., 2000) and (b) defining first the bone geometry (e.g. IGES format) from the CT scans, creating an FE mesh from this geometry and then assigning the moduli to the elements. The moduli can either be assigned as unique values to each element (Weinans et al., 2000) or by grouping elements with similar moduli together (Zannoni et al., 1998). It can be argued that the geometry based modelling technique is better as it describes the real geometry of the bone. In addition, it has been demonstrated that voxel-based FE models are likely to introduce errors in the results as all surfaces present sharp edges (discontinuities), hence stress concentration regions (Marks and Gardner, 1993).

Various authors have performed convergence analyses of voxel-based QCT FE models in which only the mesh density was varied. Keyak and Skinner (1992) have examined variation of the stress and strain distribution as well as the strain energy of models of a human proximal femur. They generated their models from CT scans with a pixel size of 1.38 mm and a separation between slices of 3 mm. Three different models were created with cubic elements of constant sizes of 4.8, 3.8 and 3.1 mm, respectively. They concluded that, for that case, a minimum element size of 3 mm (which is the same resolution of the voxels in the vertical direction, and 2.2 times the in-plane pixel size)

should be used in order to describe sharp variations in the material properties within the bone, and consequently, the stress/strain field within the model. They also suggest that due to the sensitivity of the results to the element size, the comparison of the stresses and strains predicted by different finite element models may not be valid if the element sizes used are not the same. In a later study, Marks and Gardner (1993) demonstrated that the use of the strain energy value as a parameter to assess convergence is not appropriate for this type of study. They tested a simple model and observed that even though the total strain energy appeared to have converged, the stress value at some points in fact diverged. In a recent work, Weinans et al. (2000) examined the influence of two different density-modulus correlations and four different load cases upon the stress-shielding behaviour of a prosthesis implanted in proximal femurs of dogs. They performed the study on voxel-based FE models of intact and implanted femurs of two dogs, with different stem stiffness values. They found that the difference in stress shielding between subjects was not dependent on the load case or the density-modulus correlation used, although there were slight differences in the stress shielding produced by the two density-modulus equations. Therefore, they suggested that, as long as the same load case and density-modulus correlation is used for all of the subjects, the difference in stress shielding between them can be examined.

Zannoni et al. (1998) analysed a model of a distal femur grouping the elements based on their material properties. They verified the convergence of the total strain energy by changing the number of groups of material properties, however, they used the same mesh density for the entire study. Cattaneo et al. (2001) compared two methods of assigning material properties to the glenoid part of a left embalmed scapula. The CT images that they used to create the models had a pixel size of 0.26 mm and a slice thickness of 2 mm. They checked convergence by analysing only the displacement of three sample nodes of five models with different mean element sizes, which ranged from 2.7 mm to 2.1 mm. Therefore, the elements used were significantly larger than the pixel resolution in the plane of each CT slice, but of a similar size to the slice thickness.

In the majority of the finite element models, the stress distribution is highly dependent upon the characteristics of the mesh used, i.e. element type and element edge length. If the material properties (i.e. Young's Modulus) are assigned to each element based on the QCT values, the results obtained from a finite element analysis could be even more dependent on the mesh quality, as the mechanical property distribution within the bone

model may not be adequately described. Therefore, variations in the predicted stress distribution between patients may be masked by errors induced in the mesh itself. The purpose of this study was to evaluate the effect of the mesh density on the resulting material property, stress and risk ratio distributions of three-dimensional FE models of an implanted tibia.

MATERIALS AND METHODS

Finite element models of a proximal tibia were generated from CT scan data (voxel size 0.468 x 0.468 mm with a 1 mm spacing in the proximal tibia) of a patient that was implanted with a Howmedica-Crucifix knee replacement. The model of the prosthesis was an approximation of the real design with small fillet radii removed (figure 1-a). A mesh of linear tetrahedral elements was created in I-DEAS Master Series 7.0 for both bodies (tibia and implant).

The material properties of the bone were assigned on an element-by-element basis by means of a freeware program called Bonemat, created at the Laboratorio di Tecnologia Medica – Istituti Ortopedici Rizzoli (Zannoni et al., 1998). This program functions by correlating the pixel intensity of the different slices of the CT dataset and the bone apparent density (McBroom et al., 1985; Snyder and Schneider, 1991) and between apparent density and Young's modulus (Ashman et al., 1989; Carter and Hayes, 1977; Linde et al., 1991; Linde et al., 1990). The CT scan image set used here included calibration phantoms that gave the necessary information to define the linear equation to convert image intensity in Hounsfield Units (HU) to apparent density (ρ) in g/cm^3 (equation 1). Since this equation did not work properly for small or negative values of HU, another linear equation was defined for this range, in order to avoid negative values of bone apparent density.

$$\begin{cases} \rho = 1.037 \cdot 10^{-4} \cdot (HU + 1000) & \text{for } -1000 \le HU \le 138 \\ \rho = 1.011 \cdot 10^{-3} \cdot (HU - 2000) + 2 & \text{for } HU > 138 \end{cases} \quad (1)$$

Several investigators have proposed equations to correlate apparent density with material Young's modulus (E) (Carter and Hayes, 1977; Ashman et al., 1989; Linde et al., 1990; Linde et al., 1991). In this study, the equation reported by Carter and Hayes (1977) was found to be the most suitable for cortical bone, whereas for trabecular bone, the equation reported by Linde et al. (1991) was considered more accurate, as it was generated from experimental tests performed on specimens obtained from proximal tibiae. Therefore, two different equations were used depending on the bone apparent density values (equation 2).

$$\begin{cases} E = 2003 \cdot \rho^{1.56} & \text{for } 0 \le \rho \le 0.778 \\ E = 2875 \cdot \rho^{3.0} & \text{for } \rho > 0.778 \end{cases} \quad (2)$$

Likewise, the equation reported by Linde et al. (1991) (equation 3) was used to calculate the ultimate strength based on local apparent density.

$$\sigma_u = 28.723 \cdot \rho^{1.65} \quad (3)$$

Once Bonemat has calculated the material property of each element, it creates groups of elements with Young's moduli that fall within a certain range and assigns the maximum stiffness found in each group (Zannoni et al., 1998). A separate study was performed to find the optimum parameters associated with Bonemat in order to get an adequate distribution of material properties. For this study, a logarithmic distribution function was used so that ΔE ranged between 0.5 and 10 MPa in the proximal tibia (were the moduli typically vary between 50 and 1000 MPa). This method results in an error from the unique modulus for any given element of no more than 2%. A summary of this work is given in the appendix.

Additionally, a process of "smoothing" of the CT data set was performed in order to attenuate excessive differences between neighbouring pixels. The purpose of smoothing the pixel intensity distribution throughout the image was to reduce the sensitivity of the results to the mesh density. The smoothing process was performed by converting each image from a 512 x 512 pixel format to 256 x 256 pixels of double the size (0.936 x 0.936 mm) and then converting it back to a format of 512 x 512 pixels of the original size (0.468 x 0.468 mm). The smoothing takes place in the first step as large peaks of intensity values present in a pixel are averaged with lower values of the neighbouring pixels (basically, the values of a square matrix of four pixels are grouped and converted into one single pixel of double the size). In the second conversion step, the pixels are halved in both dimensions (hence, four pixels are obtained from one) and the values of the new pixels are determined by means of a bilinear interpolation with the neighbouring ones. Both steps were performed automatically in Osiris 3.5.3 freeware. The bilinear interpolation was used to attenuate the effect of having groups of four adjacent pixels with the same intensity value, which could be significantly different than the neighbouring groups. Even though this process losses some of the information contained in the images, it was deemed appropriate as in this way, the material property

distribution was more stable. It should be noticed that in part, the large variation in the pixel intensities is caused by the instability of the scanner (mean and peak deviations of 26 HU and 133 HU, respectively, were found in the regions corresponding to air and the two calibration bars, which are supposed to have a constant value); hence it was believed that the smoothing would attenuate this problem. The number of material properties was slightly different in all models, however more than 500 material groups were used in all cases.

The mesh density of the contact surfaces were varied in order to examine the convergence of the Young's modulus, von Mises stress and risk ratio distributions on the proximal tibia. The risk ratio was calculated by dividing the von Mises stress present in an element by its correspondent ultimate compressive strength. Since the load case analysed presses the tibial plateau against the bone, it was considered that analysing the ratio between von Mises stress and compressive ultimate strength was an appropriate failure criteria in this case. For the convergence analysis, only the mesh on the surface of interest was refined, while the rest of the settings for the mesh of the entire model remained constant. The meshes of both bodies perfectly matched each other on the contact surfaces. Five different element edge lengths on the contacting surfaces were examined: 3, 2, 1.4, 1 and 0.8 mm, respectively. The number of nodes and elements used in each model are reported in table 1. The Young's modulus, von Mises stress and risk ratio distributions were reported along an arbitrarily chosen line (figure 2). In addition, mean and peak values of these parameters were also assessed for a 2-mm layer of the proximal tibia, artificially created so that the results could be assessed in exactly the same volume in all models (figure 1-b).

A bi-condylar load case was analysed, consisting of a medial force of 2029 N and a lateral force of 1352 N applied directly on the tibial plateau. The total force of 3381 N corresponds to three times the weight of the patient (115 kg) from whom the CT data was obtained. According to Morrison (1970), this is the maximum force observed during a normal gait cycle (3 x BW). The tibial polyethylene insert was not included in the model in order to simplify the analysis; hence, the forces were applied directly on the tibial plateau. Both forces were distributed between nodes situated on circular patches of 10 mm in diameter. The distal end of the tibia was rigidly fixed on all the nodes of the bottom surface of the model (figure 1-b).

All the analyses were carried out using MARC 2000.

RESULTS

The influence of mesh density was analysed in two ways, at a local level by comparing the nodal values along an arbitrarily chosen line and at the global level, by comparing the mean, peak and distribution of a given parameter within a pre-defined volume. First, let us examine the distribution of modulus, stress and risk ratio at the local level. The variation of these parameters along the line of interest (shown in figure 2) for the coarsest and finest meshes are depicted in figures 3-a to 3-c. Due to the large element size, the coarsest mesh is unable to capture the localised variations in the Young's modulus, particularly in the anterior-lateral aspect of the resected surface. In some places, there are differences of over 400% between the moduli assigned to the finest and coarsest meshes. Although the coarse mesh tends to follow the same general trend, it "averages out" the localised variations captured by the finer meshes. As a direct consequence of this poor discretisation of the material properties, large errors are propagated into the predicted von Mises stresses and the risk ratio, as shown in figure 3-b and 3-c. Both the von Mises stresses and the risk ratio are underestimated by the coarsest mesh in the regions where the material properties distribution is poorly discretised.

The convergence of the Young's modulus, von Mises stress and risk ratio distributions along the line of selected nodes were quantified by comparing the values of each node lying on the line of interest of a given mesh, with the values corresponding to the same position in the finest mesh (0.8 mm). Since in general, the node positions of any mesh are not the same as those of another mesh, a spline for each parameter (Young's modulus, stress and risk ratio) was generated with the data corresponding to the 0.8 mm mesh, in order to compare between different meshes. The degree of convergence obtained with the mesh refinement was assessed by examining the correlation coefficients and the mean residual errors (mean distance from regression line to data points) of each set of data, as shown in table 2 and figure 4. Close examination reveals that the coarser mesh densities tend to produce substantial errors in the modulus distribution by failing to capture the true stiffness variations. This is reflected by low correlation coefficients (0.66) and large residual errors (approximately 11 MPa) for the coarser meshes. However, these values were drastically improved as the element size was reduced, with the correlation coefficients and residual errors improving to 0.98 and 4.95 MPa, respectively. Comparison of the results from the two finest meshes would

suggest that the modulus distribution along the line of nodes has converged. Similar behaviour was observed in the von Mises stress (figure 4-b). There is clear evidence of improvement in the regression parameters as the element size is reduced. For the risk ratio, the regression lines and correlation coefficients did not show such large differences between models (figure 4-c and table 2); nevertheless, the mean residual error notably decreases as the element sizes are reduced, from approximately 9% with the coarsest mesh to 1% with the finest mesh.

The influence of mesh density was also assessed by examining the mean and peak values and the general distribution of each parameter within a 2mm slice of bone immediately adjacent to the implant (table 3). The mean Young's modulus value appears to have converged for all the mesh densities examined, at a value of approximately 213 MPa. However, the magnitude of the peak modulus value continues to increase as the mesh density is refined, rising from 3011 to 9310 MPa. For both the stress and the risk ratio, convergence of the mean values is slower. For the mean stress and risk ratio values there is a difference of approximately 20 and 22% respectively between the coarsest and finest mesh. There appears to be convergence for the three finest meshes, with a maximum variation in the stress and risk ratio values of 3.4 and 2.8% respectively. In a similar fashion to the modulus data, there is a corresponding increase in the peak values of stress and risk ratio as the mesh is refined.

Let us now concentrate on the risk ratio distribution within the volume of interest. In table 3 (last three columns on the right) it can be observed that, from the elements within 2-mm layer examined, the portion of volume that presented risk ratios in the bands of 60% – 80%, 80% – 100% and more than 100% seemed to have converged, as the values obtained from the three finest meshes show little variations between them. Conversely, the meshes with element sizes of 2 and 3 mm produced very different values from those corresponding to the other meshes. In figure 5 the elements were grouped in bands of 10% for the whole range of values of risk ratios found in the 2-mm layer of each model. In this graph, the same behaviour discussed above was observed, as the curves describing the risk ratio distribution in the layer of interest of the two coarsest models substantially differ from the curves corresponding to the other three models.

Even though the mean values of the parameters studied showed clear convergence, their peak values kept increasing as the mesh density was refined (table 3). For the Young's modulus, this behaviour was expected as Bonemat assigns the material properties to each element by averaging all the pixels related to it. In other words, the smaller the elements the higher the likelihood of capturing high intensity pixels without them being averaged with lower intensity pixels. This effect was then reflected in the peak von Mises values and consequently in the risk ratio (von Mises stress / ultimate compressive strength), which showed the same behaviour.

DISCUSSION

In the foreseeable future, patient specific finite element models will be used to assess the performance of total joint replacements. The quality of patient-specific finite element models is dependent on the quality of the CT images, the assignment of the material properties and the mesh density. Despite various studies having used CT based FE analysis of bony structures, very few have explicitly verified convergence of either the assigned material properties or the resulting stress/strain distribution (Zannoni et al., 1998; Weinans et al., 2000; Cattaneo et al., 2001). If the convergence of these parameters is not verified, the accuracy of a FE model may be uncertain. The objective of this study was to assess the accuracy of such models by testing the sensitivity of the assigned Young's modulus, von Mises stress and risk ratio to variations of the finite element size.

This study has shown that the assigned material properties were highly dependent on the element size. In certain areas of the resected tibial surface, there are rapid changes in modulus. Too coarse a mesh does not capture the subtle variations in the modulus distribution and in general gives highly erroneous modulus values. It was observed that unless there is convergence of the assigned material properties, convergence of the predicted stresses and risk ratios does not occur. To the authors' knowledge, no other study has examined the convergence of the assigned materials as a function of the mesh density, but as this study has shown it is critical to accurate predictions of other parameters of interest.

In this study the pixel size of the CT data was 0.468 x 0.468 mm with a slice thickness of 1 mm in the region of interest. An adequate discretisation of the material properties was only achieved when the element size approached the size of the slice thickness, i.e. when elements had an edge length of approximately 1 – 1.5 mm. Above this size, the mesh was unable to capture the rapid variations in modulus that occurred. This is due to the internal averaging of the pixel intensities when assigning the material properties to an element. Therefore it is recommended that in order to obtain convergence in the assigned material properties, the element size should be chosen to be similar to that of the pixel size of the CT scan.

Convergence was assessed at two levels, locally by examining variations at the nodal points and globally, by examining the mean and peak values within a pre-defined volume. At the local level, convergence of modulus was only achieved with an element edge length of 1.0 mm or smaller. Convergence of the stress and risk ratio was only achieved once the modulus distribution had also converged. At the global level, the mean modulus values and general distribution of the modulus appeared to have converged for all mesh densities. Even though the modulus distribution had converged, convergence was only achieved for the mean stress and risk ratio values with element edge lengths of 1.4 mm or less. Thus it would appear that at a local level, a finer mesh is required to gain convergence than at a global level. This highlights the need for performing adequate convergence checks, which are appropriate to the type of analysis being performed. If nodal values (e.g. nodal stresses) are examined, performing a convergence study of a global parameter, such as the mean stress or the strain energy within a given volume, may not be adequate.

A limitation of this study is that linear tetrahedral elements were used. The authors accept the fact that these elements have poor performance and may not accurately predict the stresses in regions with a large stress gradient. However, the conclusions of this study, with regard to gaining convergence of the assigned material properties remain valid. The majority of the material assignment programs assign the modulus to the element; therefore, if second order tetrahedral elements were used instead of the linear ones, in order to obtain the same modulus distribution, the same element size (edge length) would still be required. These statements seem to contradict the findings reported by (Polgar et al., 2001), who obtained better results using larger second order tetrahedral elements instead of smaller linear ones. They observed that using the same number of degrees of freedom, second order tetrahedral meshes produced a notably more stable solution. However, they used a model with a uniform material property throughout the whole volume. In this study, a heterogeneous material property distribution in the bone was used. Therefore, the concept of using larger higher order elements would no longer be valid, as small element sizes would be required in order to achieve convergence of the Young's modulus distribution across the model of the tibia.

This study has shown that accurate assignment of the material properties is critical in achieving convergence of other parameters such as stress and risk ratio. If convergence of the assigned material properties is not achieved, then errors are then propagated

through to other parameters of interest. To the authors knowledge, this is the first time that it has been shown that the assigned material properties in models of bony structures are influenced by the mesh density.

ACKNOWLEDGMENTS

Financial support was generously supplied by the following organizations:

- CONICIT - Universidad Simón Bolívar (Venezuela)
- The Medical Faculty, Lünd University
- The Swedish Medical Research Council (project 09509)
- The Swedish Foundation for Strategic Research

LIST OF TABLES

Table 1. Number of nodes and elements in each model.

Element edge length (mm)	**BONE**		**IMPLANT**		**TOTAL**	
	Nodes	**Elements**	**Nodes**	**Elements**	**Nodes**	**Elements**
3	1956	7345	1054	2983	3010	10328
2	3180	11790	2095	6466	5275	18256
1.4	5988	22710	4420	14813	10408	37523
1	12216	49119	8801	30562	21017	79681
0.8	19701	80995	14393	51865	34094	132860

Table 2. Correlation coefficients (r) and mean residual errors (MRE) for the different meshes compared with the 0.8 mm one.

Element edge length (mm)	**MODULUS**		**VON MISES**		**RISK RATIO**	
	r	**MRE (MPa)**	**r**	**MRE (MPa)**	**r**	**MRE (%)**
3	0.660	11.140	0.588	0.106	0.921	8.957
2	0.819	12.088	0.732	0.096	0.911	9.866
1.4	0.915	7.383	0.858	0.026	0.907	3.223
1	0.983	4.595	0.952	0.047	0.952	1.016

Table 3. Mean and peak values of Young's modulus, von Mises stress and risk ratio in the volume analysed (2-mm layer). The last three columns give a rough description of the risk ratio distribution in the layer of elements studied.

Element size (mm)	Modulus (MPa)		Von Mises (MPa)		Risk Ratio (%)		60%< R <80%	80%< R <100%	R > 100%
	mean	peak	mean	peak	mean (*)	peak	(% Vol)	(% Vol)	(% Vol)
3.0	214.1	3011	1.027	14.3	47.0 (38.7)	265.4	9.8	5.9	8.6
2.0	209.4	3434	1.086	17.6	49.3 (40.8)	289.4	12.5	8.6	7.2
1.4	212.6	6655	1.237	25.9	58.3 (49.9)	325.2	15.4	10.8	12.4
1.0	213.7	5454	1.270	33.3	59.1 (51.9)	410.2	16.1	10.2	13.8
0.8	213.4	9310	1.228	55.4	57.5 (49.6)	858.9	16.8	9.4	11.6

R = Risk Ratio
(*) Median values

LIST OF FIGURES

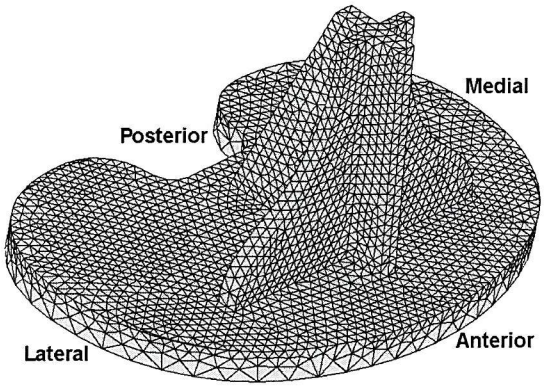

(a)

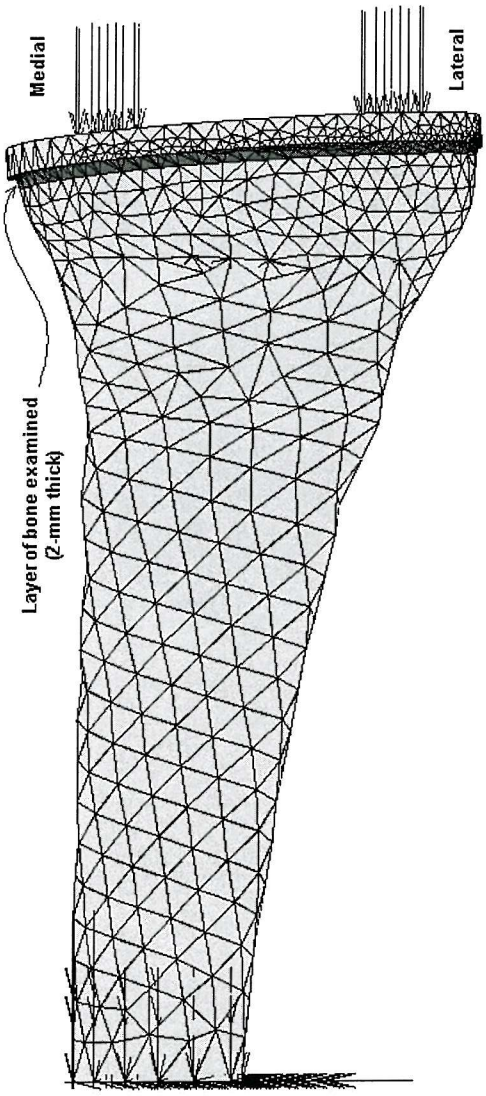

(b)

Figure 1. Model analysed. (a) FEM of the implant. (b) Complete model including boundary conditions.

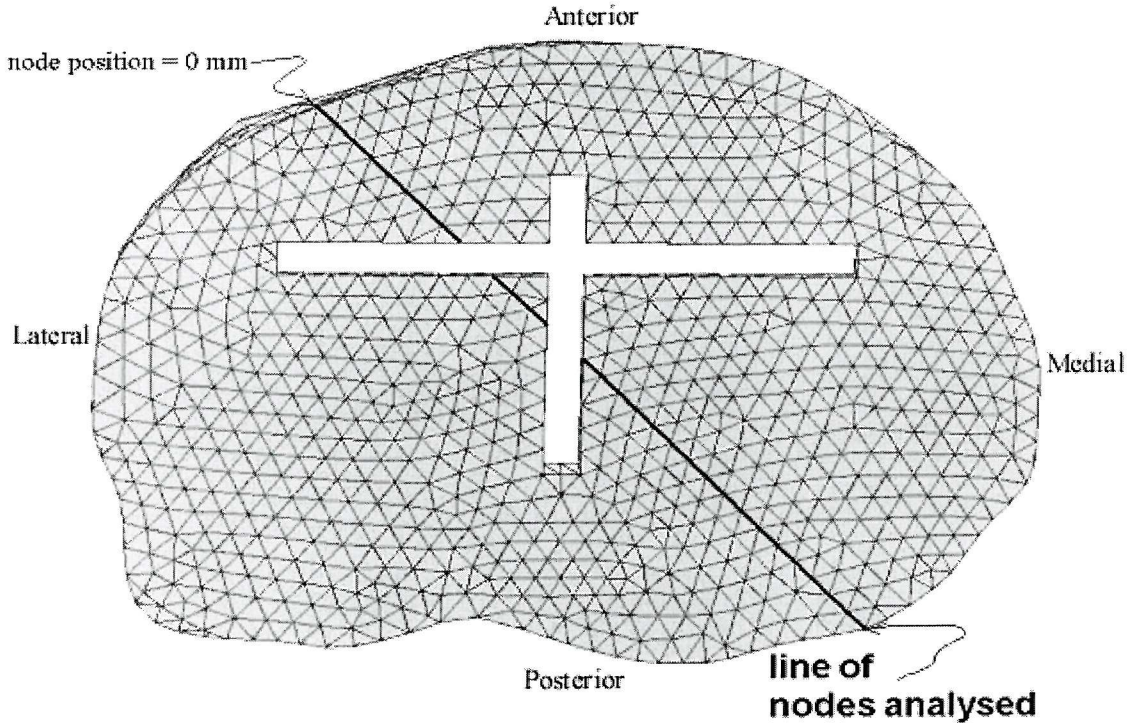

Figure 2. Line along which the results were reported (model with an element edge length = 2 mm).

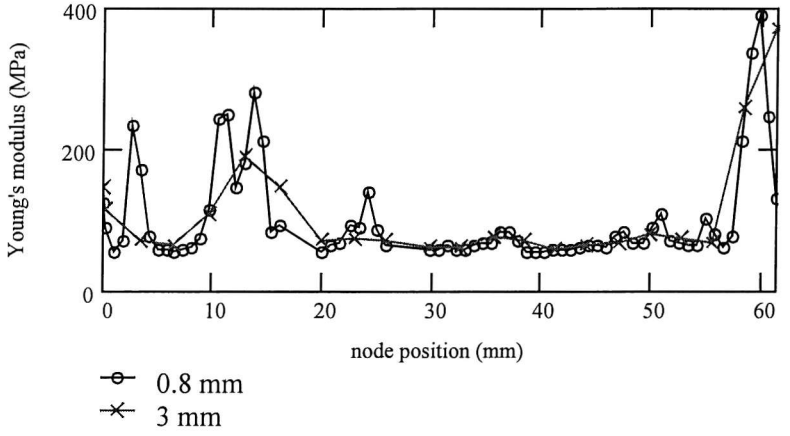

(a)

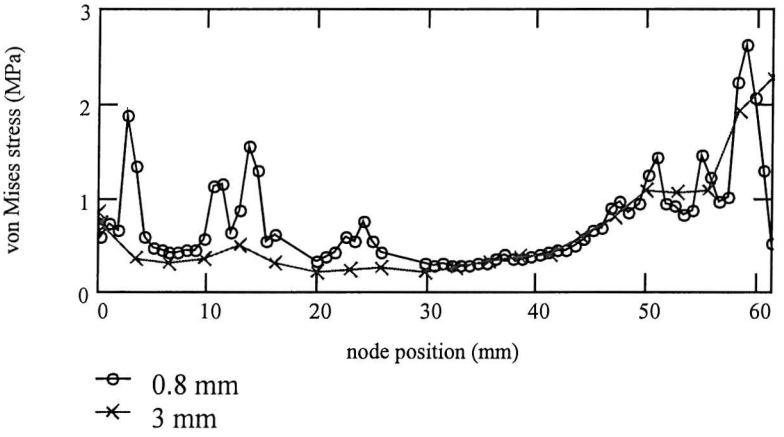

(b)

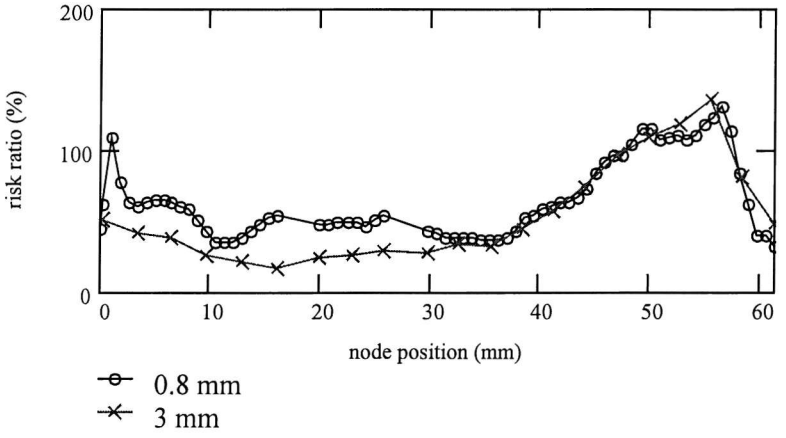

(c)

Figure 3. Stiffness (a), stress (b) and risk ratio (c) values on the nodes along the line of interest for the coarsest and finest meshes.

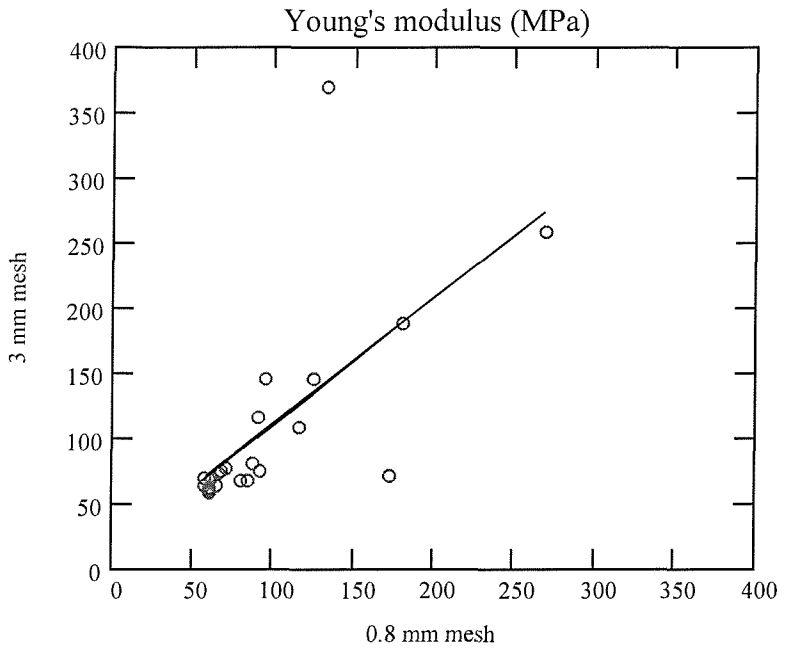

r = 0.660

MRE = 11.140

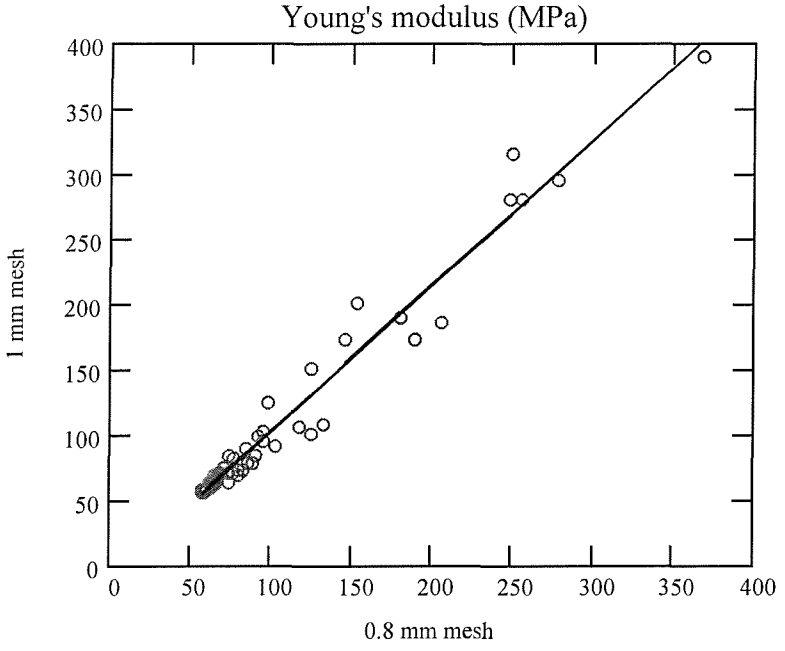

r = 0.983

MRE = 4.595

Figure 4. Regression lines for the values at the nodes along the line of interest of the 3 mm and 1 mm meshes. (a) Young's modulus.

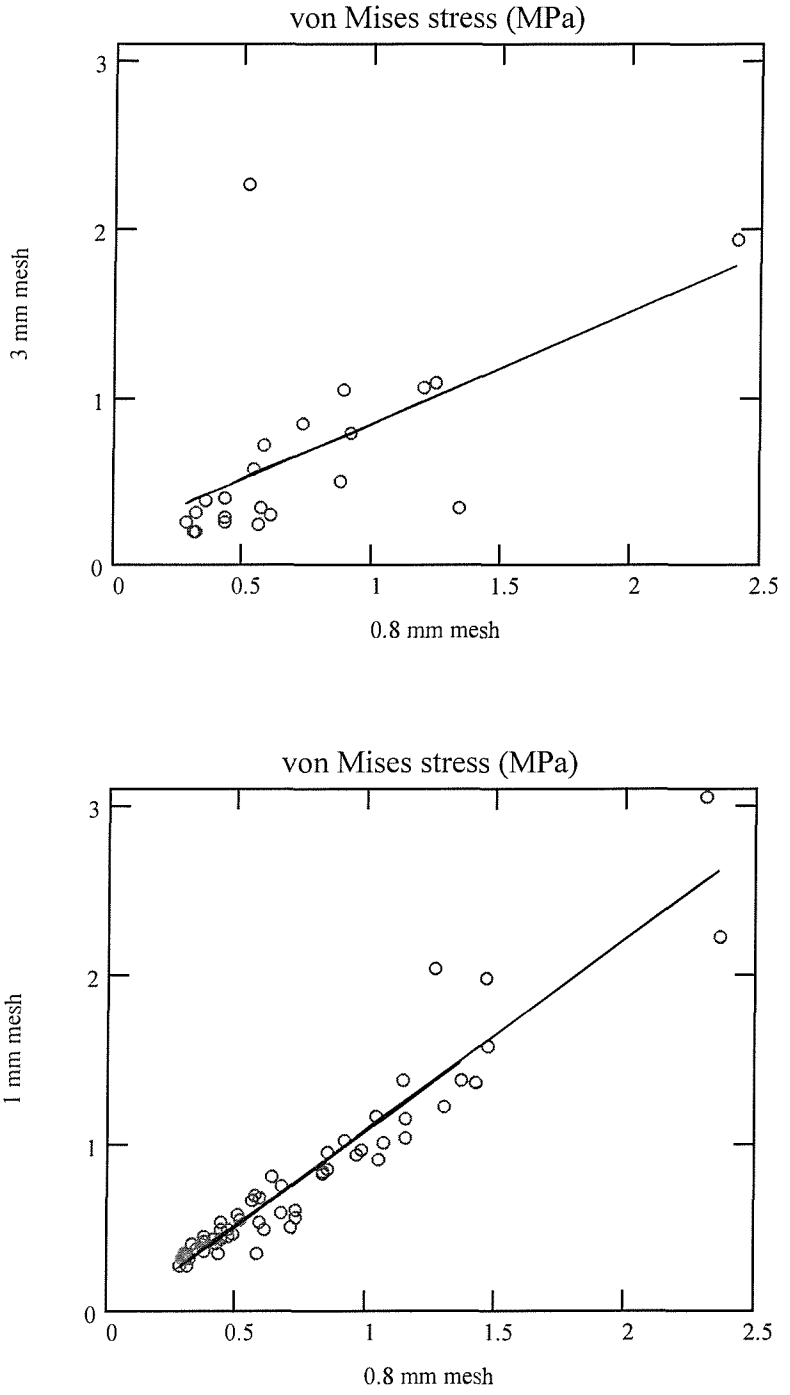

Figure 4. Regression lines for the values at the nodes along the line of interest of the 3 mm and 1 mm meshes. (b) Von Mises stress.

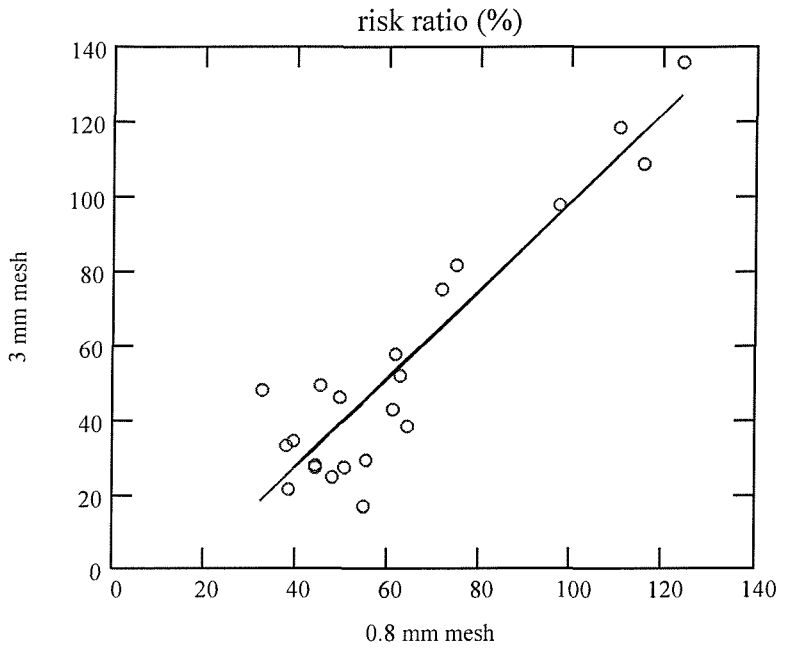

r = 0.921

MRE = 8.957

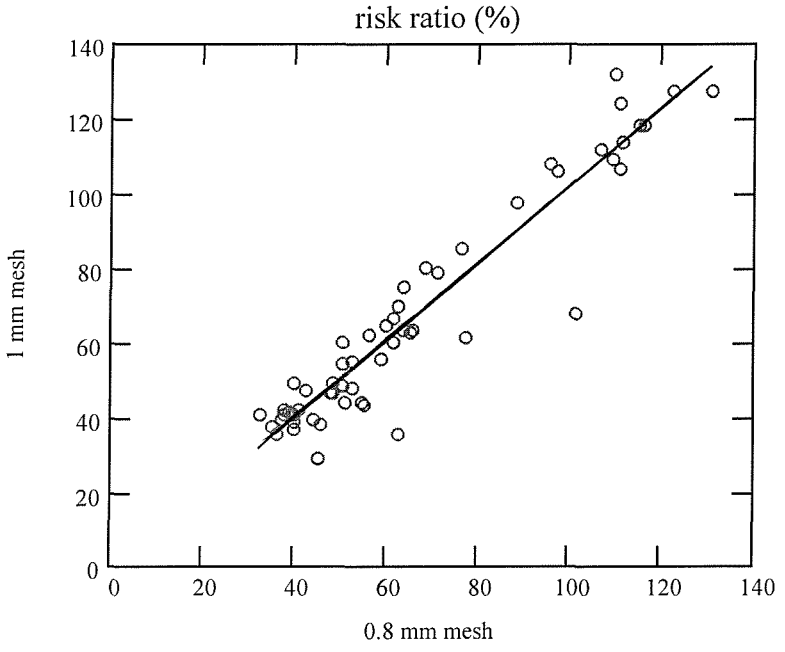

r = 0.952

MRE = 1.016

Figure 4. Regression lines for the values at the nodes along the line of interest of the 3 mm and 1 mm meshes. (c) Risk ratio.

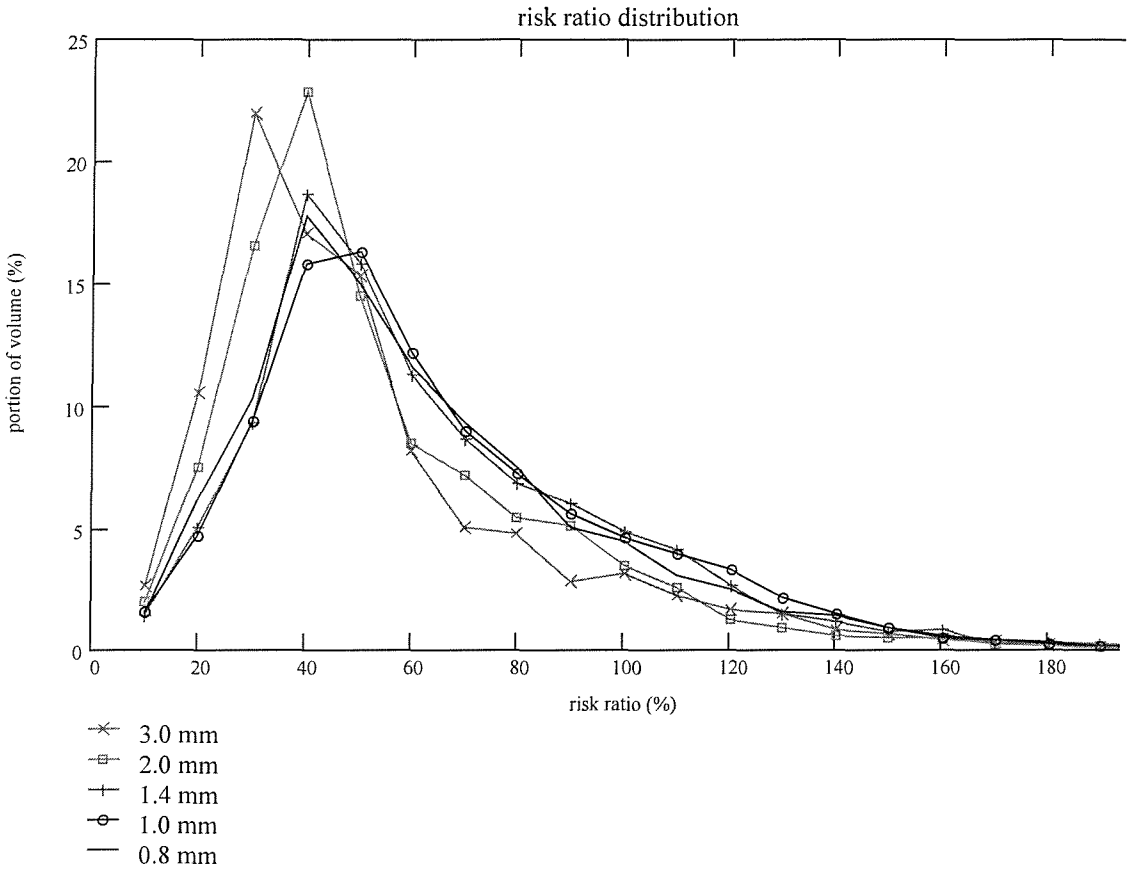

Figure 5. Risk ratio distribution in the volume of interest.

REFERENCES

Ashman, R. B., Rho, J. Y. and Turner, C. H. (1989) Anatomical variation of orthotropic elastic moduli of the proximal human tibia. J Biomech 22, 895-900.

Carter, D. R. and Hayes, W. C. (1977) The compressive behavior of bone as a two-phase porous structure. J Bone Joint Surg [Am] 59, 954-62.

Cattaneo, P. M., Dalstra, M. and Frich, L. H. (2001) A three-dimensional finite element model from computed tomography data: a semi-automated method. Proc Inst Mech Eng [H] 215, 203-13.

Charras, G. T. and Guldberg, R. E. (2000) Improving the local solution accuracy of large-scale digital image-based finite element analyses. J Biomech 33, 255-9.

Keyak, J. H. and Skinner, H. B. (1992) Three-dimensional finite element modelling of bone: effects of element size. J Biomed Eng 14, 483-9.

Linde, F., Norgaard, P., Hvid, I., Odgaard, A. and Soballe, K. (1991) Mechanical properties of trabecular bone. Dependency on strain rate. J Biomech 24, 803-9.

Linde, F., Pongsoipetch, B., Frich, L. H. and Hvid, I. (1990) Three-axial strain controlled testing applied to bone specimens from the proximal tibial epiphysis. J Biomech 23, 1167-72.

Marks, L. W. and Gardner, T. N. (1993) The use of strain energy as a convergence criterion in the finite element modelling of bone and the effect of model geometry on stress convergence. J Biomed Eng 15, 474-6.

McBroom, R. J., Hayes, W. C., Edwards, W. T., Goldberg, R. P. and White, A. A. (1985) Prediction of vertebral body compressive fracture using quantitative computed tomography. J Bone Joint Surg [Am] 67, 1206-14.

Morrison, J. (1970) The mechanics of the knee joint in relation to normal walking. J Biomech 3(1), 51-61.

Polgar, K., Viceconti, M. and O'Connor, J. J. (2001) A comparison between automatically generated linear and parabolic tetrahedra when used to mesh a

human femur. Proceedings of the Institution of Mechanical Engineers Part H-Journal of Engineering in Medicine 215, 85-94.

Snyder, S. M. and Schneider, E. (1991) Estimation of mechanical properties of cortical bone by computed tomography. J Orthop Res 9, 422-31.

Taylor, M., Tanner, K. and Freeman, M. (1998) Finite element analysis of the implanted proximal tibia: a relationship between the initial cancellous bone stresses and implant migration. J Biomech 31(4), 303-10.

Van Rietbergen, B., Muller, R., Ulrich, D., Ruegsegger, P. and Huiskes, R. (1999) Tissue stresses and strain in trabeculae of a canine proximal femur can be quantified from computer reconstructions. J Biomech 32, 443-51.

Weinans, H., Sumner, D. R., Igloria, R. and Natarajan, R. N. (2000) Sensitivity of periprosthetic stress-shielding to load and the bone density-modulus relationship in subject-specific finite element models. J Biomech 33, 809-17.

Zannoni, C., Mantovani, R. and Viceconti, M. (1998) Material properties assignment to finite element models of bone structures: a new method. Med Eng Phys 20, 735-40.

APPENDIX

For the purpose of this study, a freeware program called Bonemat (Laboratorio di Tecnologia Medica – Istituti Ortopedici Rizzoli (Zannoni, et al., 1998)) was used to assign the material properties to the tibia. Rather than assigning a unique modulus to every element, Bonemat creates groups of elements with Young's moduli that fall within a certain range and assigns the maximum stiffness found in each group (Zannoni, et al., 1998). In this way, the user controls the number of material properties utilised in the model by defining an increment in the Young's modulus (ΔE). In the original version of bonemat, ΔE remains constant throughout the whole range of stiffness values in the model, therefore, it is necessary to use a large number of different Young's moduli (small ΔE) to get a suitable distribution of material properties between the elements of the proximal tibia, which is mostly cancellous bone. The finite element solver used in this study is limited to 600 different materials and this limitation would not allow for adequate discretisation of the cancellous bone. In order to optimise the material property distribution throughout the model and maintain the number of material properties below 600, a logarithmic increment of ΔE was introduced with the aim at obtaining a finer discrimination of mechanical properties at lower stiffness values.

A finite element model, which consisted of linear tetrahedral elements (created in I-DEAS Master Series 7.0), was generated for the proximal tibia of this article (same geometry). On the resected surface of the tibia, the element edge length was set to 2 mm for the region around the stem, and 3-mm for the rest of the elements. For the rest of the model the element edge length was set to 5 mm. By defining these parameters, meshes of 15907 and 5636 elements were obtained for the bone and the tibial tray, respectively.

The material properties of the bone were assigned on an element-by-element basis by using the Bonemat program. Equations 1 to 3 were used to convert from Houndsfield Units (HU) to apparent density (ρ) and from apparent density to Young's modulus (E). Maximum and average values of Young's moduli, von Mises stresses and risk ratios on the resected surface of the tibia were examined for various numbers of material properties, in order to evaluate the convergence of these parameters. All the analyses were carried out using MARC K7.3.2.

The peak and mean values of Young's modulus, for different numbers of material properties were assessed. Convergence in the assigned material properties was achieved when more than 400 material groups were used (figure A.1).

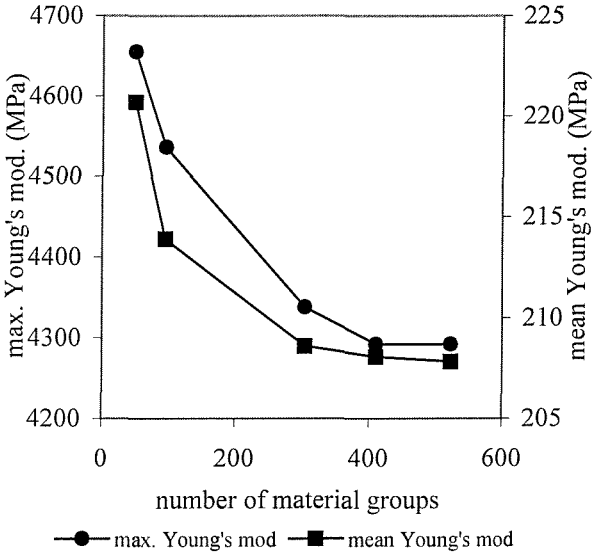

(a)

Figure A.1. Maximum and mean values of Young's modulus (a), von Mises stress (b) and risk ratio (c) on the resected surface, for models with different number of material properties.

As mentioned above, by using a logarithmic increment to assign the material properties, ΔE is smaller for lower stiffness values. Specifically, in the models studied here, the great majority of the elements in the proximal end of the tibia have Young's moduli of less than 1000 MPa. Figure A-2 shows the maximum error in the material property that an element may present with respect to its "real" value (actual value that it would have if each element were assigned a unique material property). Each circle in the graph corresponds to a material group (Young's modulus values assigned to each group indicated on the horizontal axis), for which the maximum error of the elements contained in it (i.e. ΔE) was calculated as a percentage of its assigned material property (vertical axis). In this graph, only the material groups with Young's moduli corresponding to the proximal tibia ($50 \lesssim E \lesssim 1000$) are represented.

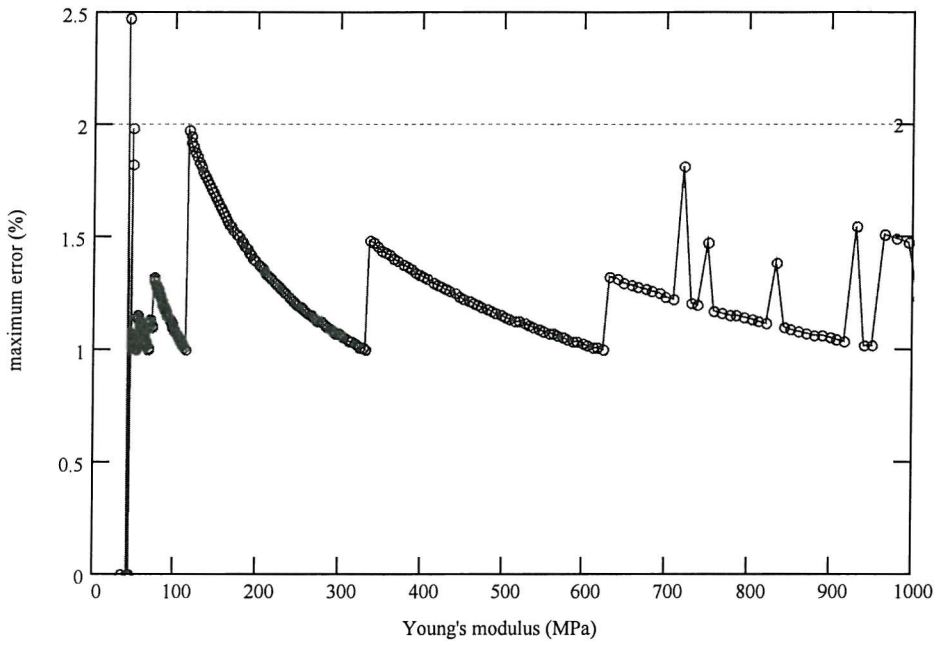

Figure A-2. Maximum error in the material properties of the elements within each material group in the proximal tibia.

It can be observed that in this case, the majority of elements have an error below 2% (i.e. less than 2% difference between their real and assigned modulus), with only one material group having an error of 2.5%. It should be mentioned that the latter is composed by only two elements, meaning that at worst one of them has the exact material property corresponding to the pixels contained in it ("real" value), and the other one may have a maximum error of 2.5% with respect to its correspondent "real" value. This small difference is very unlikely to have any significant effect on the stress and risk ratio distributions; hence, in terms of the results from the models, this method is deemed to be equivalent to assigning a unique material property to each element.

APPENDIX C

FINITE ELEMENT ANALYSIS OF PROXIMAL IMPLANTED TIBIA: ASSESSMENT OF PROSTHETIC ALIGNMENT

A. Perillo-Marcone, M. Taylor

Bioengineering Sciences Research Group, University of Southampton, Southampton/UK

(Presented at the 12th Conference of the European Society of Biomechanics, Dublin, 2000)

12th Conference of the European Society of Biomechanics, Dublin, 2000

Finite element analysis of proximal implanted tibia: assessment of prosthetic alignment

A. Perillo-Marcone, M. Taylor

Department of Mechanical Engineering, University of Southampton, Southampton, UK.

Introduction

Various clinical studies have suggested that alignment of TKR components affects the rate of aseptic loosening. Knees presenting postoperative valgus alignment have shown a lower risk of failure or loosening [1,2]. The majority of studies only examine the overall (HKA) alignment of the limb and do not examine each component separately. However, Coull et al. [3] has shown that the tibial component angle can vary from 81 to 96 degrees, with 48% of knees studied being in a sub-optimal varus orientation. To date no analytical or experimental study has been performed to confirm the observation that malalignment may increase the bone stresses and hence the risk of loosening.

Relatively few finite element analyses of the implanted proximal tibia have been carried out and all have assumed perfect alignment of the prosthesis [e.g. 4]. The aim of this investigation was to (i) examine the effect of the plateau angle on the cancellous bone stress (mal-positioning of the tibial component), (ii) analyse the significance of the anterior-posterior angles of the tibial component on these stresses and (iii) correlate these findings with clinical data.

Materials and methods

A three-dimensional finite element model of a tibia implanted with a flanged type plateau (Dual Bearing Knee, MMT Ltd, UK) was analysed. The tibia was divided into 5 different regions, those of diaphyseal and metaphyseal cortical bone and the medial, intercondylar and lateral cancellous bone. The cemented fixation was modelled by adding a 1-mm layer of cement covering the top surface of the tibia in its entirety. No cement was added around the stem or flanges, however the metal-cancellous bone interface was modelled as bonded. All materials were assumed to be isotropic, homogeneous and linear elastic. The proximal tibia was dissected at seven different PA angles (0°, ±2.5°, ±5° and ±10°).

In addition, two AP angles (sagital plane) were included in the analysis, neutral (0°) and 7° posterior slope. A distributed uni-condylar load of 2.2 kN was applied on the medial side of the plateau, in the same direction of the long axis of the tibia in all cases. The distal end of the tibia was rigidly constrained. All analyses were carried out using I-DEAS™ Master Series 6. Tetrahedral second order (10 noded) elements were used in all models. The peak and average minimum principal stresses in the medial compartment have been reported. The global risk of cancellous bone failure was also assessed by expressing the average cancellous bone stresses as a function of the ultimate compressive strength.

Results

The average medial cancellous bone stresses occurring in each model are shown in Table 1. A general trend was observed, with an increase in the average cancellous bone stresses as the tibial component was tilted in varus.

Table 1. Average medial cancellous bone stresses [Mpa]

PA angle	10° var	5° var	2.5° var	0°	2.5° val	5° val	10° val	AP= 7°
Stress (MPa)	2.53	2.40	1.70	1.65	1.57	1.56	1.31	1.81

A similar trend was observed in the peak cancellous bone stresses, increasing from 3.784 to 8.450 MPa as the tibial tray was tilted from 10 degrees of valgus to 10 degrees of varus. In the range from 5° valgus to 2.5° varus there was a 9% increase in the average cancellous bone stresses. Increasing the varus angle from 2.5° to 5° resulted in a substantial increase of 41% in the average stress on the medial resected surface. Comparing both extreme cases (±10°), the average cancellous bone stress in the model in varus is nearly double of that in valgus. The posterior-slope prosthesis generated stresses that were 9% greater than those observed in the implant in a neutral position. Risk of global failure in all models ranges from 22% in 10° valgus to 42% in 10° varus.

Discussion and conclusions

The aim of this work was to examine the influence of prosthetic alignment of the cancellous bone stresses. In general, lowest risks of cancellous bone failure were obtained when the PA angle was in valgus. Moreover, according to the tendency observed (Table 1); the larger this valgus tilt was the lower were the stresses on the cancellous bone. In terms of the AP angle, lower stresses were obtained when the tibial plateau was in a horizontal position, compared to those generated when the AP angle was 7°. The results of this study are in good agreement with clinical observations. Various clinical studies have suggested that HKA angles of a few degrees in valgus minimise the possibility of failure [1,2]. As far as we are aware, no work has been done on analysing the effect of PA angles on the likelihood of survivorship of the implant.

In general, this study supports the clinical findings in the literature. A varus orientation of the tibial plateau tends to increase the risk of cancellous bone failure, and hence the associated risk of migration and aseptic loosening.

References

[1] Bargren et al. Clin Orthop 1983; 173: 178-83. [2] Ritter et al. J Bone Joint Surg Am 1994; 76(1): 60-5. [3] Coull et al. Knee 6 (1999), 235-237 [4] Taylor et al. J Biomech 1998; 31(4): 303-10

Acknowledgements

Financial support was supplied by CONICIT and Universidad Simón Bolívar (Venezuela).

APPENDIX D

INTER-PATIENT EVALUATION OF STRESSES IN PROXIMAL IMPLANTED TIBIAE

A. Perillo-Marcone [1], L. Ryd [2], M. Taylor [1]

[1] Bioengineering Sciences Research Group, University of Southampton, Southampton/UK

[2] University Hospital Lünd, Lünd/Sweden

(Presented at the XVIIIth Congress of the International Society of Biomechanics.

ETH Zurich, Switzerland, 2001)

Inter-patient evaluation of stresses in proximal implanted tibiae

A. Perillo-Marcone[1], L. Ryd[2], M. Taylor[1]
[1]Bioengineering Sciences Research Group, University of Southampton, Southampton/UK
[2]University Hospital Lünd, Lünd/Sweden

Introduction

In biomechanics, finite element analysis (FEA) is still only a comparative tool. The predictive capabilities of FEA can only be evaluated by performing prospective clinical trials in conjunction with patient specific FE modelling. Previous 3D finite element studies of implanted tibiae (Taylor et al., 1998) have modelled a single tibia and have assumed that the results are generic and applicable to the whole patient population. To the authors' knowledge, no study has examined multiple tibiae or included patient specific data, such as body weight, bone mechanical properties and component alignment. Only by constructing finite element models taking into account these parameters in combination with prospective clinical studies can the predictive power of FEA be assessed. The purpose of this study was to evaluate the differences in the predicted stresses and risk ratios observed on the resected surface of models of proximal implanted tibiae created from patient specific data.

Materials and Methods

Finite element models of four proximal implanted tibiae were analysed. The models were created from quantitative computed tomography (QCT) data of patients operated in University Hospital-Lünd. In all patients, the type of prosthesis implanted was a cementless, hydroxyapatite (HA) coated Howmedica-Crucifix knee replacement. The immediate post-operative situation was modelled by assuming frictionless contact between the tibia and the tibial plateau. Additionally, post-operative x-ray images in both the sagittal and frontal planes were used to determine the vertical tibial plateau position and alignment relative to the tibia in each patient.

Meshes of linear tetrahedral elements were created in I-DEAS for both bone and implant. Based on a previous mesh convergence study, it was concluded that an element edge length of 1.4 mm should be used on the contact surfaces of the tibia for all the models. The mesh of the implant was created in a way that it perfectly matched that of the bone, as it was noticed that this configuration produced more stable results. A program called Bonemat, developed at the Laboratorio di Tecnologia Medica – Istituti Ortopedici Rizzoli (Bologna-Italy), was used to assign the material properties on an element-by-element basis (Zannoni et al., 1998). This process is based on the correlation between QCT data and the material properties of the bone (McBroom et al., 1985; Carter et al., 1977; Linde et al., 1991). A linear correlation was defined (using calibration phantoms present in the CT images) to convert image intensity values in Hounsfield Units (HU) to apparent density (ρ) in g/cm^3 (Equation 1). Since this equation did not work properly for small or negative values of HU, another linear equation was defined for this range, avoiding in this way negative values of bone apparent density.

$$\begin{cases} \rho = 1.037 \cdot 10^{-4} \cdot (HU + 1000) & \text{for } -1000 \le HU \le 138 \\ \rho = 1.011 \cdot 10^{-3} \cdot (HU - 2000) + 2 & \text{for } HU > 138 \end{cases} \quad (1)$$

In order to convert apparent density values (ρ) to material Young's modulus (E), the equation reported by Carter and Hayes (1977) was found to be the most suitable for cortical bone. For trabecular bone, the correlation published by Linde et al (1991) was considered more accurate, as it was generated from experimental tests performed on specimens obtained from proximal tibiae. Therefore, two different equations were used depending on the bone apparent density values (Equation 2).

$$\begin{cases} E = 2003 \cdot \rho^{1.56} & \text{for } 0 \le \rho \le 0.778 \quad \text{(Linde et al., 1991)} \\ E = 2875 \cdot \rho^{3.0} & \text{for } \rho > 0.778 \quad \text{(Carter et al., 1977)} \end{cases} \quad (2)$$

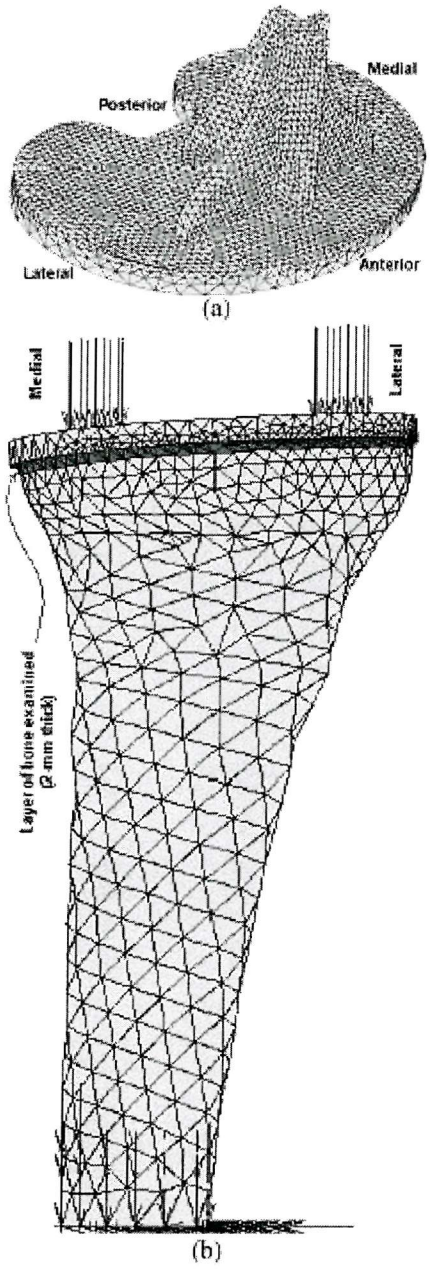

Figure 1: FE model of patient 2. (a) FEM of the implant. (b) Complete model including boundary conditions.

The distal end of the tibia was rigidly constrained. The loads used in the models (Table 1) were equivalent to three times the weight of each patient (Morrison, 1970). A bi-condylar load case was used, in which 60% of the total force was applied on the medial side and 40% on the lateral side. The tibial polyethylene insert was not included in order to simplify the analysis; therefore, the forces were applied directly on the tibial plateau (figure 1).

Risk ratio values (defined as the von Mises stress divided by the ultimate compressive strength) in a 2-mm thick layer of the proximal tibia were examined and compared between all four models (figure 1). A value greater than 100% indicates that failure of the supporting bone is likely to occur.

All the analyses were carried out using MARC 2000.

Patient No.	Weight (kg)	Medial Load (N)	Lateral Load (N)
1	135	2381	1588
2	115	2029	1352
3	89	1570	1047
4	74	1305	870

Table 1: Weights and loads used for each patient.

Results & Discussion

The risk ratio distributions on the resected surface for the four tibiae examined are shown in figure 2. In all four models, a noticeable difference in the overall risk ratio distribution on the contact surface was observed. Table 2 shows the peak and mean values of Young's modulus, von Mises stress and risk ratio for all patients.

In general, the peak values were found in the portion of cancellous bone supporting the posterior and frontal-lateral sides of the tibial plateau and (Figure 1). It was observed that, in some cases, a large portion of the resected surface of the tibia presented risk ratios greater than 100% (e.g. patient 2), whereas in patient 3, the percentage of volume with risk values exceeding 100% is significantly smaller (5.7%). This clearly shows how important it is to use patient specific data (in this case, mechanical properties of the bone).

The purpose of this study was to assess the risk of bone failure with four patient specific models. For all four tibiae, there were areas of bone, where the localised risk of failure was high. However, in general, the risk of failure was below 100% over the majority of the resected surface.

Patient Number	Modulus (MPa)		Von Mises Stress (MPa)		Risk Ratio (%)		Risk>100%
	mean	peak	mean	peak	mean	peak	(% Vol)
1	267.8	12850	1.187	61.2	60.8	262.6	8.2
2	212.6	6655	1.237	25.9	58.3	325.2	12.4
3	241.7	10090	0.741	17.3	44.1	282.0	5.7
4	141.7	11640	0.623	18.1	58.4	338.0	9.5

Table 2: Peak and mean values of Young's modulus, von Mises stress and risk ratio for the 2-mm layer of elements examined in each patient.

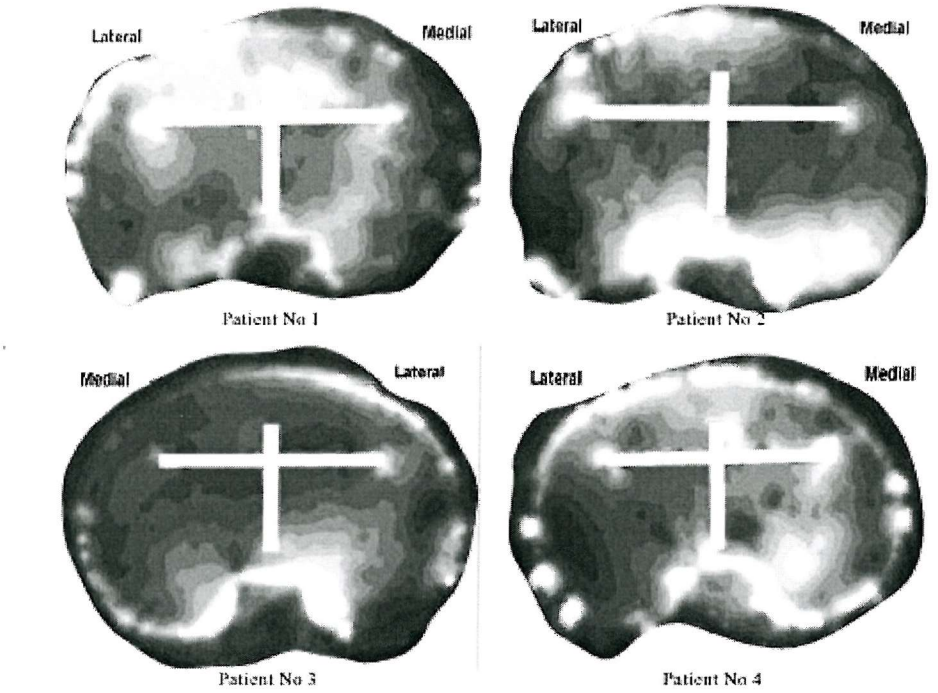

Figure 2: Risk ratio distribution on the resected surface of the four tibiae. Black indicates 0% risk of failure and white refers to a risk in excess of a 100%

Roentgen stereophotogrammetric analysis (RSA) studies of tibial plateaus have shown that during the first six months after surgery, there is a period of rapid migration. This is widely thought to be due to the implant "bedding in" (Ryd et al., 1995; Nilsson et al., 1996). The findings of this study support this view, as some regions presented considerably high risk ratios. In these regions, the cancellous bone will be crushed and the load redistributed on the resected surface until an equilibrium position is reached.

This study has shown that patient specific FE modelling does reveal significant differences in the predicted stress and risk ratio distributions. This emphasises the importance of moving away from the traditional generic modelling approach to patient specific modelling.

References

Taylor M. et al. J Biomech. 31(4) : Apr, 303-10, 1998.
Morrison J. J Biomech. 3(1): Jan, 51-61, 1970.
Zannoni C. et al. Med Eng Phys. 20 : 10, 735-40, 1998.
McBroom R.J. et al. J Bone Joint Surg [Am]. 67 : 8, 1206-14, 1985.
Carter DR et al. J Bone Joint Surg [Am]. 59 : 7, 954-62, 1977.
Linde F et al. J Biomech. 24 : 9, 803-9, 1991.
Ryd L. et al. J Bone Joint Surg Br. 77 : 3, 377-83, 1995.
Nilsson KG et al. J Bone Joint Surg Br. 78 : 1, 1-3, 1996.

Acknowledgements

Financial support was supplied by CONICIT and Universidad Simón Bolívar (Venezuela) by fully sponsoring the PhD of the main author.

APPENDIX E

OVERVIEW OF THE FINITE ELEMENT METHOD

The aim of this section is to give a brief overview of the finite element method. For more detailed descriptions of the finite element method the reader should consult the excellent texts of Zienkiewicz and Taylor or Fagan (1992).

In structural stress analysis, the displacements and stresses throughout the structure need to be determined. For objects displaying irregular geometries (e.g. bony structures), the stress/strain field cannot be determined by means of theoretical methods; hence the need of approximated techniques, such as the finite element method. The method is based on the division of a single domain into a set of simple subdomains called finite elements. These elements are connected to each other through joints, known as nodes (Figure E.1).

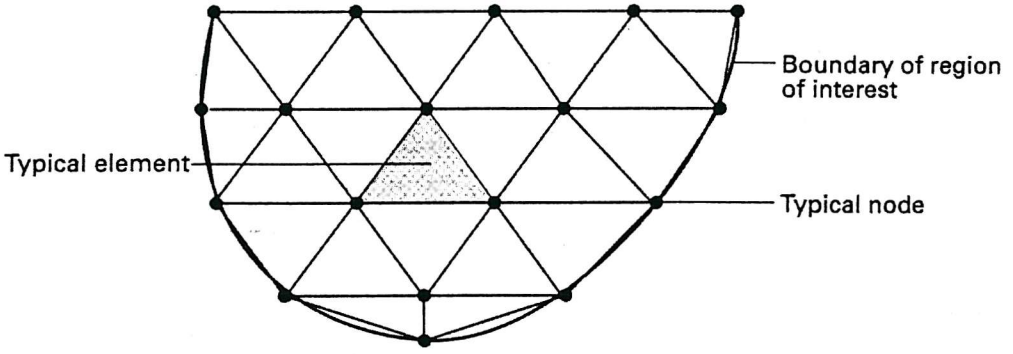

Figure E.1. Discretisation of a region by means of finite elements.

The nodal displacements together with the boundary conditions and the compatibility equations of the material define, through appropriate interpolation functions, the stress field within the element. There are seven steps involved in the analysis: formulation of the differential equations, discretisation of the body to be studied, selection of the interpolation functions, determination of the material properties of each element,

assembly of the system equations, solution of the global set of equations and analysis of the results.

The solution produced by the finite element method is different from the exact solution due to the approximations involved in the technique. The amount of error may be reduced by decreasing the element size or by increasing the order of the polynomial function that describes the element. Therefore, the analyst should perform a convergence study, i.e. repeating the analysis with a variety of mesh densities, in order to reduce the estimated error to a pre-defined acceptable level.

A finite element model is usually made of more than one element type or size. The finite element model should be created to mathematically simulate the structure. The element size should be defined sufficiently small as to capture the stress/strain variations; however, this practice is limited by the computational resources, as the solution time of the model increases considerably with the number of elements used.

E.1. Formulation for an elastic solid.

A three dimensional solid body can be discretised by means of different element types (see section E.2).

E.1.1. Displacements, deformations and stresses.

An element is defined by the number of nodes and the order of the interpolation function. For example, a two dimensional triangular element can have three nodes and have a linear interpolation function or have six nodes and have a quadratic interpolation function. The displacements **u** can be approximated using equation E.1.

$$\mathbf{u} \approx \hat{\mathbf{u}} = \sum \mathbf{N}_i \mathbf{a}_i^e = \left[\mathbf{N}_i, \mathbf{N}_j, \mathbf{N}_k, \ldots\right] \begin{Bmatrix} \mathbf{a}_i \\ \mathbf{a}_j \\ \mathbf{a}_k \\ \vdots \end{Bmatrix}^e = \mathbf{N}\mathbf{a}^e \qquad \text{(E.1.)}$$

where $\mathbf{a}_i$ are the unknown displacements of the nodes, *i, j, k* etc and $\mathbf{N}_i$ are the interpolation functions.

Equation E.2 describes the displacements in the three directions of any point of an element e.

$$\mathbf{u} = \{u(x,y,z) \quad v(x,y,z) \quad w(x,y,z)\} \tag{E.2}$$

Equation E.3 describes the displacements of the node i.

$$\mathbf{a}^e = \{u_i \quad v_i \quad w_i\}^e \tag{E.3}$$

The functions N_i, N_j, N_k,.. are selected in such a way that when substituted in equation E.1, the nodal displacements are obtained, hence:

$$\begin{aligned} &N_i(x_i,y_i,z_i) = I && \text{(Identity matrix)} \\ &N_i(x_j,y_j,z_j) = N_i(x_k,y_k,z_k) = 0, \text{ etc.} && \text{(Null matrix)} \end{aligned} \tag{E.4}$$

The deformations ($\boldsymbol{\varepsilon}$) can now be determined based on the displacements, by means of equation E.5 (matrix notation).

$$\boldsymbol{\varepsilon} = \mathbf{Su} \tag{E.5}$$

where **S** is the following linear operator:

$$\boldsymbol{\varepsilon} = \begin{Bmatrix} \varepsilon_x \\ \varepsilon_y \\ \varepsilon_z \\ \gamma_{xy} \\ \gamma_{yz} \\ \gamma_{xz} \end{Bmatrix} = \begin{Bmatrix} \dfrac{\partial u}{\partial x} \\ \dfrac{\partial v}{\partial y} \\ \dfrac{\partial w}{\partial z} \\ \dfrac{\partial u}{\partial y} + \dfrac{\partial v}{\partial x} \\ \dfrac{\partial v}{\partial z} + \dfrac{\partial w}{\partial y} \\ \dfrac{\partial u}{\partial z} + \dfrac{\partial w}{\partial x} \end{Bmatrix} = \begin{bmatrix} \dfrac{\partial}{\partial x} & 0 & 0 \\ 0 & \dfrac{\partial}{\partial y} & 0 \\ 0 & 0 & \dfrac{\partial}{\partial z} \\ \dfrac{\partial}{\partial y} & \dfrac{\partial}{\partial x} & 0 \\ 0 & \dfrac{\partial}{\partial z} & \dfrac{\partial}{\partial y} \\ \dfrac{\partial}{\partial z} & 0 & \dfrac{\partial}{\partial x} \end{bmatrix} \begin{Bmatrix} u \\ v \\ w \end{Bmatrix} = \mathbf{Su} \tag{E.6}$$

Substituting in equation E.1, equation E.7 is obtained:

$$\boldsymbol{\varepsilon} = \mathbf{SNa} = \mathbf{Ba} \tag{E.7}$$

Once the interpolation functions N_i, N_j, N_k,... are known it is easy to obtain matrix **B** (equation E.8), which correlates deformations and nodal displacements.

$$\mathbf{B} = \sum_{i=1}^{n} \mathbf{B}_i = \sum_{i=1}^{n} \begin{bmatrix} \dfrac{\partial N_i}{\partial x} & 0 & 0 \\ 0 & \dfrac{\partial N_i}{\partial y} & 0 \\ 0 & 0 & \dfrac{\partial N_i}{\partial z} \\ \dfrac{\partial N_i}{\partial y} & \dfrac{\partial N_i}{\partial x} & 0 \\ 0 & \dfrac{\partial N_i}{\partial z} & \dfrac{\partial N_i}{\partial y} \\ \dfrac{\partial N_i}{\partial z} & 0 & \dfrac{\partial N_i}{\partial x} \end{bmatrix} \tag{E.8}$$

where $\mathbf{B}_i$ is the deformation matrix of the element for a given node i.

The stresses are related to the deformations by the Hook law. Considering that the system has residual stresses σ_0 and initial deformations ε_0, the equation that describes this is the following:

$$\boldsymbol{\sigma} = \mathbf{D}(\boldsymbol{\varepsilon} - \boldsymbol{\varepsilon}_0) + \boldsymbol{\sigma}_0 \tag{E.9}$$

where **D** is the elasticity matrix that contains the material properties and is the stress vector (equation E.10).

$$\boldsymbol{\sigma} = \{\sigma_x \quad \sigma_y \quad \sigma_z \quad \tau_{xy} \quad \tau_{yz} \quad \tau_{xz}\}^T \tag{E.10}$$

For an isotropic material, **D** can be defined as a function of the Young's modulus **E** and the Poisson coefficient **ν** (equation E.11).

$$D = \frac{E(1-\nu)}{(1+\nu)(1-2\nu)} \begin{bmatrix} 1 & \frac{\nu}{(1-\nu)} & \frac{\nu}{(1-\nu)} & 0 & 0 & 0 \\ & 1 & \frac{\nu}{(1-\nu)} & 0 & 0 & 0 \\ & & 1 & 0 & 0 & 0 \\ & & & \frac{1-2\nu}{2(1-\nu)} & 0 & 0 \\ & \textit{Symetric} & & & \frac{1-2\nu}{2(1-\nu)} & 0 \\ & \textit{Matrix} & & & & \frac{1-2\nu}{2(1-\nu)} \end{bmatrix} \tag{E.11}$$

E.1.2. Equilibrium equations

The forces $\mathbf{q}^e$ acting on the nodes have to be in equilibrium with the stresses and the distributed external forces **b** acting on an element.

For equilibrium to exist between nodal forces , stresses and distributed forces, a virtual, arbitrary displacement $\delta\mathbf{a}^e$ is imposed and is made equal to the virtual work of all the forces involved (equation E.12).

$$\delta W = \delta \mathbf{a}^{eT} \mathbf{q}^e \tag{E.12}$$

The internal virtual work per unit volume exerted by the stresses and distributed forces is represented in equation E.13.

$$\delta\boldsymbol{\varepsilon}^T\boldsymbol{\sigma} - \delta\mathbf{u}^T\mathbf{b} = \delta\mathbf{a}^{eT}\left(\mathbf{B}^T\boldsymbol{\sigma} - \mathbf{N}^T\mathbf{b}\right) \tag{E.13}$$

From equations E.12 and E.13, equation E.14 is obtained:

$$\delta\mathbf{a}^{eT}\mathbf{q}^e = \delta\mathbf{a}^{eT}\left(\int_{V^e}\mathbf{B}^T\boldsymbol{\sigma}\,dV - \int_{V^e}\mathbf{N}^T\mathbf{b}\,dV\right) \tag{E.14}$$

This is true for any virtual displacement, hence equation E.14 is equivalent to equation E.15.

$$\mathbf{q}^e = \int_{V^e}\mathbf{B}^T\boldsymbol{\sigma}\,dV - \int_{V^e}\mathbf{N}^T\mathbf{b}\,dV \tag{E.15}$$

Equation E.16 represents the equilibrium equation for one element:

$$\mathbf{q}^e = \mathbf{K}^e\mathbf{a}^e + \mathbf{f}^e \tag{E.16}$$

where the stiffness matrix $\mathbf{K}^e$ is defined by equation E.17:

$$\mathbf{K}^e = \int_{V^e}\mathbf{B}^T\mathbf{D}\mathbf{B}\,dV \tag{E.17}$$

and the force vectors associated are defined in equation E.18:

$$\mathbf{f}^e = -\int_{V^e}\mathbf{N}^T\mathbf{b}\,dV - \int_{V^e}\mathbf{B}^T\mathbf{D}\boldsymbol{\varepsilon}_0\,dV + \int_{V^e}\mathbf{B}^T\boldsymbol{\sigma}_0\,dV \tag{E.18}$$

Equation E.18 describes the volumetric forces, the initial deformations and the initial stresses.

When analysing the entire system, the internal forces disappear from the equations and a force per unit area is included. As a result, the force vector is expressed as:

$$\mathbf{f} = -\int_V \mathbf{N}^T \mathbf{b}\, dV - \int_A \mathbf{N}^T \mathbf{t}\, dA - \int_V \mathbf{B}^T \mathbf{D}\boldsymbol{\varepsilon}_0\, dV + \int_V \mathbf{B}^T \boldsymbol{\sigma}_0\, dV \tag{E.19}$$

where the global stiffness matrix is:

$$\mathbf{K} = \int_V \mathbf{B}^T \mathbf{D}\mathbf{B}\, dV \tag{E.20}$$

resulting in the typical matrix equation that needs to be solved in any finite element analysis (equation E.21):

$$\mathbf{K}\mathbf{a} = \mathbf{f} \tag{E.21}$$

From the point of view of a user of commercial programs, finite element analysis consists of three major steps:

- Pre-processing
- Solution
- Post-processing

Pre-processing involves the generation of the model to be analysed. This includes the generation of the mesh of elements, definition of boundary conditions, assignment of material properties and application of loads on appropriate nodes.

The next step involves the solution of the system of equation corresponding to the parameters defined at the pre-processing stage. The appropriate numerical algorithm to solve the systems of equations is usually selected by the analyst based on the computational capabilities available, the accuracy and the solution time required.

Post-processing consists in the visualisation of the results, such as stresses, nodal displacements or any other parameter of interest. Commercial finite element codes usually offer a broad range of parameters that can be listed or plotted for a selected group of elements or nodes; however, the analyst often needs to create additional outputs to display values defined by combining parameters calculated by the software (such as the risk ratio, equation 5.4). The von Mises stress is usually selected as a parameter of interest in structural analysis, which is defined by equation E.22:

$$\sigma_{VM} = \sqrt{\frac{1}{2} \cdot \left[(\sigma_1 - \sigma_2)^2 + (\sigma_2 - \sigma_3)^2 + (\sigma_1 - \sigma_3)^2 \right]} \qquad \text{(E.22)}$$

where σ_{VM} is the von Mises stress and σ_1, σ_2 and σ_3 are the principal stresses.

E.2. Element types

One of the most important choices in building a finite element model is the element type to be used. Most finite element programs include a range a different element types, which are categorised by family, order and topology (see Table E.1).

The element family refers to the characteristics of geometry and displacement modelled by the element. The simplest element type should be used. Additionally, it is important to consider the type of output desired when selecting the element family. The order of an element refers to the order of the equation (linear, parabolic or cubic) used to

interpolate the strain between the nodes. The element topology is related to the general shape of the element, such as bricks, wedges or tetrahedrons (for 3D analysis).

Table E.1. Element types.

Family	Order	Topology
One dimensional elements		
Spring Damper Gap Constraint Rod Beam Pipe		
Two dimensional elements		
Membrane Plane stress Plane strain Thin shell Thick shell	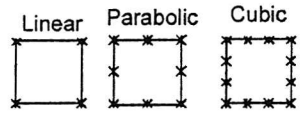	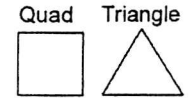
Three dimensional elements Solid	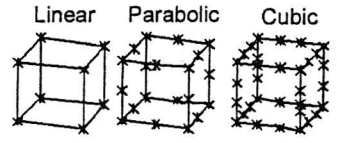	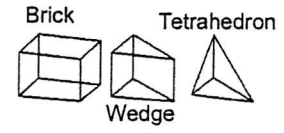

E.3. Linear vs. non-linear analysis

Finite element commercial codes make a clear distinction between linear and non-linear analyses. In general, linear analyses provide the linear response of the system based on the initial or original state (before applying the external loads). Non-linear analyses define a sequence of events that follow one another, in such a way that the end of one integration step (solution increment) represents the initial conditions for the start on the following step. Usually, in finite element analyses of solid structures, linear solutions are considered when the deformations present in the structure are small, in which case the final solution is based in the initial configuration (geometry, node coordinates, application points of the forces, etc). On the other hand, non-linear analyses are used when either the displacements resulting from the application of external forces are relatively large or when other sources of non-linearities are present in the problem, e.g. contact between two bodies. In this case, the solution process is much more complex, as the external forces usually need to be applied in various steps and the results (stresses,

displacements, deformations, etc) obtained from each step provide the initial conditions for the following step. Depending on the problem the number of increments needed to obtain an reliable solution can vary. The number of increments can be defined by the analyst based on his experience or on observations taken from tests performed on the same problem. Alternatively, commercial codes usually have internal algorithms that vary the size of the increments automatically during the solution process, based on the partial results obtained from the previous increments.

The models analysed in this thesis, included contact between two bodies, the implant and the bone. This type of problem presents several sources of non-linearities, hence all these analyses were performed using a non-linear solver, and the solution was obtained in several increments, resulting in considerably high solution times in most models (up to one week in some cases).

REFERENCES

- Collins J.A. 1981. *Failure of Materials in Mechanical Design – Analysis, Prediction, Prevention.* John Wiley & Sons.

- Fagan M.J. 1992. *Finite Element Analysis – Theory and Practice.* Prentice Hall.

- I-DEAS Master Series™ 7. Student Guide.

- Logan D.L. 1986. *A First Course in the Finite Element Method.* PWS-KENT.

- Zienkiewicz O.C., Taylor R.L. *Finite Element Method.* McGraw-Hill.